2019

Polymerized ionic liquids by condensation polymerization: Stimuli responsive polyurethane gels and dispersions

Harshit Gupta

Polymerized Ionic Liquids by Condensation Polymerization: Stimuli Responsive Polyurethane Gels and Dispersions

by

Harshit Gupta

Thesis

Submitted to the School of Engineering Technology

Eastern Michigan University

in partial fulfillment of the requirements

for the degree of

MASTER OF SCIENCE

in

Polymers & Coatings Technology

Thesis Committee:

John Texter, PhD, Chair

Vijay Kumar Mannari, PhD

Mohamed El-Sayed, PhD

March 14, 2019

Ypsilanti, Michigan

Acknowledgements

The author would like to thank Professor John Texter for his incredible support and guidance throughout this project. The author would also like to thank thesis committee members for their valuable feedback and wonderful insights in this work. The author is thankful to Forough Zareanshahraki for her precise analysis of resins by GPC on his behalf. The author would also like to thank Anuj Agarwal for his amazing assistance in getting particle size analysis of PUDs. The author would also like to thank his friend Swapnil Shukla for performing DSC when author was away from EMU. The author is grateful for the continued support and encouragement of his friends Himanshu Manchanda, Roopkatha Pallye, Raviteja Komminneni, and Shuxiao Li during this work. The author is indebted to his family for their unflinching faith in him which has been continued source of motivation for him. On a final note, the author appreciates words of wisdom and advice given by his colleagues at Axalta Coating Systems, which paved the way for successful completion of this work.

Abstract

Ionic liquids have been used in free radical polymerizations to make polymerized ionic liquid (PIL) materials of various types. PIL gels based on imidazolium cations have been found to exhibit an anion-exchange induced stimuli responsiveness. This thesis explores incorporation of ionic liquids in polyurethane (PU) polymers to make PIL PU gels and dispersions through condensation polymerization. PIL gels are synthesized through a single-pot approach that show stimuli response to solvents. This approach allows one to make these gels rapidly and cheaply on-site. These gels can reversibly porate in different solvents and are found to be porous when analyzed by scanning electron microscope (SEM). PIL based resins are also made in two steps, that show self-dispersion properties in water forming thermodynamically stable nano-scale particles. These materials can be transported as 100% solid resins, where they can be transformed into polyurethane dispersions (PUDs) onsite. These particles also show stimuli responsiveness to different anions and solvents.

Table of Contents

List of Tables

List of Figures

Chapter 1

Introduction and Background

1.1. Polyurethanes

Polyurethanes and polyureas (PUs) compose an important class of polymers used to make composites and materials in various industrial segments. Their structure-property relationships promote their use in diverse applications because it is easy to tune their physical properties by modifying their molecular components. They are the only class of materials that can provide thermoplastic, elastomeric, and thermosetting behaviors based on different chemistries and morphologies.[1] PUs are used in a variety of applications, including thermal insulation;[2] foams used for cushioning[3] and sound absorption,[4] as binders in coatings,[5] sealants,[6] and adhesives;[7] and as elastomers.[8] Therefore, PUs are important materials in industries like furniture and bedding,[9] automotive,[10] aircraft,[11] marine,[12] plastics,[1] textiles,[1] footwear,[1] construction,[1] pipelines,[1] and many more.[1,13] PU-based technology has been growing and is predicted to increase even more due to PU's growing demand from end applications in these industries.

Industrial and consumer polyurethanes are made by step-growth polyaddition polymerization of different combinations and selections of monomers, oligomers, or polymers of various diisocyanates and diols. A fairly high reactivity of isocyanate groups with nucleophilic hydroxy groups makes this chemistry favorable. It was seen that reactivity of isocyanates was higher in tertiary nitrogen atoms containing polyols and primary hydroxyls had higher reactivity compared to secondary hydroxyl groups.[14] A general trend in reactivity has been observed to decrease in order: primary alcohols > secondary

alcohols > 2-alkoxyethanols > 1-alkoxy-2-propanols > tertiary alcohols.[15] Also, isocyanates containing aromatic oligomers have higher reactivity than their aliphatic counterparts. Though urethane formation can occur without a catalyst at ambient temperatures, reactivity can be increased by using a variety of catalysts including bases (tertiary amines, alkoxides, carboxylates), metal salts and chelates, organometallic compounds, acids, and urethanes.[15] Some examples of compounds used for catalysis are tertiary amines, commonly diazabicyclo[2.2.2]octane (DABCO), and organotin(IV) compounds, most commonly, dibutyltindilaurate (DBTDL).[15] Formation times of polyurethane networks and formation times of interpenetrating polymer networks (IPNs), gel times, also depend upon catalyst concentration at a particular temperature.[16]

Polyurethanes are also widely used in coatings with various chemistries tailoring curing behaviors. They are used as 2K (two part) solventborne coatings having a hardener derived from diisocyanate precursors to form crosslinked networks with polyols.[17] They can also be used as 1K (single part) systems having blocked isocyanates as a crosslinker,[18] e.g., in cathodic electrodeposition coatings, where in the presence of a catalyst and elevated temperature, crosslinker deblocks and crosslinks with polyols and amines to form urethane and urea networks respectively.[15] DBTDL has better catalytic activity for 2K hydroxyl-isocyanate crosslinking systems then for 1K deblocking-based crosslinking systems.[15] It was reported that DBTDL did not catalyze deblocking of MEKO blocked isocyanates, but rather, it catalyzed formation of allophanates, thus reducing availability NCO groups.[18] Many other catalysts that are effective in 2K curing reactions do not perform in blocked isocyanates curing reactions.[18,19] Hydrolysis during cure and loss of ligands (carboxylate or dionate) deactivates the catalyst.[19,20] Bismuth tris(2-ethyl hexanoate), cobalt bis(2-ethyl hexanoate), and Ti tetra(ethyl acetoacetato) showed

good catalytic activity for 1K blocked isocyanate-hydroxy reactions. At ambient temperature, isocyanates can also react with water to form urea and carbon dioxide gas. This phenomenon is used to develop moisture curable coatings that can cure at very low temperatures[21] and to develop PU foams. Polyurethanes are also very popular in water-based coating systems where they are used as polyurethane dispersions (PUDs),[15,22] discussed in section 1.2.

Urethane and urea –NH– groups always act as proton donors, whereas oxygen atoms within a urethane C=O group, or within ester and ether groups in a polymer backbone chain act as proton acceptors. Therefore, urethane, ester, and ether groups in PUs do not only affect the polymer cohesion energy but are also active in forming hydrogen bonds.[23] Polyols, when reacted with diisocyanates to form isocyanate terminated prepolymers, are further reacted with short chain diols or diamines called the chain extenders, to form higher molecular weight PUs. These smaller equivalent weight diols and diamine as chain extenders lead to formation of hard segments of urethane and urea, respectively, whereas polyols with high equivalent weight and flexible chains make soft segments. These soft segments impart softness and flexibility to the material as their glass transition temperatures are below the lower use temperature of the polymer, resulting in a rubbery material. Hydrogen bonds and dispersion influences of polar urethane groups in hard segments can contribute to aggregation of those groups and formation of a compact rigid phase, whereas many fewer polar interactions in soft segments contribute to formation of a soft phase. Miscibility of these phases might vary in each system based on interactions between the phases. It is also possible that if these phases are completely immiscible, two separate phase transition points can be observed as two clearly different glass temperatures and a microphase separated morphology typically develops. Glass transition temperatures and mechanical properties such as hardness and flexibility can, therefore, be tailored by incorporation

of soft and hard segments and by controlling interactions between these segments through careful selection of polyols. For example, in a polyethyleneglycol (PEG)-based segments in a PHU, hydroxyl groups can hydrogen bond to soft segments with accessible ether groups resulting in phase mixing. This interaction can be reduced by using soft segments with sterically hindered ether oxygen such as in polypropyleneglycol (PPG), which results in robust and nanophase-separated PHU.[23] These hard and soft segments also affect amounts of crystalline and amorphous structures developed and affect different physical properties including abrasion and solvent resistance.[24-27]

This intermolecular hydrogen bonding distinguishes polyurethanes from some other engineering polymers. These attractive forces transfer stress from one molecular polymer chain to another. Applied stress results in absorption of energy by separation of hydrogen bonds. However, these bonds subsequently reform when the stress is removed.[15,28] Thus, the probability of mechanical degradation of polyurethanes is reduced due to this bond-breaking and re-forming mechanism.[28] This property makes PU coatings an excellent choice for aerospace applications because interchain hydrogen bonding can provide low temperature flexibility and fluid resistance.[11] Temperatures experienced by aircraft external coatings during a flight can vary from −54 to 177 °C (−65 to 350 °F). An aircraft undergoes frequent pressurization and depressurization cycles and varied exposure to high temperature, humidity, and salt water during flight between different regions in the world. Therefore, aircraft coating systems need to perform well under both environmental and mechanical stresses during multiple flights.[29]

1.2. Polyurethane Dispersions (PUDs)

It has become clear since the 1950s that our environment has been severely impacted by chemistries emanating from coating formulations and from coating.[30] A major reason to modify coating technologies is to reduce volatile organic compounds (VOCs) entering our atmosphere. Many new technologies have emerged to mitigate such VOCs such as powder coatings, high solids coatings, UV curable coatings, and waterborne coatings.[15] Waterborne coating systems involve replacing a large percentage of organic solvent by water. Since most polymers used as binders in coatings are not soluble in water, they can be modified for waterborne applications by introducing hydrophilic segments into respective polymer backbones, which can be either anionic, cationic or nonionic.[31] These hydrophilic sites can make polymers dispersible or soluble in water. Polyurethane dispersions are increasingly contributing to this transformation. Polyurethane dispersion resins are generally high molecular weight polyurethane polymers that are dispersed in water. These dispersed polymers are also latex particles, but they are called polyurethane dispersions (PUDs) since hydrogen-bonding with water molecules allow particles to swell in water and they get different properties than conventional acrylic system-based latexes. This interaction with water results in plasticizing the polymer, which helps in better coalescing and film formation with higher T_g polymers than is possible with acrylic latexes.[15]

Industrially, anionic and cationic polyurethanes are prepared in three to five steps. In cases of anionic (anionically charged chains) PUDs, a first step is to prepare an isocyanate-terminated prepolymer by reacting diols and a polymerizable anionically ionizing monomer, such as dimethylol propionic acid (DMPA), with excess diisocyanate in a solvent such as acetone or *N*-methylpyrrolidone (NMP). A next step is to create hydrophilic sites by adding tertiary amines that interact with acidic groups to make carboxylic anions in an amphiphilic

chain. This step is also known as neutralization step. This amphiphilic material is then added to water to form a two-phase suspension, and a dispersion is made by adding mechanical shear energy. Next, the molecular weight of this material is increased by extending the chain using low equivalent weight diamine to rapidly form urea linkages between prepolymer isocyanate end groups.[32] In an optional last step, solvents are stripped out to reduce VOC in the final product.[33,34] This multi-step synthesis and dispersion process is illustrated in Fig 1.1.

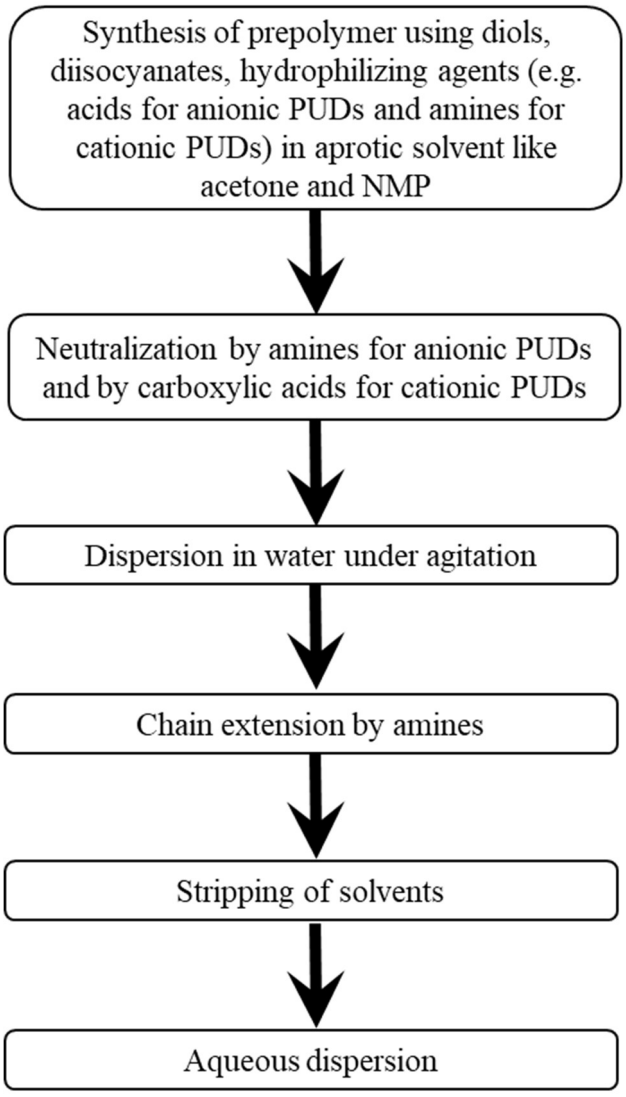

Figure 1.1. Synthetic process to prepare anionic or cationic PUDs in the industries.

Similarly, in cationic PUDs, a prepolymer is first made which consists of polyols, diisocyanates, and a tertiary amine containing diol such as *N*-methyl diethanolamine (NMDEA) in a suitable solvent. Selected solvents such as acetone, NMP, and methylethyl ketone should not react with isocyanates. In a next step, these prepolymers are neutralized with a carboxylic acid or quaternized with an alkyl halide to make amphiphilic salts or cations. This amphiphilic material is then added to water under mechanical shear to form a dispersion. Next, the molecular weight of this prepolymer is increased by extending the chain using low equivalent weight diamine to rapidly form urea linkages between prepolymer isocyanate end groups.[32] In the last step, solvents are stripped out to reduce VOC from the final product.[33]

Anionic PUDs are used in various applications, such as waterborne automotive topcoats, adhesives, primers for metals, binders in hygiene coatings, architectural coatings, floor coatings, wood finishes, coatings for aircraft, defoamers, associative thickeners, pigment pastes, and textile dyes.[11,35,36] Cationic PUDs are used in cathodic electrodeposition, where cations play an important role in applications of coatings on a substrate. They are also used in inkjet printing applications and as coatings on anionic substrates.[37] Cationic quaternary ammonium salt-based PUDs have shown good wetting properties and are, therefore, widely used as pigment dispersants.[38] Tertiary amine acid salt containing resins are used as pigment dispersants for cathodic electrodeposition coatings.[39] Other applications are discussed later in Chapter 7.

1.3. Ionic Liquids

Organic salts that can melt at temperatures below 100 °C are categorized as ionic liquids (ILs).[40] Those ILs that melt at and below ambient temperature are known as room temperature ionic liquids (RTIL).[41] ILs possess enhanced properties such as chemical and thermal stability,

ionic conductivity, low vapor pressure, specific solvating strength, and solubility, which have made them popular.[42-44] RTILs are popular as green solvents in polymerization reactions because they provide a highly polar environment and can be recovered and recycled effectively. Additionally, they have negligible vapor pressure, no flash point, and no flammability.[41,45] ILs can also be used as catalysts and as well as monomers and ionomers in various polymerization reactions such as free radical chain and controlled radical polymerization reactions including atom transfer radical polymerization (ATRP) and reversible addition-fragmentation transfer (RAFT) polymerizations.[42,46]

Typical IL cations include pyridinium, pyrrolidinium, piperidinium, imidazolium, phosphonium, and sulfonium ions with one or more alkyl chains. These charged molecules are paired by anions such as PF_6^-, $CF_3SO_3^-$, Br^-, Cl^-, I^-, BF_4^-, and $(CF_3SO_2)_2N^-$. IL properties are highly dependent on an IL's specific cation-anion pair. Imidazolium ILs can be made hydrophilic by using anions such as Br^-, Cl^-, and S^{2-}, and they can be made hydrophobic by using anions such as I^-, CN^-, and PF_6^-. Therefore, solubility and hydrophobicity of an imidazolium IL can be tuned over orders of magnitude by varying the counter anion.[47,48]

1.4. Polymerized Ionic Liquids

IL monomers are used in polymerizations to make polymerized ionic liquid (PIL) materials of various types. These types include gels that have high ionic conductivity and can also exhibit stimuli responsiveness. Polymeric gels can be prepared by any of the following techniques: (a) free radical polymerization of polymerizable ILs, (b) doping ILs into a polymer matrix, and (c) in situ polymerization of vinyl monomers in ILs. [42,46]

PIL gels based on imidazolium cations have been found to exhibit an anion-exchange-induced stimuli responsiveness by exchange of anions like bromide and tetrafluoroborate with anions like hexafluorophosphate. In aqueous gels, reversible porosity accompanies such exchange. A hydrogel was synthesized by using free radical polymerization technique with 1-(2-acryloyloxyundecyl)-3-methylimidazolium tetrafluoroborate (IL-BF_4), methyl methacrylate (MMA), ethylene glycol dimethylacrylate (EGDMA), 1-propanol, and H_2O. In Fig 1.2, this transparent hydrogel turned opaque during immersion in 0.1 M aqueous KPF_6 solution. This KPF_6 treated opaque film became clear after it was immersed in DMSO, which again became opaque when DMSO was replaced with water.[43]

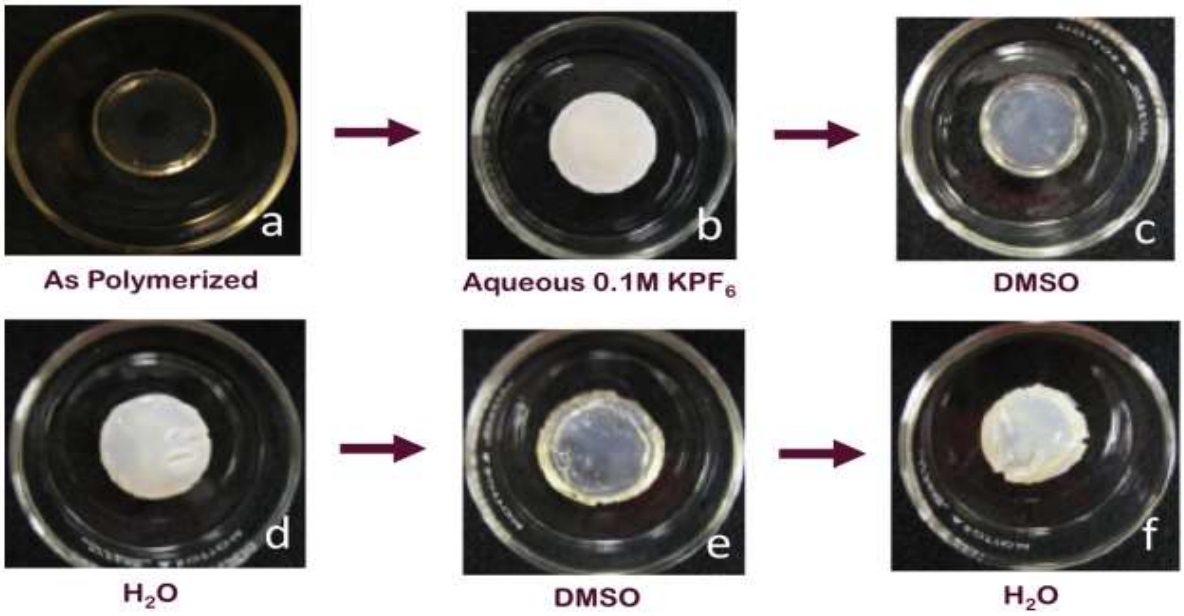

Figure 1.2. Pictures of hydrogel: (a) as polymerized; (b) after immersion in 0.1 M KPF_6; (c) after immersion in dimethyl sulfoxide (DMSO); (d) after immersion in H_2O; (e) after immersion in DMSO; (f) after immersion in H_2O, by Gu. (Reprinted from ref. 43).

Yan and Texter synthesized an IL based nonpolymerizable surfactant 1-dodecyl-3-methylimidazolium bromide (a-Br) and an IL-based polymerizable surfactant 1-(2-

acryloyloxyundecyl)-3-methylimidazolium bromide (b-Br). They were successfully able to make latex nanoparticles by using a microemulsion polymerization technique with MMA and water using these surfactants separately. Free radical polymerization was initiated by 2,2-azobisisobutyronitrile (AIBN). In Fig. 1.3, polymerization using a nonpolymerizable surfactant, a-Br, produced a monodisperse latex, which had an average particle diameter of ~50 nm.[49]

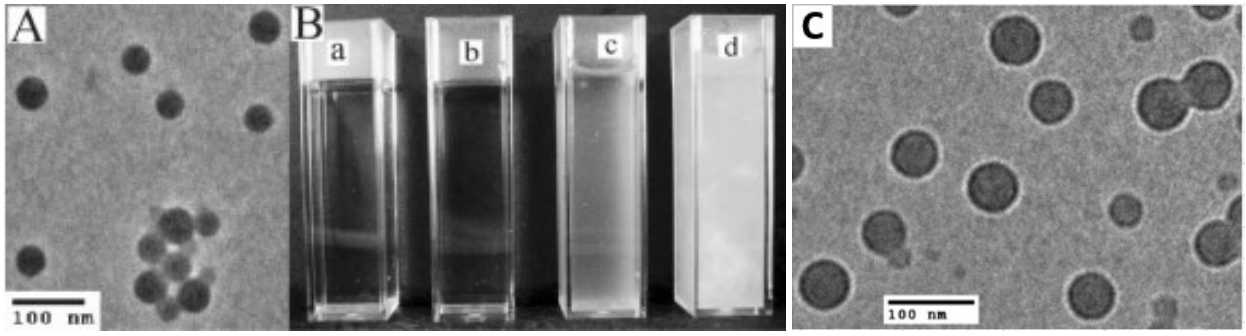

Figure 1.3. (A) TEM image of polymer latexes produced from microemulsion stabilized by b-Br; (B) polymer latexes dispersed in (a) water, (b) 0.1 M NaBr solution, (c) 0.1 M $NaBF_4$ solution, and (d) 0.1 M KPF_6 solution; (C) TEM image of polymer latexes produced from microemulsion stabilized by a-Br, by Yan and Texter. (Reprinted from ref. 49).

Polymerization using a polymerizable surfactant, b-Br, produced a monodisperse and clear latex suspension, which had an average particle size of ~30 nm. On increasing the amount of surfactant and MMA in microemulsion polymerization, they were able to make transparent gels. Such gels shrank and became opaque when immersed in aqueous KPF_6 (Fig. 1.4(B)). When observed under scanning electron microscopy (SEM), an open-cell porous structure was formed (Fig. 1.4(B)). This opaque gel became semitransparent and expanded after it was immersed in aqueous NaBr, and pores appeared to significantly close (Fig. 1.4(C)).[49]

England and Texter also observed similar behavior in materials prepared by microemulsion polymerization from the reactive ionic liquid, 1-(2-acryloyloxyundecyl)-3-methyl-imidazolium bromide (ILBr, b-Br), with MMA and water. Free radical polymerization

was initiated by AIBN. Latex particles formed by this microemulsion polymerization were used to form a clear film on a glass slide, which became porous and turbid when treated with 0.1 M aqueous KPF_6 solution. Other gels formed by increasing the amount of MMA also resulted in the formation of pores when treated with aqueous 0.1 M KPF_6 solution.[50,51] Ion exchange of Br^- by PF_6^- increased the hydrophobicity resulting in porosity by a pinned spinodal decomposition mechanism.[52]

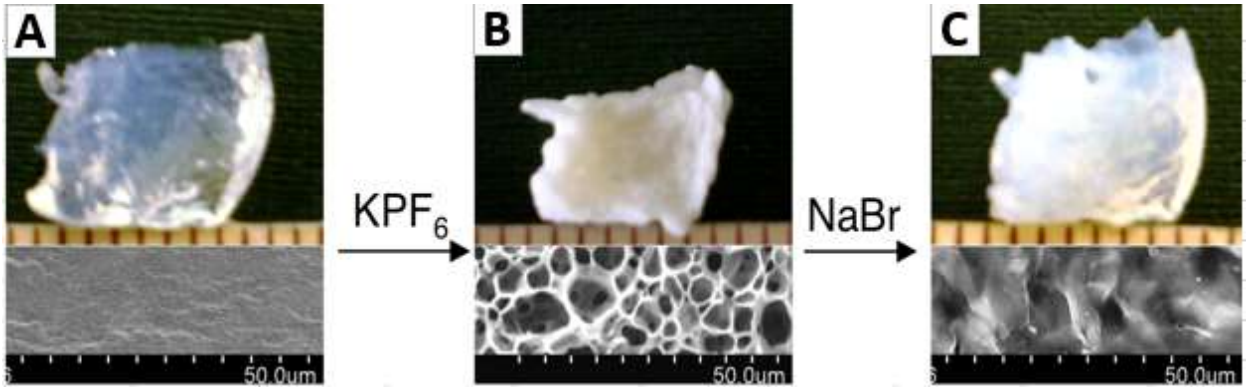

Figure 1.4. (A) Polymer gel after microemulsion polymerization with an SEM image underneath; (B) gel in (A) treated with 0.1 M KPF6 solution with an SEM image underneath showing porosity; (C) gel in (B) treated with 0.1 M NaBr solution with an SEM image underneath showing decrease in porosity, by Yan and Texter. (Reprinted from ref. 49).

In addition to open-cell porosity produced in gels, the nanolatexes formed at lower surfactant compositions in the ternary ILBr, water, and MMA system were found to form transparent films on coating and following coalescence. This behavior is illustrated in Fig. 1.5.

This thesis explores PILs synthesized by condensation polymerization. All these new PILs are polyurethanes (PUs), and these PUs are doped with an IL monomer. After describing general methods and experimental procedures, we synthesize and characterize the IL monomer used in these studies, 1-undecyl-3-methyl-imidazolium bromide, $C_{11}C_1ImBr$. The use of this monomer to make new PU gels, and characterizing their stimuli-responsiveness are described

next. We then explore an exciting new phenomenon, self-dispersing polyurethane dispersions, PUDs. Possible future applications for these new materials are summarized.

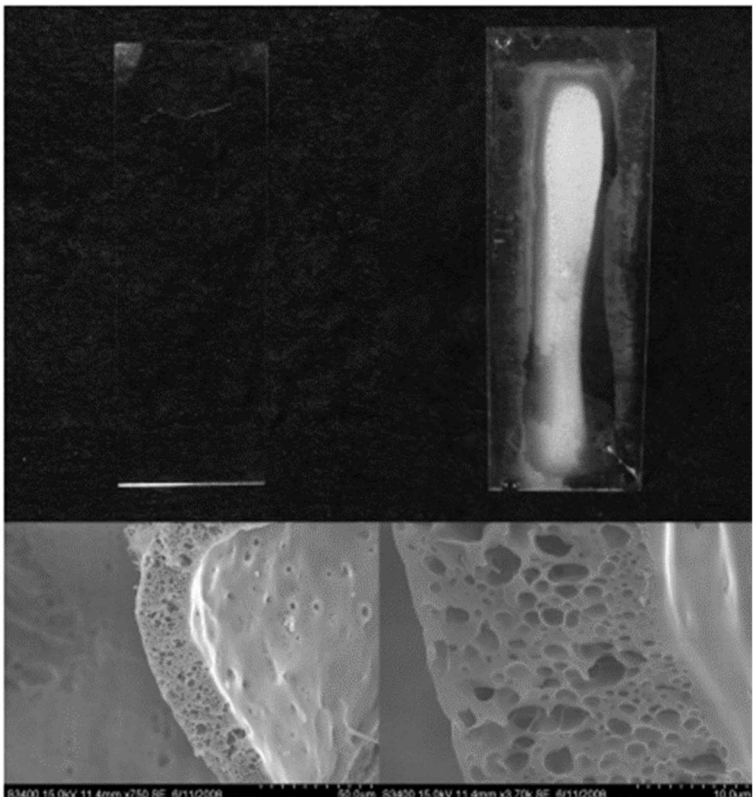

Figure 1.5. Optical micrographs of nanolatex coating on a glass slide, before (top left) and after (top right) treatment with 0.1 M KPF_6. Bottom images are SEM of a nanolatex film treated with 0.1 M KPF_6, by England. (Reprinted from ref. 50).

Chapter 2

Experimental

2.1. Materials

1-Methylimidazole (≥99%), triethyl amine (≥99%), and 11-bromo-1-undecanol (≥99%) were purchased from Sigma Aldrich and were used to synthesize reactive IL monomers used in this thesis work. Glycerol (≥99%), 1,6-diisocyanato hexane (HDI, 98%), dibutyl tin dilaurate (DBTDL, 95%, catalyst), tri-propylene glycol ($HO(PO)_3H$, 97%, average molecular weight of 192 Da), and glycerol 1,3-diglycerolate diacrylate (containing 1000 ppm monomethyl ether hydroquinone as inhibitor) were purchased from Sigma Aldrich. Polyethylene glycol (number average molecular weight of 200 Da, PEG-200) was purchased from Alfa Aesar.

Solvents including dichloromethane (CH2Cl2, ≥99.8%, anhydrous, 150 ppm amylene as stabilizer), N,N-dimethylformamide (DMF, 99.8%), tetrahydrofuran (THF, ≥99.9%, anhydrous, inhibitor free), and dimethyl sulfoxide (DMSO, ≥99%, ACS reagent) were also purchased from Sigma Aldrich.

Salts used in this research, including sodium bromide (NaBr), potassium iodide (KI), potassium hexafluorophosphate (KPF_6), sodium dicynamide ($NaN(CN)_2$), sodium trifluoromethanesulphonate (CF_3SO_3Na), and sodium tetrafluoroborate ($NaBF_4$), were purchased from Sigma Aldrich. The photoinitiator Darocur-1173 was purchased from Ciba Specialty Chemicals.

2.2. Methods

2.2.1. Synthesis of monomers

2.2.1.1. Synthesis of $HOC_{11}C_1ImBr$ ionic liquid

1-Hydroxyundecyl-3-methyl-imidazolium bromide ($HOC_{11}C_1ImBr$) was synthesized by reacting 1-methyl imidazole with 1-bromo-11-undecaneol dissolved in THF for 24 hours at 60 °C. The product $HOC_{11}C_1ImBr$ is insoluble in THF and was separated by gravity filtration. THF was removed by heating the product in a vacuum oven at 100 °C for 4 h. After this vacuum heating treatment, the ionic liquid product was cooled to solidify and stored in a glass vial inside a desiccator. This ionic liquid was used to make stimuli-responsive polyurethane gels and dispersions.

2.2.1.2. Synthesis of HUTEAB

HUTEAB, hydroxyundecyltriethyl ammonium bromide is used as a control material in PUD synthesis and preparation, described later in Chapter 6. Its behavior and performance is compared with $HOC_{11}C_1ImBr$.

A reactor was put in an oil bath and sparged with nitrogen gas. An excess amount of triethylamine was refluxed with bromoundecanol at 60 °C for 24 hours under continuous stirring using a magnetic stirrer (Fig 2.1). Bromoundecanol melted at 60° C, making the reaction a clear liquid solution. After 24 hours, the main reaction product, HUTEAB, was observed as a white powder precipitate in the reaction suspension.

The product HUTEAB was filtered using a sintered glass filter funnel and was collected in a flask. It was washed with 25 mL of THF while being stirred for 30 minutes. This product salt was insoluble in THF and was filtered. This filtered salt was washed again using acetonitrile as solvent at room temperature, where all the salt dissolved. Salt was recovered after evaporation

of acetonitrile first by evaporation in a hood and then by using a vacuum oven at 65 °C for 2 h. After this vacuum heating treatment, the product was cooled to solidify and stored in a glass vial inside a desiccator.

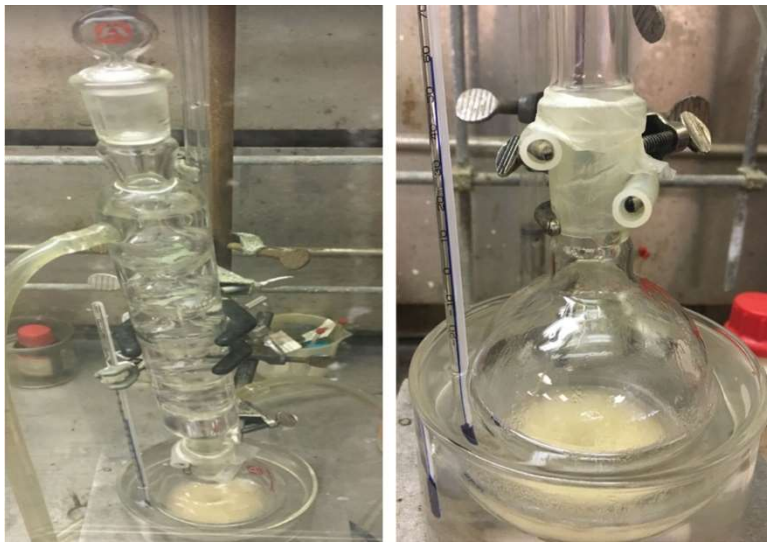

Figure 2.1. Reaction setup for HUTEAB synthesis. White precipitated reaction product can be seen at 60° C.

2.2.2. Synthesis of PIL gels and PUDs

Different combinations of polyols, such as glycerol, PEO200, $HO(PO)_3H(PO)$, $OHC_{11}C_1ImBr$, glycerol 1,3-diglycerolate diacrylate, and hydroxyundecyltriethyl ammonium bromide, were dissolved in dichloromethane and DMF mixtures in glass vials of 16 mL volume. HDI was then added, followed by addition of DBTDL catalyst. Capped glass vials containing reactant solutions were stirred by a vibratory stirrer and were incubated in an oven at a temperature of 80 ºC for 24 hours.

Reactant mixtures containing certain amounts of crosslinkers such as glycerol resulted in formation of crosslinked gels, whereas those that had large amounts of diols such as PEO200 and $HO(PO)_3H(PO)$ resulted in resins that were used to make PUDs. To prepare PUDs from these

resins, solvent was completely removed by first drying in air in a hood and then by using a vacuum oven. These solid samples were put in glass vial and DI water was added to make different weight mixtures. These samples were kept at ambient temperatures for about 24 hours, where self-dispersion of these resins made dispersed PU particles in water. Moderate stirring by vibratory stirrer was given for uniform distribution of particles in aqueous dispersion using a Touch Mixer, Model 232 (Fisher Scientific, Waltham, MA, USA); see Fig. A.2.1 in Appendix A.

2.2.3. Ultrasonication

High intensity ultrasonication was done using a SONIS Vibra Cell system, Model VC 30 (Newtown, CT), with a microtip sonic horn of about 3-4 mm diameter at the tip. Typically, PUD samples were sonicated in glass vials of 20 mL volume, which were held in an ice-water bath inside of a sound-attenuating chamber. Sonication was done for 10 minutes at full amplitude. Vial reactors were covered by aluminum foil during the process of sonication (Fig. A.2.2 in Appendix A).

2.2.4. Coatings

Sonicated PUDs were used to make drawdown coatings on glass slides by using a 1-inch-square drawdown bar. An aim wet film thickness of 75 μm was used. After flashing off water, coatings were heated in an oven at 60 ˚C for 6 min for better coalescence.

In sonicated PUDs containing glycerol 1,3-diglycerolate diacrylate (triglycerol diacrylate) in the polymer chain, the photoinitiator Darocur-1173 was added before coating films on glass slides. After the evaporation of water, these slides were exposed to UV light by using UV-curing equipment (Fusion UV with a H-bulb, Hareas, Gaithersburg, MD)) at a belt speed of 12 ft/min (6 cm/s) with variable numbers of passes.

2.3. Instrumental Measurements

2.3.1. Thermal gravimetric analysis (TGA)

TGA was performed using a TA Instruments (New Castle, DE) TGA Q500 thermogravimetric analyzer in a non-reactive environment of nitrogen gas. Samples were placed in aluminum differential scanning calorimetry (DSC) Tzero-equivalent pans obtained from DSC Consumables, Inc. (Austin, MN, USA), which in turn were placed in platinum TGA suspension pans that were suspended from an arm of the TGA electrobalance. Samples were then heated from room temperature to about 580 °C at a rate of 10 °C/min to generate weight versus temperature data. Weight as a function of temperature and derivatives of these data were generated for analysis.

2.3.2. Differential scanning calorimetry (DSC)

A TA Instruments DSC Q2000 was used to characterize thermal behavior of samples. Samples (5 mg to 12 mg) were placed in Tzero-equivalent DSC aluminum pans and sealed with matching aluminum lids. DSC analysis was done by heating at a given rate to an upper target temperature, held there for five to ten minutes, cooled to a lower target temperature at a given rate, held there for a given hold time, and then heated to a final upper target temperature at a specified heating rate. The resulting data were analyzed to examine glass transitions and melting and heating phenomena.

2.3.3. Gel permeation chromatography (GPC)

A Malvern Viscotek 270 GPC system equipped with refractometer, right angle light scattering, and viscometer detectors on a set of four columns was used to analyze molecular weight distributions of the samples. Filtered (0.2 μ) samples (60-70 mg in 10 ml THF) were manually injected into the system. THF was used as an eluent and was permeated through the

columns at the flow rate of 1 mL/min. Data collected was processed and analyzed using OmniSEC 4.7.0 software. Molecular weights were determined by calibrating with polystyrene standards. Molecular weights are therefore given in terms of polystyrene equivalent weights.

2.3.3. Scanning Electron Microscopy (SEM)

Scanning electron microscopy was done with a Hitachi 3400-N instrument (Hitachi America, Pleasanton, CA). This analysis was used to analyze microscopic structures of PU gels. Secondary electron detection was used. Typically, a high voltage of 15 kV was used during imaging.

2.3.4. Particle size analysis (PSA)

Particle size was investigated by using a Brookhaven 90 Plus nanoparticle size analyzer (Brookhaven Instruments, Hopewell Junction, NY). This instrument uses dynamic light scattering (DLS) of an incident laser (about 622 nm) at a detection angle of 90º. Lognormal and MSD (multimodal size distribution) particle size distributions based on number weighting, volume weighting, and light intensity weighting are generated by proprietary Brookhaven software. Multiple runs were conducted for each sample to gather data, where each run lasted for 3 min.

2.3.5. UV-VIS absorbance

A Beckman DU-800 single beam UV/Vis spectrophotometer (Beckman Coulter, Atlanta, GA, USA) was used for absorbance and turbidity measurements. These measurements were done in a single-beam mode. UV-visible spectroscopy was used to measure turbidity at 500 nm at all stages in 5 mm pathlength spectrosil quartz cuvettes.

2.3.6. Contact angle measurement

Short duration videos were made by using Amscope MU853B 14MP high-speed digital camera to capture dynamic change in contact angle and screenshots at different time intervals from videos were used to measure contact angles of different samples. Contact angles of DI water drops on coated films were evaluated using a software "ImageJ" with a plugin of "drop analysis-dropsnake."[53] Each right and left angle were measured twice to help provide reliable measurements.

PUD coated glass slides were dipped in various 0.1 *M* salt solutions of KI, KPF_6, $NaN(CN)_2$, CF_3SO_3Na, and $NaBF_4$ for 15 min and then rinsed with DI water and air dried for 30 min before measuring contact angles of DI water drops.

Chapter 3

Poly(Ionic Liquid) Gels

3.1. Overview

PILs through condensation polymerization were prepared with their controls without any ionic liquid to compare to solvent induced stimuli-responsiveness that was observed in addition polymerized poly($ILPF_6$-co-MMA) gels reported earlier.[43] First, the monomer 1-hydroxyundecyl-3-methyl-imidazolium bromide ($HOC_{11}C_1ImBr$) was synthesized and characterized by TGA and DSC analysis. This monomer was then used to synthesize PILs. These PILs were characterized by TGA and DSC analysis. Solvent induced stimuli responsive behaviors were checked, and SEM was used to analyze some of the structural changes induced in surface regions of these gels by different solvents.

3.2. Synthesis of $HOC_{11}C_1ImBr$

The 1-Hydroxyundecyl-3-methyl-imidazolium bromide ($HOC_{11}C_1ImBr$) was synthesized by reacting 1-methyl imidazole with 1-bromo-11-undecaneol dissolved in THF. To obtain 5 g of product, 3.77 g of bromoundecanol (251.2 Da) was dissolved in 25 mL THF and 1.23 g of 1-methylimidazole (82.1 Da) was added into this solution. The reaction mechanism is explained by Menshutkin reactions using SN1 and SN2 mechanisms, where two neutral reactants react to produce two charged species[54] (Fig. 3.1). This reaction mixture was purged with nitrogen gas and heated in an oil bath at 60 °C for 24 hours under continuous stirring. The product, $HOC_{11}C_1ImBr$, is insoluble in THF and was separated by gravity filtration. THF was removed by heating the product in a vacuum oven at 100 °C for 4 h. After this vacuum heating treatment, the

ionic liquid product was cooled to solidify and stored in a glass vial inside a desiccator; product in the amount of 3.42 g of this ionic liquid was recovered (68.4% yield). This ionic liquid was used to make stimuli-responsive polyurethane gels and dispersions.

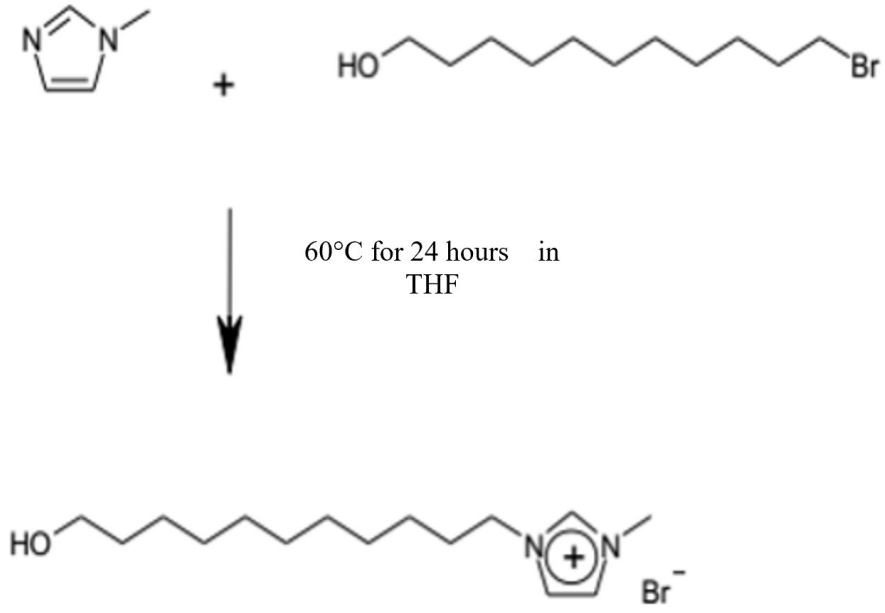

Figure 3.1. Reaction scheme of $HOC_{11}C_1ImBr$. It involves the coupling of neutral 11-bromoundecanol and 1-methylimidazole to yield an ionic liquid.

TGAs were done in an inert atmosphere of nitrogen gas from room temperature to 580 °C at a rate of 10 °C/min. In Fig 3.2, a TGA of $HOC_{11}C_1ImBr$ is compared with the TGAs of its constituents, bromoundecanol and 1-methylimidazole (bp – 198 °C). A single derivative peak at 350 °C can be seen in the $HOC_{11}C_1ImBr$ data. Most of bromoundecanol decomposes at about 230 °C (bp – 170 °C) and 1-methylimidazole at 160 °C. These apparent decompositions may simply be vaporizations. In any case, these TGA comparisons clearly show conversion of both reactants into $HOC_{11}C_1ImBr$.

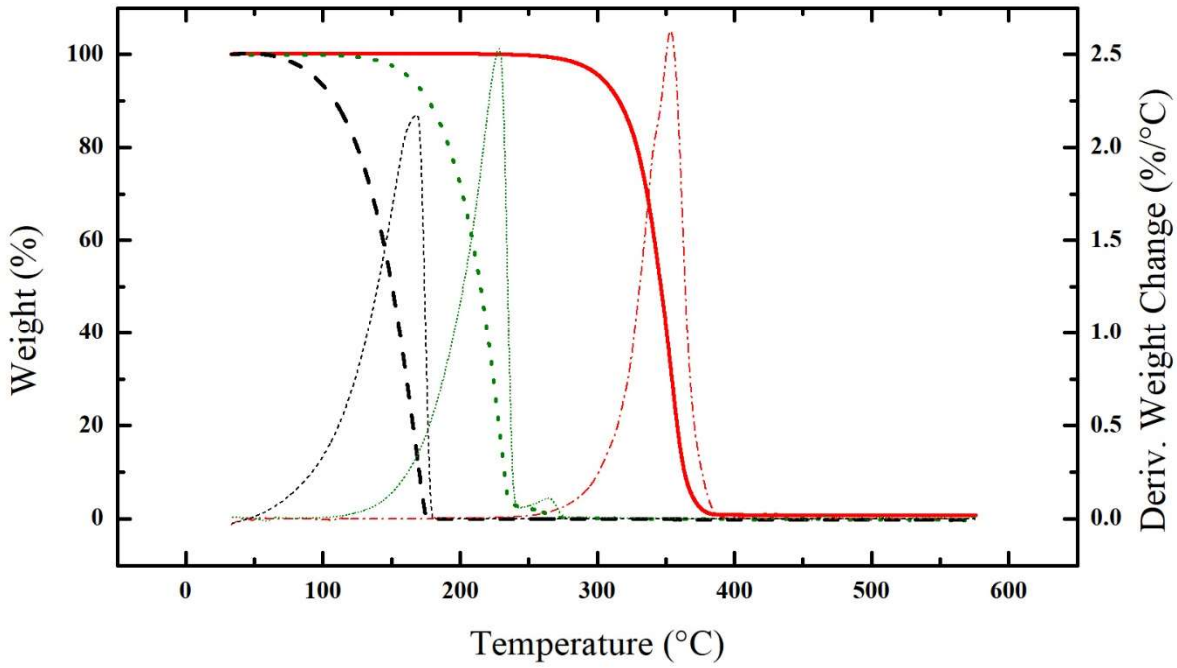

Figure 3.2. Weight percent versus temperature during TGA of $HOC_{11}C_1ImBr$ (——); bromoundecanol (- - - - -) and 1-methylimidazole (– – – –). Derivative weight percent change (right axis), during TGA of $HOC_{11}C_1ImBr$ (-·-·-·-); bromoundecanol (——) and 1-methylimidazole (·····).

During DSC scans of $HOC_{11}C_1ImBr$ and bromoundecanol, samples were first heated to 120 °C to remove any thermal history. Then samples were cooled to -80 °C at a rate of 10 °C/min. Then $HOC_{11}C_1ImBr$ was heated to 150 °C and bromoundecanol was heated to 120 °C (Fig. 3.3).

During cooling, a freezing peak of $HOC_{11}C_1ImBr$ was seen starting at 73.5 °C with a freezing peak at 73.4 °C and a freezing enthalpy of 82.2 J/g. A freezing peak of bromoundecanol was seen starting at 39.5 °C with a freezing peak of 38.1 °C and a freezing enthalpy of 110 J/g. During sample heating, a melting peak for bromoundecanol begins at 43.7 °C with a melting peak at 45.3 °C and 88.8 °C and a melting enthalpy of 82.2 J/g. DSC peaks clearly distinguish $HOC_{11}C_1ImBr$ from its constituent reactant bromoundecanol and also shows that $HOC_{11}C_1ImBr$ is an ionic liquid because its melting point at 89 °C is less than 100 °C (Fig. 3.3).

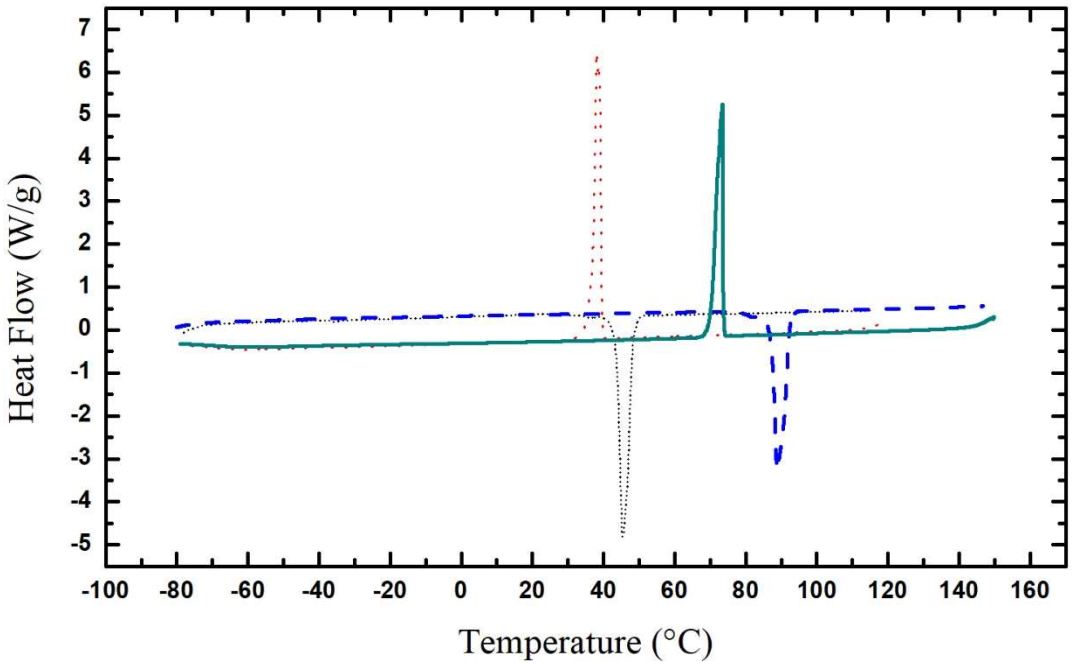

Figure 3.3. DSC of $HOC_{11}C_1ImBr$ and bromoundecanol: (a) $HOC_{11}C_1ImBr$ – cooling (——); heating (– – –); (b) bromoundecanol - cooling (· · · · ·); heating (·····).

3.3. Synthesis of Gels

For each resin, first a pre-resin mixture comprising hydroxy-functional materials were combined in a 15 mL vial prior to polymerization. These hydroxy-functional materials were dissolved using methylene chloride and DMF. DMF was required to achieve room temperature solubilization of the IL. Then, HDI was added, and then these reactant mixtures were stirred using a vibratory mixer. Lastly, DBTD was added as catalyst. Compositions of various ge formulaitons are given in Table 3.1 and Table 3.2.

Table 3.1. Composition of $HOC_{11}C_1ImBr$ PU1 and control PU1

Component	$HOC_{11}C_1ImBr$ PU1		Control PU1	
	Weight (mg)	Millimoles	Weight (mg)	Millimoles
Glycerol	448.8	4.87	914	9.92
$OHC_{11}C_1ILBr$	1120.1	3.36	0	0
HMDI	1801	10.71	1860.6	11.06
CH_2Cl_2	9433.2		8367	
DMF	1522.2		1359	
DBTD	286		286	
Solids	25.02%		23.94%	
NCO/OH ratio	1.19		0.74	
Catalyst based on solids	7.82%		9.34%	

These reaction mixtures invials were stirred, and the vials were observed to become warm and hot because of the exothermic reactions. Control PU1 gelled in 20 s after stirring. Vials were put in an an oven at 80 °C for about 24 hours. $HOC_{11}C_1ImBr$ PU1 and $HOC_{11}C_1ImBr$ PU2 were observed to gel in about 30 min after the vials were put in the oven. Control PU2 was observed to gel in 5 min after it was put in the oven.

Table 3.2. Composition of $HOC_{11}C_1ImBr$ PU2 and control PU2

Component	$HOC_{11}C_1ImBr$ PU2		Control PU2	
	Weight (mg)	Millimoles	Weight (mg)	Millimoles
Glycerol	220.6	2.395	403.3	4.379
$OHC_{11}C_1ILBr$	506.1	1.518	0	0
HMDI	757.9	4.506	1109.8	6.598
CH_2Cl_2	4290.7		4990	
DMF	1346.5		818.2	
DBTD	138.2		160	
Solids	22.35%		22.36%	
NCO/OH ratio	1.04		1.004	
Catalyst based on solids	8.52%		9.56%	

Our $HOC_{11}C_1ImBr$ PU1 and control PU1 had non-stoichiometric ratios, whereas $HOC_{11}C_1ImBr$ PU2 and control PU2 had stoichiometric ratios of NCO and OH functionalities. Figure 3.4 shows a reaction scheme where crosslinking from triple hydroxy functionality of glycerol makes the formation of gels possible. $HOC_{11}C_1ImBr$ is monofunctional and, therefore, acts as a chain terminator.

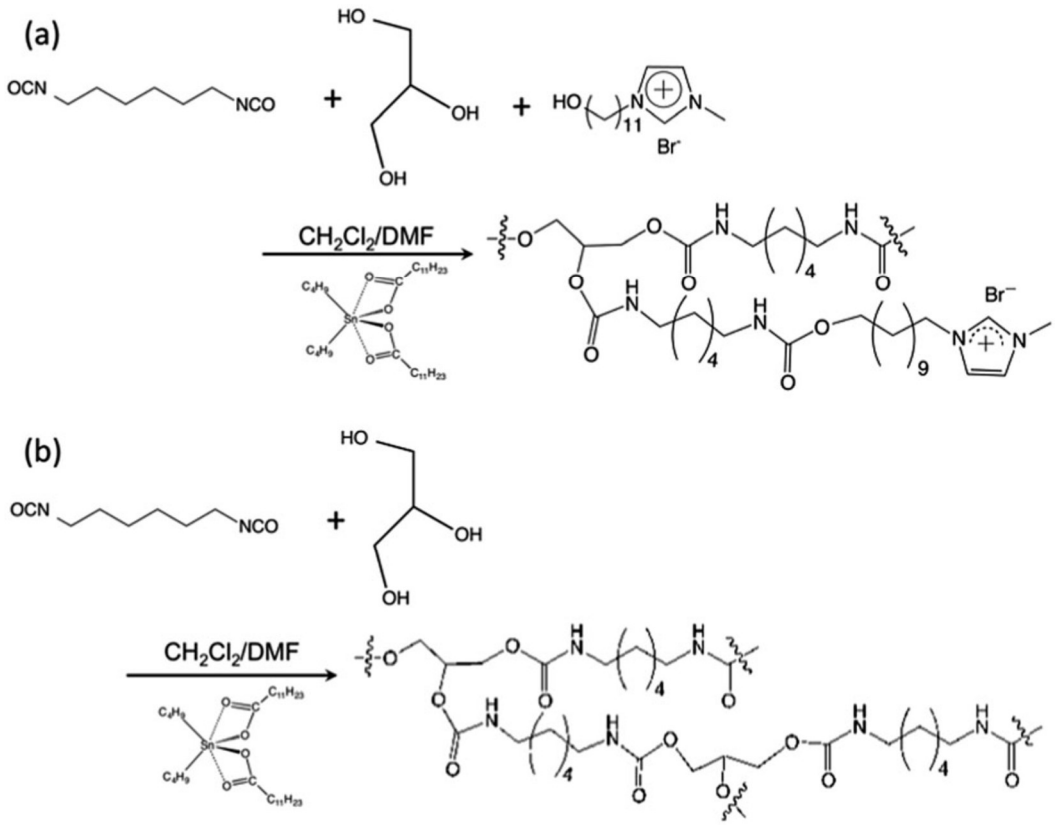

Figure 3.4. Reaction scheme for (a) $HOC_{11}C_1ImBr$ PU1 and $HOC_{11}C_1ImBr$ PU2; (b) control PU1 and control PU2.

Free solvent from syneresis was seen in both control samples after they were removed from the heating oven. Very little solvent was visible in $HOC_{11}C_1ImBr$ containing PILs (Fig. 3.5 and Fig. 3.6). This syneresis seen in control gels suggests that polymer chains are tightly packed compared to PIL gels, which might be porous. $HOC_{11}C_1ImBr$ PU1 had a bright orange color, whereas $HOC_{11}C_1ImBr$ PU2 had a pale yellowish color. The respective controls were white. These orange and yellow colors suggest the presence of bromide ion interactions with imidazolium ions. These gels were very soft and were scooped out in small chunks from their respective reaction vials. These gels were then heated at 120 °C for about 12 h in a vacuum oven to remove solvent.

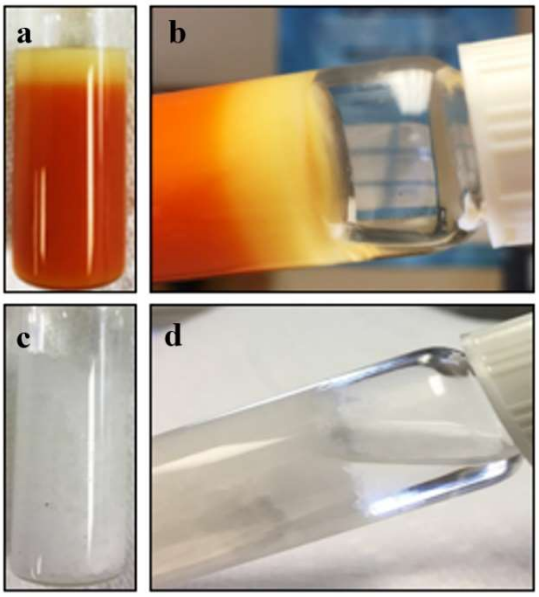

Figure 3.5. (a) $HOC_{11}C_1ImBr$ PU1 in glass vial after removal from oven; (b) 'a' tilted to show free solvent after syneresis; (c) control PU_1 in glass vial after removal from oven; (d) 'c' tilted to show free solvent after syneresis.

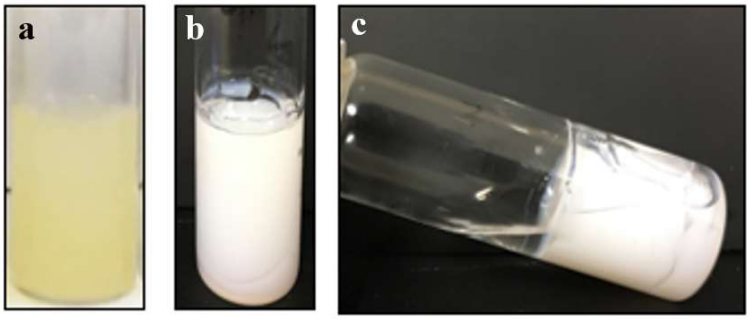

Figure 3.6. (a) $HOC_{11}C_1ImBr$ PU2 in glass vial after removal from oven; (b) control PU2 in glass vial after removal from oven; (c) 'b' tilted to show free solvent after syneresis.

3.4. Thermal Analysis

TGAs were done in an inert atmosphere of nitrogen from room temperature to 580 °C at a rate of 10 °C/min. Figure 3.7 and Fig. 3.8 compare TGAs of $HOC_{11}C_1ImBr$ PU1 and $HOC_{11}C_1ImBr$ PU2 along with their controls without ionic liquid, respectively. From both figures, it can be seen that PILs start to degrade earlier at 230 °C than their controls, which start at about 260 °C, which may be because of lower crosslink densities in PILs. There are three

different decomposition rates in these samples. All the samples decompose sharply from 320 °C to 370 °C, but in case of PILs, decomposition is broadened from 320 °C to 430 °C.

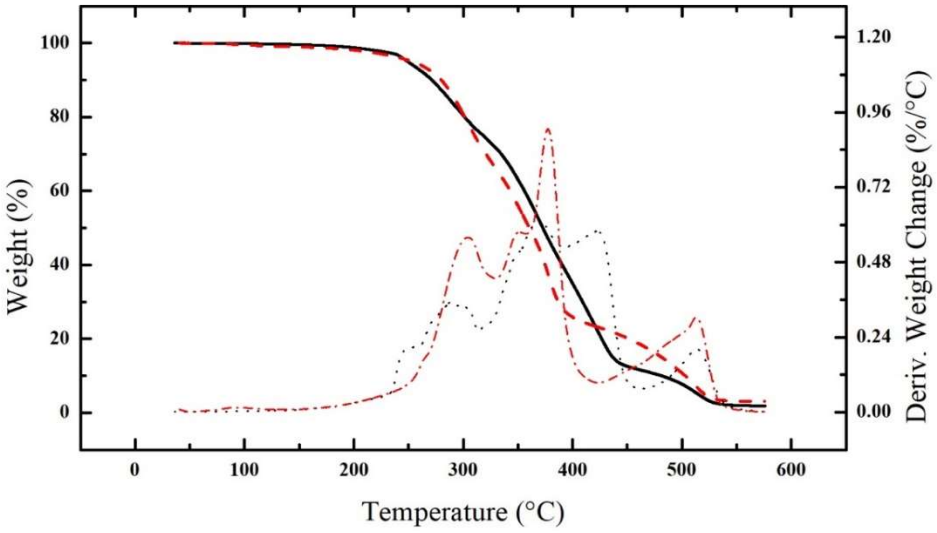

Figure 3.7. Weight percent change, during TGA of $HOC_{11}C_1ImBr$ PU1 (——); control PU1 (– – –). Derivative weight percent change, during TGA of HOC11C1ImBr PU1 (· · · ·); control PU1 (–·–).

During DSC scans of $HOC_{11}C_1ImBr$ PU1 and control PU1 (Fig. 3.9), samples were first heated to 130 °C to remove any thermal history. Samples were then cooled to -80 °C at a rate of 10 °C/min and then were heated to 130°C at the same rate. It was seen that PIL had a slightly lower glass transition temperature (T_g) of 36 °C during the cooling segment and 45 °C during the heating segment.

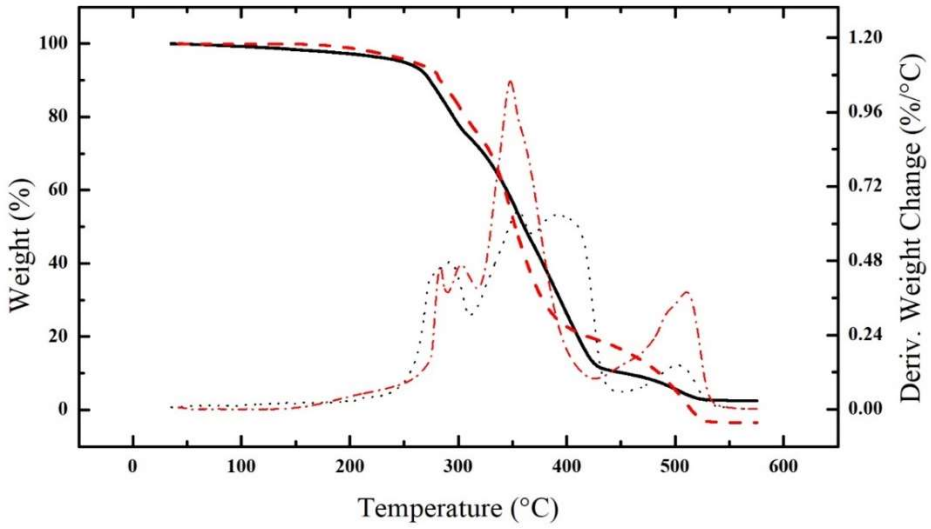

Figure 3.8. Weight percent change, during TGA of $HOC_{11}C_1ImBr$ PU2 (——); control PU2 (- - -). Derivative weight percent change, during TGA of HOC11C1ImBr PU2 (· · · ·); control PU2 (– · –).

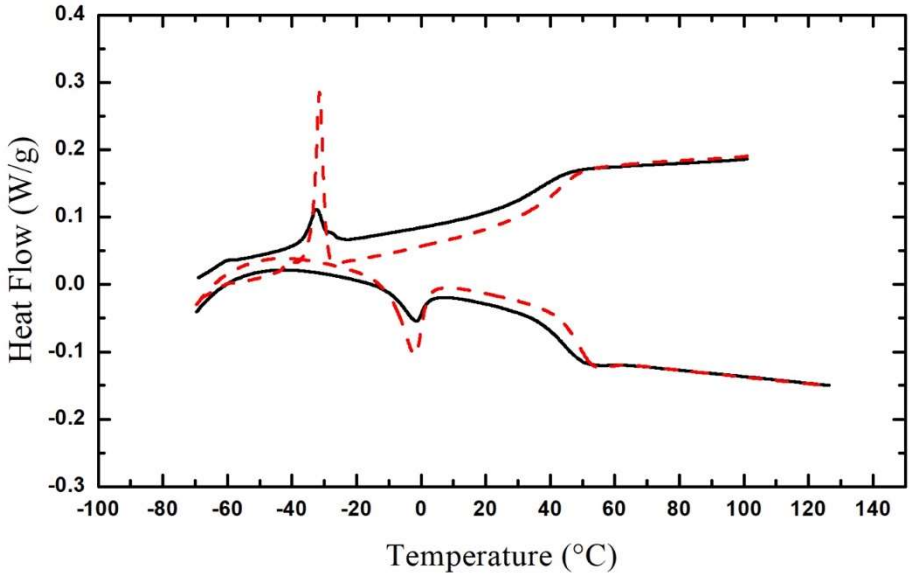

Figure 3.9. DSC at rate of 10 °C/min of: $HOC_{11}C_1ImBr$ PU1 (————) and control PU1 (– – – –).

During the DSC of the $HOC_{11}C_1ImBr$ PU2 sample (Fig. 3.10), it was first heated to 150 °C to remove any thermal history. It was then cooled to -80 °C at a rate of 10 °C/min and then was heated to 150 °C at the same rate. The control PU2 sample was first heated to 130 °C to

remove any thermal history. This sample was then cooled to -90 °C at a rate of 10 °C/min and then was heated to 130 °C at the same rate. This DSC comparison also shows that PIL had a glass transition temperature (T_g) of 39 °C during cooling and 44 °C during the heating. slightly lower than its control that has a T_g of 54 °C during cooling and 58 °C during heating. It was also observed that both samples had a freezing peak below their T_g during cooling and a melting peak below their T_g during heating because of catalyst DBTD. In the $HOC_{11}C_1ImBr$ PU2 sample the freezing peak had an enthalpy of 1.6 J/g with a peak temperature of -25 °C and the melting peak had enthalpy of 1.4 J/g with a peak temperature of -1.3 °C (Fig. A.3.3 in Appendix B). In the control PU2 sample the freezing peak had an enthalpy of 1.4 J/g with a peak temperature of -45 °C and the melting peak had an enthalpy of 1.6 J/g with a peak temperature of -6.8 °C (Fig. A.3.4 in Appendix B). These lower T_gs observed in PILs suggest that ILs have plasticizing effect, and it is likely that their respective polymer matrices have lower crosslink densities.

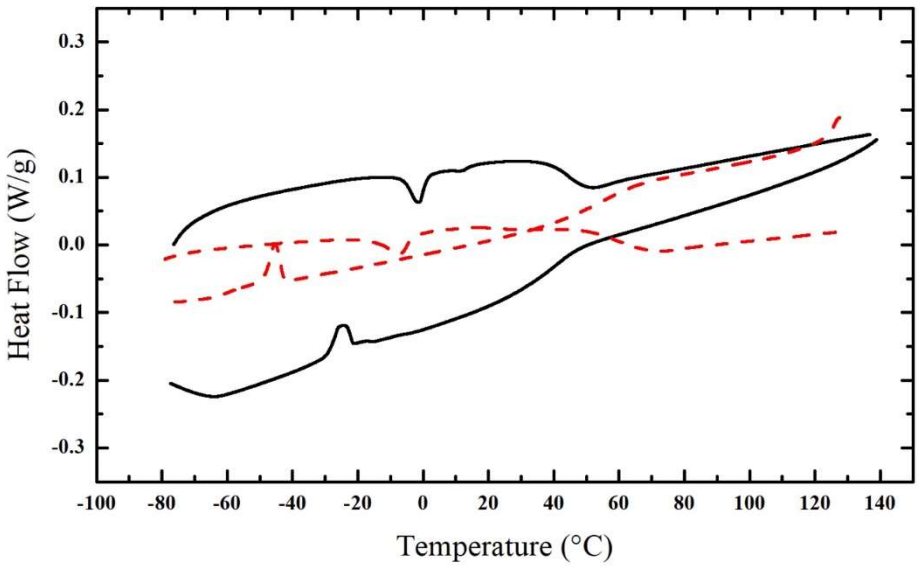

Figure 3.10. DSC at rate of 10 °C/min of: $HOC_{11}C_1ImBr$ PU2 (———) and control PU2 (- - - -).

3.5. Stimuli-Responsiveness

One of the main objectives for preparing these PILs through condensation polymerization was to compare the solvent induced stimuli-responsiveness with that observed for PILs made by addition polymerization, poly(ILPF$_6$-co-MMA) gels, reported earlier.[43] Vacuum-oven-dried pieces of opaque HOC$_{11}$C$_1$ImBr PU$_1$ gel were dipped in DMSO, where they swelled and became translucent as seen in Fig. 3.11(a). When these swelled gels are dipped in 0.1 *M* KPF_6 solution, their decreased segmental solubility, due to more hydrophobic imidazolium-anion pairs involving PF_6^- after exchanging for Br^- ions, causes them to porate and become more highly light scattering and opaque (Fig. 3.11(b)). After KPF_6 treatment, these pieces were dipped in DMSO, which made them translucent again (Fig. 3.11(c)).

When this material is removed from DMSO and flooded with water, it becomes opaque again (Fig. 3.11(d)). Placing this material back into DMSO results in re-solvation of polymer and becomes translucent again (Fig. 3.11(e)). This solvation induced stimuli responsive phenomenon is analogous to what was seen in addition polymerized poly(ILPF$_6$-co-MMA) gels reported earlier.[43] However, this condensation polymerized system differs from the addition polymerized system[43] in an important aspect. This condensation polymerized system, with imidazolium-Br^- ion pairs, is fundamentally more hydrophobic.

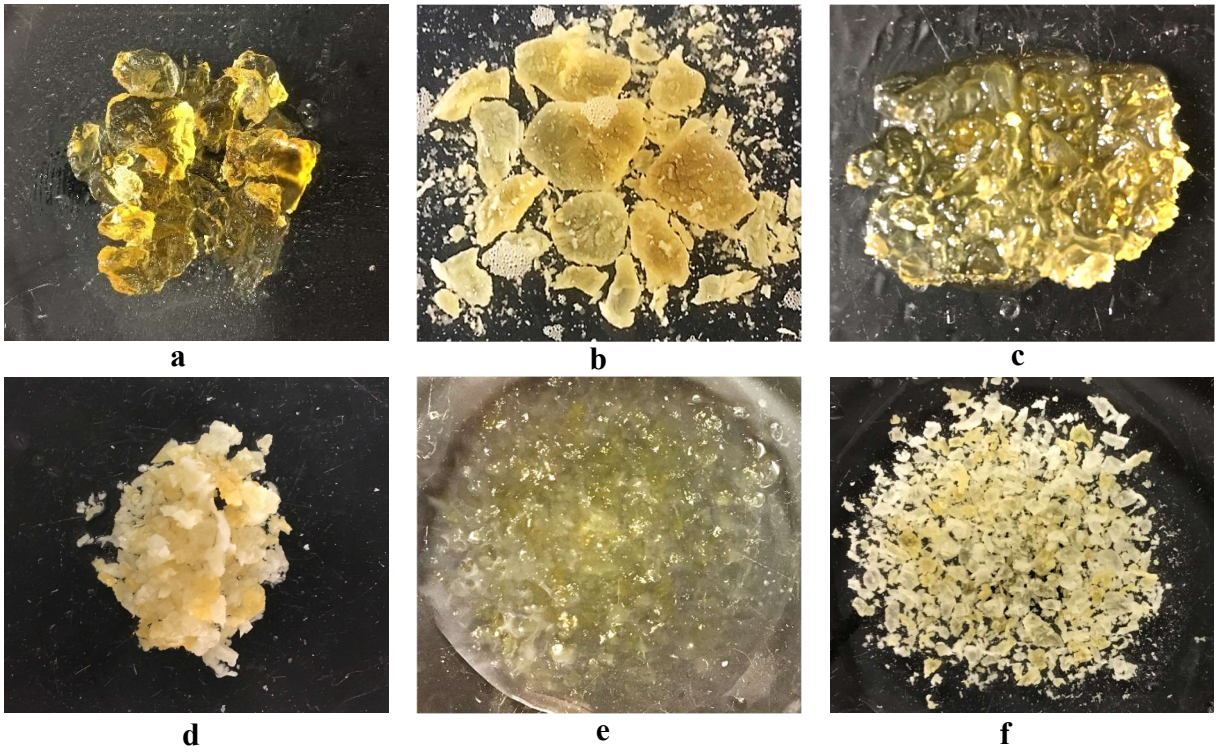

Figure 3.11. Stimuli response to solvents in KPF_6 treated $HOC_{11}C_1ImBr$ PU1: (a) Vacuum-oven-dried $HOC_{11}C_1ImBr$ PU1 gel dipped in DMSO where it swelled and became translucent; (b) 'a' treated with aqueous 0.1 *M* KPF_6 solution; (c) 'b' submerged in DMSO where gel becomes translucent; (d) 'c' submerged in water where gel becomes opaque; (e) 'd' submerged in DMSO where gel becomes translucent again; (f) 'e' submerged in water where gel becomes opaque again.

This greater hydrophobicity effect is made clear in the following sequence of experiments. These vacuum oven dried pieces of opaque $HOC_{11}C_1ImBr$ PU1 gel (Fig. 3.12(a)) were dipped in DMSO, where they swelled and became translucent (see Fig. 3.12(b)). DMSO is a good solvent for the backbone structures and for the imidazolium-Br^- ion pair. These swelled pieces were then removed from DMSO and flooded by excess water. This resin is less soluble in water than in DMSO, even though the imidazolium-Br^- ion pair is hydrophilic. This overall decreased solubility causes this gel to porate and become highly light scattering and opaque again (Fig. 3.12(c)). Placing these pieces back into DMSO results in re-solvation of the

imidazolium bromide ion pairs, as pictured in Fig. 3.12(d) and makes them opaque again when again replaced by water (Fig. 3.12(e)).

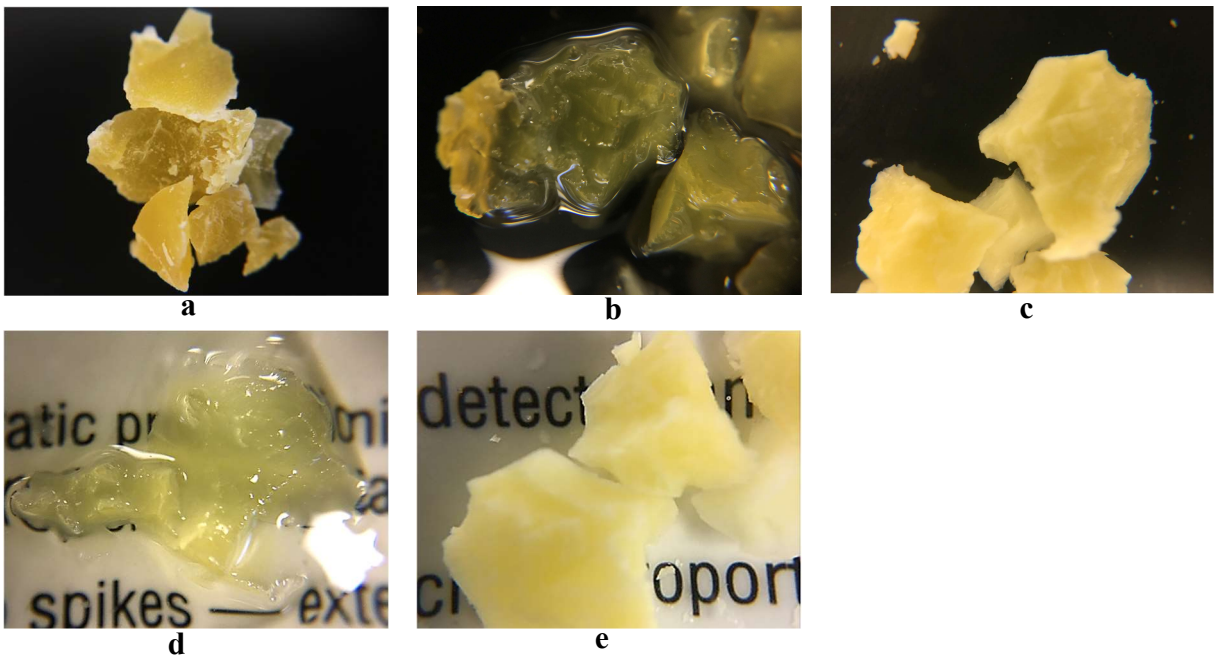

Figure 3.12. Stimuli response to solvents in untreated $HOC_{11}C_1ImBr$ PU1: (a) Vacuum-oven-dried $HOC_{11}C_1ImBr$ PU1 gel; (b) 'a' dipped in DMSO where it became translucent; (c) 'b' dipped in water where gel becomes turbid; (d) 'c' dipped in DMSO where gel becomes translucent; (e) 'd' dipped in water where gel becomes turbid.

When a similar experiment was done with a vacuum dried opaque control PU1 material, where pieces of this material were dipped in DMSO, these pieces swelled, but there was almost no visual change in the turbidity, as can be seen in Fig. 3.13(a) and Fig. 3.13(b). When these swollen pieces were removed from DMSO and put in excess DI water, very slight increase in their opacity were observed (Fig. 3.13(c)). They were again submerged in DMSO and then in DI water, where not much change in turbidity was seen (Fig. 3.13 (c) and Fig. 3.13 (d)).

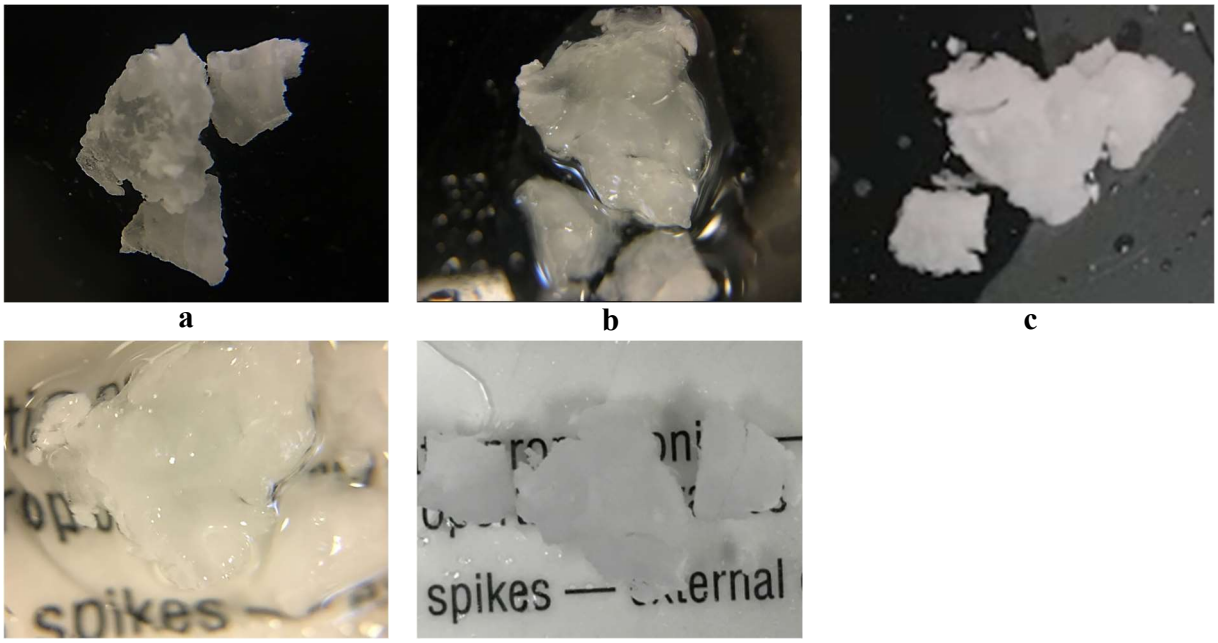

Figure 3.13. Comparing stimuli response to solvents in control PU1: (a) Vacuum-oven-dried control PU1 turbid gel; (b) 'a' submerged in DMSO where it remains turbid; (c) 'b' submerged in water where gel remains turbid; (d) 'c' dipped in DMSO where gel remains turbid; (e) 'd' dipped in water where gel remains turbid.

Similarly, vacuum oven dried pieces of opaque $HOC_{11}C_1ImBr$ PU2 gel (Fig. 3.14(a)) were dipped in DMSO, where they swelled and became transparent as seen in Fig. 3.14(b). These swelled pieces were then removed from DMSO and flooded by excess water. Their decreased solubility caused them to porate and become highly light scattering, where they became opaque again (Fig. 3.14(c)). Placing these pieces back into DMSO results in re-solvation of the imidazolium bromide ion pairs and thus make them transparent, as pictured in Fig. 3.14(d), and makes them opaque again when again replaced by water (Fig. 3.14(e)).

Pieces of vacuum-oven-dried control PU2 samples were transparent, and when they were dipped in DMSO, they swelled and remained translucent as seen in Fig. 3.15 (a) and Fig. 3.15 (b)

respectively. On removing DMSO and flooding them with DI water, they remained translucent with a bluish tinge (Fig. 3.15 (c)). On replacing DI water by excess DMSO, no change in the turbidity was observed as seen in Fig. 3.15 (d) and after replacing DMSO by excess DI water again, transparency/turbidity of the pieces remained same (Fig. 3.15 (e)).

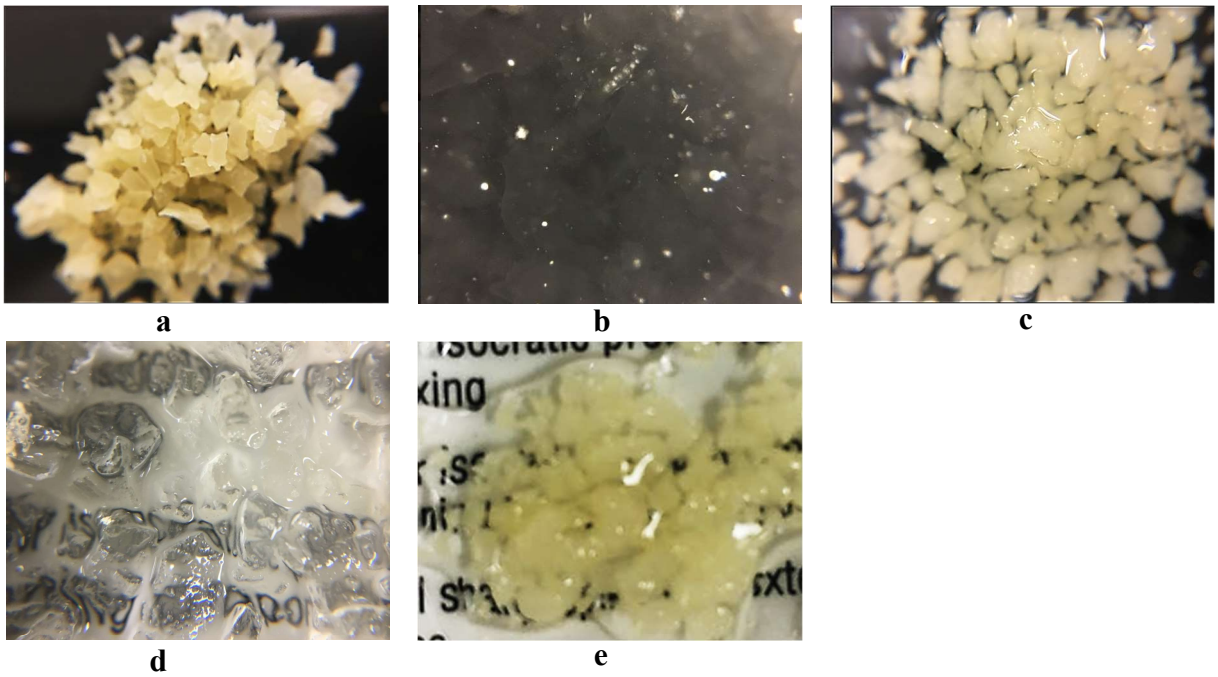

Figure 3.14. Stimuli response to solvents in untreated $HOC_{11}C_1ImBr$ PU2: (a) Vacuum-oven-dried $HOC_{11}C_1ImBr$ PU2 gel; (b) 'a' submerged in DMSO where it became transparent; (c) 'b' submerged in water where gel becomes turbid; (d) 'c' dipped in DMSO where gel becomes transparent; (e) 'd' dipped in water where gel becomes turbid.

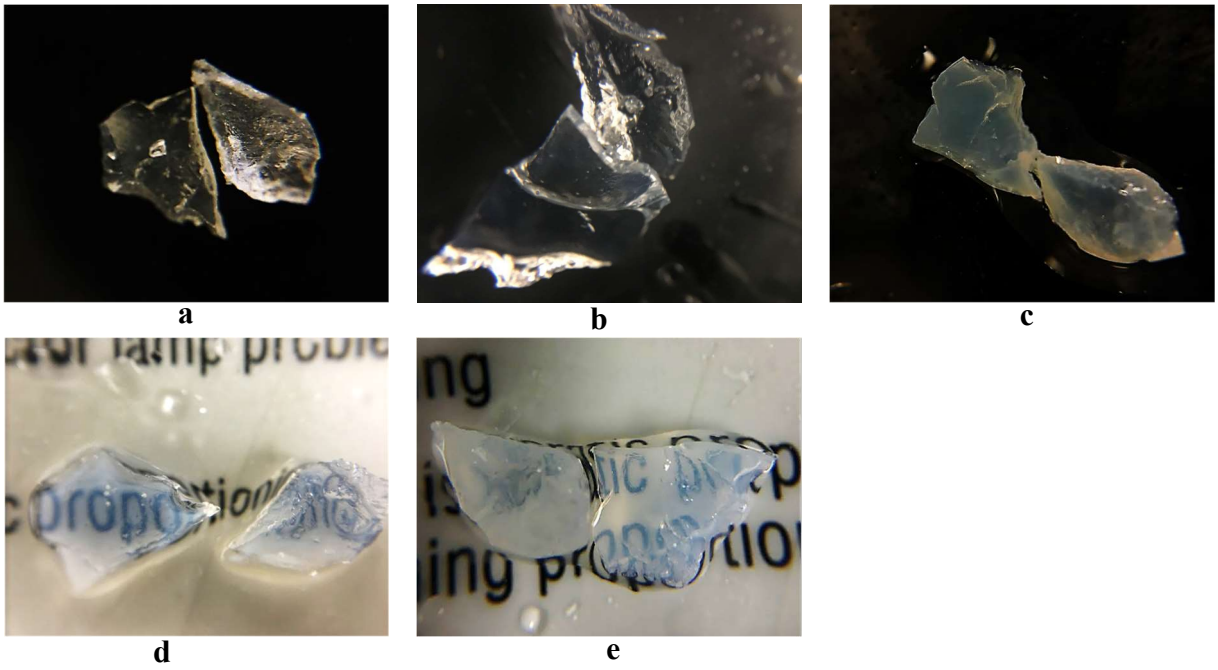

Figure 3.15. Comparing stimuli response to solvents in control PU2: (a) Vacuum-oven-dried control PU2 translucent gel; (b) 'a' submerged in DMSO where it remains translucent; (c) 'b' submerged in water where gel remains translucent; (d) 'c' dipped in DMSO where gel remains translucent; (e) 'd' dipped in water where gel remains translucent.

3.6. Analysis of Gels by SEM

3.6.1. SEM of vacuum-oven-dried gels

SEM was used to analyze the surface structures of various gels. It was observed that $HOC_{11}C_1ImBr$ PU1 and $HOC_{11}C_1ImBr$ PU2 had an open porous structure. $HOC_{11}C_1ImBr$ PU1 had 50 μm pores containing 5μm pores inside and between boundaries distributed all over in the polymer as seen in Fig. 3.16. $HOC_{11}C_1ImBr$ PU2 had 25 μm pores containing 5 μm as seen in Fig. 3.18. $HOC_{11}C_1ImBr$ PU1 as DMSO collapsed smaller pores between boundaries of bigger pores (Fig. 3.16(d)). The control PU1 did not have an open porous structure. Its surface was covered by spheroids of about 5 μm diameter (Fig. 3.17). Regions without these spheroidal structures were also observed (Fig. 3.17(a) and Fig. 3.17(d)). The control PU2 had a very smooth

outer surface without any pores. This microstructure explains its corresponding transparency (Fig. 3.19).

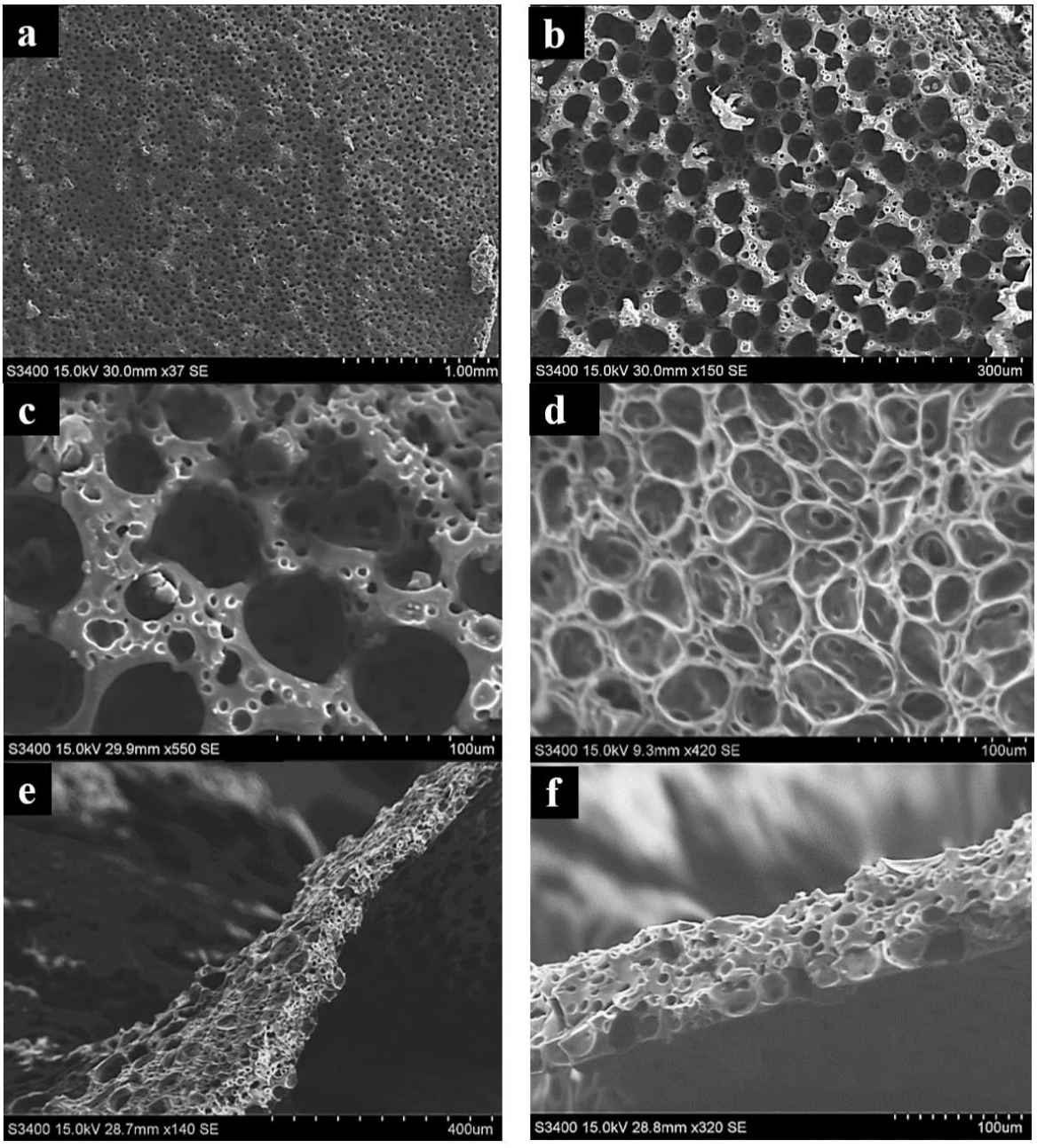

Figure 3.16. SEM of $HOC_{11}C_1ImBr$ PU1 gel: (a, b, c) vacuum-oven-dried piece at different magnifications; (d) open-cell porous structure with about 50 μm pores containing 5 μm pores connecting pores can be seen; after vacuum-oven-dried piece is swelled in DMSO, collapsing of smaller pores between boundaries of bigger pores can be observed; (e, f) not heated in vacuum oven, same structure can be seen as in vacuum-oven-dried sample.

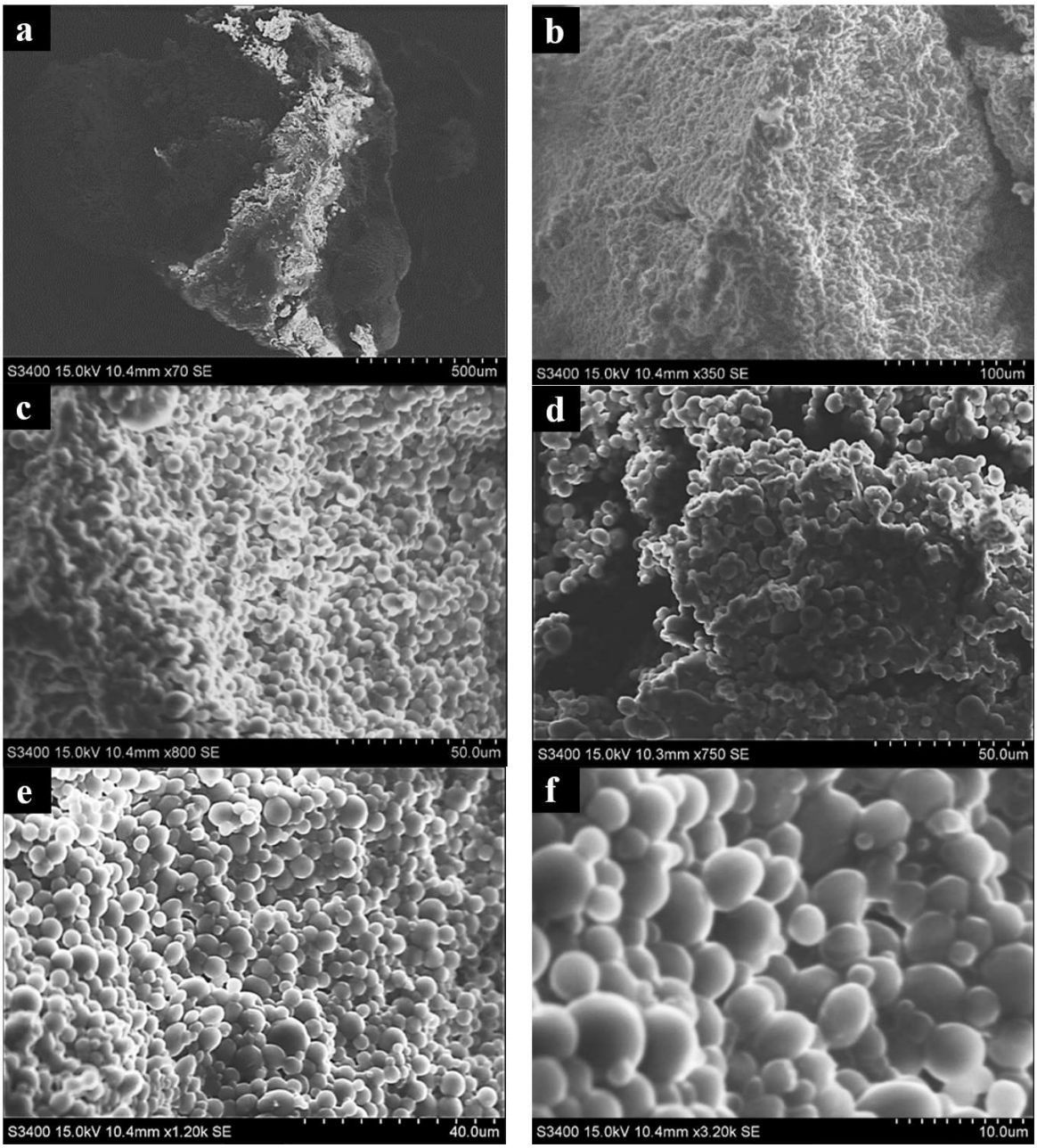

Figure 3.17. SEM of control PU1 gel: (a, b, c, d, e, f) vacuum-oven-dried piece at different magnifications – globular structures seen without any pores.

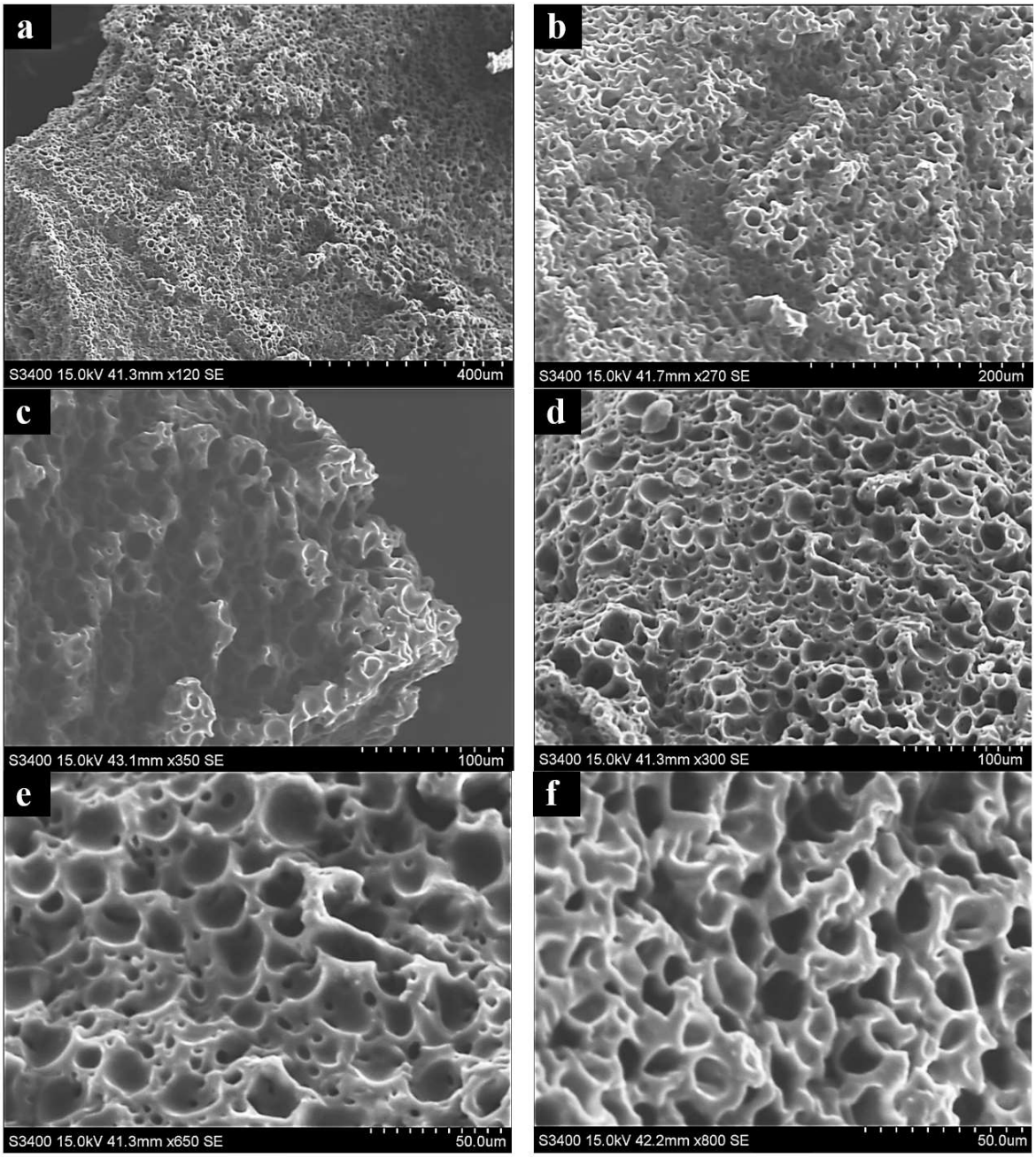

Figure 3.18. SEM of $HOC_{11}C_1ImBr$ PU2 gel: (a, b, c, d, e, f) vacuum-oven-dried piece at different magnifications open porous structure with about 25 μm pores containing 5 μm pores inside and between pore walls can be seen.

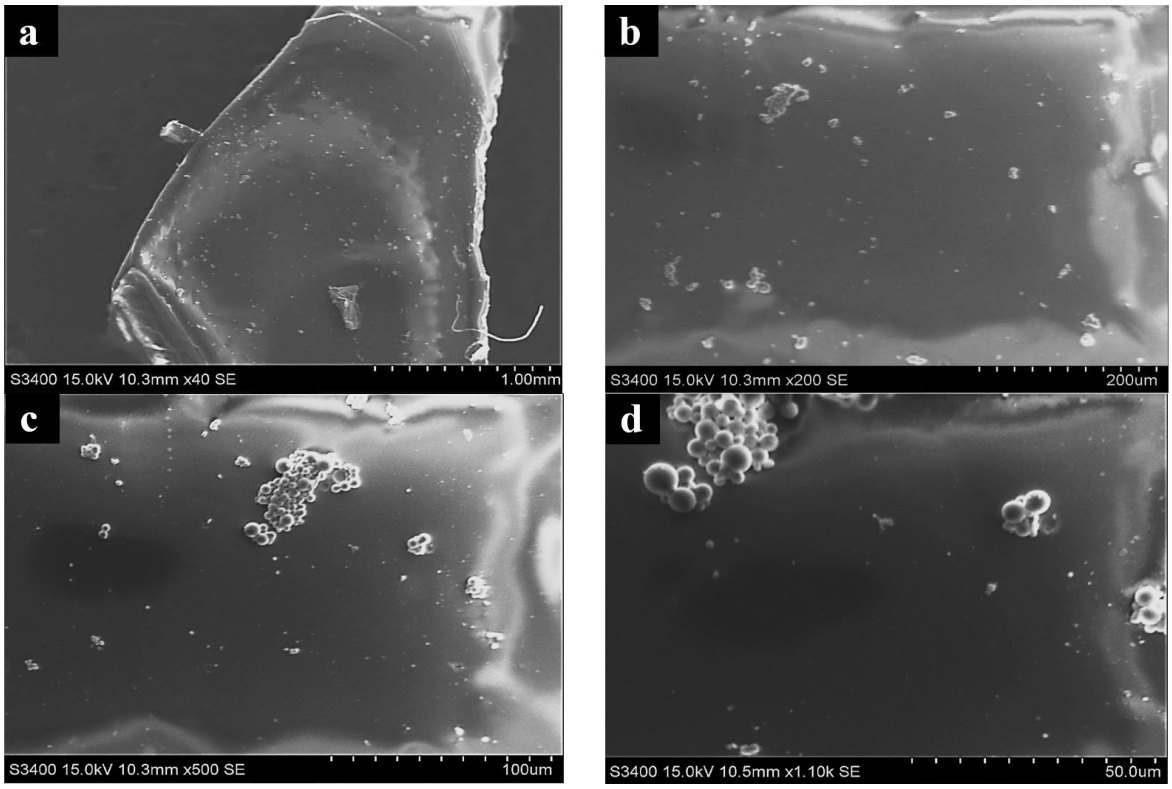

Figure 3.19. SEM of control PU2 gel: (a, b, c, d) vacuum-oven-dried piece at different magnifications; smooth surface without any pores can be clearly seen with some globular particles on top.

3.6.2. SEM of gels without vacuum oven drying

$HOC_{11}C_1ImBr$ PU3 was synthesized as a repeat batch of $HOC_{11}C_1ImBr$ PU2. After this synthesis, the gel was removed from its reactor (glass vial) by carefully breaking the glass vial. This sample was not subjected to any heat treatment in a vacuum oven. A disk was cut and put in a petri dish (Fig. 3.20(a)). This disk appeared opaque but in Fig. 5.21(a), a thin slice of this material appears translucent. When DMSO was flooded into the petri dish, this sample disk swelled about three times in size and became clear (Fig. 3.20(b)). When the DMSO was replaced by excess water, this disk shrank in size by about 50% and became turbid and opaque (Fig. 3.20(c)). Another piece of this gel was dipped in 0.1 *M* KPF_6 solution, where it became turbid, but did not swell (Fig. 3.20 (d) and Fig. 3.20(e)).

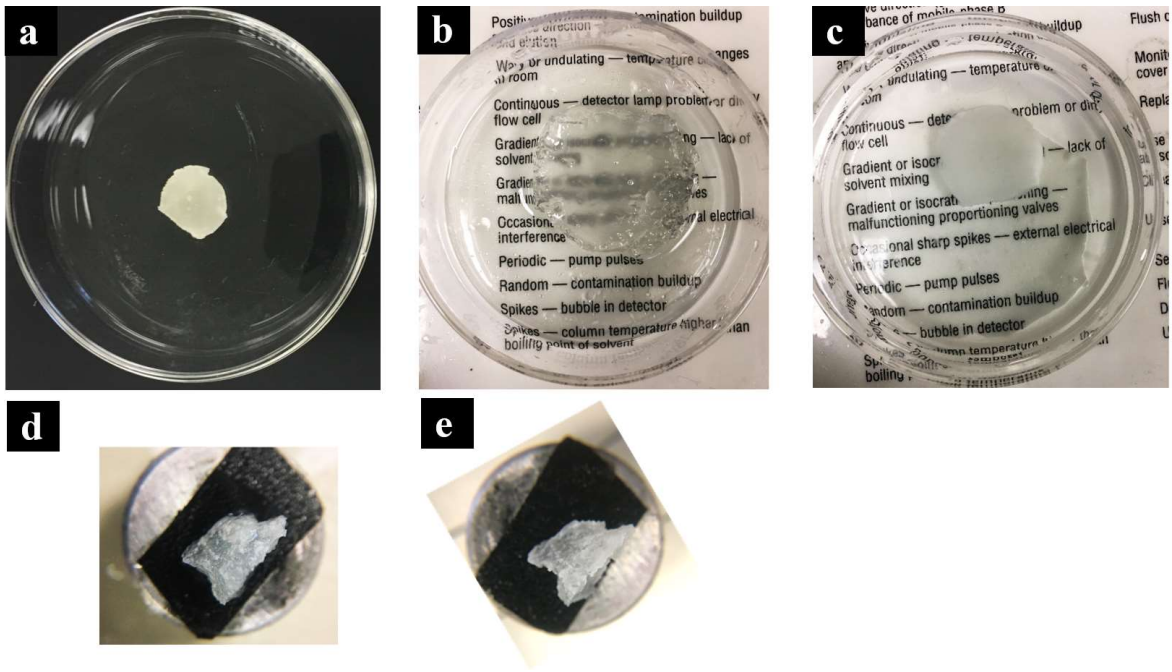

Figure 3.20. Stimuli response to solvents in $HOC_{11}C_1ImBr$ PU3: (a) $HOC_{11}C_1ImBr$ PU3 as unheated disk; (b) 'a' dipped in DMSO where it swelled and increased in size by about 300%; (c) 'b' dipped in DI water where it shrank by about 50%; (d) piece on conductive tape on SEM stage, dipped in 0.1 *M* KPF_6 solution for 2 minutes where it became turbid; (e) 'd' after 2 h in 0.1 *M* KPF_6 solution where turbidity increased but it did not swell or increase in the size.

A thin slice of $HOC_{11}C_1ImBr$ PU3 was put on a conductive tape applied to an SEM stage. It can be seen in Fig. 3.21(a) that this slice was translucent. This sample (while mounted) was then placed in a petri dish and flooded by DI water. It can be seen that this slice became turbid and swelled in DI water (Fig. 3.21(b)). When this turbid slice was dipped in DMSO, it swelled further and became transparent (Fig. 3.21(c)). Half of this transparent slice became turbid when it was dipped in 0.1 *M* KPF_6 solution (Fig. 3.21(d)). The other half of this slice desolvated under the vacuum conditions of the SEM sample chamber and remained transparent (Fig. 3.21(e)). This transparent slice was then dipped in 0.1 *M* KPF_6 solution, where it became turbid and swelled further, as seen in Fig. 3.21(f).

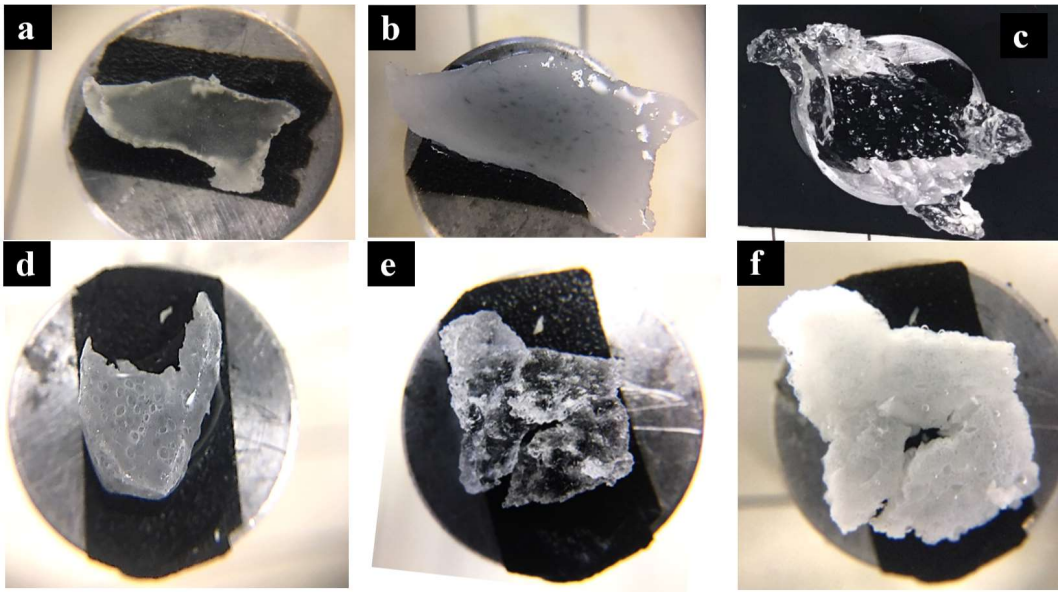

Figure 3.21. Stimuli response to solvents in $HOC_{11}C_1ImBr$ PU3 on SEM stage: (a) slice is translucent; (b) 'a' dipped in DI water where it swelled and increased in turbidity; (c) 'b' dipped in DMSO where it became transparent and swelled further; (d) half part of 'c' dipped in 0.1 *M* KPF_6 solution where it became turbid again; (e) other half part of 'c' after SEM analysis where it desolvated in vacuum of SEM chamber; (f) 'e' dipped in 0.1 *M* KPF_6 solution where it became turbid and swelled.

SEM analysis of $HOC_{11}C_1ImBr$ PU3 reveals that this batch of PIL was not porous and is therefore translucent, at the stage it was made (Fig. 3.22). When this material was dipped in water, it became turbid and swelled. SEM images reveal that the additional turbidity was an effect of high light scattering caused by pores (Fig. 3.23). A highly open-cell porous surface was formed with polydisperse pore sizes. Big circular open-cell pores of about 100 μm were formed, which connect to adjacent pores via 5 μm-10 μm diameter windows (Fig. 3.23 (d)). When this material is dipped in DMSO, it becomes transparent, and SEM images show that previously formed pores disappear, as shown in Fig. 3.24. This SEM analyzed sample (Fig. 3.21 (e)) was

then dipped in KPF_6 solution for 2.5 hours where it became turbid and slightly increased in size (Fig. 3.21 (f)). SEM images reveal porous structure with pores ranging from 100 μm to 250 μm with thick cell walls as seen in Fig. 3.25.

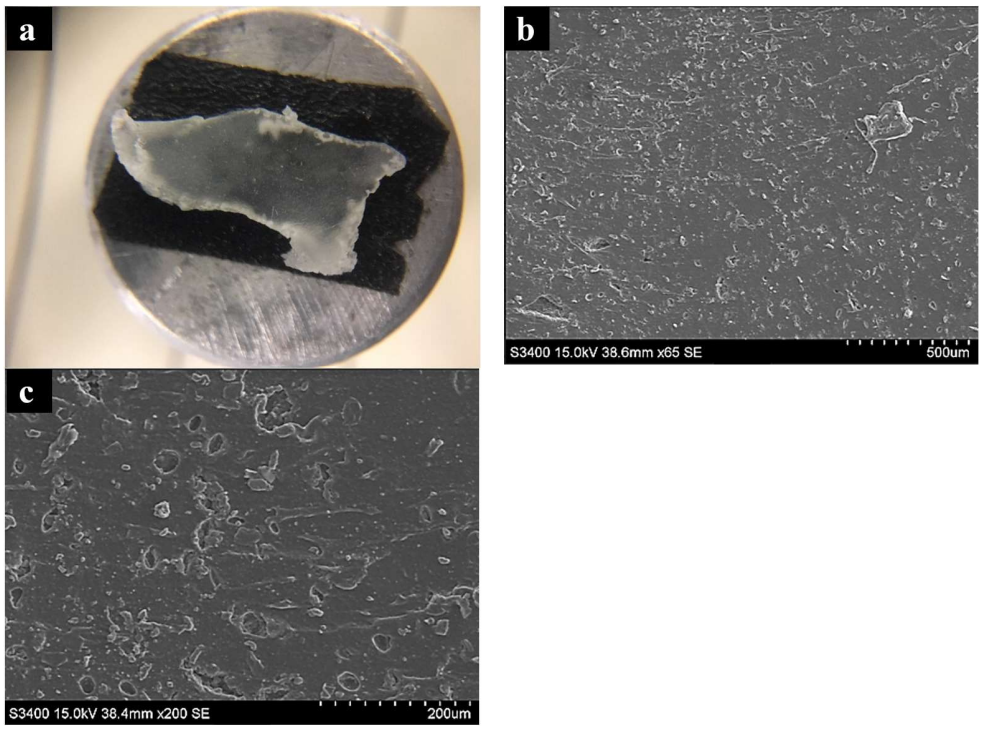

Figure 3.22. SEM of untreated $HOC_{11}C_1ImBr$ PU3: (a) $HOC_{11}C_1ImBr$ PU3 slice on conductive tape on SEM sample holder; same image as Fig. 3.21(a); (b, c) SEM image at different magnifications; surface is almost smooth with few pores.

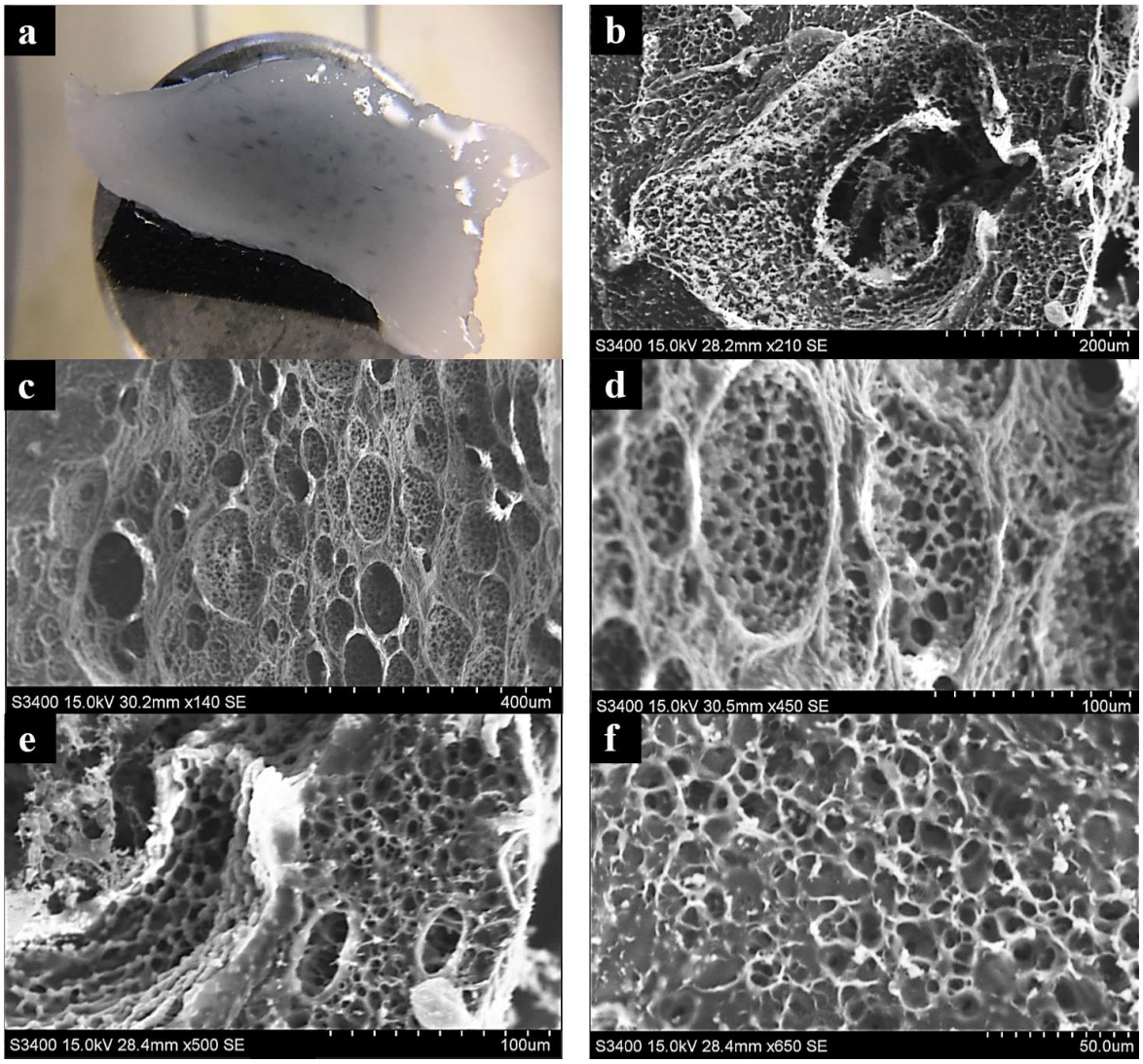

Figure 3.23. SEM of water saturated $HOC_{11}C_1ImBr$ PU3: (a) $HOC_{11}C_1ImBr$ PU3 slice 'a' from Fig. 3.22 dipped in DI water, where it swelled and became turbid; same image as Fig. 3.21(b); (b, c, d, e, f) SEM images at different magnifications, open-cell porous surface can be seen with 100 μm pores having multiple 5 μm-10 μm diameter pores inside them, which explains the turbidity in 'a'.

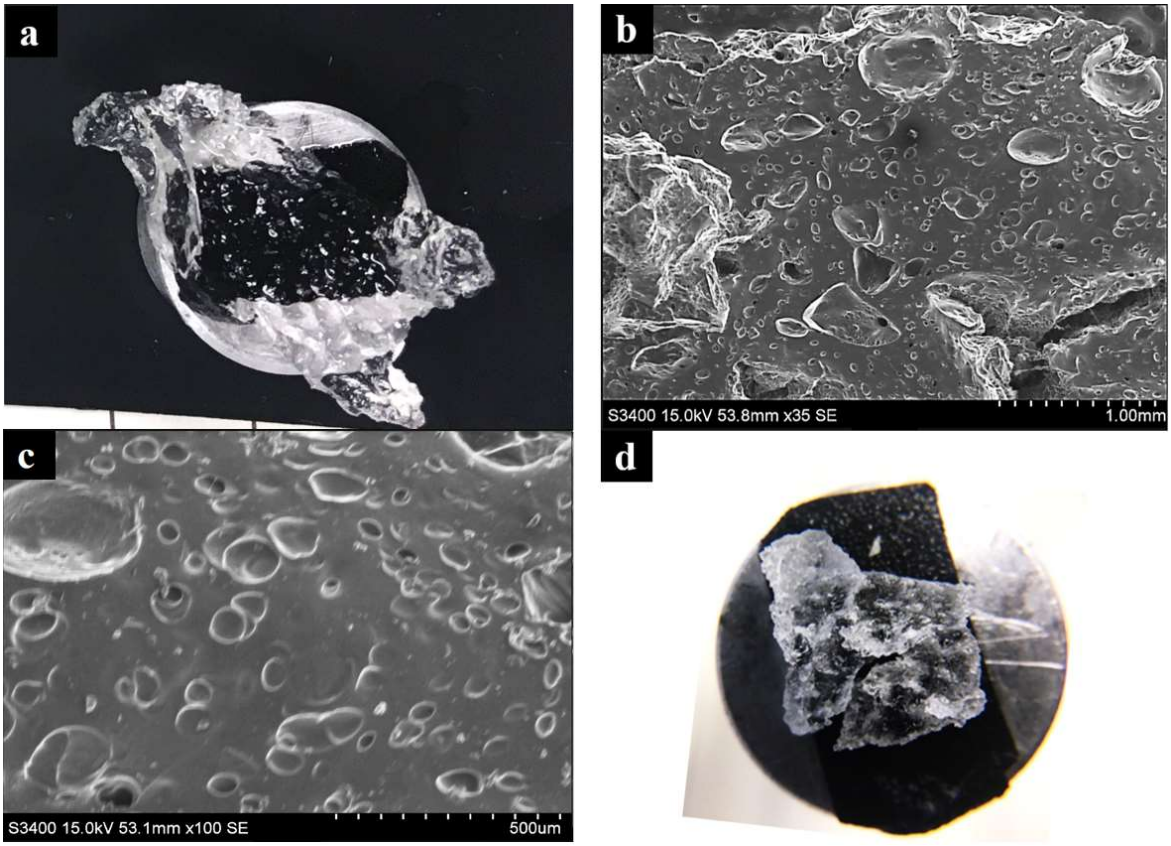

Figure 3.24. SEM of DMSO saturated $HOC_{11}C_1ImBr$ PU3: (a) $HOC_{11}C_1ImBr$ PU3 slice 'a' from Fig. 3.22 dipped in DI water where it swelled, became turbid, became clear, and swelled further when dipped in DMSO, half of this sample is analyzed in SEM; (b, c) SEM images of 'a' at different magnifications where pores seen in Fig. 3.23 (b, c, d, e, f) are disappeared, which explains why 'a' is transparent; (d) 'a' after removal from SEM chamber where all the solvent is evaporated in vacuum.

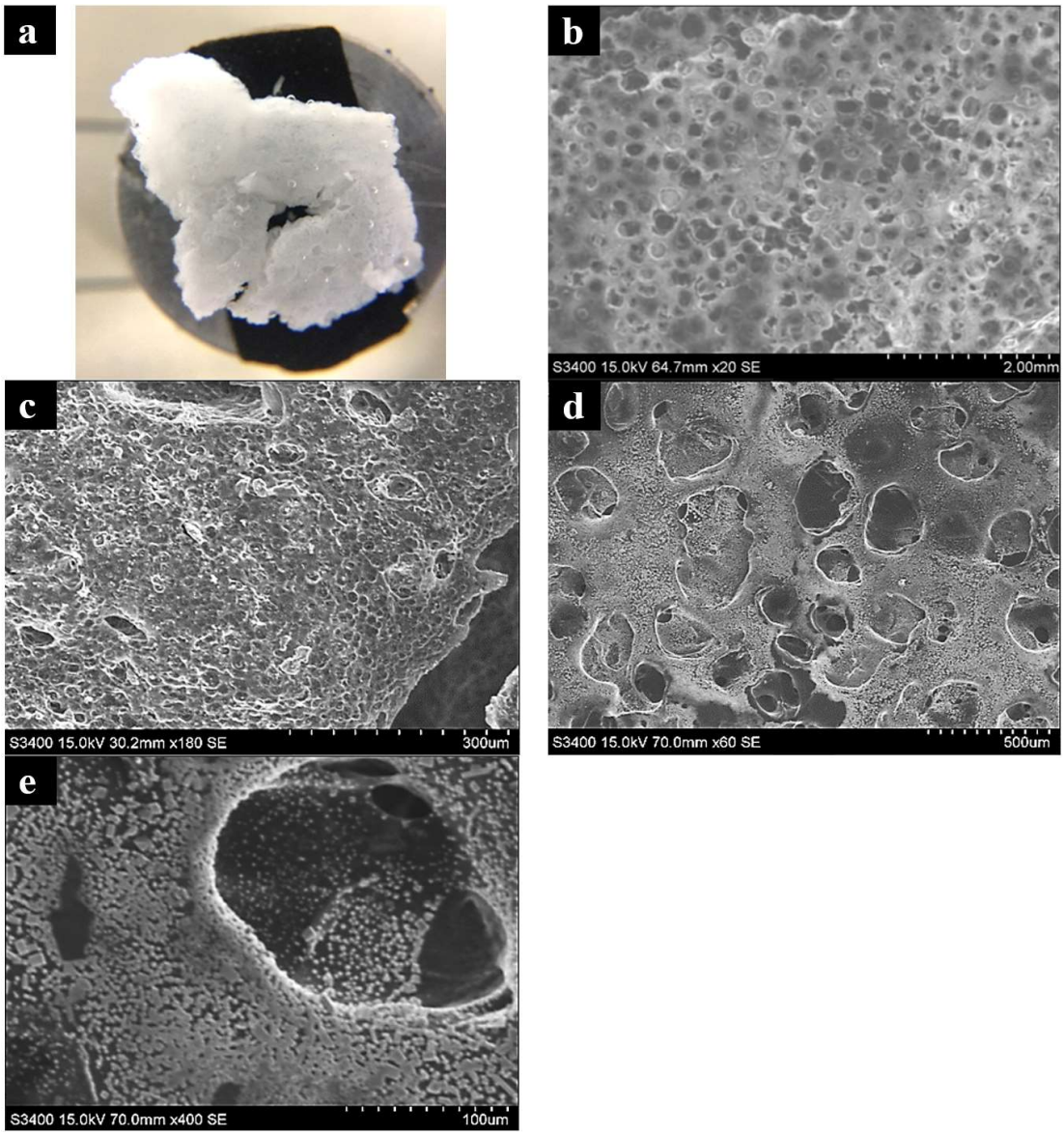

Figure 3.25. SEM of KPF_6 solution saturated $HOC_{11}C_1ImBr$ PU3: (a) $HOC_{11}C_1ImBr$ PU3 slice 'a' from Fig. 3.22 dipped in DI water where it swelled and became turbid and then became clear and swelled further when dipped in DMSO, after SEM, dipped in 0.1 *M* KPF_6 solution, where it became turbid; (b, c, d, e) 'a' in SEM at different magnifications, open-cell porous structure can be seen with precipitated KPF_6 crystals over it. Pores formed are about 100 μm to 250 μm with thick boundaries between them.

Chapter 4

Fate of Catalyst

4.1. Overview

DSC of $HOC_{11}C_1ImBr$ PU1, $HOC_{11}C_1ImBr$ PU2, and their controls, revealed that there were melting and freezing events below their respective glass transitions as seen in Fig. 3.9 and Fig. 3.10 in Chapter 3. Experiments were done to establish the source of these melting and freezing events, which suggested that these thermal events were the result of catalyst, DBTD, in PUs. Variations in integral enthalpies of these freezing and melting peaks were observed as a result of DBTD amount, through which swell ratios of catalyst in polymer was calculated. Aging effects on enthalpies of these peaks were measured, and effects of extraction of DBTD from PUs was also studied.

4.2. Water as a Source

A small sample of vacuum-oven-dried control PU2 was put in a water filled desiccator for 1 month, where it swelled in humid conditions. DSC of this water swelled polymer was done with multiple cycles of cooling and heating events. DSC was done at rate of 5 °C/min. Cycles during a complete DSC run are listed in Table 4.1.

Another sample of vacuum-oven-dried control PU2 from a storage desiccator was heated in a vacuum oven twice at 120 °C for 2 h before examining it by DSC. DSC of this sample was done at rate of 10 °C/min. This sample was heated first to 120 °C, then cooled to -80 °C, and then heated to 120°C. Enthalpies in this vacuum-oven-dried sample are compared with the enthalpies of water saturated polymer below.

Table 4.1. Cycles during a complete DSC run of water swelled control PU2

DSC Cycle	Cooling ramp to (°C)	Isothermal at (°C)	Heating ramp to (°C)	Isothermal at (°C)
1st	-85	-85 for 5 min	60	60 for 5 min
2nd	-85	-85 for 5 min	65	65 for 5 min
3rd	-85	-85 for 5 min	100	100 for 5 min
4th	-85	-85 for 5 min	120	120 for 5 min
5th	-85	-85 for 5 min	150	150 for 5 min
6th	-85	-85 for 5 min	120	Cycle ends

It was observed that in the DSC of the water saturated control PU2, during the first cycle, two freezing peaks were seen during the cooling segment, one starting at -35 °C with a freezing enthalpy ($\triangle H_f$) of 0.2 J/g and another starting at -49 °C ($T_{f,\,onset}$) with $\triangle H_f$ of 5.9 J/g having a peak ($T_{f,\,peak}$) at -52 °C (Fig. A.4.1). During the heating segments in this first cycle, a melting peak was seen having $T_{m,onset}$ of -11 °C and $T_{m,peak}$ of -5.7 °C with $\triangle H_m$ of 8.1 J/g (see Fig. A.4.2 in Appendix C for enthalpy integration). When this sample was heated in further cycles, endotherms were seen at high temperatures, suggesting evaporation of water (Fig. 4.1). A decrease in $\triangle H_f$ and $\triangle H_m$ in consecutive cycles was also noticed. In the sixth cycle, heating to 130 °C suggests that no more water is left in the sample as we do not see endotherm after 100 °C, yet we see freezing and melting peaks during cooling and heating events, respectively. The $\triangle H_f$ during cooling event in sixth cycle is 1.7 J/g with -41 °C as $T_{f,\,onset}$ and -44 °C as $T_{f,\,peak}$ (see

Fig. A.4.3 in Appendix C for enthalpy integration). $\triangle H_m$ during heating event in sixth cycle is 2.1 J/g with -16 °C as $T_{m,\,onset}$ and -6 °C as $T_{m,\,peak}$ (see Fig. A.4.4 in Appendix C for enthalpy integration).

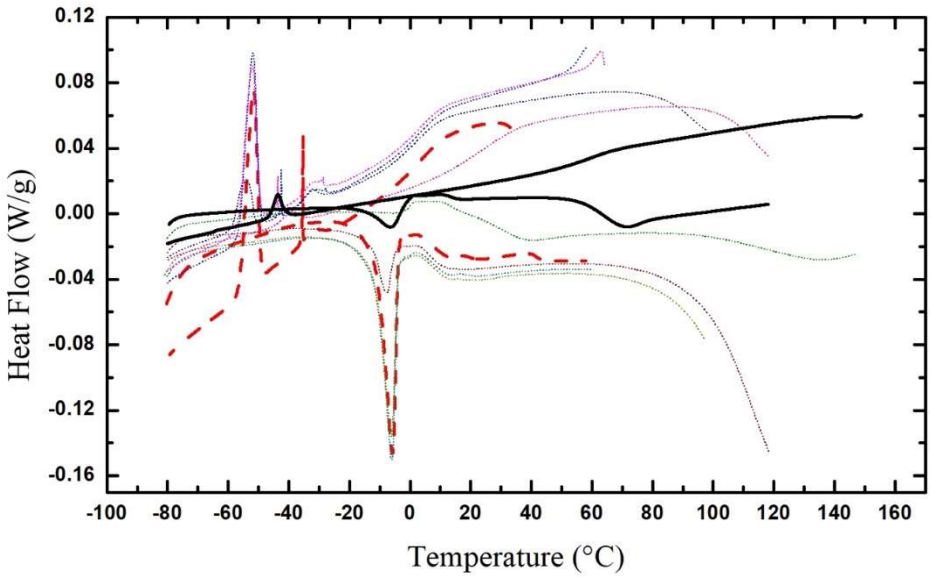

Figure 4.1. DSC of water saturated control PU2 at scan rate of 5 °C/min: 1st cycle (- - - -); 6th cycle (————).

Figure 4.2 shows the DSC of vacuum-oven-dried control PU, where during cooling, a freezing exotherm yields a $\triangle H_f$ of 2 J/g having -42 °C as $T_{f,onset}$ and -45 °C as $T_{f,peak}$ (see Fig. A.4.5 in Appendix C for enthalpy integration). During the heating segment the melting endotherm yields $\triangle H_m$ of 2 J/g with -17 °C as $T_{m,onset}$ and -7 °C as $T_{m,peak}$ (see Fig. A.4.5 in Appendix C for enthalpy integration). Enthalpies in vacuum-oven-dried control PU2 are very similar to enthalpies in the sixth cycle of DSC of water saturated control PU2. This experiment shows that water cannot be the source of these thermal events because purposely added water exhibits shifted exotherms and endotherms that disappear on vacuum heating. The exotherms and endotherms we are trying to identify do not change significantly with vacuum heating.

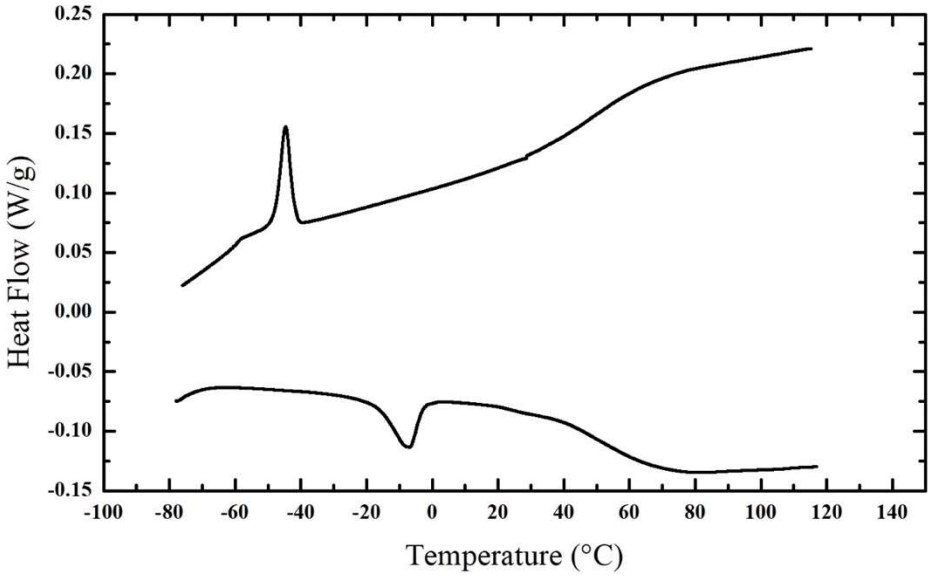

Figure 4.2. DSC of control PU2 heated twice at 120 °C for 2 hours in vacuum oven.

4.3. DSC of DBTD

DSC of the DBTD catalyst was done at a scan rate of 10 °C/min. It was seen that during cooling, DBTD froze at a $T_{f,peak}$ of -29 °C with a $\triangle H_f$ of 39 J/g, and during heating, it melted at $T_{m,peak}$ of -2.5 °C with $\triangle H_m$ of 42 J/g (Fig. 4.3). This suggests that DBTD is the source of melting and freezing events in Fig. 3.9 and Fig. 3.10 (and in Fig. 4.2).

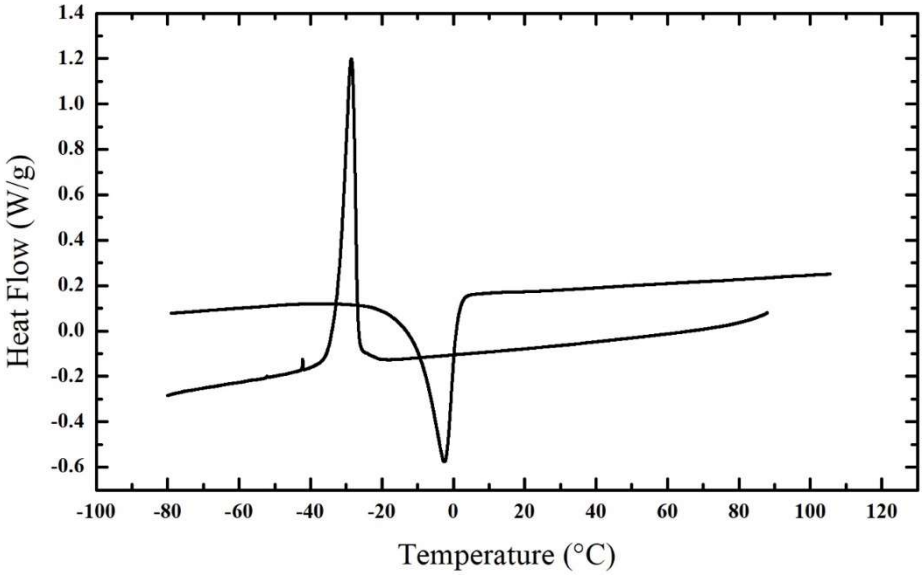

Figure 4.3. DSC of DBTD catalyst at scan rate of 10 °C/min.

4.4. Swell Ratio of Catalyst

The procedure described in section 3.3 was used to synthesize different stoichiometrically balanced control PUs having the formula of control PU2 with varying amounts of added DBTD catalyst. It was found that DSCs of these materials had varying $\triangle H_f$ and $\triangle H_m$ during cooling and heating segments, respectively. DSC results for these PUs and control PU2 are compared in Table 4.2. It was observed that PU3 gelled in 30 s after the addition of catalyst at room temperature. Control PU2, PU4, PU5, and PU6 gelled within 5 min after they were put in an oven at 80 °C. PU7 gelled within 24 hours at 80 °C; PU9 gelled after 4 days at 80 °C.

Table 4.2 suggests that during DSCs of these materials, $\triangle H_f$ and $\triangle H_m$, during cooling and heating events, respectively, reduced in values as catalyst amount was reduced. No melting or crystallization peaks were observed in PUs having DBTD less than 1% by weight.

$\triangle H_f$ and $\triangle H_m$ of 100% DBTD catalyst are 39 J/g and 41 J/g, respectively, whereas, $\triangle H_f$ and $\triangle H_m$ of PU3 having 10% catalyst are both 2.0 J/g. This 2.0 J/g value is per g polymer with catalyst. In this sample, the catalyst level is 10% or 10 g polymer and catalyst per g catalyst.

Therefore, this 2.0 J/g value transforms (2.0 J/g polymer+catalyst x 10 g polymer+catalyst/g catalyst) to 20 J/g catalyst. Similar trends are seen in control PU2, PU4, PU5, and PU6. We do not see any peaks in PU7 and PU8, though they also have 0.3% and 0.1 % DBTD catalyst. This suggests that some amount of DBTD is dissolved in the polymer matrix phase, and the other amount that we see during DSCs is from an undissolved phase of DBTD within the polymer matrix. It can be said that the DBTD dissolved in the polymer matrix is strongly bound to the polymer matrix, whereas undissolved DBTD is excess free catalyst in the polymer matrix. $\triangle H_f$ and $\triangle H_m$ in the PU3 sample suggest that about 50% of the catalyst is dissolved in the matrix and the remaining 50% is in excess and is (not dissolved) present as a separate phase.

Table 4.2. Comparison of melting and freezing events by varying amount of DBTD in PU

Material	% DBTD	$\triangle H_f$ (J/g)	$T_{f,peak}$ (°C)	$\triangle H_m$ (J/g)	$T_{m,peak}$ (°C)
DBTD	100	39	-29	41	-2.5
PU 3	10	1.99	-34.4	1.95	-5
Control PU2	9.6	1.40	-45	1.64	-6.8
PU4	5.6	1.05	-45	1.04	-8.5
PU5	2.9	0.11	-36	0.15	-11
PU6	1	-	-	0.05	-5
PU7	0.3	-	-	-	-
PU8	0.1	-	-	-	-
PU9	0	-	-	-	-

In Fig. 4.4, the weight fraction of catalyst in resin samples is plotted against excess amount of catalyst (g) per gram of resin sample. This excess amount of catalyst is calculated by dividing the average of enthalpies during DSCs of resin samples by average enthalpies of 100% DBTD catalyst. Square data points are from control PU resins which do not have IL. Linear regression shows a slope of 0.639 with an x-intercept of 0.0087. This suggests that the swelling ratio of catalyst in resin is 0.639. The x-axis intercept suggests that 0.87% DBTD catalyst amount is strongly bound or dissolved in the resin matrix, and higher amounts of DBTD will lead to free unbound DBTD sequestered in the matrix as a separate phase. The swelling ratio tells us that as we keep on increasing the DBTD amount in the resin, we can have higher amounts of dissolved DBTD in the matrix. This is characteristic of chemical equilibria of the partitioning type. After including three more data points for PIL resins (circular data points), the x-axis intercept of linear regression becomes 0.0071 and the slope of the linear regression becomes 0.597.

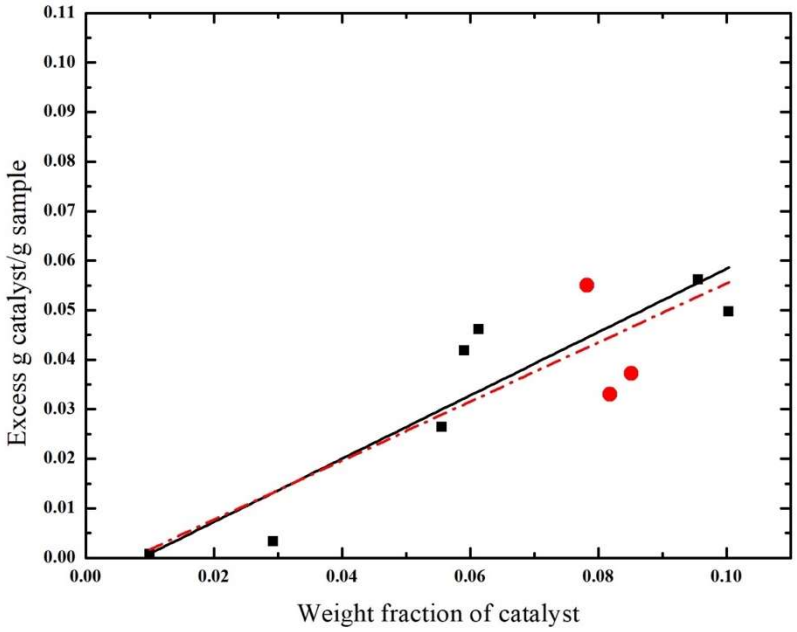

Figure 4.4. Weight fraction of catalyst in PU samples vs excess catalyst per g sample to measure swell ratio of catalyst (slope of linear regression) and strong binding amount of catalyst (x-axis intercept of linear regression) in PUs: stoichiometrically balanced control PUs without IL(■); PILs (●); linear regression in control PU datapoints (——); linear regression including PIL data points with control PU data points (- - - - -).

4.5. Aging Effect of the Catalyst

It was observed that with time, more of the excess catalyst appeared to be getting dissolved in the resin. Enthalpies during DSCs could be seen reducing with aging of the samples (see Fig. 4.5 and Fig. A.4.7). After the control PU1 was synthesised and dried in a vacuum oven (see section 3.4 and section 3.5), its DSC at a rate of 10 °C/min, revealed that during cooling, a freezing peak had $T_{f,onset}$ of -29 °C, a $\triangle H_f$ of 5.47 J/g, and $T_{f,peak}$ of -31 °C. During heating, the melting peak had $T_{m,onset}$ of -10 °C, a $\triangle H_m$ of 5.56 J/g, and $T_{m,peak}$ of -2 °C.

When after one month, a vacuum-oven-dried control PU1 sample was removed from storage in a desiccator and heated in a vacuum oven at 100 °C for 12 hours, its DSC at a scan rate of 15 °C/min during cooling and 10 °C/min during heating revealed that, during cooling, the

freezing peak had $T_{f,onset}$ of -31 °C, a $\triangle H_f$ of 3.45 J/g, and $T_{f,peak}$ of -32 °C. During heating, the melting peak had $T_{m,onset}$ of -12 °C, a $\triangle H_m$ of 4.04 J/g, and $T_{m,peak}$ of -4 °C.

After 6 months, a vacuum-oven-dried control PU1 sample was removed from storage in a desiccator and was heated at 130 °C in a vacuum oven for 4 h and 30 min. DSC at a scan rate of 15 °C/min during cooling and 10 °C/min during heating revealed that, during cooling, the freezing peak had $T_{f,onset}$ of -26 °C, a $\triangle H_f$ of 1.56 J/g, and $T_{f,peak}$ of -29 °C. During heating, the melting peak had $T_{m,onset}$ of -10 °C, a $\triangle H_m$ of 1.7 J/g, and $T_{m,peak}$ of -3 °C.

After 11 months, a vacuum-oven-dried control PU1 sample was removed from desiccator storage and DSC was done at a scan rate of 15 °C/min during cooling and 10 °C/min during heating. Data revealed that during cooling, the freezing peak had $T_{f,onset}$ of -32 °C, a $\triangle H_f$ of 1.7 J/g, and a $T_{f,peak}$ of -33 °C. During heating, the melting peak had $T_{m,onset}$ of -12 °C, a $\triangle H_m$ of 1.6 J/g, and a $T_{m,peak}$ of -4 °C (see Fig. A.4.7 in Appendix C for enthalpy integration detail).

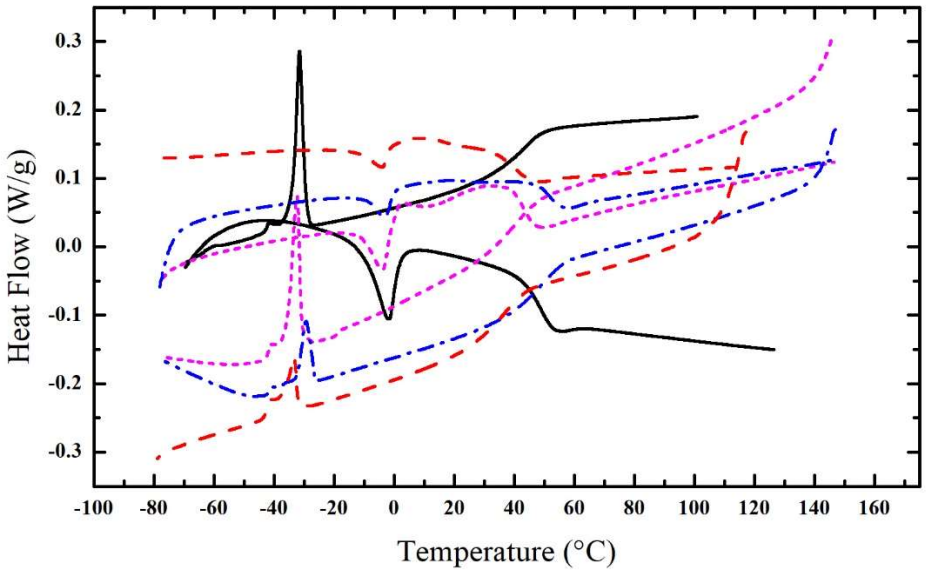

Figure 4.5. DSC comparison of control PU1 at different periods of aging time: after it was synthesized (——); after 1 month (- - - - -); after 6 months (— · — · —); after 11 months (— — —).

A 16-months-aged control PU1 sample was removed from storage in a desiccator and was heated in a vacuum oven at 130 °C for 2 hs. During its DSC at a scan rate of 10 °C/min, it was first heated to 110 °C, where it was held for 5 minutes, and then during its first cycle, it was cooled to -85 °C and then heated to 130 °C, where it was held for 15 minutes. In a second DSC cycle, it was cooled to -80 °C and then heated to 150 °C and held for 15 minutes at 150 °C. Lastly, in a third DSC cycle, it was cooled to -75 °C and then heated to 160 °C (Fig. 4.6).

It was observed that in the first cycle, during cooling, the freezing peak had a $T_{f,onset}$ of -33 °C, a $\triangle H_f$ of 2.4 J/g, and a $T_{f,peak}$ of -38 °C. During heating, the melting peak had a $T_{m,onset}$ of -10 °C, a $\triangle H_m$ of 2.0 J/g, and a $T_{m,\,peak}$ of -9.9 °C (see Fig. A.4.8 for enthalpy integration detail). In the second cycle during cooling, the freezing peak had a $T_{f,onset}$ of -26 °C, a $\triangle H_f$ of 4.2 J/g, and a $T_{f,peak}$ of -29 °C. During heating, the melting peak had a $T_{m,onset}$ of -11 °C, a $\triangle H_m$ of 4.1 J/g, and a $T_{m,peak}$ of -3.5 °C (see Fig. A.4.8 in Appendix C for enthalpy integration detail). In a third cycle, during cooling the freezing peak had a $T_{f,onset}$ of -22 °C, a $\triangle H_f$ of 5.9 J/g, and a $T_{f\,peak}$ of -24 °C. During heating, the melting peak had a $T_{m,onset}$ of -5 °C, a $\triangle H_m$ of 5.9 J/g, and a $T_{m,peak}$ of 0.66 °C (see Fig. A.4.8 in Appendix C for enthalpy integration detail). These changes in endotherm and exotherm peak areas (enthalpies) suggest that high temperatures with longer hold times “remove” some amount of dissolved catalyst from the polymer matrix into a separate DBTD phase. This change is a type of syneresis caused by thermal annealing of the polymer matrix that decreases solubility of DBTL in the polymer matrix.

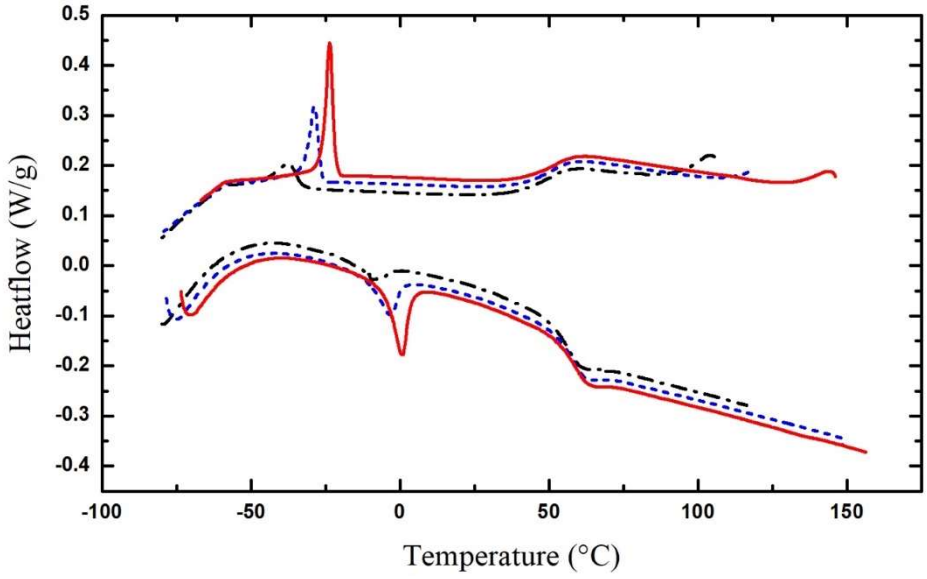

Figure 4.6. DSC comparison of 16-month-aged control PU1. Sample was heated in vacuum oven at 130 °C for 2 hours before doing DSC at rate of 10°C/min: 1st DSC cycle (-·-·-); 2nd DSC cycle (- - - -); 3rd DSC cycle (——).

After 2 h of heating at 130 °C in a vacuum oven, the 16-months-aged control PU1 sample, used in Fig. 4.6, was heated in the vacuum oven at a higher temperature of 150 °C for an additional 3.5 hs. DSC of this sample was done at a scan rate of 10 °C/min; it was first heated to 110 °C where it was held for 5 minutes. Then during the first cycle, it was cooled to -85 °C and then heated to 130 °C, where it was held for 15 minutes. In a second cycle, it was cooled to -80 °C and then heated to 150 °C and held for 15 minutes at 150 °C. Lastly, in a third cycle, it was cooled to -75°C and then heated to 160 °C (Fig. 4.7).

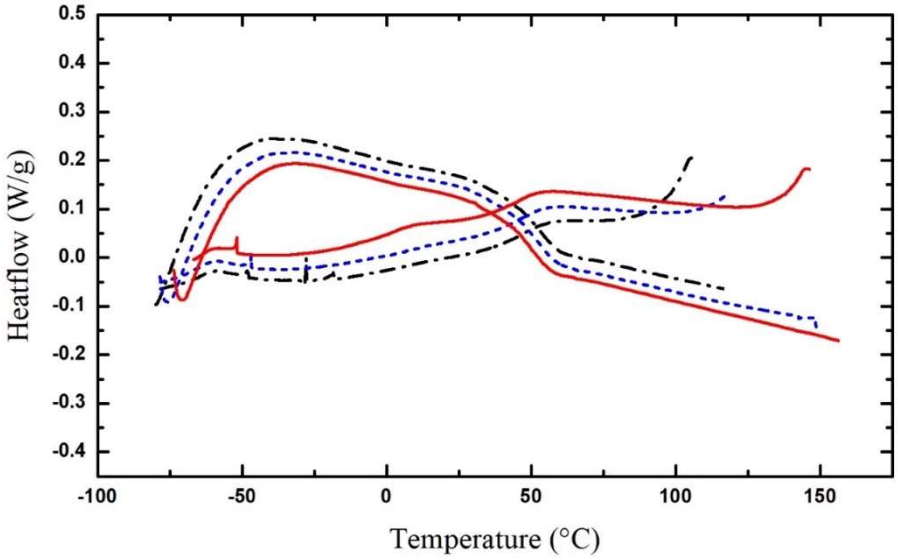

Figure 4.7. DSC comparison of 16-month-aged control PU1. Sample was heated in vacuum oven at 130 °C for 2 hours and then further heated at 150 °C for 3.5 hours before doing DSC at rate of 10°C/min: 1st DSC cycle (-·-·-); 2nd DSC cycle (----); 3rd DSC cycle (——).

During the DSC of this sample, no major DBTL peak was observed in any cycle (Fig. 4.7). Results suggested that prolonged heating at 150 °C would have decomposed the catalyst or catalyst would have boiled off under vacuum at 150 °C. (boiling point of DBTL is 205 °C [55]). A TGA of DBTL shows that weight loss starts after 200 °C with a peak decomposition temperature of 350 °C in an inert atmosphere (Fig. 4.8). Prolonged heating of 400 min at 150 °C in an inert atmosphere during TGA shows a loss of 3% weight of DBTL (Fig. 4.9).

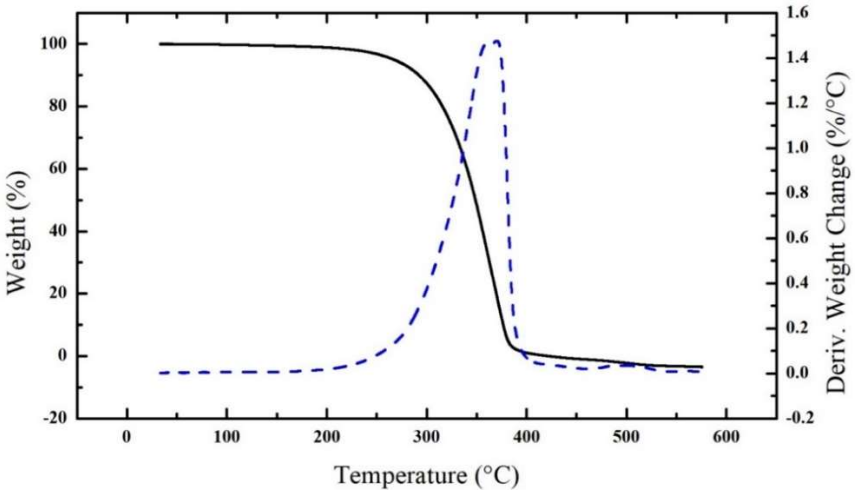

Figure 4.8. TGA of DBTD catalyst: weight percent change (left axis) (——); Derivative weight percent change (right axis) (- - -).

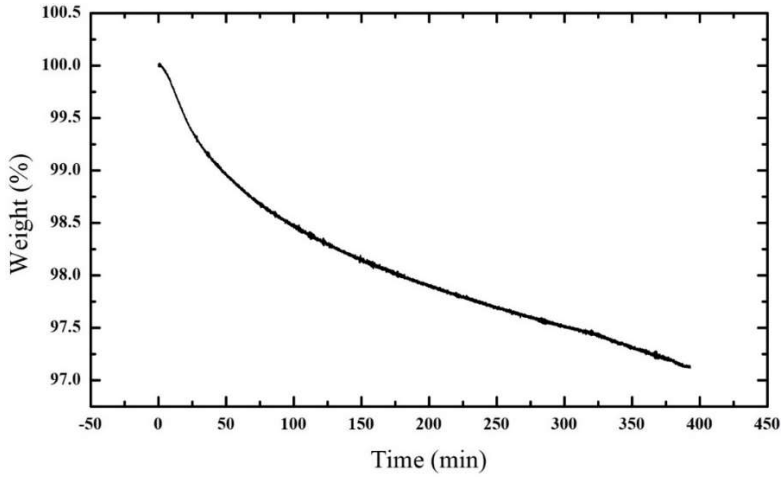

Figure 4.9. TGA of DBTD catalyst at constant temperature of 150 °C for 300 minutes then at 160 °C for 60 more minutes in inert atmosphere of nitrogen gas.

4.6 Soxhlet Extraction

Soxhlet extraction of samples of PU3, PU4, PU5, PU6, and PU7 was done using CH_2Cl_2 as solvent for 24 h. This was done to see if DBTL could be extracted efficiently from PU samples and to see what effects such extraction would have on glass transitions. These samples

were then heated in a vacuum oven at 100 °C for 4 hours before analyzing by DSC. Control samples of these PUs, which did not undergo soxhlet extraction, were also heated in a vacuum oven for 4 h at 100 °C. TGAs of these vacuum-oven-treated samples were done in an inert atmosphere of nitrogen from room temperature to 580°C at a rate of 10 °C/min. These TGAs suggest that these PUs start to decompose at about 160 °C (Fig. 4.10).

In Fig. 4.10, it can be seen that between 350 °C to 450 °C, PU3 containing 10% DBTD catalyst exhibits a sharp decrease in weight, while PU9 containing no catalyst has the most gradual decrease. The slopes of these decreases increase in magnitude with increasing DBTD. Fig. 4.8 shows that the peak temperature of decomposition of DBTD is about 370 °C. This suggests that variability in slope among PUs between 350 °C to 450 °C is likely due to decomposition of DBTD in the respective resins.

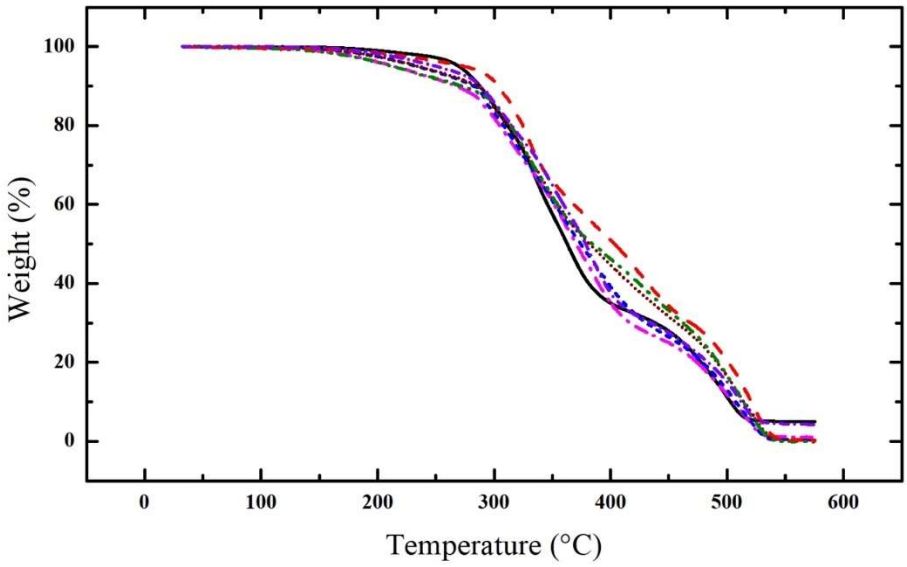

Figure 4.10. Comparison of TGAs of PU samples having different amounts of catalyst: PU3 with 10% DBTD (——); PU5 with 3% DBTD (– · – ·); PU6with 1% DBTD (– – – –); PU7 with 0.3% DBTD (·····); PU8 with 0.1% DBTD (– · – ·); PU9 with no DBTD (– – – –).

It was seen that a TGA of soxhlet extracted PU9 (made without catalyst), aged seven months, remained the same (Fig. 4.10 and Fig. 4.11). A TGA of soxhlet extracted PU4, aged seven months, with about 5.6% catalyst, shifted towards the TGA of PU9 in Fig. 4.11 from Fig. 4.10. DSC of these samples was done at scan rate of 10 °C /min by using various cycles with heat treatment at various temperatures and various hold temperatures as listed in Table 4.3.

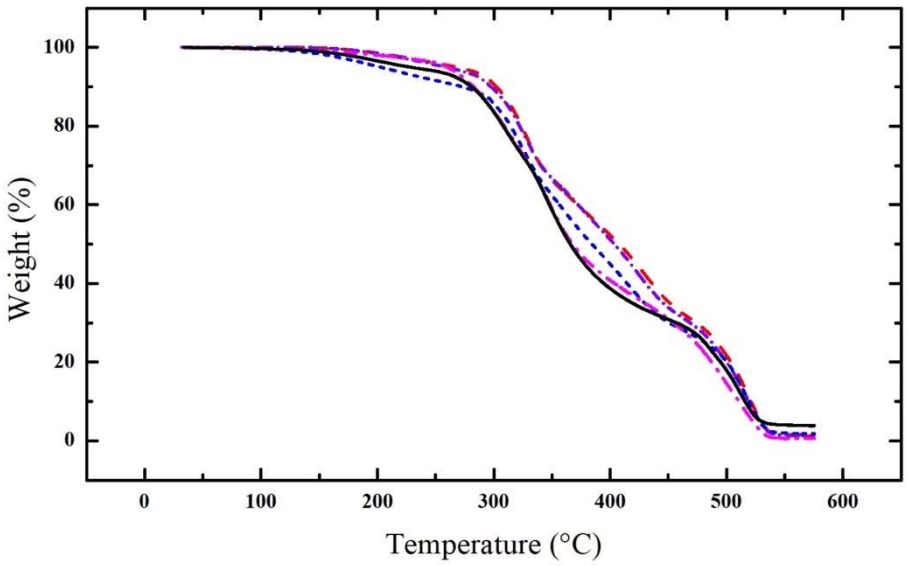

Figure 4.11. Comparison of TGAs of soxhlet extracted samples of PUs: PU3 having 10% DBTD (——); 7 month-aged PU4 having 5.6% DBTD (-·-·-·-) PU5 having 3% DBTD (-·--·-); PU6 having 1% DBTD (- - - - -); 7 months aged PU9 having no DBTD (- - - -).

It was observed that the T_g of samples was increased after performing soxhlet extraction (Fig. 4.12 to Fig. 4.19 and Table 4.4). This suggests that during the extraction process, chemical annealing by CH_2Cl_2 would have reduced intermolecular free spaces between chains and, therefore, increased the packing density and, therefore, the T_g of the polymer. It also is possible that very low molecular weight components, such as unreacted glycerol and very short

oligomers, may have leached out during this soxhlet extraction. Any such loss also would be a removal of de facto plasticizer and result in increasing T_g.

Table 4.3. Cycles during a complete DSC run used in section 4.6.

DSC Cycle	Cooling ramp to (°C)	Isothermal at (°C)	Heating ramp to (°C)	Isothermal at (°C)
1st	-80	-80 for 5 min	130	130 for 15 min
2nd	-80	-80 for 5 min	150	150 for 15 min
3rd	-80	-80 for 5 min	150	150 for 30 min
4th	-80	-80 for 5 min	150	150 for 60 min
5th	-80	-80 for 5 min	150	150 for 120 min
6th	-80	-80 for 5 min	160	160 for 60 min
7th	-80	-80 for 5 min	160	Cycle ends

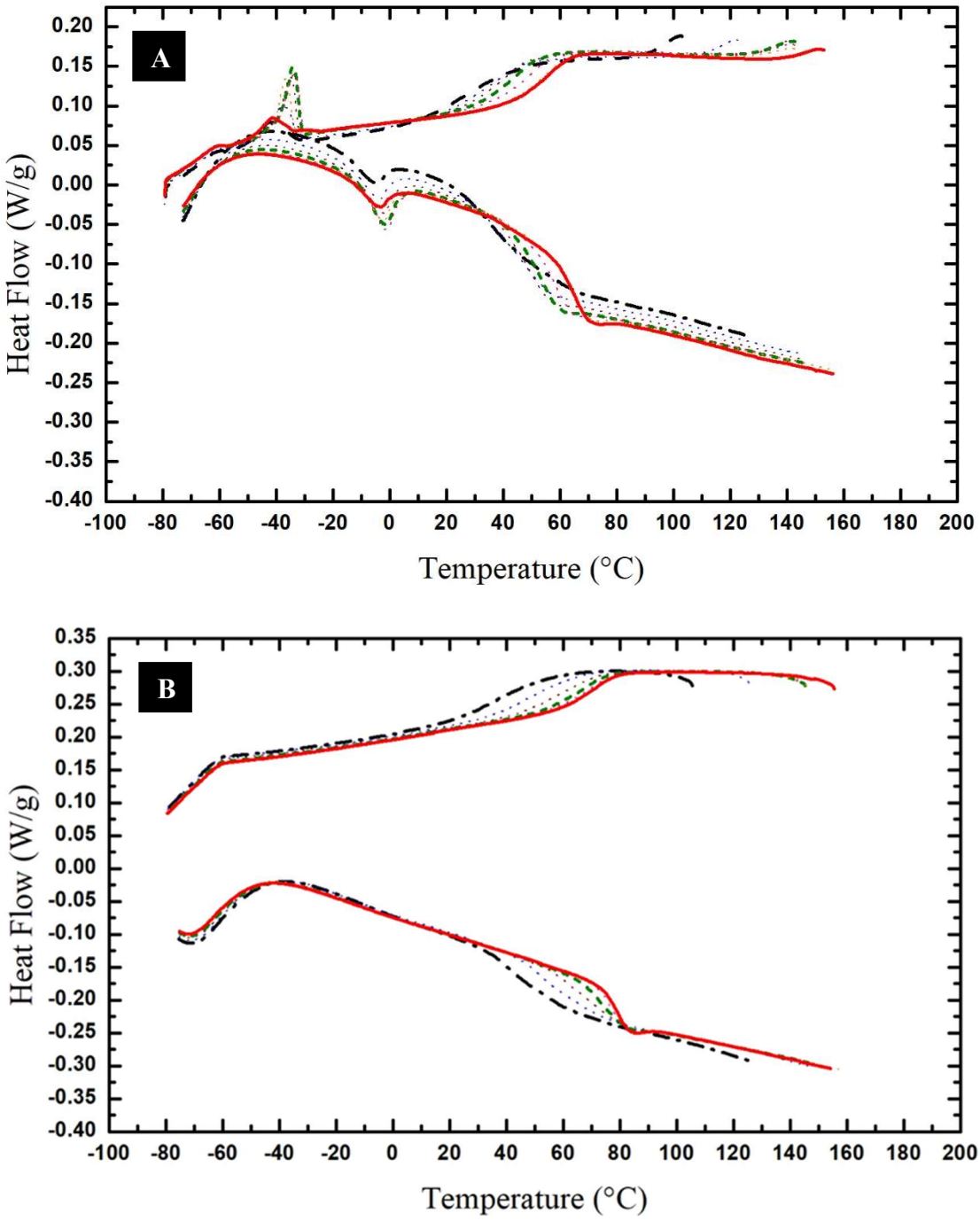

Figure 4.12. DSC before and after soxhlet extraction of PU3 having 10% catalyst: (A) before soxhlet extraction 1st cycle (–·–·–); 4th cycle (- - - - -); 7th cycle (——); (B) after soxhlet extraction 1st cycle (–·–·–); 4th cycle (- - - - -); 7th cycle (——).

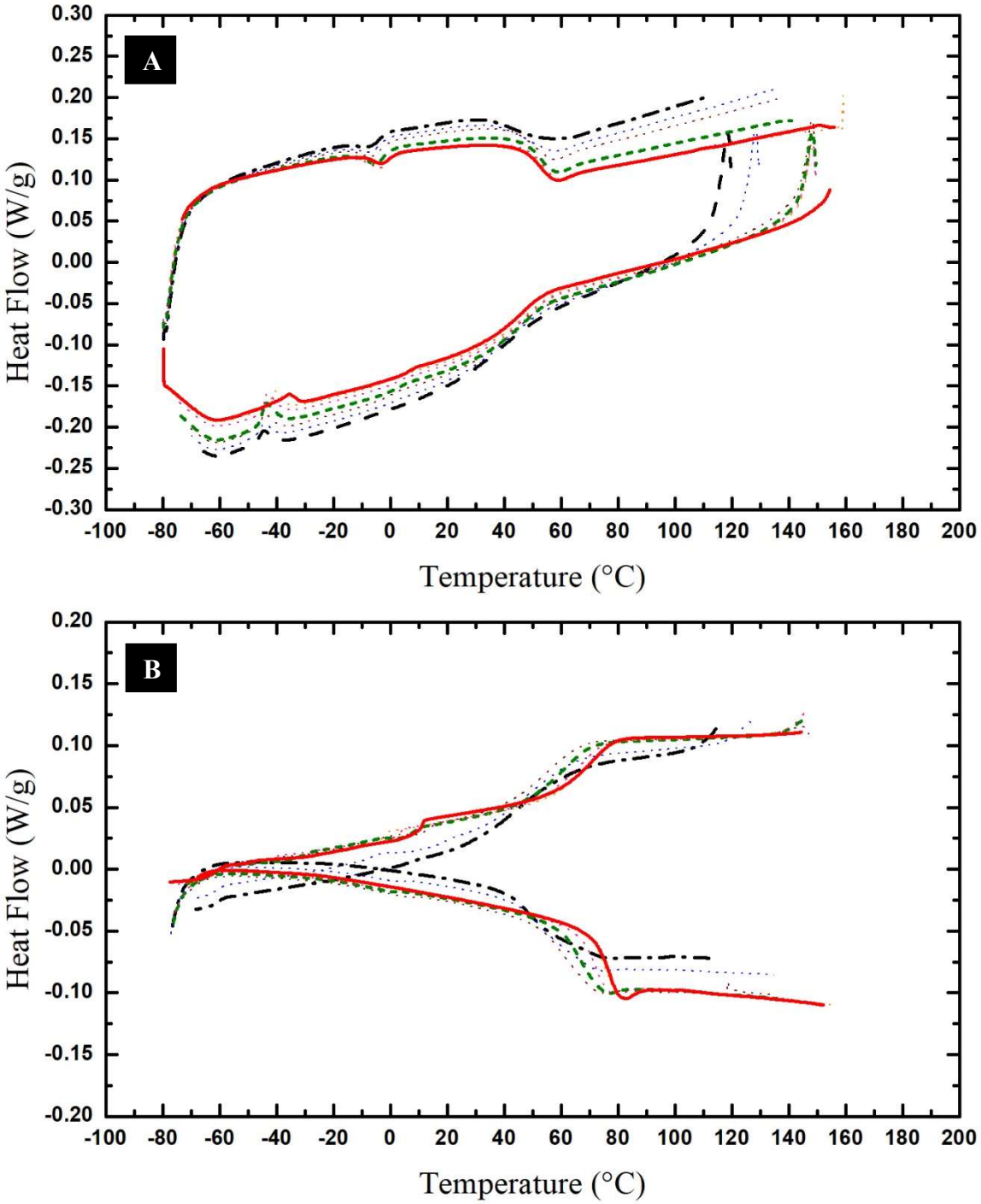

Figure 4.13. DSC before and after soxhlet extraction of PU4 having 5.6% catalyst: (A) before soxhlet extraction 1st cycle (–·–·–); 4th cycle (– – –); 7th cycle (——); (B) after soxhlet extraction 1st cycle (–·–·–); 4th cycle (– – –); 7th cycle (——).

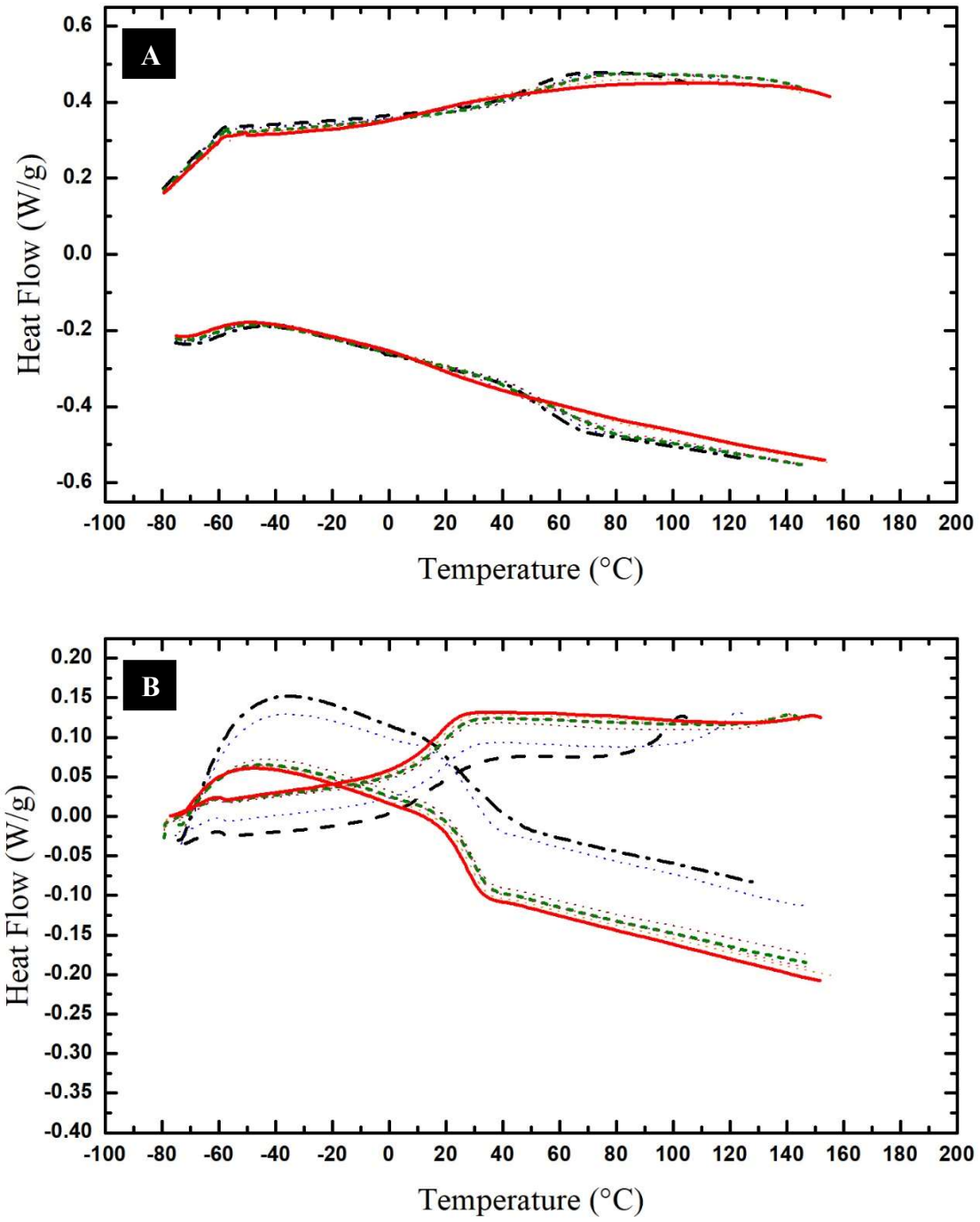

Figure 4.14. DSC before and after soxhlet extraction of PU5 having 3% catalyst: (A) before soxhlet extraction 1st cycle (–·–·–); 4th cycle (- - - - -); 7th cycle (——); (B) after soxhlet extraction 1st cycle (–·–·–); 4th cycle (- - - - -); 7th cycle (——).

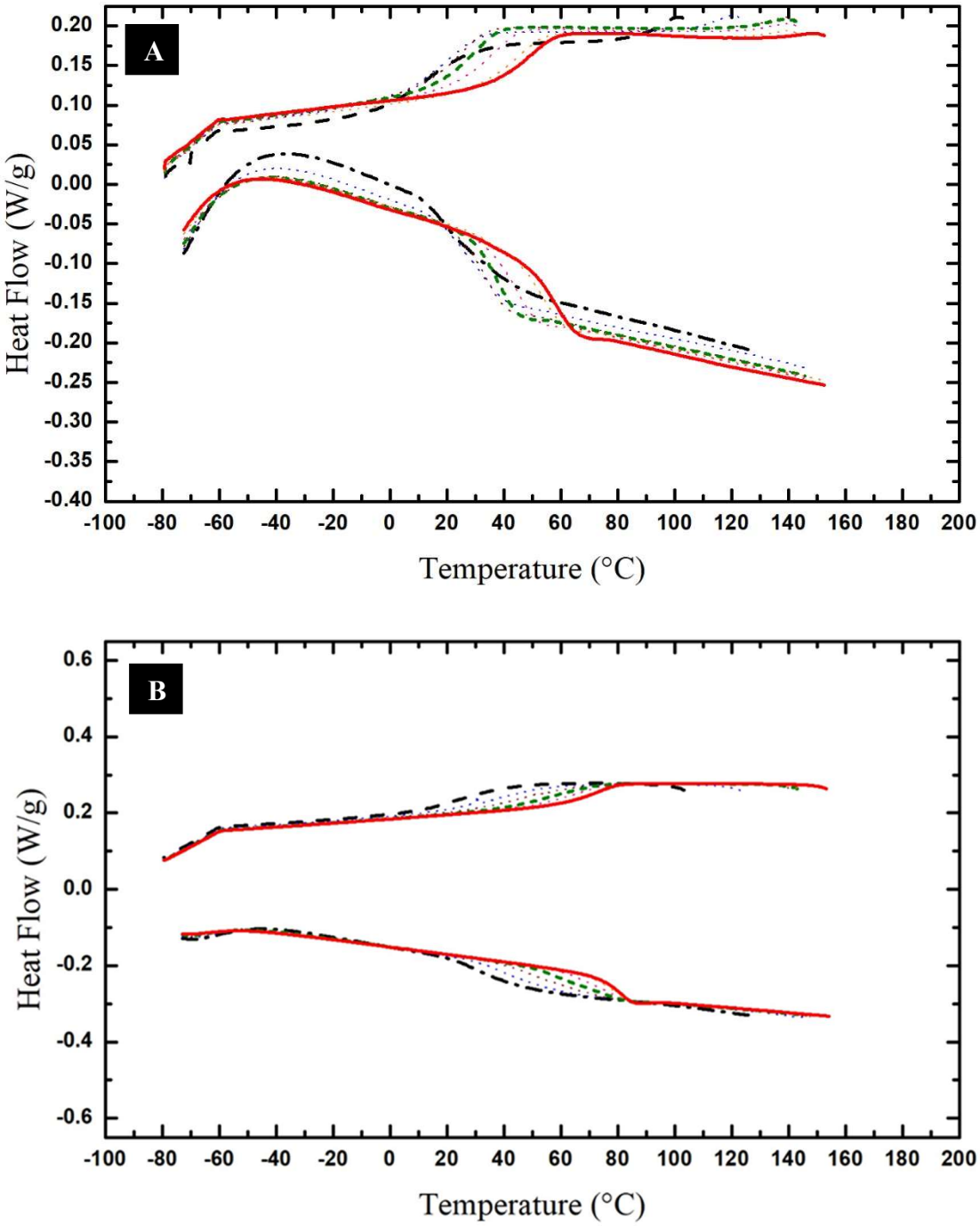

Figure 4.15. DSC before and after soxhlet extraction of PU6 having 1% catalyst: (A) before soxhlet extraction 1st cycle (–·–·–); 4th cycle (- - - - -); 7th cycle (——); (B) after soxhlet extraction 1st cycle (–·–·–); 4th cycle (- - - - -); 7th cycle (——).

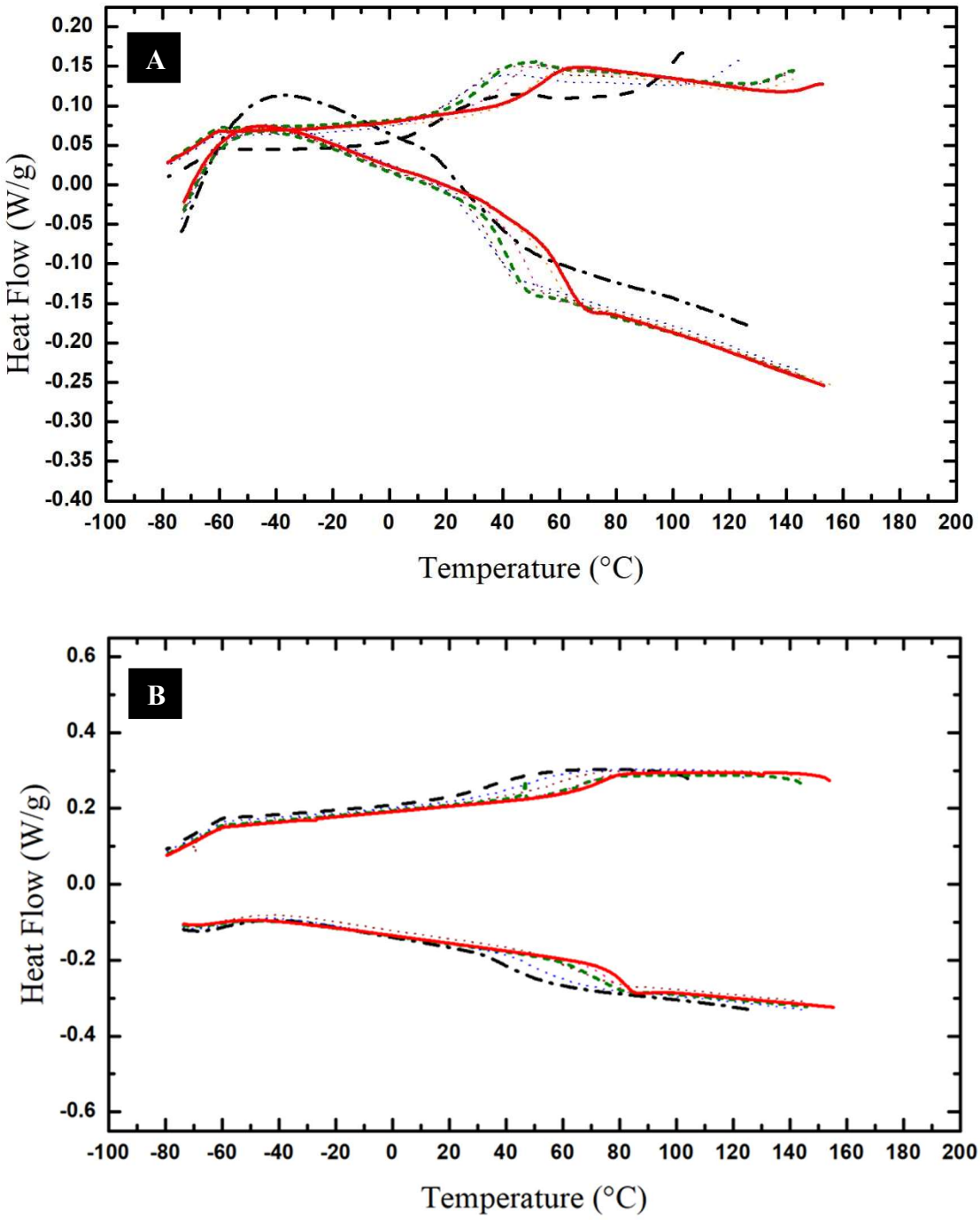

Figure 4.16. DSC before and after soxhlet extraction of PU7 having 0.3% catalyst: (A) before soxhlet extraction 1st cycle (–·–·); 4th cycle (- - - -); 7th cycle (——); (B) after soxhlet extraction 1st cycle (–·–·); 4th cycle (- - - -); 7th cycle (——).

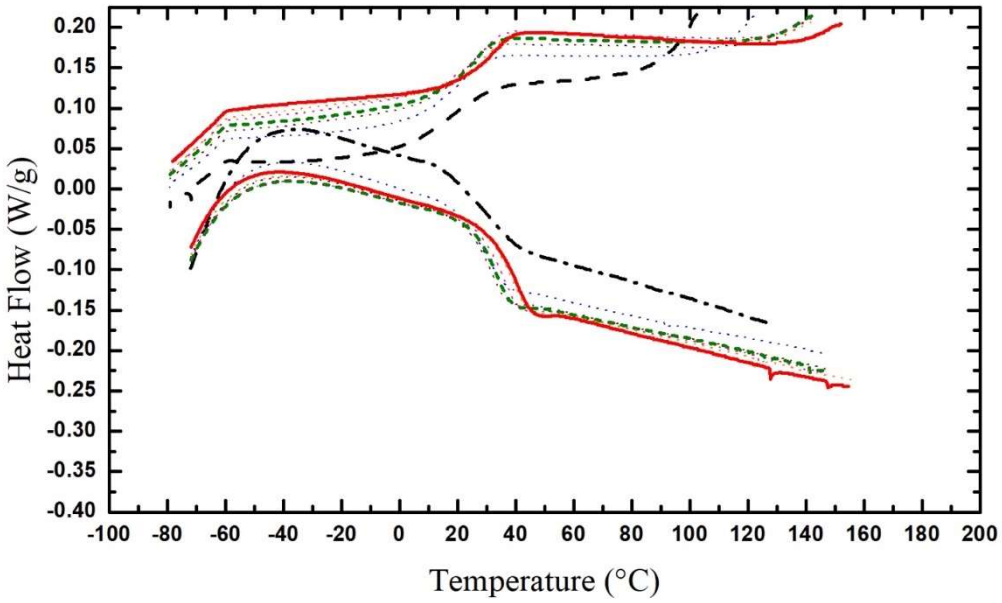

Figure 4.17. DSC of PU8 having 0.1% catalyst: before soxhlet extraction 1st cycle (–·–·–); 4th cycle (- - - - -); 7th cycle (——).

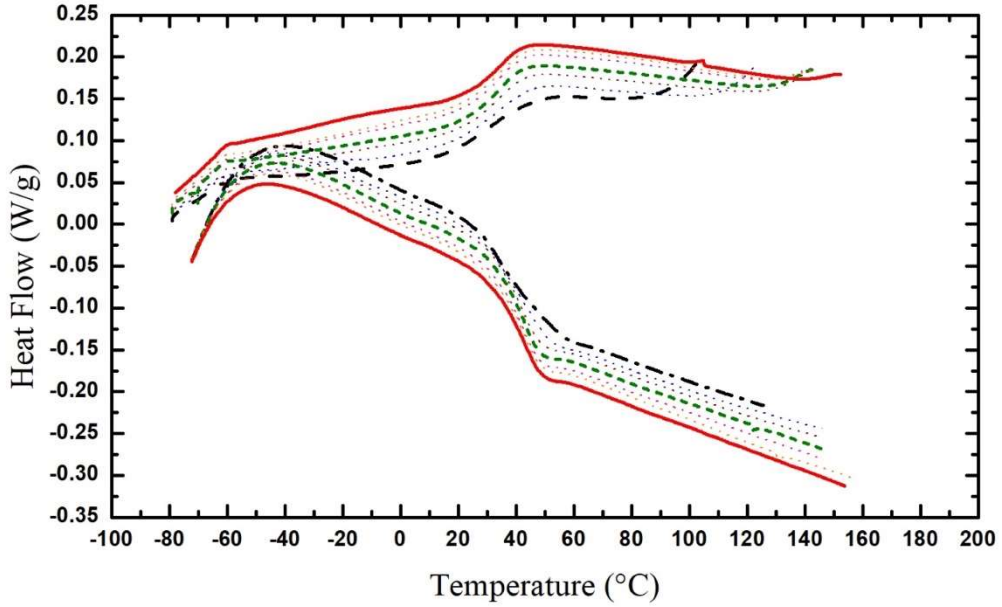

Figure 4.18. DSC of PU9 having no catalyst: before soxhlet extraction 1st cycle (–·–·–); 4th cycle (- - - - -); 7th cycle (——).

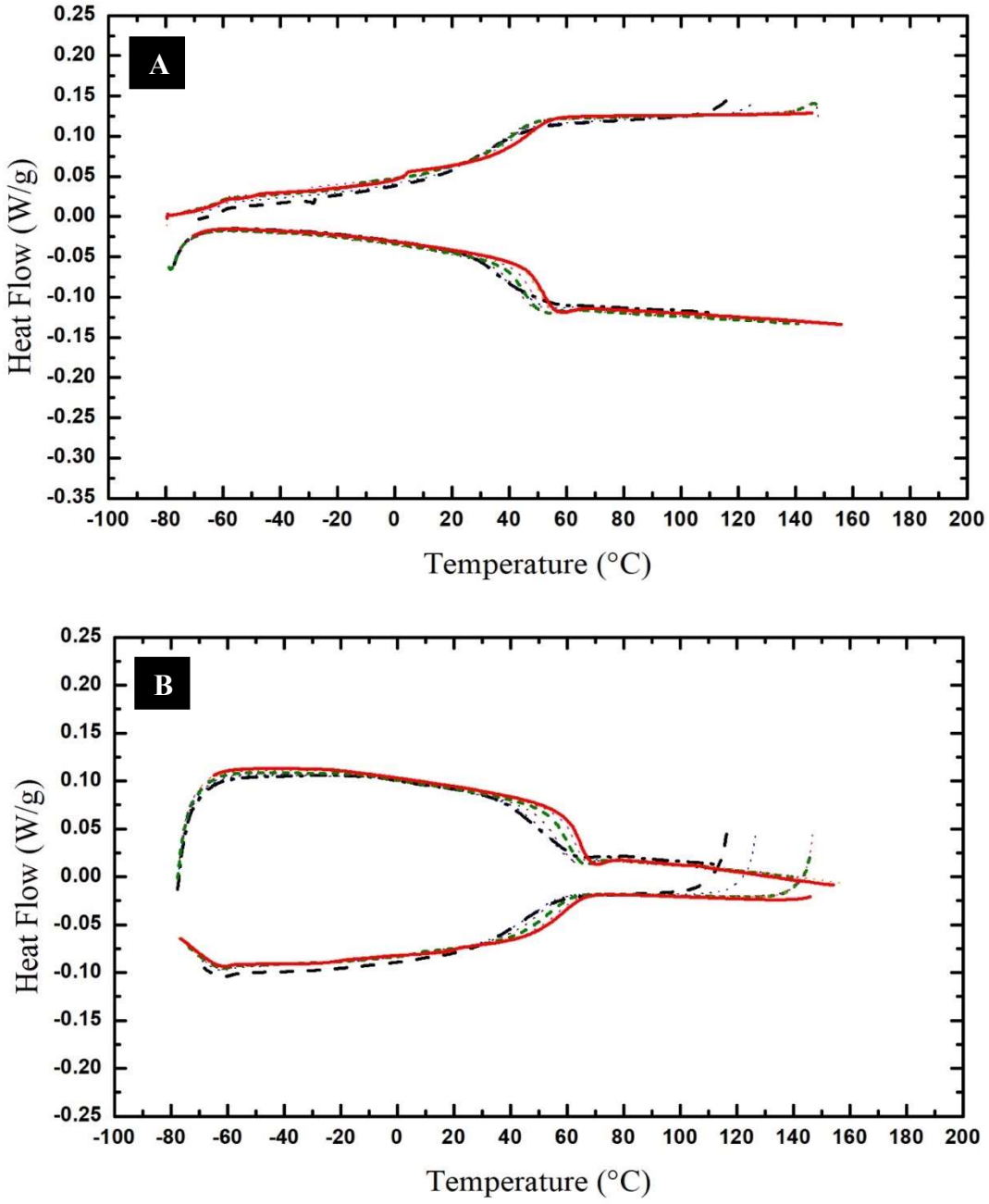

Figure 4.19. DSC before and after soxhlet extraction of 7 month-aged PU9 having no catalyst: (A) before soxhlet extraction 1st cycle (–·–·–); 4th cycle (- - - - -); 7th cycle (——); (B) after soxhlet extraction 1st cycle (–·–·–); 4th cycle (- - - - -); 7th cycle (——).

Table 4.4. Comparison of T_gs before and after soxhlet extraction (see Fig. A.4.8 to Fig. A.4.15 in Appendix C).

PU	% DBTD	Before Soxhlet extraction				After Soxhlet extraction			
		1st cycle		7th cycle		1st cycle		7th cycle	
		$T_{g\ cool}$ (˚C)	$T_{g\ heat}$ (˚C)	$T_{g\ cool}$ (˚C)	$T_{g\ heat}$ (˚C)	$T_{g\ cool}$ (˚C)	$T_{g\ heat}$ (˚C)	$T_{g\ cool}$ (˚C)	$T_{g\ heat}$ (˚C)
PU3	10	29	36	56	65	40	44	73	78
Aged PU4	5.6	41	45	41	54	49	56	54	76
PU5	3	17	17	27	26	50	56	55(4th cycle)	64 (4th cycle)
PU6	1	19	23	47	58	27	32	69	79
PU7	0.3	19	31	27	61	34	43	70	81
PU8	0.1	19	27	26	40	-	-	-	-
PU9	0	31	41	31	41	-	-	-	-
Aged PU9	0	35	37	41	51	42	50	54	63

Chapter 5

Self-dispersing $HOC_{11}C_1ImBr$ Polyurethane Dispersions (PUDs)

5.1 Overview

Incorporation of ILs into polyurethanes also provides hydrophilic sites to tune water interactions. These resins were thermally characterized. These 100% solid materials exhibited properties of self-dispersion in water forming thermodynamically stable nanoparticles in PUDs. Particle size and turbidity of these PUDs were analyzed, and effects of series of filtration and sonication treatments were examined. Stimuli responsive behavior was studied by using various anions such as PF_6^-, $CF3SO_3^-$, $N(CN)_2^-$, BF_4^-, I^-,and Br^-. Coatings of PUDs were made on glass slides and were subjected to various anion exchange treatments and were compared for their wetting properties by water using contact angle measurements. Rheological differences among various resins and PUDs were also observed. Stimuli responses to water were also observed in treated coatings.

5.2 Synthesis

Four different resins were simultaneously synthesized to examine effects of crosslinking (with glycerol) and to compare a PEO-based di-ol with a PPO-based di-ol. These variations yield backbones containing oligoethylene oxide and oligopropylene oxide. The cross-linker, glycerol, competes with di-ol for isocyanate linkages. These compositional variations are compared in Table 5.1.

For each resin, a pre-resin mixture comprising hydroxy-functional materials were first combined in a 15 mL vial prior to polymerization. These hydroxy-functional materials were

dissolved by using methylene chloride and DMF. DMF was used to achieve room temperature solubilization of the IL chain terminating $HOC_{11}C_1ImBr$. HDI was then added to stoichiometrically balance the hydroxyl reactants (NCO/OH ratio = 1.01), and then these reactant mixtures were stirred using a vibratory stirrer. Lastly, DBTD was added as catalyst to transparent and yellowish solutions of reactants. These reaction mixtures in vials were stirred and then placed in an oven at 80 °C for about 24 hours. After about 24 hours, the reaction mixtures were stripped of solvent at ambient conditions by allowing the reaction vial to vent in a hood, and then any remaining solvent was removed in a vacuum oven at 100 ºC for 3.5 hours.

An additional resin, which also had the backbone of PPO, was also synthesised. However, instead of using glycerol as a crosslinker, glycerol 1,3-diglycerolate diacrylate (triglycerol diacrylate) was used as an alternative cross-linker, which added two acrylate functionalities to the existing three hydroxy functionalities of glycerol moiety as shown in Fig. 5.1. This crosslinker was selected to facilitate incorporation of coupling additional crosslinking in coatings via acrylate group coupling. During synthesis of this resin, similar steps were taken as were taken for these other four resins, except that before adding catalyst, this reactant solution was cooled by putting it in a refrigerator freezer for 10 minutes at -5 ºC to -10 ºC. Also, this composition was reacted at an oven temperature of 60 °C for about 24 hours to avoid thermally polymerizing the acrylate groups.

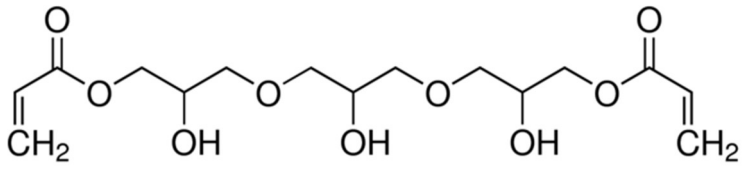

Figure 5.1. Structure of cross-linker glycerol 1,3-diglycerolate diacrylate.

Table 5.1. Compositional variations in different resin samples

Ingredient	PEO200/Gly PU	PEO200 PU	PPO192 PU	PPO192/Gly PU	PPO192/ Trigly PU
$OHC_{11}C_1ILBr$ (mmol)	3.10	3.10	3.10	3.10	3.10
PEO200 (mmol)	3.97	4.65	-	-	-
PPO192 (mmol)	-	-	4.64	3.97	3.97
Glycerol (mmol)	0.45	-	-	0.45	-
Triglycerol Diacrylate (mmol)	-	-	-	-	0.45
HDI (mmol)	6.28	6.22	6.24	6.27	6.21
CH_2Cl_2 (mg)	4544	4553	4446	4549	4549
DMF (mg)	880	882	811	881	881
DBTD (mg)	99	96	97.9	102	32
% solids	35.80%	35.60%	36.88%	35.53%	35.57%
Catalyst %	3.27%	3.09%	3.19%	3.41%	1.05%
NCO/OH ratio	1.01	1	1.01	1.01	1

All of our resin samples incorporated 25% of the hydroxyl equivalents using the IL chain termiantor, $HOC_{11}C_1ImBr$. The total number of hydroxyl equivalents in each sample as compared in Table 5.2. The most probable step-growth reaction product chains expected to form are shown in Fig. 5.2. Crosslinked chains are illustrated in Fig. 5.2(a). The uppermost chain in Fig. 5.2(a) ends with a radical on the right that connects with another glycerol moiety. These cross-linked chains comprise a certain number, x, of diols (PEO200) x+1 HDI. The lower chain

in Fig. 5.2(a) is terminated with an IL moiety. It comprises n-x diols and n-x+1 HDI. The chain illustrated in Fig. 5.2(b) illustrates one of several types of free chains that might be formed and that are not cross-linked, This particular one is terminated on the left by a diol and terminatd on the right by an IL moiety. This chain termination by an IL moiety blocks furher chain extension "to the right."

Table 5.2. Variation of percentage hydroxyl group equivalents in different resin samples

Resin Sample	Glycerol	Triglycerol diacrylate	PEO200	PPO192	$HOC_{11}C_1ImBr$
PEO200/Gly PU	11%	-	64%	-	25%
PEO200 PU	-	-	75%	-	25%
PPO192 PU	-	-	-	75%	25%
PPO192/Gly PU	11%	-	-	64%	25%
PPO192/Trigly PU	-	11%	-	64%	25%

Chain termination by a diol such as PEO200 on the lefthand side of the chain of Fig. 5.2(b) requires that this terminal hydroxyl does not meet an activated isocyanate. If another IL moiety reacted with the left-most isocyante in Fig. 5.2 (b), the resulting free chain could not be further extended. Chain termination also could occur if the left-most group were an isocyanate, and this situation would require that hydroxyl group availability were blocked or sequestered.

Other isolated chain structures are possible. They include chains similar to those of

Fig. 5.2(b), wherein both ends are terminated with an IL moiety, both ends are terminated with a diol species, and where both ends are terminated by an HDI fragment. Having one end terminated with a diol and the other terminated with an HDI and having one end terminated with an IL and the other with HDI are additional types of free chains that might be obtained. Further, crosslinking by allophonate coupling between NH groups in urethane linkages and isocyanate are possible ways that any chain might be crosslinked to others.

Multiple additional approaches can be used to further increase crosslinking among PUs such as an introduction of trifunctional or higher functional isocyanates (polyisocyanates) or higher functional hydroxyls (polyols). Such crosslinking increases material strength and modulus. Other crosslinking chemistries can also be used, such as diacrylate polyols as used in resin sample PPO192/Trigly PU.

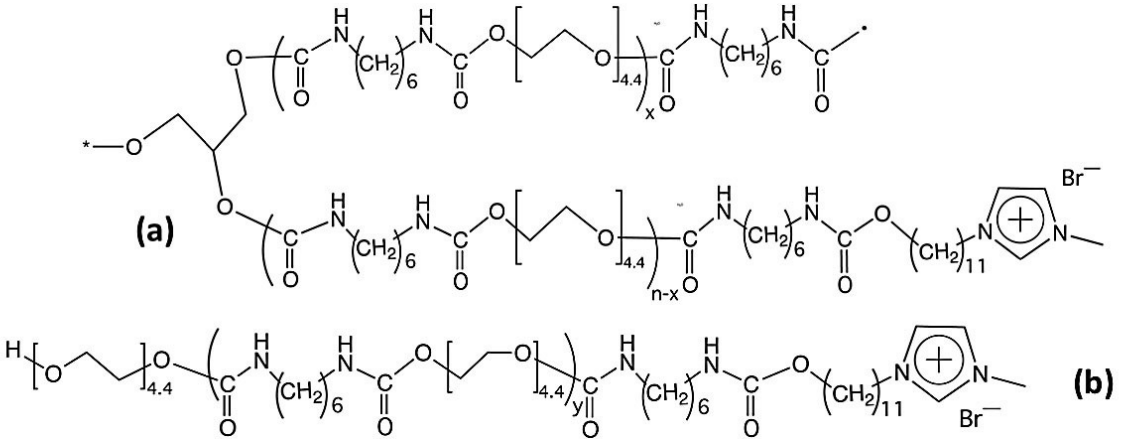

Figure 5.2. Structures of resin reaction products. (a) Primary cross-linked polyurethane chains resulting from glycerol, HDI, PEO200, and IL; (b) one of multiply possible free chain products.

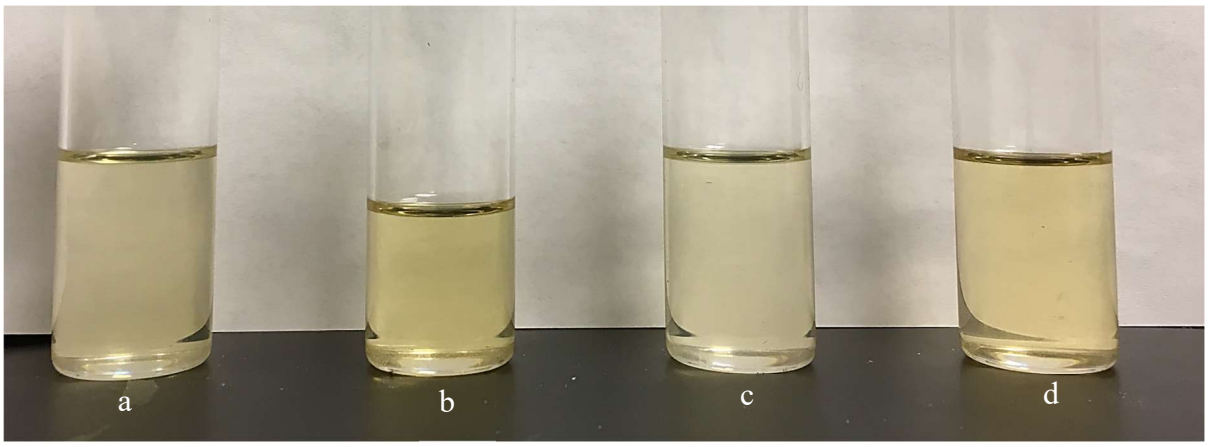

Figure 5.3. Reaction products after removal from oven. (a) PEO200 PU; (b) PPO192 PU; (c) PEO200/Gly; (d) PU PPO192/Gly PU.

Reaction products just after removal from heating oven are illustrated in Fig. 5.3. The PPO192-containng products appear "more yellow" than the PEO200-resins. This is most likely because the environment for the bromide associated with the IL, $HOC_{11}C_1ImBr$, interacts differently with PPO groups compared to PEO.

5.3. Thermal Characterization of Resins

5.3.1. TGA of resins

TGA of all five resin samples was done in an inert atmosphere of nitrogen by heating from room temperature to 580 °C at a rate of 10 °C/min. It can be seen in Fig. 5.4 that there was no solvent left in these 100% solid materials. All of these materials decompose very similarly. The five curves illustrated in Fig. 5.4 are nearly superimposable. Some minor weight loss over the 150 °C to 300 °C interval is not assigned, and there the variation is less than 5%, with the Trigly-containing material being less stable. Much more significant decomposition of these materials starts at about 320 °C, and a variation of about 10% between samples is evident over

320 °C to 400 °C. Thermal decomposition of Triglycerol ether bonds make this cross-linker likely less thermally stable than glycerol.

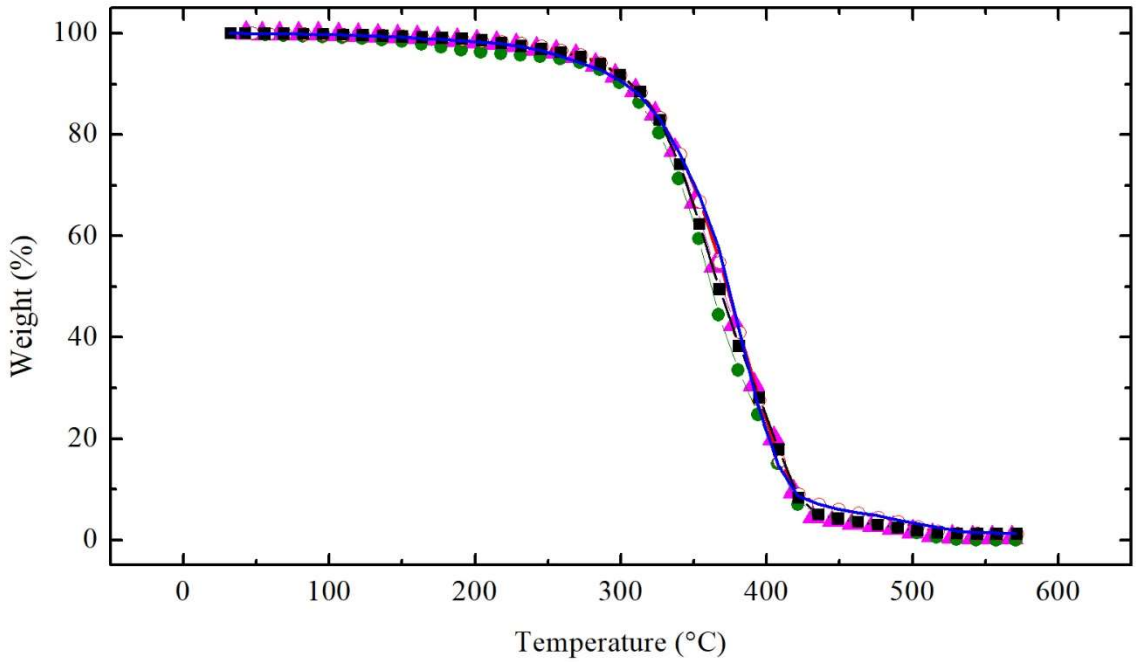

Figure 5.4. TGA comparison of resins: PEO200/Gly PU (——); PEO200 PU (—○—); PPO192 PU (—■—); PPO192/Gly (—▲—); PPO192/Trigly (—●—).

5.3.2 DSC of resins

PEO200 PU, PEO200/Gly PU, PPO192 PU, and PPO192/Gly PU were together heated in a vacuum oven at 100 °C for two hours prior to studying them by DSC. The PPO192/Trigly PU sample was heated at 85 °C for two hours in a vacuum oven. It was observed that during heating in a vacuum oven, solid materials in all resin samples started to flow at about 60-70 °C (Fig. A.5.1 in AppendixD). During running their DSCs, samples were first heated to 110 °C.

After keeping them isothermal for 5 minutes, they were cooled to -80 °C at a rate of 10 °C/min and kept isothermal for 5 minutes. Samples were then heated to 110 °C to complete the cycle.

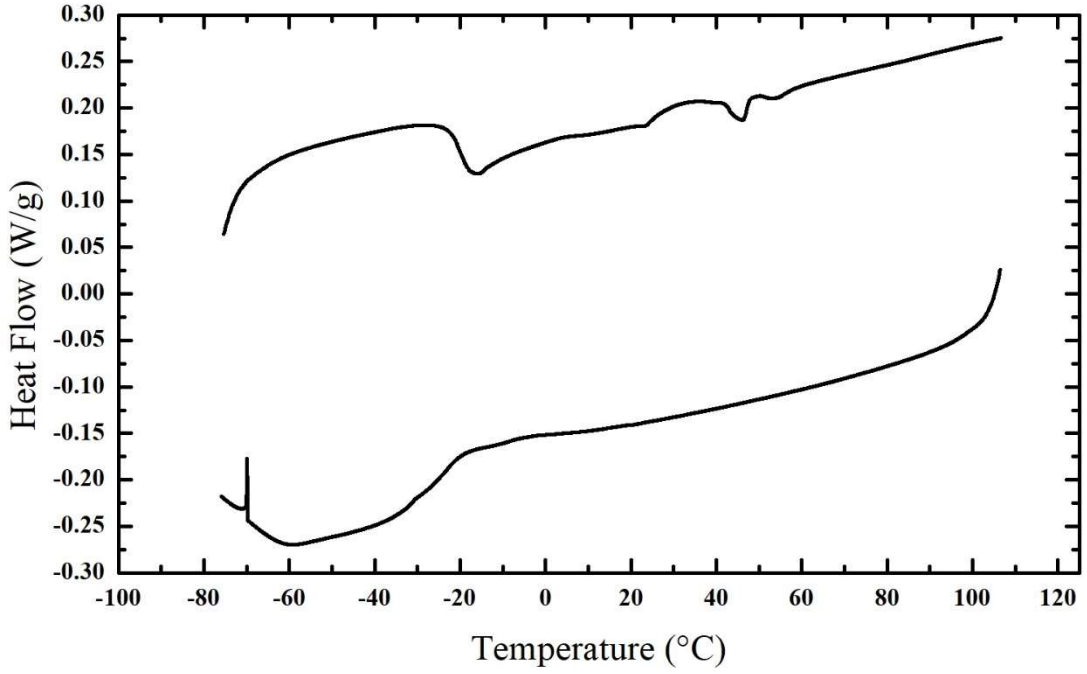

Figure 5.5. DSC of PEO200 PU at a scan rate of 10 °C/min. Sample was degassed in a vacuum oven for two hours at 100 °C prior to DSC.

In Fig. 5.5, during the cooling segment, a T_g can be seen at -23 °C. On further cooling, a freezing peak is seen at -70 °C with a freezing enthalpy ($\triangle H_f$) of 0.26 J/g. This freezing peak is because of undissolved DBTD catalyst in the resin sample. During heating, a T_g can be seen at -20 °C. On further heating, two melting peaks are seen. A first peak has $T_{m,onset}$ at 15 °C with $T_{m,peak}$ at 23 °C and a melting enthalpy ($\triangle H_m$) of 0.57 J/g. A second peak has $T_{m,onset}$ at 42 °C with $T_{m,peak}$ at 46 °C and a $\triangle H_m$ of 0.66 J/g (see Fig. A.5.2 in Appendix D for enthalpy integration).

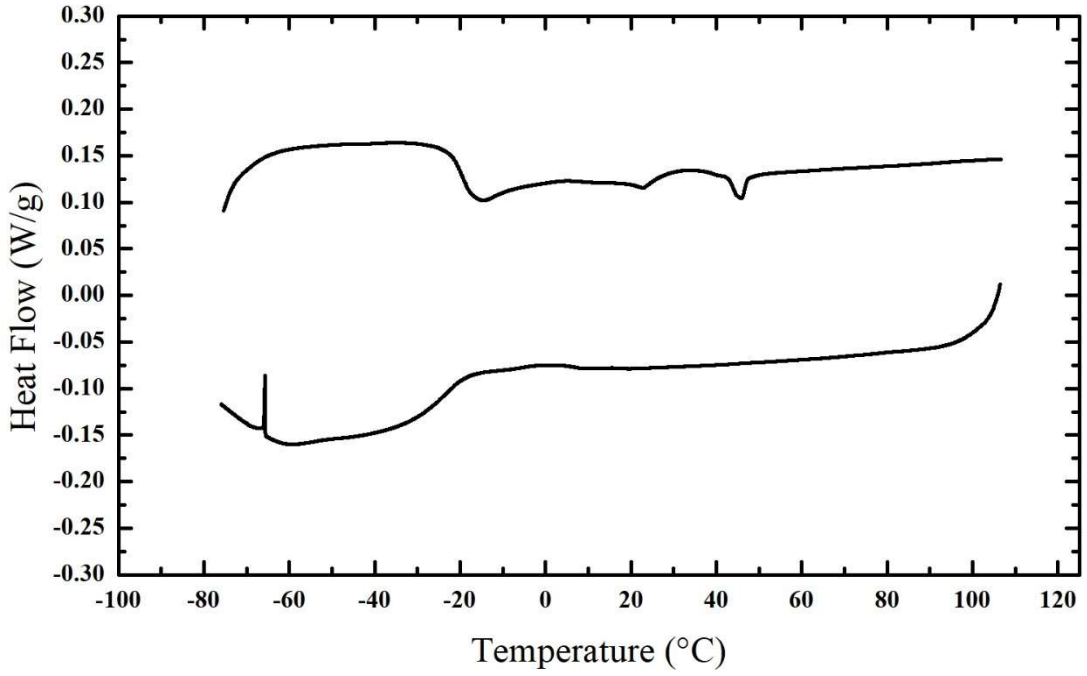

Figure 5.6. DSC of PEO200/Gly PU at a scan rate of 10 °C/min. Sample was degassed in vacuum oven for two hours at 100 °C prior to DSC.

In Fig. 5.6, during cooling, T_g can be seen at -23°C. On further cooling, a freezing peak is seen at -66°C with a $\triangle H_f$ of 0.18 J/g. This freezing peak is from undissolved DBTD catalyst in the resin sample. During heating, a T_g can be seen at -20 °C. On further heating, two melting peaks are seen. The first peak has $T_{m,onset}$ at 16 °C with $T_{m,peak}$ at 23 °C and a $\triangle H_m$ of 0.68 J/g. A second peak has $T_{m,onset}$ at 43 °C with $T_{m,peak}$ at 46 °C and a $\triangle H_m$ of 0.66 J/g (see Fig. A.5.3 for enthalpy integration).

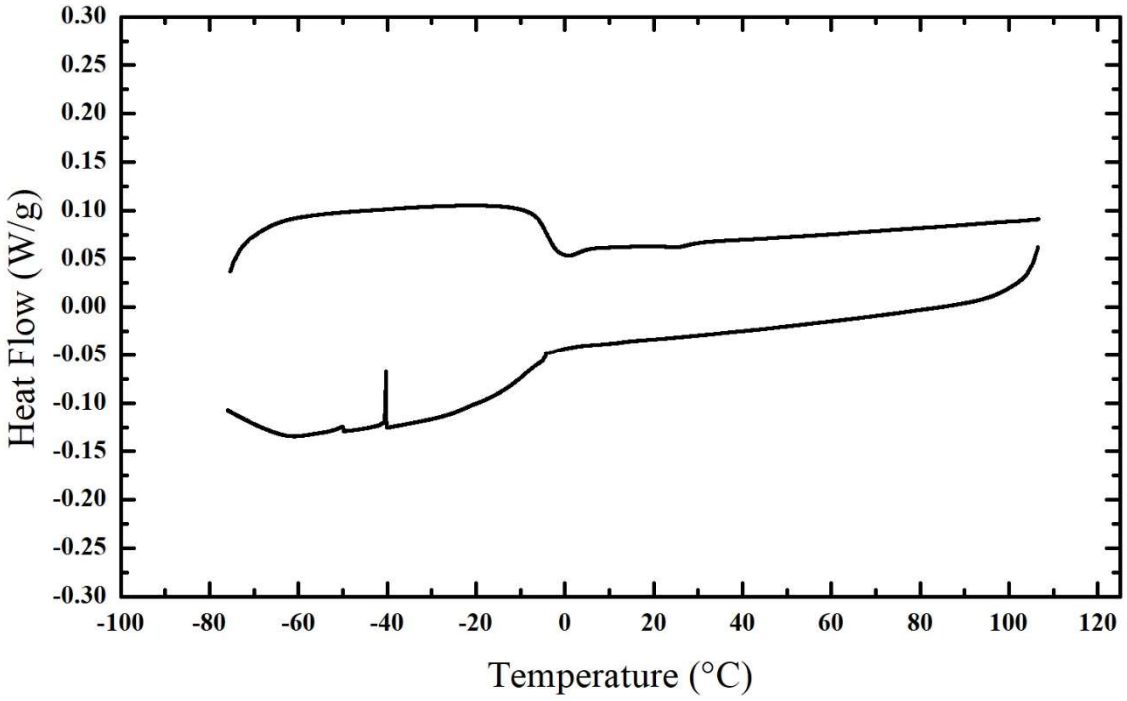

Figure 5.7. DSC of PPO192 PU at a scan rate of 10 °C/min. Sample was degassed in vacuum oven for two hours at 100 °C prior to DSC.

In Fig. 5.7 during cooling, a T_g can be seen at -10 °C. On further cooling, a freezing peak is seen at -40 °C with a $\triangle H_f$ of 0.13 J/g and at -50 °C with a $\triangle H_f$ of 0.08 J/g. These freezing peaks are because of undissolved DBTD catalyst in the resin sample. During heating, T_g can be seen at -4 °C. No melting peaks are seen during heating (see Fig. A.5.4 in Appendix D for enthalpy integration).

In Fig. 5.8, during cooling, a T_g can be seen at -13 °C. On further cooling, a freezing peak is seen at -39 °C with a $\triangle H_f$ of 0.26 J/g. This freezing peak is due to undissolved DBTD catalyst in the resin sample. During heating, a T_g can be seen at -8 °C. No melting peaks are seen during heating (see Fig. A.5.5 in Appendix D for enthalpy integration).

In Fig. 5.9 during cooling, a T_g can be seen at 2°C. On further cooling, a freezing peak is seen at -22 °C with a $\triangle H_f$ of 0.19 J/g. This freezing peak is from undissolved DBTD catalyst in

the resin sample. During heating, a T_g can be seen at 8 °C. No melting peaks are seen during the following heating segment (see Fig. A.5.6 in Appendix D for enthalpy integration).

From Table 5.3, it can be seen that resins containing PEO 200 have lower T_gs than PPO-based resin samples. PPO192/Trigly PU has the highest T_g. DSCs of PEO200-based resin samples also show melting peaks during heating events which are not present in PPO192-based resin samples. These peaks can be assigned to melting of hard phases in the PU matrices. These hard phases would be higher because of hydrophilic sites of PEO, which would have a higher level of hydrogen bonding compared to PPO-based chains.

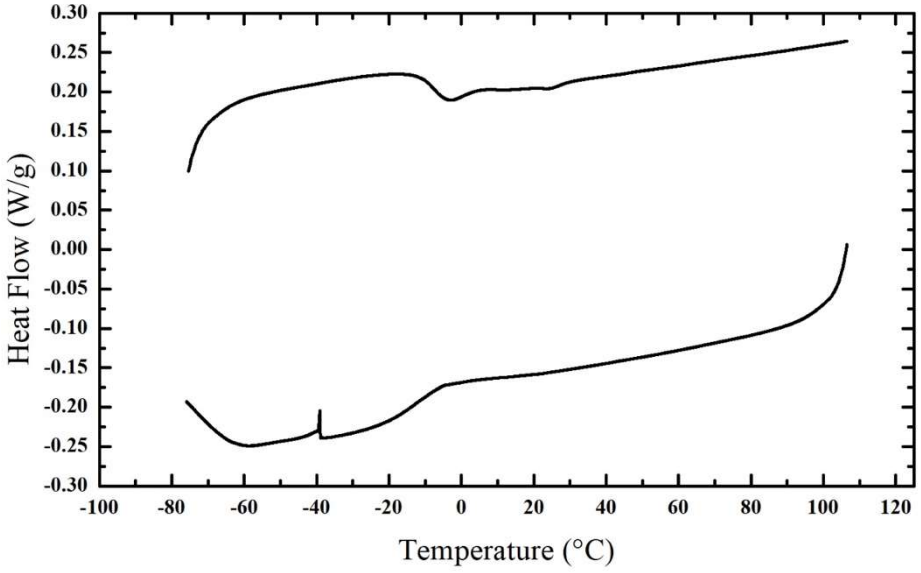

Figure 5.8. DSC of PPO192/Gly PU at a scan rate of 10 °C/min. Sample was degassed in a vacuum oven for two hours at 100 °C prior to DSC.

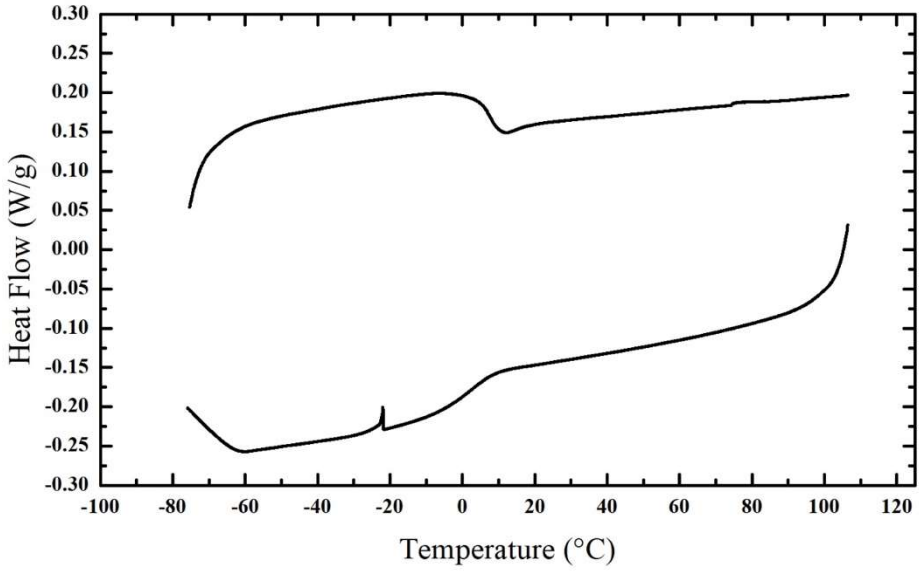

Figure 5.9. DSC of PPO192/Trigly PU at a scan rate of 10 °C/min. Sample was degassed in a vacuum oven for two hours at 80 °C prior to DSC.

Table 5.3. Comparison of DSC among resin samples

Resin	$T_{g\ cool}$ (˚C)	$T_{g\ heat}$ (˚C)
PEO200 PU	-23	-20
PEO200/Gly PU	-23	-20
PPO192 PU	-10	-4
PPO192/Gly PU	-13	-8
PPO192/Trigly PU	2	8

5.4 Preparation of PUDs (Self-Dispersion)

5.4.1 Preparation of 1% (w/w) PUDs

About 100 mg of five 100% solid resin samples, PPO192/Gly PU, PEO200/Gly PU, PPO192 PU, PEO200 PU, and PPO192/Trigly PU, were put in glass vials (Fig. 5.10). To make 1% (w/w) dispersions, about 900 g of DI water was added to each of these solids, and auto-dispersion was immediately evident. On contact with water, convective turbidity "streams" due to dispersed particle-induced turbidity appeared near the solid resin surfaces as shown in Fig. 5.11. After 19 hours of ambient storage, almost all of these samples showed apparently "complete" auto-dispersion; a cloudy dispersion in the lower part of each vial can be seen in Fig. 5.12. Resin sample PEO200 PU did not show complete dispersion, even after 36 hours (Fig. 5.13 (d)), though just 1 min of vibratory stirring completely dispersed this sample. Vibratory stirring (10 sec) was given to other samples to make more uniform appearing dispersions and to dilute the auto-dispersed particulates in the available water (Fig. 5.14). Visually, all dispersions had different turbidities; PPO192/Trigly PUD was least turbid, and PEO200 PUD was most turbid. Particle sizes of these PUDs were analyzed and are discussed in the next section. Sonic-horn sonication of these PUDs reduced their turbidity by reducing their particle size (see next section).

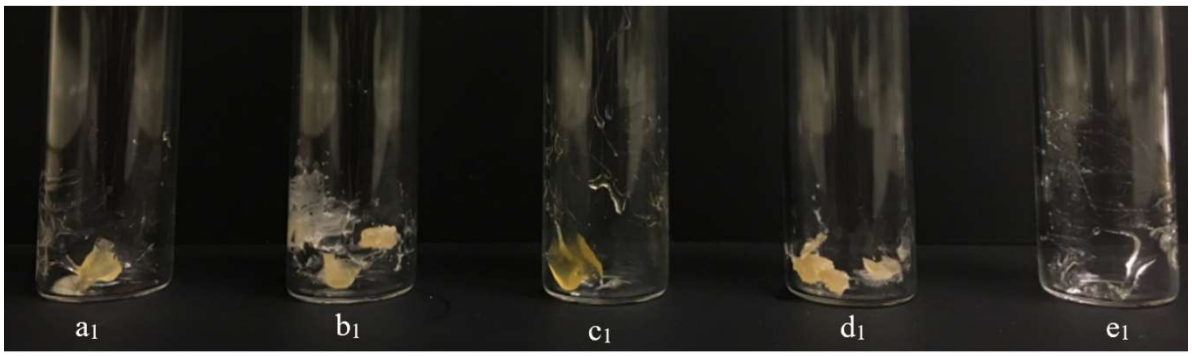

Figure 5.10. Solid resin samples in glass vials: (a_1) PPO192/Gly PU; (b_1) PEO200/Gly PU; (c_1) PPO192 PU; (d_1) PEO200 PU; (e_1) PPO192/Trigly PU

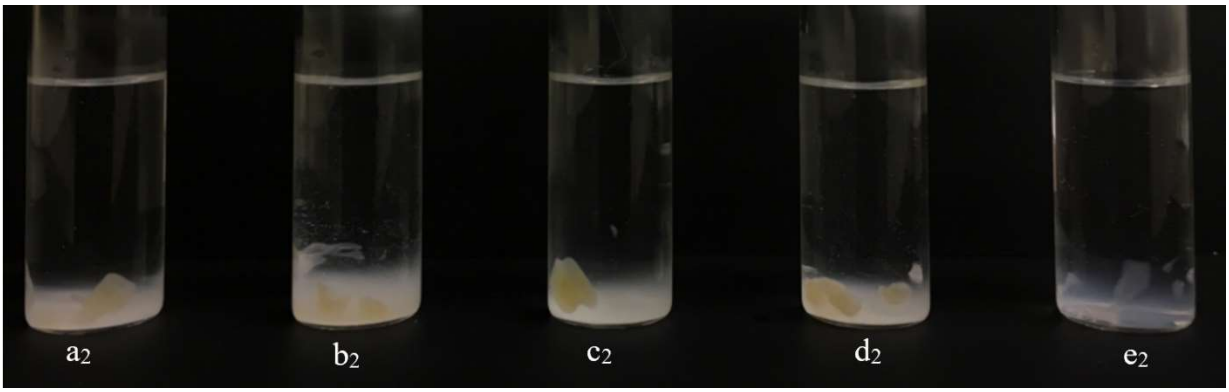

Figure 5.11. Resins of Fig. 5.10 after adding 10 ml DI water into: (a_2) PPO192/Gly PU; (b_2) PEO200/Gly PU; (c_2) PPO192 PU; (d_2) PEO200 PU; (e_2) PPO192/Trigly PU; auto-dispersion of resin solids is illustrated.

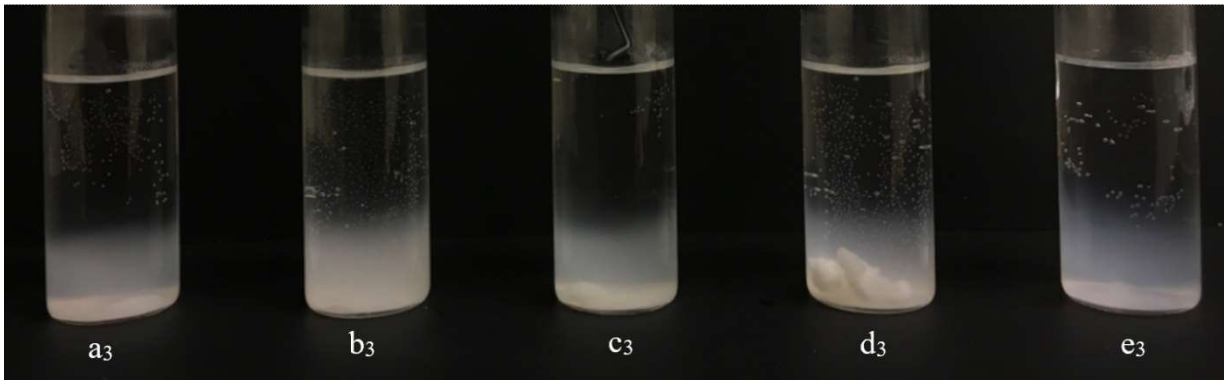

Figure 5.12. Dispersions of Fig. 5.11 after 19 hours ambient storage: (a_3) PPO192/Gly PU; (b_3) PEO200/Gly PU; (c_3) PPO192 PU; (d_3) PEO200 PU; (e_3) PPO192/Trigly PU.

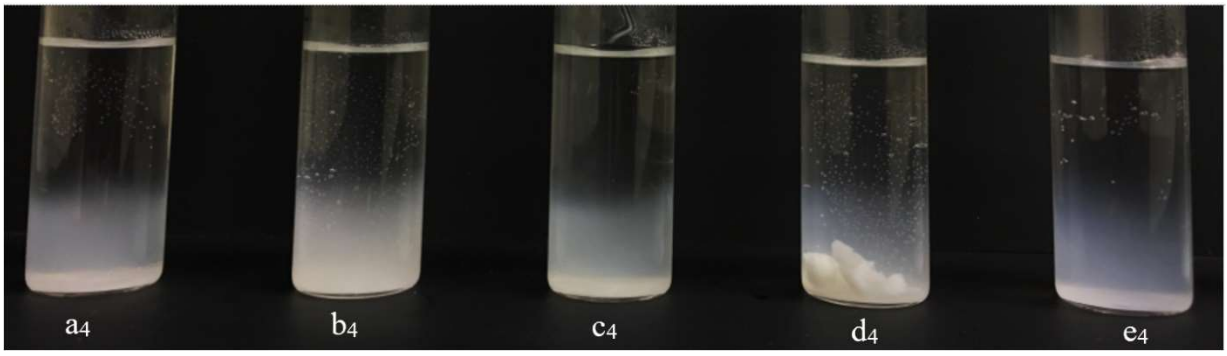

Figure 5.13. Dispersions of Fig. 5.11 after 36 hours ambient storage; (a_4) PPO192/Gly PU; (b_4) PEO200/Gly PU; (c_4) PPO192 PU; (d_4) PEO200 PU; (e_4) PPO192/Trigly PU.

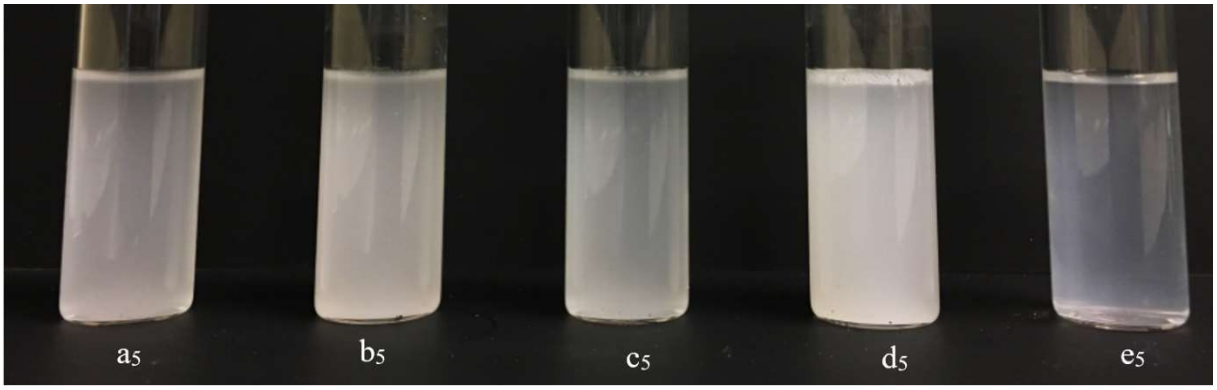

Figure 5.14. Dispersions of Fig. 5.11 after 36 hours ambient storage and after 10 seconds of stirring; (a_5) PPO192/Gly PUD; (b_5) PEO200/Gly PUD; (c_5) PPO192 PUD; (d_5) PEO200 PUD (stirred for 1 minute); (e_5) PPO192/Trigly PUD.

5.4.2 Preparation of 25% (w/w) PUDs

About 1 g each of these five 100% solid resin samples were put in glass vials (Fig. 5.15). To make dispersions 25% by weight, about 3 gm of DI water was added, which immediately turned resin samples cloudy near the surfaces of contacts with water as shown in Fig. 5.16. After 15 hours almost all "bulk parts" of resin samples were cloudy as seen in Fig. 5.17. After 60 hours storage and 3 min of vibratory stirring, uniform dispersions were obtained (Fig. 5.18). Visually, all dispersions had variable turbidity. The PPO192/Trigly PUD was least turbid, and the PEO200 PUD was most turbid. Sonication for 10 min using micro-tip sonication of these PUDs reduced turbidity of PPO192-based PUDs and made them translucent. The PPO192/Trigly PUD had the least turbidity. PEO200-based PUDs did not show much change in turbidity and were opaque (Fig. 5.19). After sonication, these PUDs were used to make draw-down coatings on glass slides using a small rectangular drawdown bar. It was observed that non-sonicated samples yielded rough coatings and sonicated samples yielded more uniform and smoothly coalesced coatings.

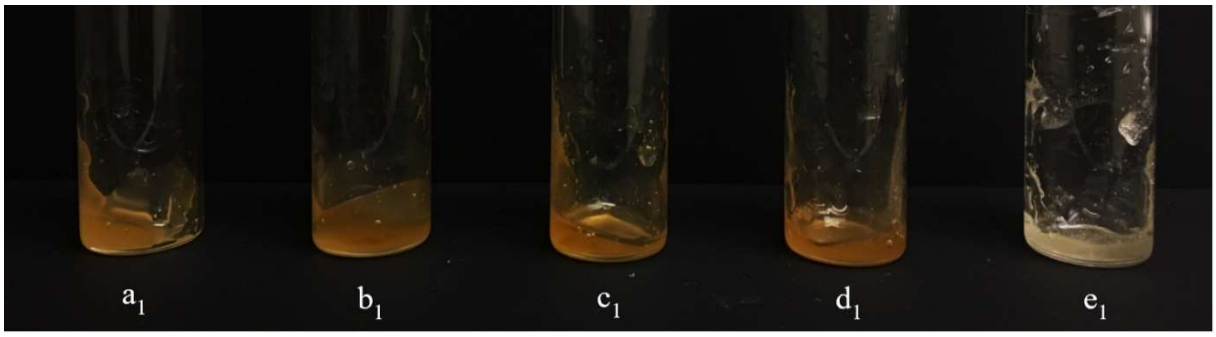

Figure 5.15. Solid resin (1 g) samples in glass vials: (a_1) PPO192/Gly PU; (b_1) PEO200/Gly PU; (c_1) PPO192 PU; (d_1) PEO200 PU; (e_1) PPO192/Trigly PU.

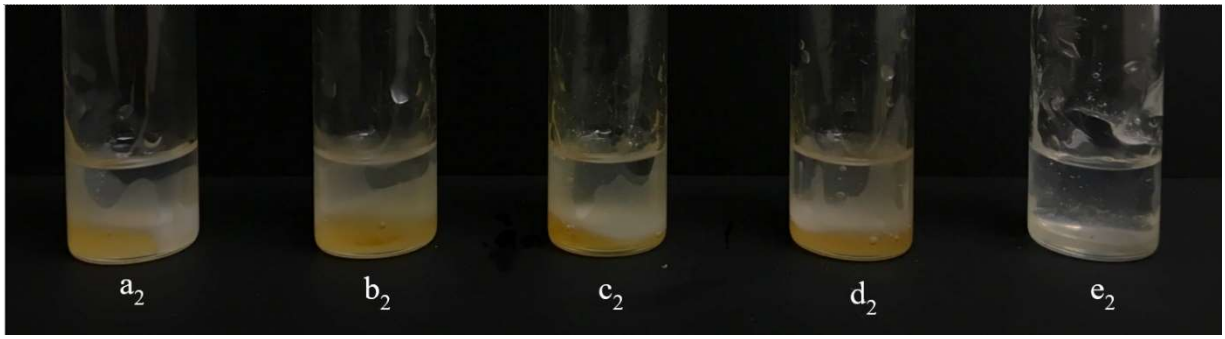

Figure 5.16. Resins of Fig. 5.15 after adding 3 ml DI water into: (a_2) PPO192/Gly PU; (b_2) PEO200/Gly PU; (c_2) PPO192 PU; (d_2) PEO200 PU; (e_2) PPO192/Trigly PU.

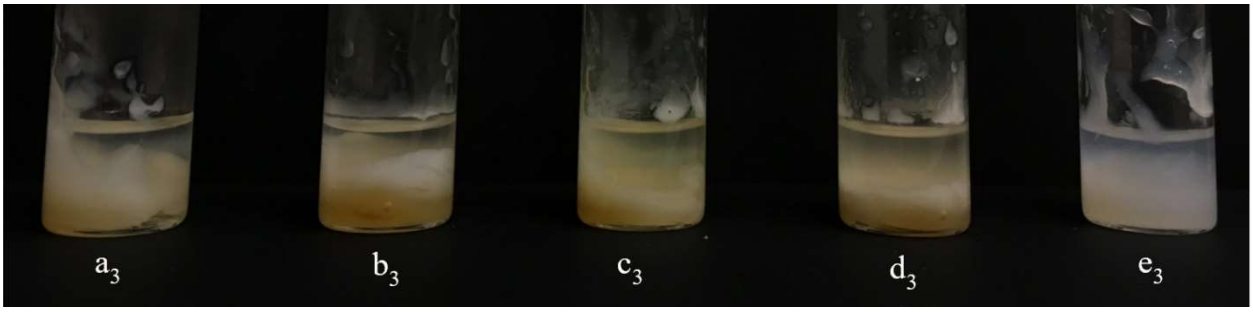

Figure 5.17. Resins of Fig. 5.16 after 15 hours storage at ambient: (a_3) PPO192/Gly PU; (b_3) PEO200/Gly PU; (c_3) PPO192 PU; (d_3) PEO200 PU; (e_3) PPO192/Trigly PU.

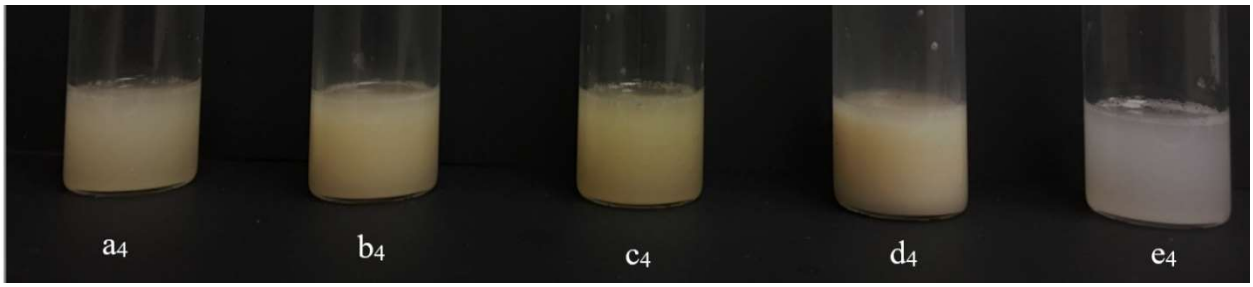

Figure 5.18. Resins of Fig. 5.16 after 60 hours storage following stirring for 3 minutes: (a_4) PPO192/Gly PUD; (b_4) PEO200/Gly PUD; (c_4) PPO192 PUD; (d_4) PEO200 PUD; (e_4) PPO192/Trigly PUD.

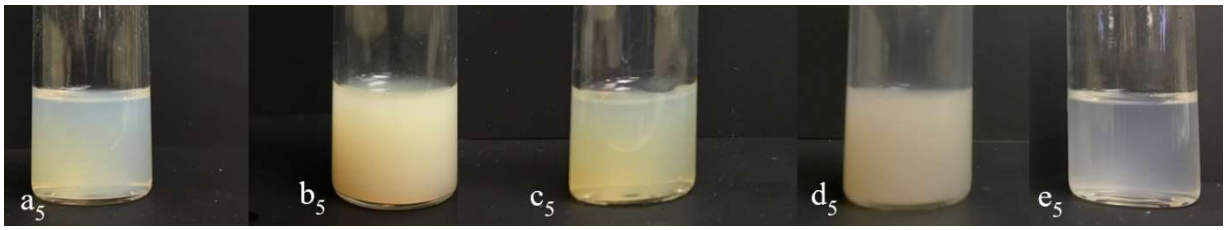

Figure 5.19. Dispersions of Fig. 5.18 after 10 minutes of sonication: (a_5) PPO192/Gly PUD; (b_5) PEO200/Gly PUD; (c_5) PPO192 PUD; (d_5) PEO200 PUD (stirred for 1 minute); (e_5) PPO192/Trigly PUD.

5.5 Particle Size Characterization of PUDs

To measure particle sizes and particle size distributions of various PUDs by dynamic light scattering, 0.5% by weight dispersions were made in a way similar to that discussed in section 5.4. Samples of self-dispersed PUDs were put in glass cuvettes for particle size analysis. Particle size analysis was first done for PUD samples without any filtration; then samples were filtered through a 1-μm filter and were analyzed again. Lastly, 1-μm filtered samples were passed through 0.45-μm filter and were again analyzed for particle size. In parallel, unfiltered PUD samples were sonicated using a 3-4 mm diameter sonic horn for 10 min while being chilled in an ice-water bath. These sonicated samples were analyzed for particle size without any filtration; then samples were filtered through a 1-μm filter and were analyzed again. Finally,

1-μm filtered samples were passed through a 0.45-μm filter and were again analyzed for particle size. Percentage solids were measured before and after filtrations. UV-visible spectroscopy was used to measure turbidity at 500 nm at all stages in 5 mm pathlength spectrosil quartz cuvettes. Particle size parameters including various modes and means and volume-number frequency polydispersity indexes, experimental dispersion solids determinations, and specific turbidity at 500 nm are compared in Table 5.4, Table 5.5, Table 5.6, Table 5.7, and Table 5.8.

All samples showed reductions in turbidity after sonication as well as after each filtration process as illustrated in Fig. 5.20, Fig. 5.21, Fig. 5.22, Fig. 5.23, and Fig. 5.24. Lognormal and multimodal size distributions (MSD) on bases of volume, number, and intensity weightings are summarized in Table 5.4, Table 5.5, Table 5.6, Table 5.7, and Table 5.8. It can be seen visually, as well as from specific turbidity measurements, that for all samples, filtrations with a 1-μm filter followed by 0.45-μm filtration significantly decreased the turbidity with a negligible loss in solids content. This experiment suggests that there are only a few big particles that are negligible in their number but mainly impact turbidity and intensity-weighted results. By filtration of those big particles, intensity of their scattering and turbidity can be reduced. There are multiple modes in the size distributions that can be seen in MSD data and reduction in intensities of modes having bigger particles can be seen as consequences of filtration and sonication. Sonication also reduced the particle size and, hence, turbidity by de-aggregating bigger particles. Filtering a few remaining bigger particles reduced the intensity and turbidity further as seen in figures and tables in this section.

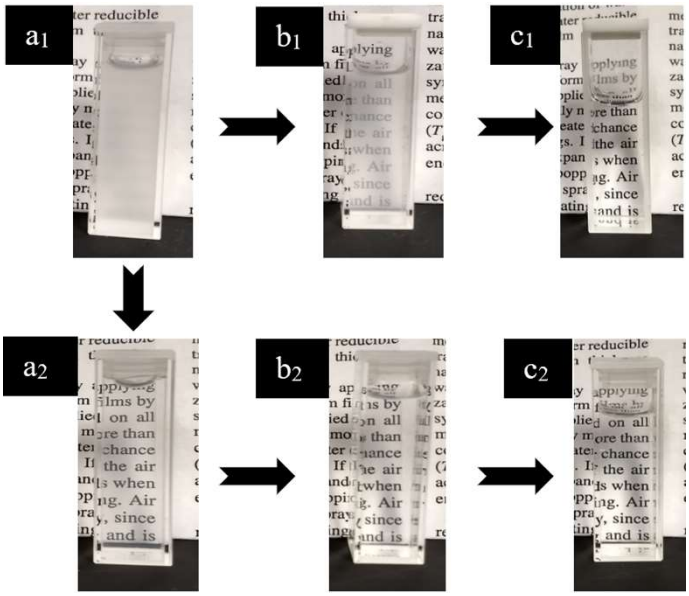

Figure 5.20. Filtration and sonication effects on apparent turbidity of 0.5% PUD from PEO200 PU: (a_1) after self-dispersion of resin; (b_1) after filtering (a_1) through 1-micron filter; (c_1) after filtering (b_1) through 0.45-micron filter; (a_2) after sonicating (a_1) for 10 minutes; (b_2) after filtering (a_2) through 1-micron filter; (c_2) after filtering (b_2) through 0.45-micron filter.

Table 5.4(a) Particle size parameters, solids, and turbidity for 0.5% (w/w) PEO200 PU PUD subjected to filtration and sonication

Measured Parameters	Non-sonicated			Sonicated		
	not filtered	filtered (1 μm)	filtered (0.45 μm) (after 1 μm)	not filtered	filtered (1 μm)	filtered (0.45 μm) (after 1 μm)
$^{LN}\langle d\rangle_I$/nm	610	497	238	206	159	152
$^{LN}\langle d\rangle_V$/nm	585	310	121	104	88	72
$^{LN}\langle d\rangle_n$/nm	562	178	54	47	44	38
$^{MSD}\langle d\rangle_I$/nm	723	538	198	279	206	152
$^{MSD}\langle d\rangle_V$/nm	534	620	1.5	210	83	61
$^{MSD}\langle d\rangle_n$/nm	481	310	1.5	66	33	25
Solids/%	0.46	--	0.42	0.45	--	0.46 ± 0.01
τ_{500}/OD	1.094	0.415	0.057	0.162	0.054	0.062

Table 5.4(b) Multimode size distribution parameters for 0.5% (w/w) PEO200 PU PUD subjected to filtration and sonication

Estimated Parameters	Not-Sonicated			Sonicated		
	Not Filtered	Filtered (1 μm)	Filtered (0.45 μm) (after 1 μm)	Not Filtered	Filtered (1 μm)	Filtered (0.45 μm) (after 1 μm)
$^{mode1}d_I$/nm	2853	654	227	386	276	225
% I	8	73	86	68	62	57
$^{mode2}d_I$/nm	511	219	38	68	74	68
% I	92	27	8	32	37	42
$^{mode3}d_I$/nm	--	--	1.6	--	26	21
% I			6		1	1
$^{mode1}d_V$/nm	2677	689	227	451	304	225
% V	1	88	<1	41	10	5
$^{mode2}d_V$/nm	474	219	38	68	74	62
% V	98	12	<1	59	69	70
$^{mode3}d_V$/nm	--	--	1.3	--	26	21
% V			100		21	25
$^{mode1}d_n$/nm	2677	654	227	450	276	224
% n	<1	21	<1	<1	<1	<1
$^{mode2}d_n$/nm	474	219	38	63	67	62
% n	100	79	<1	100	15	9
$^{mode3}d_n$/nm	--	--	1.3	--	26	21
% n			100		85	91

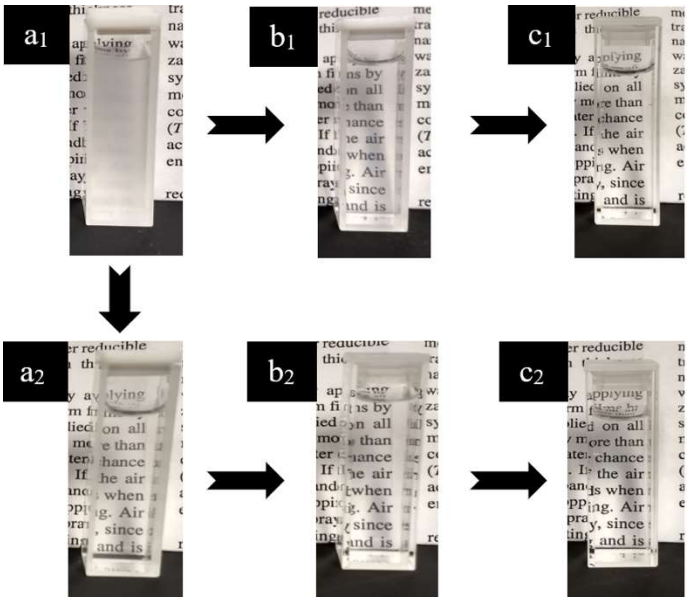

Figure 5.21. Filtration and sonication effects on apparent turbidity of 0.5% PUD of PEO200/Gly PU: (a_1) after self-dispersion of resin; (b_1) after filtering (a_1) through 1-micron filter; (c_1) after filtering (b_1) through 0.45-micron filter; (a_2) after sonicating (a_1) for 10 minutes; (b_2) after filtering (a_2) through 1-micron filter; (c_2) after filtering (b_2) through 0.45-micron filter.

Photographs of the PUDs as well as UV-Vis spectroscopy results indicate that in non-sonicated and unfiltered samples, the order of absorption of 500 nm wavelength light, turbidity, increases in the following order: PPO192/Trigly PU 0.5% PUD (0.155) < PPO192/Gly PU 0.5% PUD (0.382) < PPO192 PU 0.5%PUD (0.444) < PEO200/Gly PU 0.5% PUD (0.859) < PEO200 PU 0.5% PUD (1.094). A similar trend is observed in number based mean values seen in MSD plots: PPO192/Trigly PU 0.5% PUD (10.9 nm) < PPO192/Gly PU 0.5% PUD (292 nm) < PPO192 PU 0.5% PUD (340 nm) < PEO200/Gly PU 0.5% PUD (452 nm) < PEO200 PU 0.5% PUD (481 nm).

Table 5.5(a) Particle size parameters, solids, and turbidity for 0.5% (w/w) PEO200/Gly PU PUD subjected to filtration and sonication

Measured Parameters	Non-sonicated			Sonicated		
	not filtered	filtered (1 μm)	filtered (0.45 μm) (after 1 μm)	not filtered	filtered (1 μm)	filtered (0.45 μm) (after 1 μm)
$^{LN}\langle d\rangle_I$/nm	540	408	394	246	226	184
$^{LN}\langle d\rangle_V$/nm	526	242	198	127	122	102
$^{LN}\langle d\rangle_n$/nm	515	130	88	56	58	51
$^{MSD}\langle d\rangle_I$/nm	629	584	383	354	315	219
$^{MSD}\langle d\rangle_V$/nm	491	785	358	64	26	48
$^{MSD}\langle d\rangle_n$/nm	452	176	57	13	8	20
Solids/%	0.47	--	0.49 ± 0.04	--	--	0.44
τ_{500}/OD	0.859	0.167	0.060	0.131	0.064	0.058

On the other hand, non-sonicated and unfiltered PPO192/Trigly PU 0.5% PUD had the highest values of particle sizes through mean of intensity-weighting in lognormal as well as in MSD plots (Fig. 5.8(b)). Through MSD distributions, we can see that a few big particles (3260 nm) have less than 1% in number weighting and account for 66% of the intensity weighting. After filtrations, these big particles are removed and a mean of intensity weighted size in lognormal plots shift from 1313 nm to 427 nm (after 1-μm filter) to 130 nm (after 1-μm and then by 0.45-μm filter) (Table 5.8(a)).

Table 5.5(b) Multimode size distribution parameters for 0.5% (w/w) PEO200/Gly PU PUD subjected to filtration and sonication

Estimated Parameters	Not-Sonicated			Sonicated		
	Not Filtered	Filtered (1 μm)	Filtered (0.45 μm) (after 1 μm)	Not Filtered	Filtered (1 μm)	Filtered (0.45 μm) (after 1 μm)
$^{mode1}d_I$/nm	1531	1402	--	485	515	285
% I	15	25		58	48	68
$^{mode2}d_I$/nm	460	328	402	112	134	92
% I	85	72	92	40	51	30
$^{mode3}d_I$/nm	--	110	57	14	9	21
% I		3	8	2	1	2
$^{mode1}d_V$/nm	1727	1402	--	485	435	285
% V	3	44		9	3	6
$^{mode2}d_V$/nm	460	418	439	96	114	82
% V	97	52	79	6	2	18
$^{mode3}d_V$/nm	--	110	57	12	8	19
% V		4	21	85	95	76
$^{mode1}d_n$/nm	1531	1402	--	485	514	285
% n	<1	<1		<1	<1	<1
$^{mode2}d_n$/nm	460	328	439	112	134	92
% n	100	29	1	<1	<1	<1
$^{mode3}d_n$/nm	--	98	52	12	8	19
% n		71	99	100	100	100

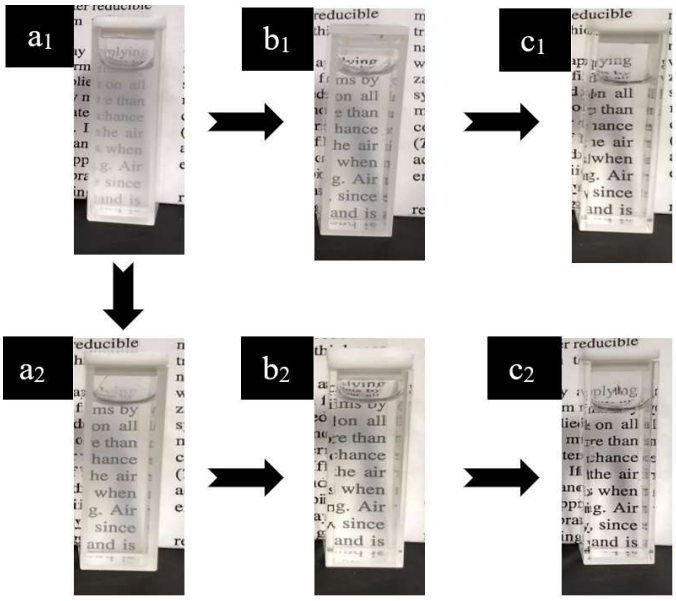

Figure 5.22. Filtration and sonication effects on apparent turbidity of 0.5% PUD from PPO192 PU: (a_1) after self-dispersion of resin; (b_1) after filtering (a_1) through 1-micron filter; (c_1) after filtering (b_1) through 0.45-micron filter; (a_2) after sonicating (a_1) for 10 minutes; (b_2) after filtering (a_2) through 1-micron filter; (c_2) after filtering (b_2) through 0.45-micron filter.

Mean number weighted particle size data in MSD, as well as lognormal plots, suggest that PPO192-based systems have lower particle sizes than PPO200-based systems. An explanation for this observation is that a more hydrophilic nature of PEO chains in particles have higher hydrogen bonding interactions with water, making them swell more than PPO-based particles. Effect of crosslinking agents can be also seen in mean particle size data by number weightings in MSD where addition of crosslinkers have reduced the particle size in both PEO-based and PPO-based systems.

Table 5.6(a) Particle size parameters, solids, and turbidity for 0.5% (w/w) PPO192 PU PUD subjected to filtration and sonication

Measured Parameters	Non-sonicated			Sonicated		
	not filtered	filtered (1 μm)	filtered (0.45 μm) (after 1 μm)	not filtered	filtered (1 μm)	filtered (0.45 μm) (after 1 μm)
$^{LN}\langle d\rangle_I$/nm	362	324	262	308	261	189
$^{LN}\langle d\rangle_V$/nm	254	213	179	182	160	107
$^{LN}\langle d\rangle_n$/nm	168	130	115	98	90	54
$^{MSD}\langle d\rangle_I$/nm	400	392	293	348	294	225
$^{MSD}\langle d\rangle_V$/nm	460	514	53	382	198	12
$^{MSD}\langle d\rangle_n$/nm	340	239	9	109	23	8
Solids/%	0.46	--	0.49 ± 0.005	0.53	--	0.50 ± 0.05
τ_{500}/OD	0.444	0.241	0.033	0.275	0.169	0.048

Table 5.6(b) Multimode size distribution parameters for 0.5% (w/w) PPO192 PU PUD subjected to filtration and sonication

Estimated Parameters	Not-Sonicated			Sonicated		
	Not Filtered	Filtered (1 μm)	Filtered (0.45 μm) (after 1 μm)	Not Filtered	Filtered (1 μm)	Filtered (0.45 μm) (after 1 μm)
$^{mode1}d_I$/nm	502	653	367	395	329	288
% I	68	40	99	83	81	69
$^{mode2}d_I$/nm	190	221	175	93	101	89
% I	32	60	1	17	18	30
$^{mode3}d_I$/nm	--	--	9	--	23	8.4
% I			<1		1	1
$^{mode1}d_V$/nm	455	727	426	456	455	288
% V	95	65	10	86	44	<1
$^{mode2}d_V$/nm	190	221	151	93	101	77
% V	5	35	3	14	17	2
$^{mode3}d_V$/nm	--	--	9	--	23	7.9
% V			87		39	97
$^{mode1}d_n$/nm	455	653	367	456	329	288
% n	53	6	<1	6	<1	<1
$^{mode2}d_n$/nm	190	209	175	93	101	89
% n	47	94	<1	94	<1	<1
$^{mode3}d_n$/nm	--	--	9	--	23	7.3
% n			100		100	100

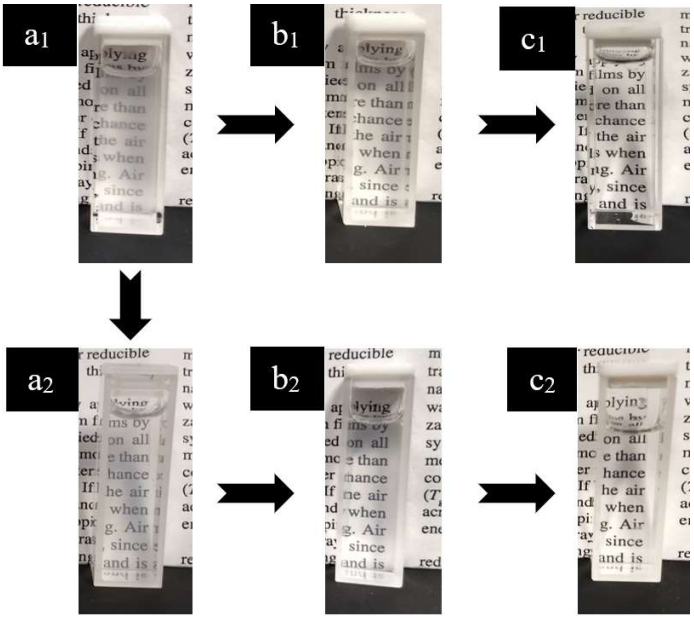

Figure 5.23. Filtration and sonication effects on apparent turbidity of 0.5% PUD from PPO192/Gly PU: (a_1) after self-dispersion of resin; (b_1) after filtering (a_1) through 1-micron filter; (c_1) after filtering (b_1) through 0.45-micron filter; (a_2) after sonicating (a_1) for 10 minutes; (b_2) after filtering (a_2) through 1-micron filter; (c_2) after filtering (b_2) through 0.45-micron filter.

All of these data suggest that sonication played an effective role in breaking down big agglomerates and reduces particle sizes and hence reduces turbidity. For example, in an unfiltered PEO200 PU 0.5% PUD sample, the volume weighted lognormal particle size reduces from a mean of 585 nm to 104 nm after 10 minutes of sonication with a change in turbidity value of 1.094 to 0.162 optical density units. The mean particle size in intensity-weighted lognormal size fits changed from 610 nm to 206 nm and by number weighting changed from 562 to 47 nm after sonication. (Table 5.4(a)). This PUD became transparent (Fig. 5.20(a_2)) from opaque (Fig. 5.20(a_1)) after sonication. Similar effects of sonication were seen in other PUD samples.

Table 5.7(a) Particle size parameters, solids, and turbidity for 0.5% (w/w) PPO192/Gly PU PUD subjected to filtration and sonication

Measured Parameters	Non-sonicated			Sonicated		
	not filtered	filtered (1 μm)	filtered (0.45 μm) (after 1 μm)	not filtered	filtered (1 μm)	filtered (0.45 μm) (after 1 μm)
$^{LN}\langle d\rangle_I$/nm	697	520	351	383	314	236
$^{LN}\langle d\rangle_V$/nm	344	268	176	215	180	119
$^{LN}\langle d\rangle_n$/nm	148	122	77	109	93	52
$^{MSD}\langle d\rangle_I$/nm	1013	745	373	429	383	279
$^{MSD}\langle d\rangle_V$/nm	1288	822	67	420	48	127
$^{MSD}\langle d\rangle_n$/nm	292	30	9.3	39	11	17
Solids/%	0.45	0.48	0.43 ± 0.06	0.48	--	0.45 ± 0.03
τ_{500}/OD	0.382	0.191	0.056	0.227	0.172	0.053

Table 5.7(b) Multimode size distribution parameters for 0.5% (w/w) PPO192/Gly PU PUD subjected to filtration and sonication

Estimated Parameters	Not-Sonicated			Sonicated		
	Not Filtered	Filtered (1 μm)	Filtered (0.45 μm) (after 1 μm)	Not Filtered	Filtered (1 μm)	Filtered (0.45 μm) (after 1 μm)
$^{mode1}d_I$/nm	1449	1099	396	525	570	328
% I	63	55	96	76	56	74
$^{mode2}d_I$/nm	265	259	28	153	1764	79
% I	37	45	3	23	42	26
$^{mode3}d_I$/nm	--	30	9.2	36	12	17
% I		<1	1	1	2	<1
$^{mode1}d_V$/nm	1449	1099	463	474	482	415
% V	85	70	13	85	7	25
$^{mode2}d_V$/nm	265	299	30	153	176	79
% V	15	14	10	7	1	26
$^{mode3}d_V$/nm	--	30	9.2	36	10.1	17
% V		16	77	8	92	49
$^{mode1}d_n$/nm	1449	1099	400	525	570	328
% n	3	<1	<1	<1	<1	<1
$^{mode2}d_n$/nm	265	259	28	153	176	79
% n	97	<1	<1	<1	<1	<1
$^{mode3}d_n$/nm	--	30	9.2	36	10.1	17
% n		100	100	100	100	100

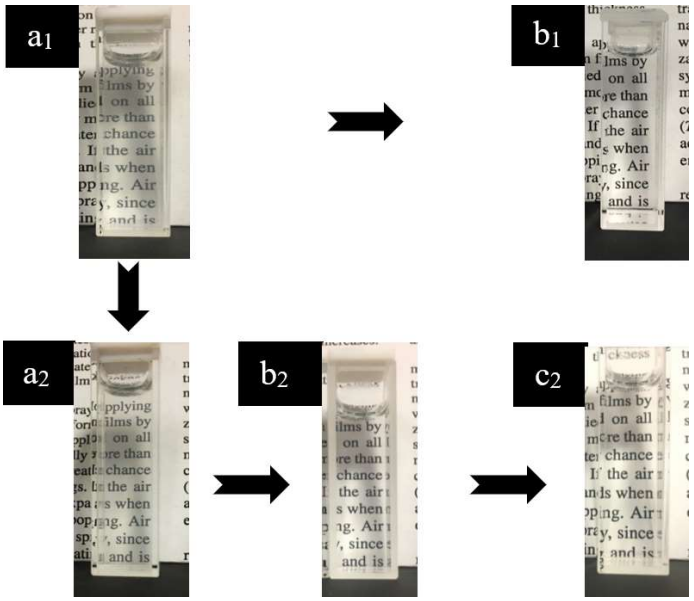

Figure 5.24. Filtration and sonication effects on apparent turbidity of 0.5% PUD from PPO192/Trigly PU: (a_1) after self-dispersion of resin; (b_1) after filtering (a_1) through 1- micron filter and then through 0.45-micron filter; (a_2) after sonicating (a_1) for 10 minutes; (b_2) after filtering (a_2) through 1-micron filter; (c_2) after filtering (b_2) through 0.45-micron filter.

Table 5.8(a) Particle size parameters, solids, and turbidity for 0.5% (w/w) PPO192/Trigly PU PUD subjected to filtration and sonication

Measured Parameters	Non-sonicated			Sonicated		
	not filtered	filtered (1 μm)	filtered (0.45 μm) (after 1 μm)	not filtered	filtered (1 μm)	filtered (0.45 μm) (after 1 μm)
$^{LN}\langle d\rangle_I$/nm	1312	427	130	892	557	188
$^{LN}\langle d\rangle_V$/nm	564	167	32	386	249	70
$^{LN}\langle d\rangle_n$/nm	206	54	6.1	143	96	21
$^{MSD}\langle d\rangle_I$/nm	2294	720	77	1322	790	123
$^{MSD}\langle d\rangle_V$/nm	92	16	3.4	22	21	8.8
$^{MSD}\langle d\rangle_n$/nm	10.9	8.7	3.4	8.2	7.9	8.1
Solids/%	0.52	--	0.50	--	--	--
τ_{500}/OD	0.155	0.104	0.003	0.104	--	0.013

Table 5.8(b) Multimode size distribution parameters for 0.5% (w/w) PPO192/Trigly PU PUD subjected to filtration and sonication

Estimated Parameters	Not-Sonicated			Sonicated		
	Not Filtered	Filtered (1 μm)	Filtered (0.45 μm) (after 1 μm)	Not Filtered	Filtered (1 μm)	Filtered (0.45 μm) (after 1 μm)
$^{mode1}d_I$/nm	3260	998	104	1508	1138	--
% I	66	65	75	75	60	
$^{mode2}d_I$/nm	402	117	8.3	147	260	143
% I	31	28	9	22	35	79
$^{mode3}d_I$/nm	12	11.4	3.8	9.3	8.9	8.7
% I	3	7	16	3	5	21
$^{mode1}d_V$/nm	3260	998	104	1508	1405	--
% V	2	1	<1	1	1	
$^{mode2}d_V$/nm	4022	117	8.3	147	260	143
% V		<1	3	<1	1	<1
$^{mode3}d_V$/nm	9.7	9.3	2.7	7.5	7.2	8.7
% V	96	99	97	99	98	100
$^{mode1}d_n$/nm	3260	998	104	1508	1138	--
% n	<1	<1	<1<1	<1	<1	
$^{mode2}d_n$/nm	402	117	8.3	147	260	143
% n	<1	<1	1	<1	<1	<1
$^{mode3}d_n$/nm	9.7	9.3	2.7	7.5	7.2	7.6
% n	100	100	99	100	100	100

5.6 Rheological Observations

It was first observed that aqueous PEO based-PUDs at high concentration formed gels that did not flow at all at ambient temperature as seen in Fig. 5.25(a_1), Fig.5.25(b_1), Fig. 5.26(a_1), and Fig. 5.26(b_1). When these samples were equilibrated in an oven at 35 ºC for 6 hours, the respective gels melted and viscosity was reduced, which resulted in flow when vials were tilted. Also, when these PUDs in a gel state were subjected to shear by application of vibratory stirring for 4 s, they became able to flow, and such gels were established to be shear thinning. On reduction of temperature and removal of shear, these flowing PUDs thicken and form non-flowing gels.

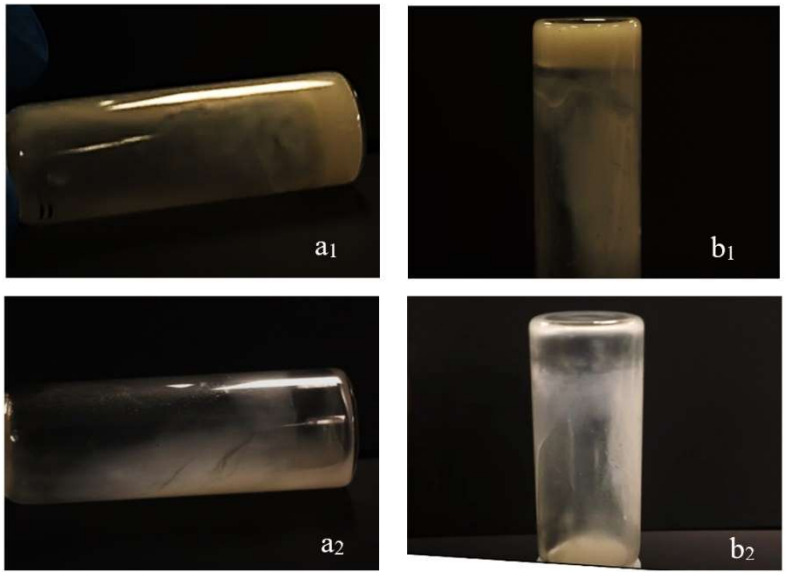

Figure 5.25. Rheological observations on 25% by weight PEO200 PUD: (a_1) sample at ambient temperature without any external shear, vial laid horizontally; (b_1) a_1 tilted upside down; (a_2) sample after removing from oven where it was kept at 35 ºC for 6 hours without any external shear -vial laid horizontally; (b_2) sample from a_2, vial turned upside down.

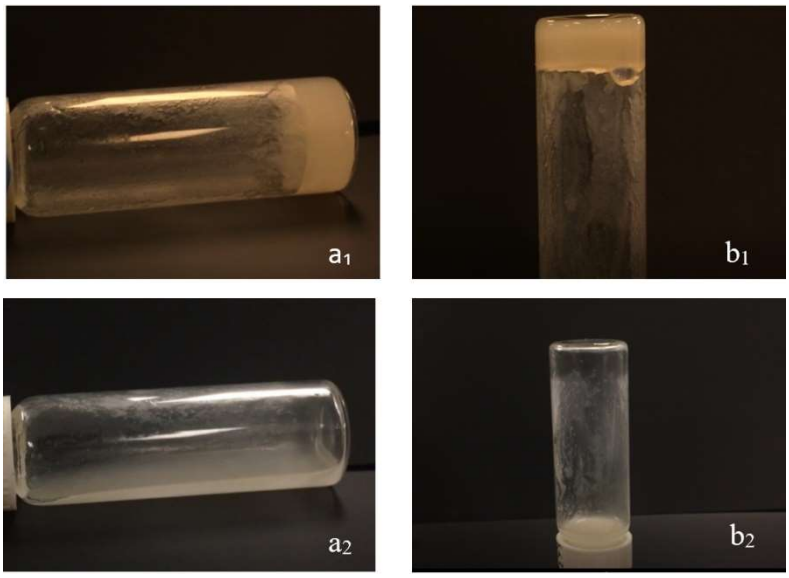

Figure 5.26. Rheological observations on 25% by weight PEO200/Gly PUD: (a_1) sample at ambient temperature without any external shear, vial laid horizontally; (b_1) a_1 tilted upside down; (a_2) sample after removing from oven where it was incubated in the illustrated horizontal position at 35 ºC for 6 hours without any external shear applied – sample is liquified; (b_2) sample from a_2, vial turned upside down.

All five PUD samples made in section 5.4.2 exhibit this gelling and shear thinning phenomena. PUDs, 25% by weight (w/w), of PEO200 PU, PEO200/Gly, PPO192, PPO192/Gly, and PPO192/Trigly exhibited increasing viscosity and, eventually, gelation at ambient temperatures (about 22 ºC to 25 ºC) while quiescently resting. This is a useful property from a storage point of view.

Gels are also formed in our PPO based systems, but these gels flow at ambient temperature as shown in Fig. 5.27(a_1), Fig. 5.28(a_1), and Fig. 5.29(a_1). When these samples were equilibrated in an oven at 35 ºC for 6 hours, these respective gels melt (and viscosity was reduced) flow when tilted (Fig. 5.27(a_2) and Fig. 5.28(a_2). Also, when these PUDs in gel form were given external shear by application of vibratory stirring for 4 s, they shear thinned and were able to flow (Fig. 5.29(a_2)). On reduction of temperature and removal of shear, these flowing PUDs thicken, become viscous, and gel.

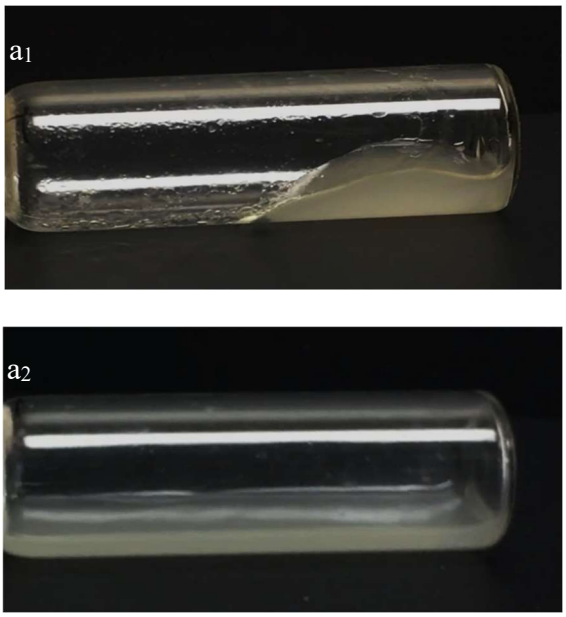

Figure 5.27. Rheological observations on 25% by weight PPO192 PUD: (a_1) sample at ambient temperature without any external shear, vial laid horizontally; (a_2) sample after removing from oven where it was kept at 35 ºC for 6 hours without any external shear, vial laid horizontally.

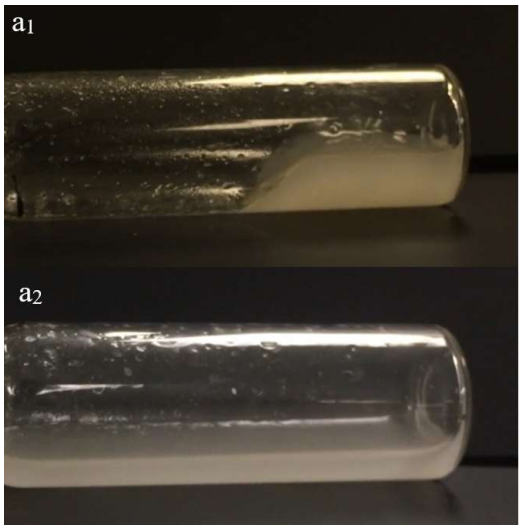

Figure 5.28. Rheological observations on 25% by weight PPO192/Gly PUD: (a_1) sample at ambient temperature without any external shear, vial laid horizontally; (a_2) sample after removing from oven where it was put at 35 ºC for 6 hours without any external shear, vial laid horizontally.

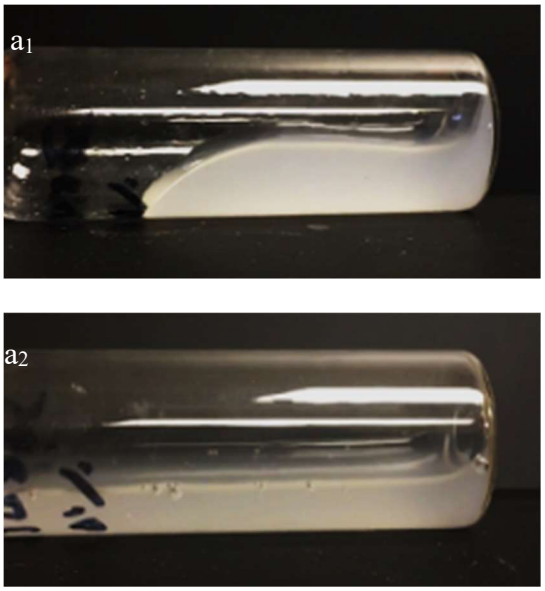

Figure 5.29. Rheological observations on 10% by weight PPO192/Trigly PUD: (a_1) sample at ambient temperature without any external shear, vial laid horizontally; (a_2) sample after 4 seconds of vibratory stirring to apply shear at ambient temperature, vial laid horizontally.

It was observed that PEO-based PUDs formed thicker gels than PPO-based systems which may be because of a greater extent of inter particle interactions and hydrogen bonding between PEO chains and water molecules than in PPO-based PUDs. These interactions can be broken by higher temperatures and by application of shear. This property indicates a type of stimuli responsiveness of these PUDs to changes in temperature and shear.

5.7 Anion Stimuli-Responsiveness

Anion-dependent stimuli-responsive behavior was observed in these PUDs. This stimuli-responsiveness appears based on tuning imidazolium-anion pair solubility by anion exchange. Two approaches were used to analyze this stimuli-responsiveness. One approach measures turbidity of dilute PUD in various salt solutions. The degree of turbidity is related to how anion exchange destabilizes the PU particles and promotes their aggregation, thereby increasing their apparent light scattering cross-sections. The second approach quantifies how contact angles of

DI water on coatings treated by various salt solutions vary with increasing amounts of particular anion-containing salts.

5.7.1 Effects on PUD destabilization

In "the first named approach," turbidity of a PIL PUD sample was measured in various salt solutions at different concentrations. The PPO192/Trigly PUD at 0.5% w/w was prepared using the method described in section 5.4. It was sonicated using a 3-4 mm diameter sonic horn for 10 min in an ice-water bath and was first filtered using a 1-μm filter and then by a 0.45-μm filter. This PUD looked clear and had a solids content of 0.48%. Various 0.1 *M* stock solutions were prepared by dissolving potassium iodide (KI), potassium hexafluorophosphate (KPF_6), sodium dicynamide ($NaN(CN)_2$), sodium trifluoromethane sulphonate (CF_3SO_3Na), sodium tetrafluoroborate ($NaBF_4$), and sodium bromide (NaBr) salts in DI water. These stock solutions were diluted by DI water to make various required concentrations of different salts.

In different test tubes, 250 μL of clear PUD was drawn using a Finn pipet and mixed with 2.25 mL of various salt solutions to give a total volume of 2.5 mL in each test tube. After addition, samples were stirred by using a vibratory stirrer for 3-4 s and then kept at rest. After 1 hour, turbidity of each sample was measured by measuring absorbance at 500 nm wavelength a Beckman DU800 UV-Vis spectrophotometer. Pictures of samples were also taken after 1 hour of addition of salts.

Two approaches were used to make plots by using the optical absorption data from UV-Vis measurements. In an "early onset of turbidity" approach, a linear regression of data points having negligible turbidity was plotted, and then a linear regression of data points having low turbidity was plotted. Intersection of these two linear regression lines was noted as an early onset of particle aggregation causing turbidity. In a "delayed onset of turbidity" approach, a first linear

regression of data points having near-zero to low turbidity values was plotted, and then a linear regression of data points having much high turbidity values was plotted. Intersection of these two linear regression lines was noted as delayed onset of turbidity.

Onset of turbidity by visual analysis of photographs was done by taking an average of largest log(concentration) (logC) of salt that showed no turbidity and the lowest logC that showed slight turbidity. These estimates are summarized in Table 5.9.

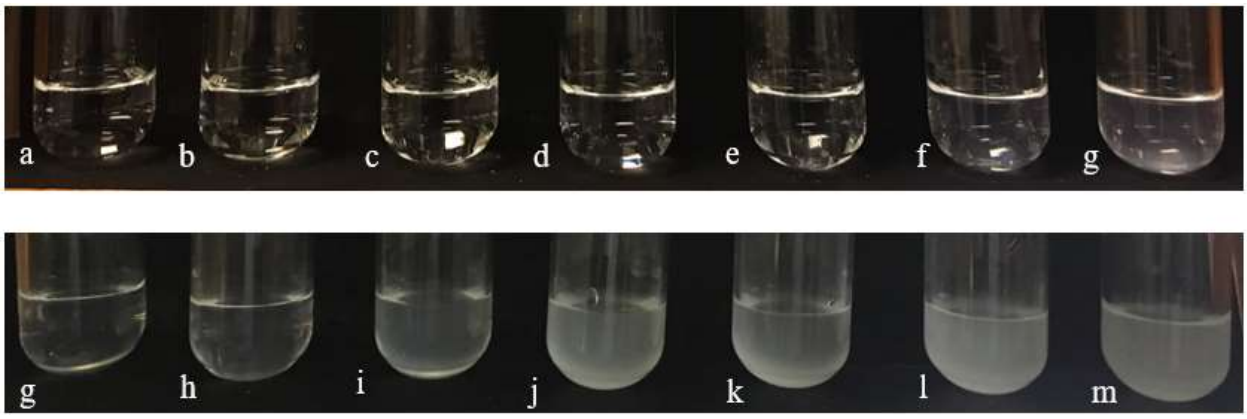

Figure 5.30. After 1 hour of addition of 2.25 ml KPF_6 solution of concentration, log([KPF_6]/*M*): (a) -7; (b) -6; (c) -5; (d) -4.25; (e) -4; (f) -3.75; (g) -3.5; (h) -3.25; (i) -3; (j) -2.5; (k) -2; (l) -1.5; (m) -1, all in 0.25 mL of 0.5% PPO192/Trigly PUD.

Figure 5.30 shows an effect of KPF_6 salt solution on turbidity of this PUD. Visually, there was no change in turbidity by addition of concentration of KPF_6 from -7 to -4 (in log (*M*)). At a concentration of -3.75 (in log (*M*)), slight turbidity appeared after 1 hour of addition of salt as seen in Fig. 5.30(f). The magnitude of turbidity increased at higher concentrations of salt. Trends of increasing turbidity can be seen in Fig. 5.30, Fig. 5.31 and Fig. A.5.9 (in Appendix D). Increases followed by decreases in turbidity were observed at concentrations greater than 10^{-2} *M* because of settling of large aggregates (Fig. A.5.9 in Appendix D).

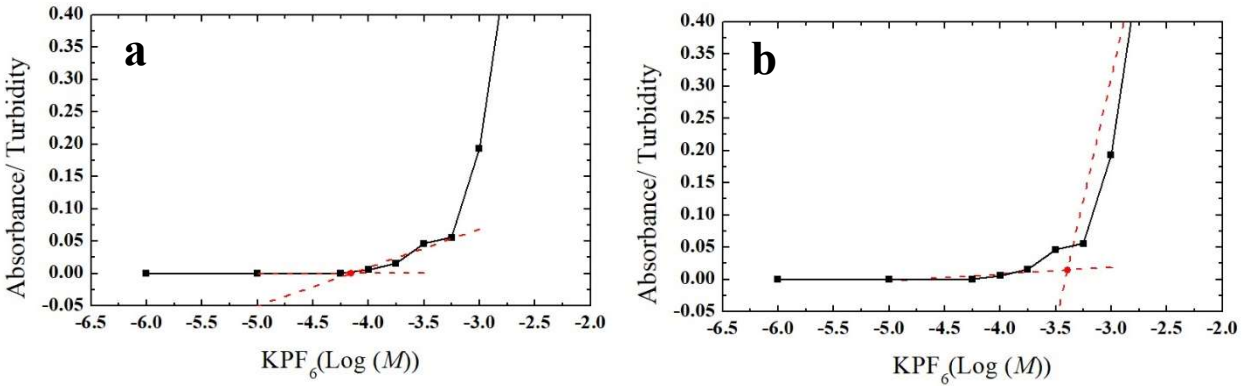

Figure 5.31. Plot of turbidity vs. concentration of KPF_6 solution in PPO192/Trigly PUD: (a) plot using early onset of turbidity approach; (b) plot using delayed onset of turbidity approach; (■) data points from UV-Vis measurements; (- - -) linear regression of data points.

Figure 5.32. After 1 hour of addition of 2.25 ml NaBr solution of concentration, log([NaBr]/M): (a) -3; (b) -2; (c) -1.5; (d) -1.4; (e) -1.3; (f) -1.2; (g) -1.1 in 0.25ml of 0.5% PPO192/Trigly PUD.

From Fig. 5.31, the intersection of regression lines using the early onset of turbidity approach suggests that onset of aggregation of particles starts at a concentration of KPF_6 of -4.16 (log(*M*). The intersection of regression lines using the delayed onset of turbidity approach suggests that an onset of aggregation of particles starts at a concentration of KPF_6 of -3.39 (log(*M*).

Addition of NaBr showed signs of turbidity only at much higher concentrations. From Fig. 5.32, it can be observed that turbidity starts to appear at a concentration of about -1.3 (in log(*M*)). From Fig. 5.33, the intersection of regression lines using the early onset of turbidity approach suggests that aggregation of particles starts at a concentration of NaBr of -1.42 (log(*M*).

The intersection of regression lines using the delayed onset of turbidity approach suggests that aggregation of particles starts at a concentration of NaBr of -1.38 (log(*M*).

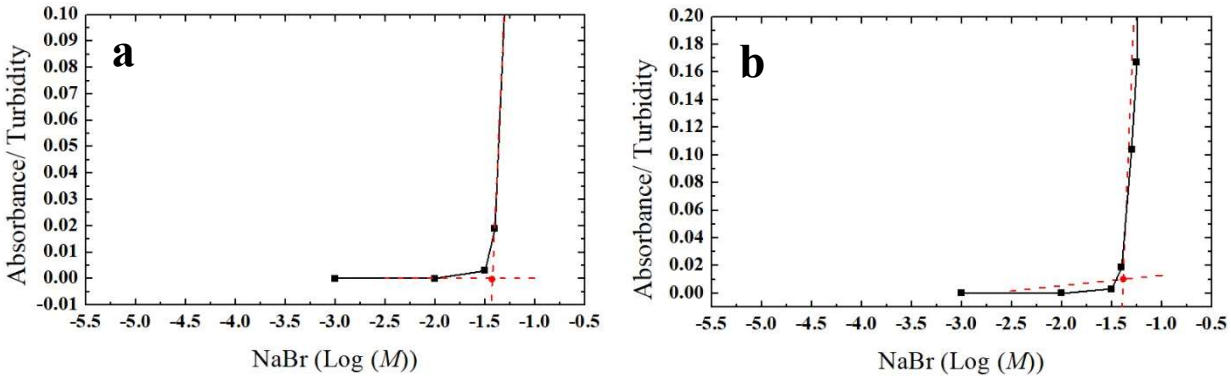

Figure 5.33. Plot of turbidity vs. concentration of NaBr solution in PPO192/Trigly PUD: (a) plot using the early onset of turbidity approach; (b) plot using the delayed onset of turbidity approach; (■) data points from UV-Vis measurements; (- - -) linear regression of data points.

From Fig. 5.34, visual photographs suggest that addition of KI showed signs of turbidity at about a concentration of -2 (in log(M)). From Fig. 5.35, the intersection of regression lines using the early onset of turbidity approach suggests that onset of aggregation of particles start at a concentration of KI of -3 (log(*M*). The intersection of regression lines using the delayed onset of turbidity approach suggests that onset of aggregation of particles start at a concentration of KI of -2 (log(*M*).

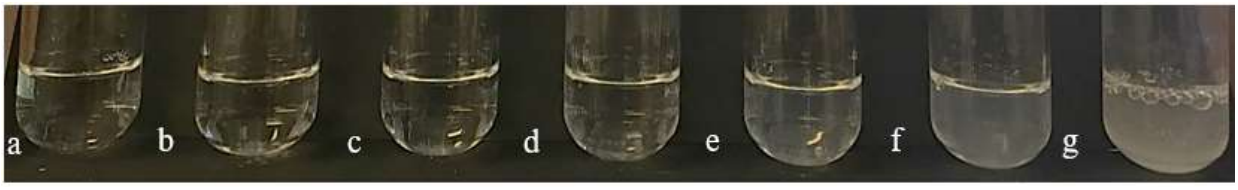

Figure 5.34. After 1 hour of addition of 2.25 ml KI solution of concentration, log([KI]/M): (a) -5; (b) -4; (c) -3; (d) -2.25; (e) -2; (f) -1.75; (g) -1 in 0.25 ml of 0.5% PPO192/Trigly PUD.

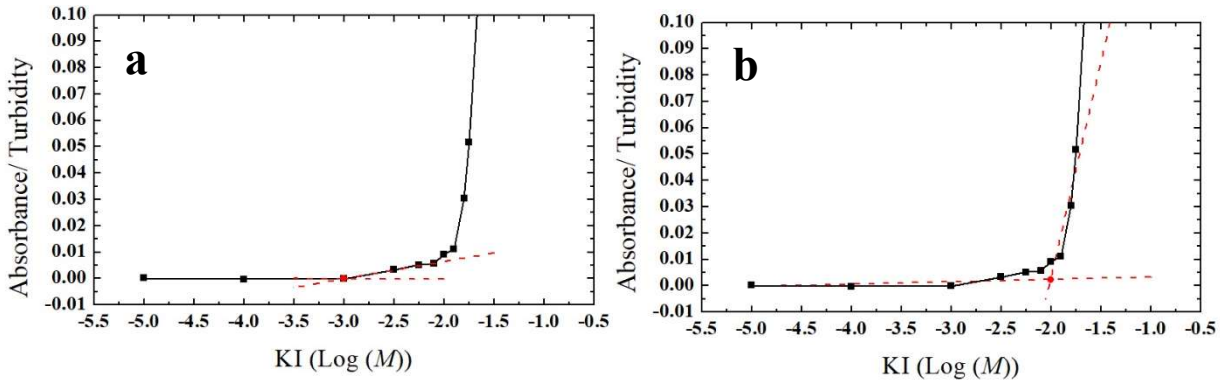

Figure 5.35. Plot of turbidity vs. concentration of KI solution in PPO192/Trigly PUD: (a) plot using the early onset of turbidity approach; (b) plot using the delayed onset of turbidity approach; (■) data points from UV-Vis measurements; (- - -) linear regression of data points.

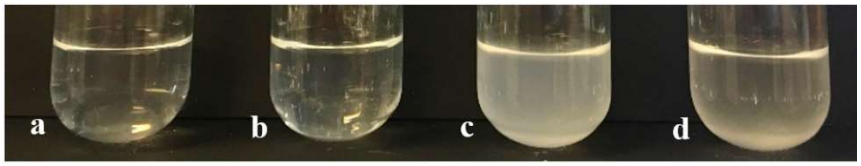

Figure 5.36. After 1 hour of addition of 2.25 ml $NaN(CN)_2$ solution of concentration, log([$NaN(CN)_2$]/M): (a) -2.25; (b) -2; (c) -1.75; (d) -1 in 0.25ml of 0.5% PPO192/Trigly PUD.

From Fig. 5.36, visual photographs suggest that addition of $NaN(CN)_2$ showed signs of turbidity at about concentration of -2.25 (in log(M)). From Fig. 5.37, the intersection of regression lines using early onset of turbidity approach suggests that onset of aggregation of particles start at a concentration of $NaN(CN)_2$ of -3.87 (log(*M*). The intersection of regression lines using delayed onset of turbidity approach suggests that onset of aggregation of particles start at -2.17 (log(*M*).

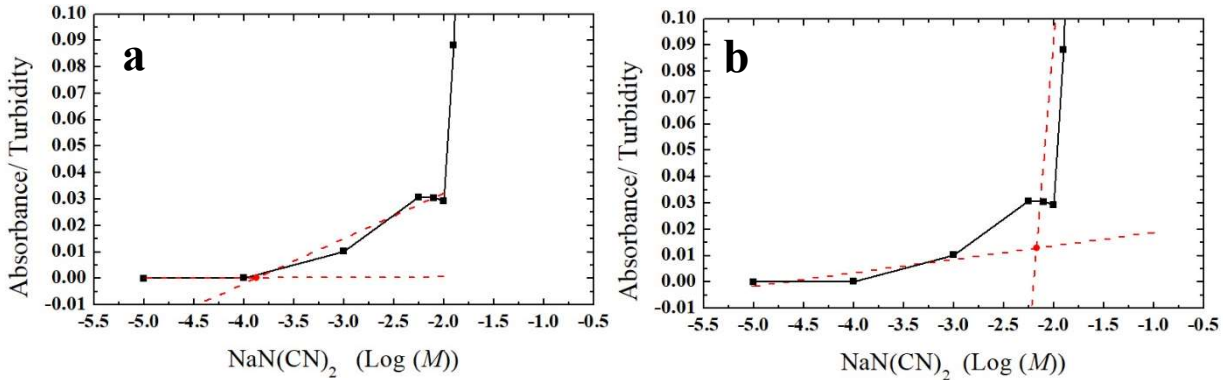

Figure 5.37. Plot of turbidity vs. conc. of $NaN(CN)_2$ solution in PPO192/Trigly PUD: (a) plot using the early onset of turbidity approach; (b) plot using the delayed onset of turbidity approach; (■) data points from UV-Vis measurements; (- - -) linear regression of data points.

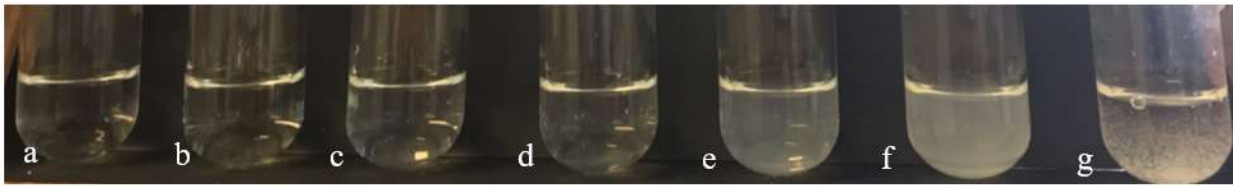

Figure 5.38. After 1 hour of addition of 2.25 ml $NaBF_4$ solution of concentration, log([NaBF4]/M): (a) -5; (b) -4; (c) -3; (d) -2.25; (e) -2; (f) -1.75; (g) -1 in 0.25 ml of 0.5% PPO192/Trigly PUD.

From Fig. 5.38, visual photographs suggest that addition of $NaBF_4$ showed signs of turbidity at about concentration of -2.25 (in log(M)). On increasing the concentration of salt, turbidity increased and settling of large aggregated particles can be seen then from Fig. 5.38 (g).

From Fig. 5.39, the intersection of regression lines using the early onset of turbidity approach suggests that onset of aggregation of particles start at a concentration of $NaBF_4$ of -3.07 (log(*M*). The intersection of regression lines using the delayed onset of turbidity approach suggests that onset of aggregation of particles start at a concentration of $NaBF_4$ of -2.07 (log(*M*).

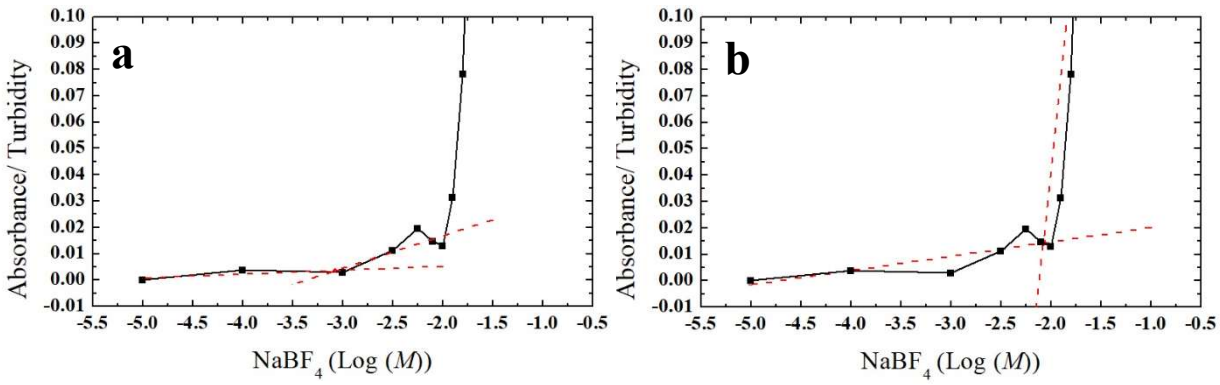

Figure 5.39. Plot of turbidity vs. concentration of $NaBF_4$ solution in PPO192/Trigly PUD: (a) plot using the early onset of turbidity approach; (b) plot using the delayed onset of turbidity approach; (■) data points from UV-Vis measurements; (- - -) linear regression of data points.

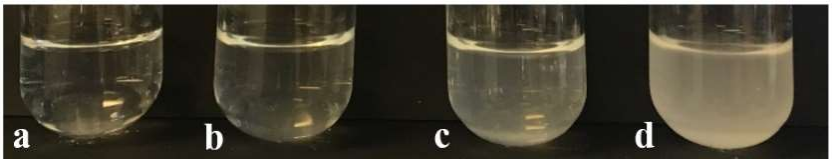

Figure 5.40. After 1 hour of addition of 2.25 ml CF_3SO_3Na solution of concentration, log([CF_3SO_3Na]/M): (a) -3; (b) -2.25; (c) -2; (d) -1.75 in 0.25 ml of 0.5% PPO192/Trigly PUD.

In Fig. 5.40, visual photographs suggest that addition of CF_3SO_3Na showed signs of turbidity at concentration of -2.25 (in log(M)). From Fig. 5.41, the intersection of regression lines using the early onset of turbidity that onset of aggregation of particles start at a concentration of CF_3SO_3Na of -3.9 (log(*M*). The intersection of regression lines using the delayed onset of turbidity approach suggests that onset of aggregation of particles start at a concentration of CF_3SO_3Na of -2.46 (log(*M*).

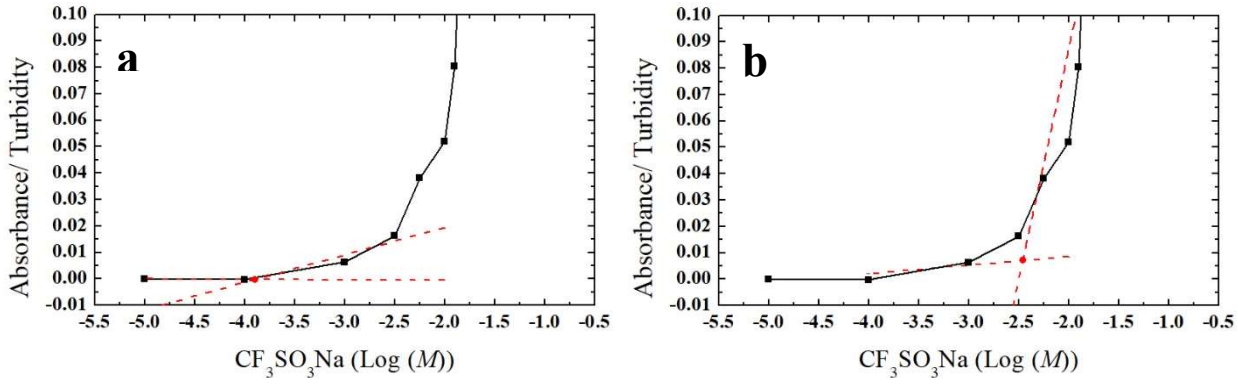

Figure 5.41. Plot of turbidity vs. concentration of CF_3SO_3Na solution in PPO192/Trigly PUD: (a) plot using the early onset of turbidity approach; (b) plot using the delayed onset of turbidity approach; (■) data points from UV-Vis measurements; (- - -) linear regression of data points.

Turbidity is caused because of particle aggregation and, therefore, by an increase in the particles' light scattering coefficients. This aggregation is caused because of two reasons: (a) change from hydrophilic to hydrophobic nature of particle surfaces induced by anion exchange of more hydrophilic counter ions, such as than Br^- ions for anions that form more hydrophobic imidazolium-anion pairs; and (b) destabilization of charged particles because of electrical shielding effect induced by high concentrations of salt. This second mechanism has not yet been studied or shown to be a significant contributor to destabilization of PUD prepared in this work.

Table 5.9. Comparison of onset of turbidity amongst various salts.

Anion	Early onset of turbidity (log(*M*))	Delayed onset of turbidity (log(*M*))	Visually determined onset of turbidity (log(*M*))
PF_6^-	-4.16	-3.39	-3.87
$CF_3SO_3^-$	-3.90	-2.46	-2.13
$N(CN)_2^-$	-3.87	-2.17	-2.0
BF_4^-	-3.07	-2.07	-2.63
I^-	-3.00	-2.00	-2.63
Br^-	-1.42	-1.38	-1.45

Particles in these PUDs are stabilized in water through electro-steric repulsion between them. This is a combination of charge-charge repulsion and steric repulsion. Introduction of salt increases the ionic strength of the solution and changes the environment of stable particles. This increase in the ionic strength shields the particles and causes the compression in electrical double layer, which leads to agglomeration. The higher the concentration of the salt, the higher the agglomeration that can occur, which can be seen in the results. However, a more detailed study will be required to really resolve the stabilization mechanism. In view of the specific anion effects at very low concentration seen for PF_6^- and BF_4^-, classical Debye-Hückel charge-based destabilization is likely not the dominating mechanism, since very small amounts of PF_6^- destabilize more effectively than much larger amounts of Br^-. These considerations have been explored earlier for nanolatexes based on other imidazolium monomers.[47,48]

A very high concentration of NaBr can destabilize these particles, and a more detailed examination of concentration effects is needed to resolve whether destabilization is due to shrinking the Debye-Hückel layer thickness or due to specific neutralization of charged groups on the particle surface. In the case of other salts, turbidity can be seen at lower ion concentrations because of ion exchange between Br^- of IL in PUD and respective anions in the salt solutions, making IL increasingly hydrophobic compared to what they are with the Br^- counterions. A threshold value exists where enough Br^- counterions are replaced by hydrophobic anions, which causes destabilization of particles leading to agglomeration and rise in the turbidity. This threshold value varies between anions where stronger anions act at lower concentrations. As concentration of these exchanged anions increase, imidazolium-anion pairs become neutralized leading to more aggregation. As the amount of aggregates increase, the mass of aggregates also increases, which starts to decrease the turbidity as fewer intermediately sized particles remain suspended in dispersion. This effect leads to increased sedimentation of aggregates as can be seen in Fig. 5.38(g).

Table 5.9 clearly show that KPF_6 has the highest effect while NaBr has the least effect on aggregation of particles in these PIL PUDs. Other anions have similar anion strength to make PUD particles hydrophobic. From Table 5.9 it can be inferred that decreasing order of anion destabilizing strength is $PF_6^- > CF_3SO_3^- \sim N(CN)_2^- > BF_4^- \sim I^- > Br^-$.

5.7.2 Effects on coated glass slides

5.7.2.1 Anion effects on coated glass slides

PUDs of all five resins described in section 5.4 at 25% w/w were used after sonication to make drawdown coatings on glass slides by using a 1-inch-square drawdown bar. An aim wet film thickness of 75 μm was used. After flashing off water, coatings were heated in an oven at 60 ˚C for 6 minutes for better coalescence.

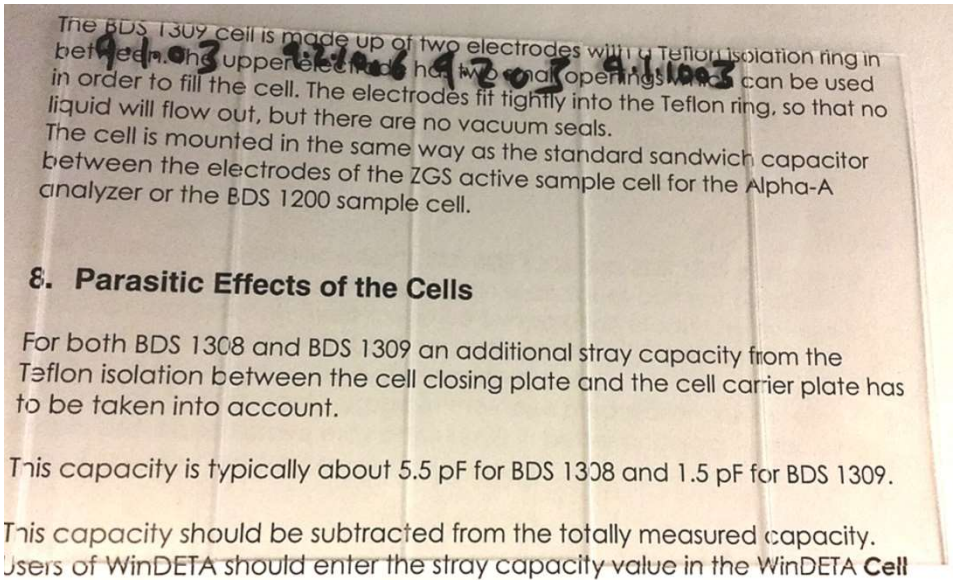

Figure 5.42. Glass slides coated with PUDs: (a) PEO200 PUD; (b) PPO192/Gly PUD; (c) PEO200/Gly PUD; (d) PPO192 PUD; (e) not coated.

After these coated glass slides were prepared (Fig. 5.42), each slide was dipped in 0.1 *M* salt solutions of KI, KPF_6, $NaN(CN)_2$, CF_3SO_3Na, and $NaBF_4$ for 15 minutes and then rinsed in DI water and air-dried for 30 min before measuring contact angles discussed in next section. It was observed that in all these coatings, untreated coatings would disperse back into water, whereas treated coatings with all the salts mentioned in this section, did not disperse when contacted by DI water.

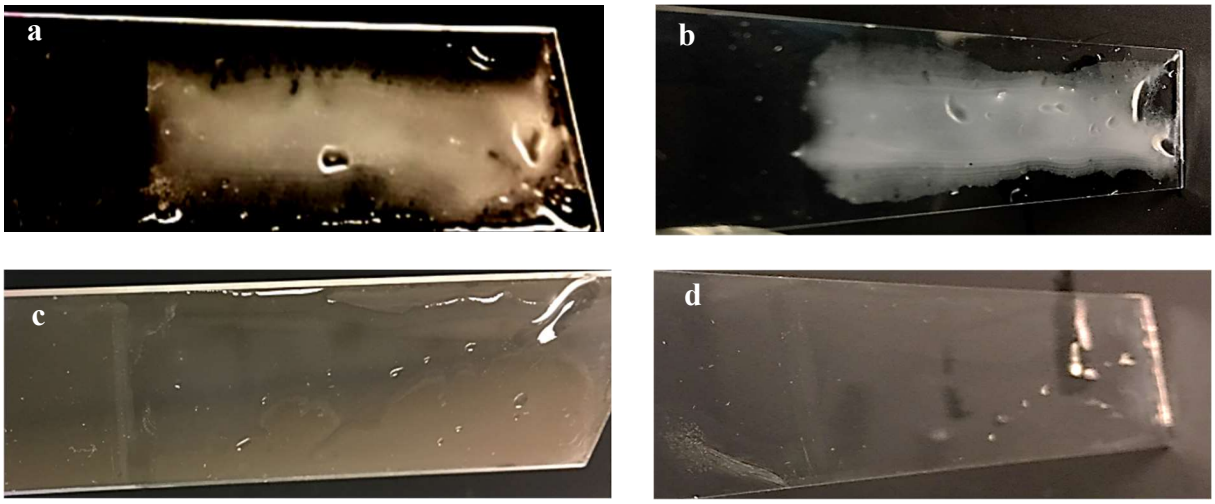

Figure 5.43. Comparison of coatings during treatment by various salt solutions: (a) PPO192 PUD coated glass slide after dipping in aqueous 0.1 *M* $NaBF_4$; (b) PPO192 PUD coated glass slide after dipping in aqueous 0.1 *M* KPF_6; (c) PEO200 PUD coated glass slide after dipping in aqueous 0.1 *M* $NaBF_4$; (d) PEO200 PUD coated glass slide after dipping in aqueous 0.1 *M* KPF_6.

Results showed that both PPO192-based and PEO200-based PUD coatings became resistant to redispersion back into water after anion exchange by anions in 0.1 *M* salt solutions of KI, KPF_6, $NaN(CN)_2$, CF_3SO_3Na, and $NaBF_4$. It was also observed that all PPO192-based coatings became turbid when they were dipped in various salt solutions. However, PEO-based coatings did not (Fig. 5.43 and Fig. 5.44). Figure A.5.7 in Appendix D also shows similar results during KI treatment. This turbidity effect suggests that PPO192-based treated coatings are hydrophobic and become porous when contacted with water.

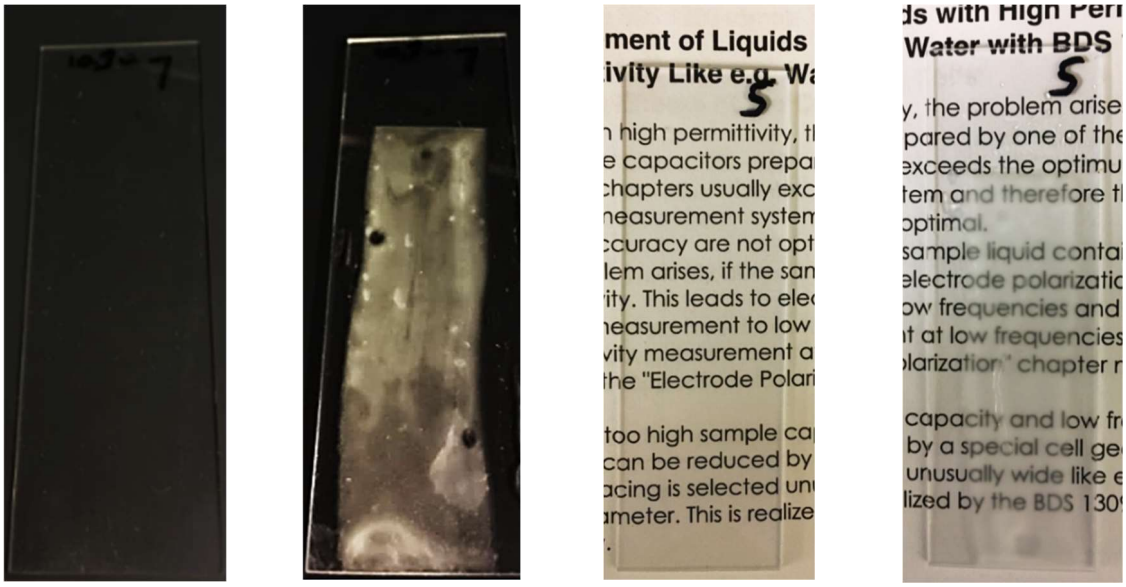

Figure 5.44. Coating getting turbid during treatment by KPF_6 solution: (a,c) Untreated PPO192/Trigly PUD coated glass slide; (b,d) PPO192/Trigly PUD coated glass slide after dipping in aqueous 0.1 *M* KPF_6 for 15 minutes, which made the coating turbid and resistant to redispersion in water.

DI water drops were used to measure contact angles off water on coatings made on glass slides. Short duration videos were made to capture dynamic change in contact angle and screenshots at different time intervals from videos were used to measure contact angles of different samples. ImageJ software was used by a plugin of drop snake analysis to measure contact angles. Each right and left angle were measured twice to help provide reliable measurements.

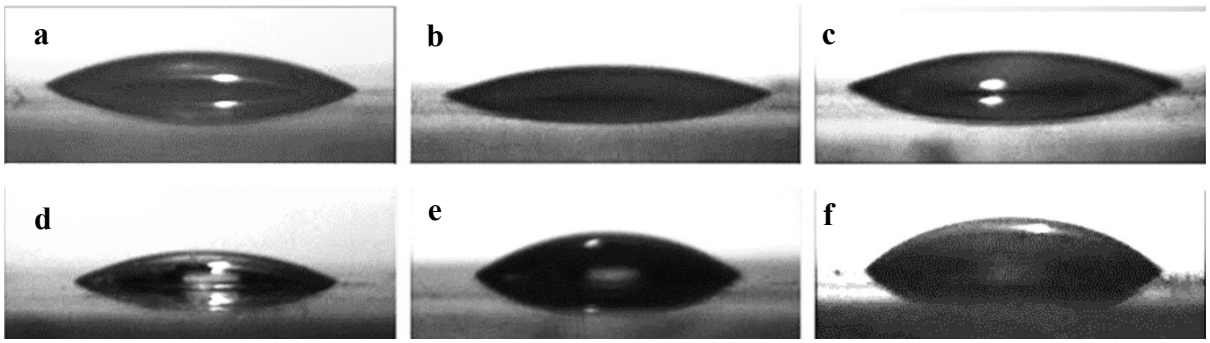

Figure 5.45. Contact angle measurements on PEO200/Gly PUD coatings. Water droplets (DI water) after 10 seconds of being placed on coatings subjected to various aqueous 0.1 *M* salt treatments: (a) untreated sample; (b) KI; (c) $NaBF_4$; (d) $NaN(CN)_2$; (e) CF_3SO_3Na; (f) KPF_6.

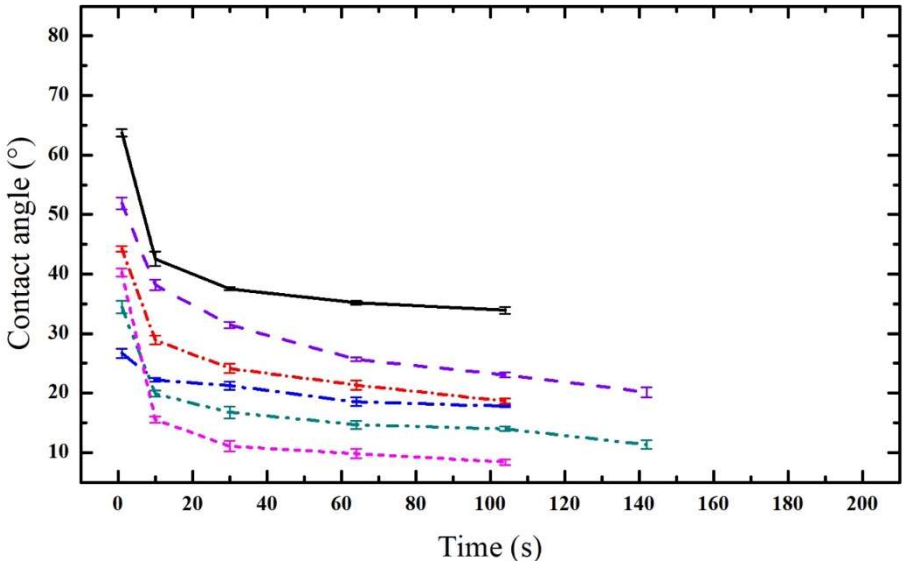

Figure 5.46. Comparison of dynamic contact angles on PEO200/Gly PUD coatings. Water droplets (DI water) after being placed on coatings subjected to various aqueous 0.1 *M* salt treatments: untreated (—·—·—); KI (·····); $NaBF_4$(—··—··—); $NaN(CN)_2$ (—··—); CF_3SO_3Na (– – –); KPF_6 treated (——).

Comparison of dynamic contact angles obtained for different salt treatments on PEO200/Gly PUD-based coatings show that different anions induce very different responses to changes in surface energy and contact angle as a result of undergoing anion exchange with bromide. KPF_6, CF_3SO_3Na, and $NaN(CN)_2$ increased the contact angle relative to that for the

untreated bromide film, whereas $NaBF_4$ and KI decreased the contact angle of an untreated film while making them slightly hydrophobic (not dispersing back in water). After 10 seconds of contact with a DI water drop, measured contact angles in anion exchanged coatings decreased in the following order: PF_6^- (43˚) > $CF_3SO_3^-$ (38˚) > $N(CN)_2^-$ (29˚) > untreated (22˚) > BF_4^- (20˚) > I^- (16˚) (Fig. 5.45 and Fig 5.46). From Fig. 5.46, an overall trend in decreasing order of dynamic contact angle was PF_6^- > $CF_3SO_3^-$ > $N(CN)_2^-$ > untreated > BF_4^- > I^-.

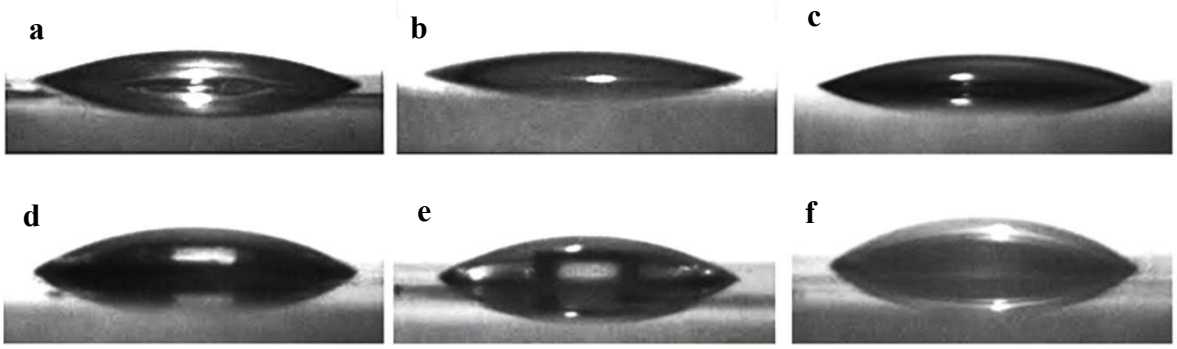

Figure 5.47. Contact angle measurements on PEO200 PUD coatings. Water droplets (DI water) after 10 seconds of being placed on coatings subjected to various aqueous 0.1 *M* salt treatments: (a) untreated sample; (b) KI treated; (c) $NaBF_4$ treated; (d) $NaN(CN)_2$ treated; (e) CF_3SO_3Na treated; (f) KPF_6 treated.

Similarly, in PEO200-PUD based coatings, after 10 seconds, measured contact angle in anion exchanged coatings decrease in the following order: PF_6^- (45˚) > $CF_3SO_3^-$ (38˚) > $N(CN)_2^-$ (35˚) > untreated (26˚) ≈ BF_4^- (26˚) > I^- (23˚) as seen in Fig. 5.47 and Fig. 5.48. From Fig. 5.48, an overall trend in decreasing order of dynamic contact angle was PF_6^- > $N(CN)_2^-$ > $CF_3SO_3^-$ > untreated > BF_4^- > I^-.

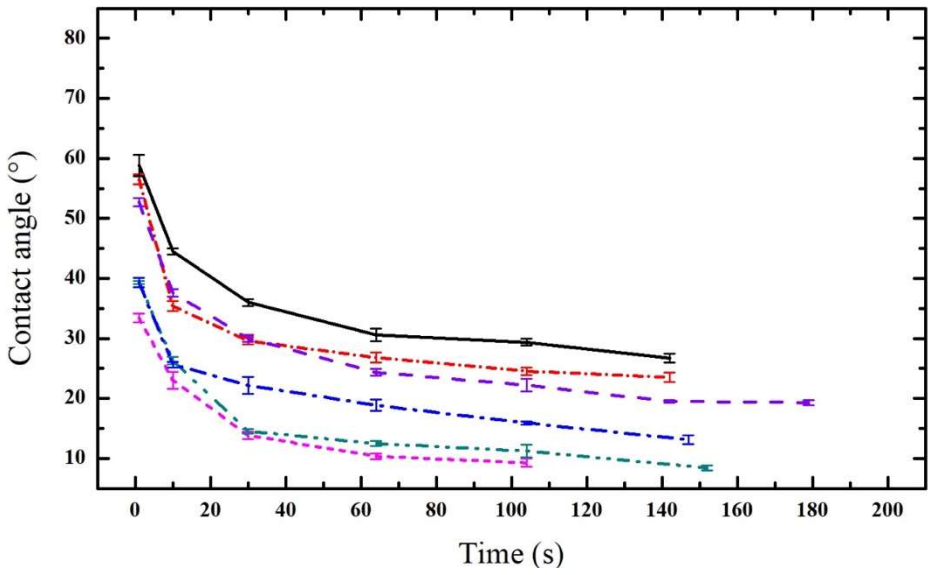

Figure 5.48. Comparison of dynamic contact angles on PEO200 PUD coatings. Water droplets (DI water) after being placed on coatings subjected to various aqueous 0.1 *M* salt treatments: untreated (—·—·—); (b) KI treated (·····); (c) $NaBF_4$ treated (—··—··—); (d) $NaN(CN)_2$ treated (—··—··—); (e) CF_3SO_3Na treated (– – –); (f) KPF_6 treated (———).

In PPO192-PUD based coatings on glass slides, after 10 seconds of contact with DI water drops, measured contact angles in anion exchanged coatings decreased in the following order: PF_6^- (62˚) > $CF_3SO_3^-$ (60˚) > BF_4^- (54˚) > untreated (41˚) > $N(CN)_2^-$ (36˚) > I^- (34˚) as can be seen in Fig. 5.49 and Fig. 5.50. From Fig. 5.50 an overall trend of decreasing order of dynamic contact angle was: PF_6^- > $CF_3SO_3^-$ > BF_4^- > untreated > $N(CN)_2^-$ > I^-.

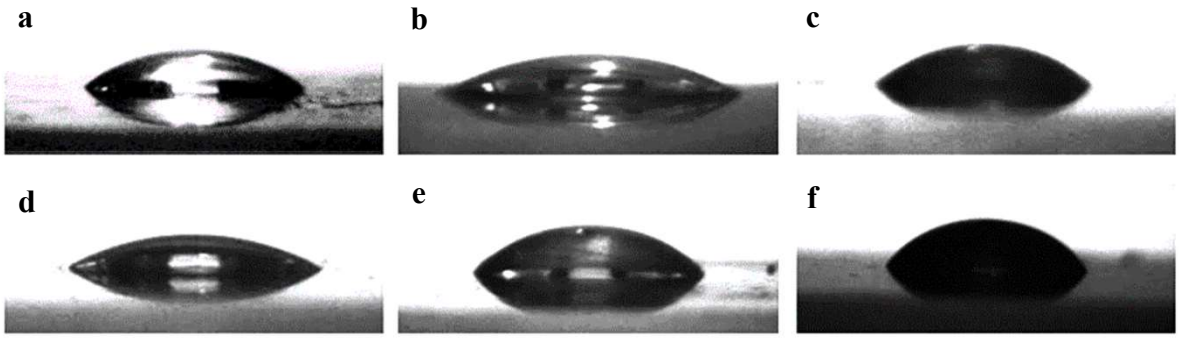

Figure 5.49. Contact angle measurements on PPO192 PUD coatings. Water droplets (DI water) after 10 seconds of being placed on coatings subjected to various aqueous 0.1 *M* salt treatments: (a) untreated sample; (b) KI treated; (c) $NaBF_4$ treated; (d) $NaN(CN)_2$ treated; (e) CF_3SO_3Na treated; (f) KPF_6 treated.

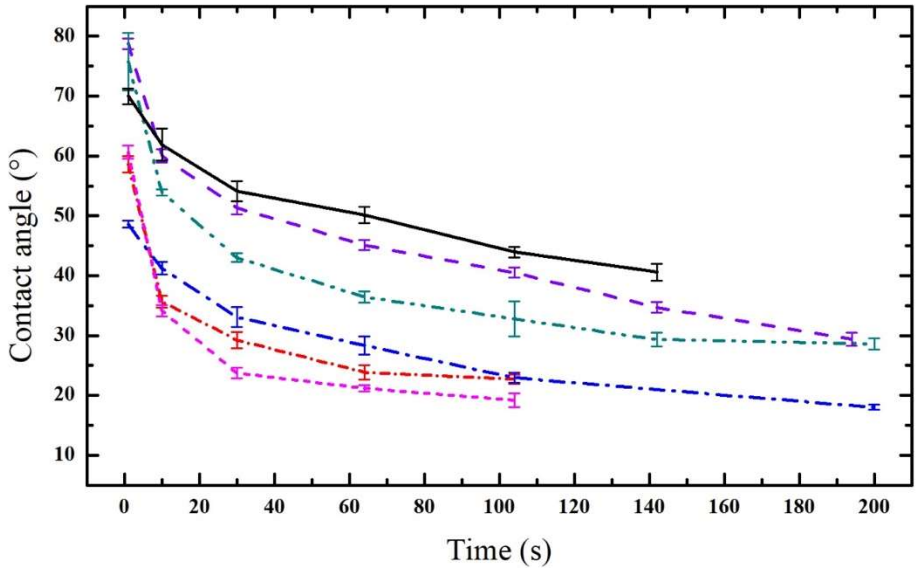

Figure 5.50. Comparison of dynamic contact angles on PPO192 PUD coatings. Water droplets (DI water) after being placed on coatings subjected to various aqueous 0.1 *M* salt treatments: untreated (-·-·-); (b) KI treated (- - - -); (c) $NaBF_4$ treated (-··-··-); (d) $NaN(CN)_2$ treated (-··-); (e) CF_3SO_3Na treated (- - -); (f) KPF_6 treated (———).

In PPO192/Gly PUD-based coatings on glass slides, after 10 seconds of contact with a drop of DI water, measured contact angles with anion exchanged coatings decreased in the following order: PF_6^- (60˚) > $CF_3SO_3^-$ (55˚) = BF_4^- (55˚) > untreated (46˚) > $N(CN)_2^-$ (35˚) > I^-

(30˚) as can be seen in Fig. 5.51 and Fig. 5.52. From Fig. 5.52 an overall trend in decreasing order of dynamic contact was: PF_6^- > $CF_3SO_3^-$ > BF_4^- > untreated > $N(CN)_2^-$ > I^-.

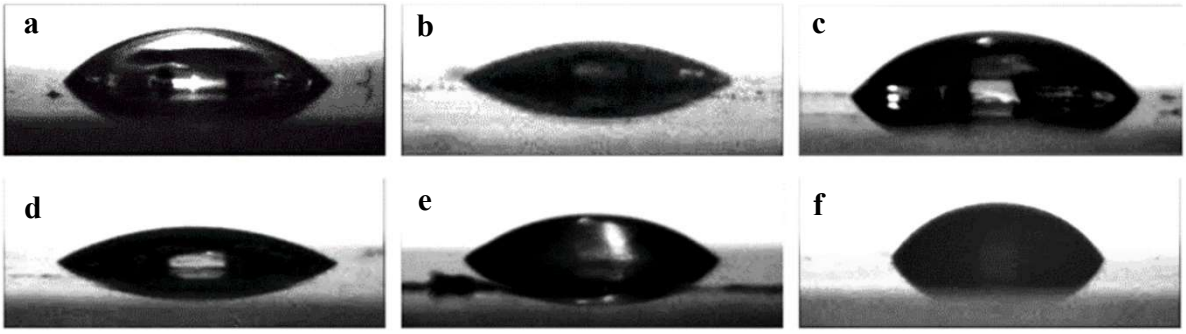

Figure 5.51. Contact angle measurements on PPO192/Gly PUD coatings. Water droplets (DI water) after 10 seconds of being placed on coatings subjected to various aqueous 0.1 *M* salt treatments: (a) untreated sample; (b) KI treated; (c) $NaBF_4$ treated; (d) $NaN(CN)_2$ treated; (e) CF_3SO_3Na treated; (f) KPF_6 treated.

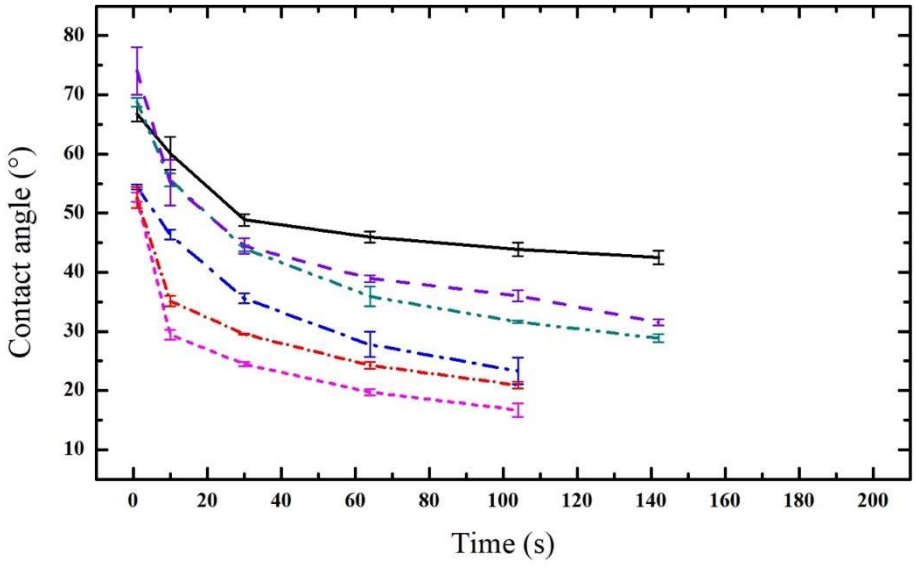

Figure 5.52. Comparison of dynamic contact angles on PPO192/Gly PUD coatings. Water droplets (DI water) after being placed on coatings subjected to various aqueous 0.1 *M* salt treatments: untreated (—·—·—); (b) KI treated (·····); (c) $NaBF_4$ treated (—·—·—); (d) $NaN(CN)_2$ treated (—··—··—); (e) CF_3SO_3Na treated (– – –); (f) KPF_6 treated (———).

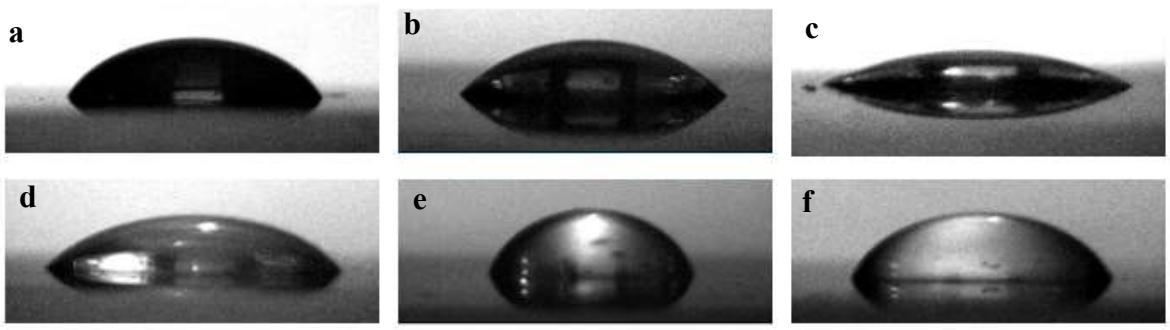

Figure 5.53. Contact angle measurements on PPO192/Trigly PUD coatings. Water droplets (DI water) after 10 seconds of being placed on coatings subjected to various aqueous 0.1 *M* salt treatments: (a) untreated sample; (b) KI treated; (c) $NaBF_4$ treated; (d) $NaN(CN)_2$ treated; (e) CF_3SO_3Na treated; (f) KPF_6 treated.

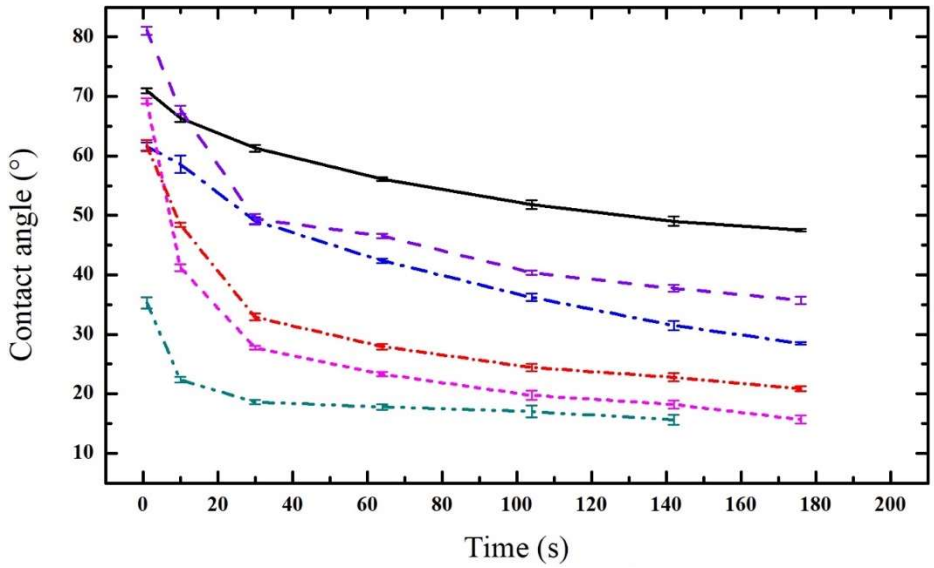

Figure 5.54. Comparison of dynamic contact angles on PPO192/Trigly PUD coatings. Water droplets (DI water) after being placed on coatings subjected to various aqueous 0.1 *M* salt treatments: untreated (-·-·-); (b) KI treated (·····); (c) $NaBF_4$ treated (-·-·-); (d) $NaN(CN)_2$ treated (-··-··-); (e) CF_3SO_3Na treated (- - -); (f) KPF_6 treated (———).

In PPO192/Trigly PUD-based coatings on glass slides, after 10 seconds contact with a DI water drop, measured contact angles in anion exchanged coatings decrease in the following order: $CF_3SO_3^-$ (68˚) > PF_6^- (66˚) > untreated (58˚) > $N(CN)_2^-$ (48˚) > I^- (41˚) > BF_4^- (22˚) as

can be seen in Fig. 5.53 and Fig. 5.54. From Fig. 5.54, an overall trend of decreasing order was: PF_6^- > $CF_3SO_3^-$ > untreated > $N(CN)_2^-$ > I^- > BF_4^-.

Different salts had different effects on apparent contact angles of these coatings. Overall, it seems that PPO-based coatings had higher contact angles then PEO-based coatings. PEO-based coatings are more hydrophilic and interact attractively with water, so it is not surprising that they wet more easily with water and exhibit lower contact angles. We also observed that after treatment with aqueous 0.1 *M* KPF_6 solution, PPO-based coatings have a higher resistance to water and better film robustness then PEO-based coatings. This is consistent with PPO being much more hydrophobic than PEO, in addition to effects of the anion exchange being one of making a more hydrophobic environment.

It should be noted that untreated coatings were not resistant to water, and with time, contact angles become zero (can be seen in Fig. 5.60(d)). However, in the above experiments we see that untreated coatings have higher contact angles then some other anions. It is possible that 15 minutes of treatment time was not enough for anions to completely undergo anion exchange with bromide ions. Another difference observed was that during these measurements, untreated coatings were completely dried, whereas treated coatings were air dried for about 30 minutes. These results might not be equilibrium results and improved experiments are needed in the future.

5.7.2.2 Effect of KPF_6 anion with UV crosslinking on contact angle

A PPO192/Trigly coating contained unreacted acrylate groups, which could be used to crosslink in the presence of a photoinitiator during UV exposure. The photoinitiator

Darocur-1173 was mixed into this PUD at 0.31% relative to dispersion solids, before coating this PPO192/Trigly as a film on glass slides. After drying (of water), these slides were exposed to UV light by using a Fusion UV exposure system (Heareus, Gaithersburg, MD, USA) with an H-bulb at a belt speed of 12 ft/min with variable numbers of passes (exposures). DI water drops were used to measure contact angles of these UV exposed coatings. Short duration videos were made to capture dynamic changes in contact angle and screenshots at different time intervals from these videos were used to measure contact angles of different samples. ImageJ software was used by a plugin for dropsnake analysis to measure contact angles. Each right and left side angle was measured twice for repeatability.

One can see that contact angle was increased with an increased number of UV passes, though the films remained water sensitive and were re-dispersing back into water until they were treated with aqueous 0.1 IM KPF_6. Treatment by KPF_6 solution after consecutive UV passes also increased the contact angle as seen in Fig. 5.55 and Fig. 5.56. After 30 seconds of contact with a DI water drop, measured contact angles in decreasing order were as follows: treated by aqueous 0.1 *M* KPF_6 for 15 min after 3 UV passes (74˚) > untreated with 3 UV passes (67˚) > untreated with 1 UV pass (60˚) > untreated without UV exposure (49˚).

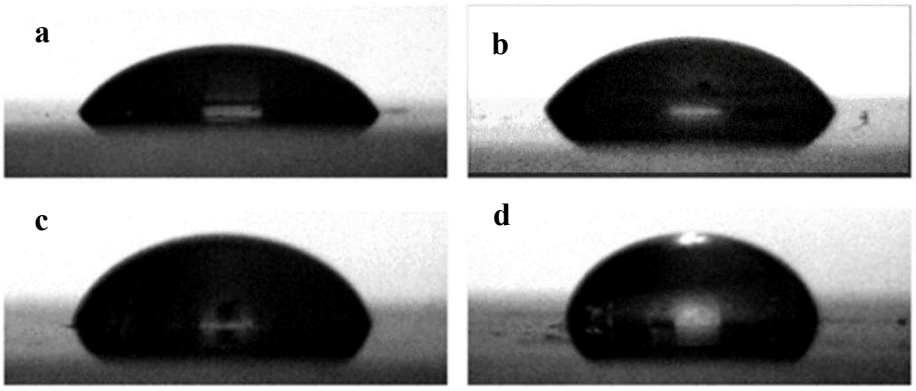

Figure 5.55. Contact angles on PPO192/Trigly PUD coatings subjected to UV exposure. DI water drops 30 seconds after contacting coatings: (a) untreated without UV exposure; (b) untreated with 1 UV pass; (c) untreated with 3 UV passes; (d) treated with aqueous 0.1 *M* KPF_6 for 15 minutes after 3 UV passes.

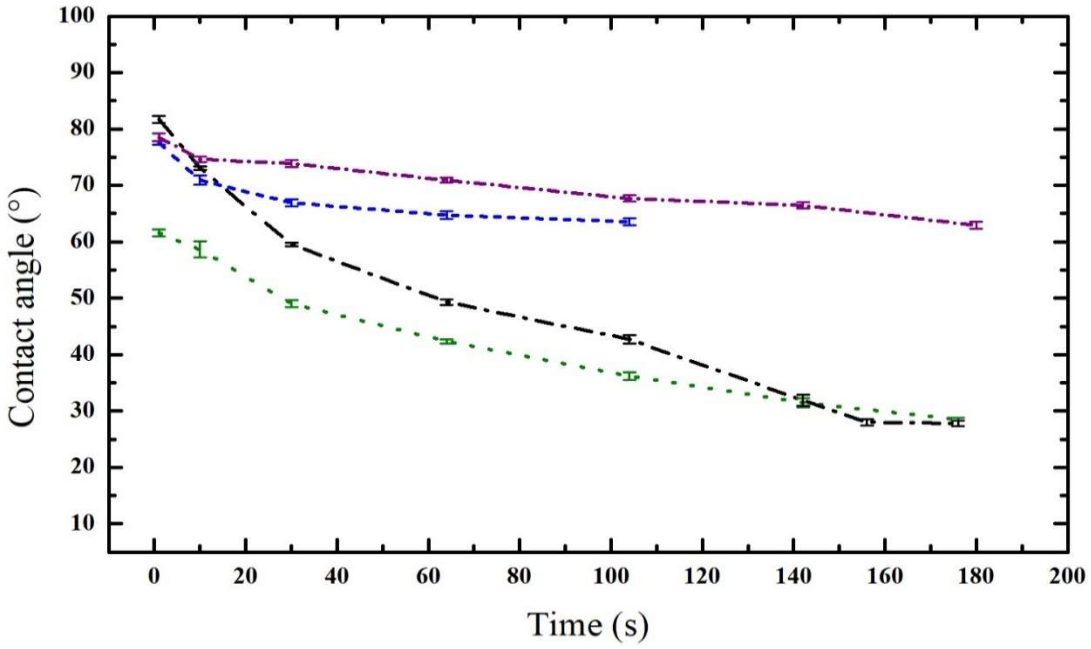

Figure 5.56. Comparison of dynamic contact angle measurements on PPO192/Trigly PUD coatings subjected to UV exposure. DI water drop on coatings: untreated without UV exposure (· · · ·); untreated with 1 UV pass (— · — ·); untreated with 3 UV passes (- - - - -); with aqueous 0.1 *M* KPF_6 for 15 minutes after 3 UV passes (— · · — · · —).

UV exposure after a coating was treated with aqueous KPF_6 solution yielded higher contact angles then treating with aqueous KPF_6 after UV exposure. Contact angles of drops placed on such coatings increased with increasing number of UV passes until becoming independent of number of UV exposure passes. From Fig. 5.57 and Fig. 5.58 this saturation effect appears to happen after two passes.

An increase in contact angle with increasing UV exposure suggests that crosslinking of acrylate groups somehow increase surface hydrophobicity. DSC data of dried PUD samples before and after UV exposure shows an increase in T_g value, suggesting formation of crosslinked networks (Fig. A.5.8 in Appendix D).

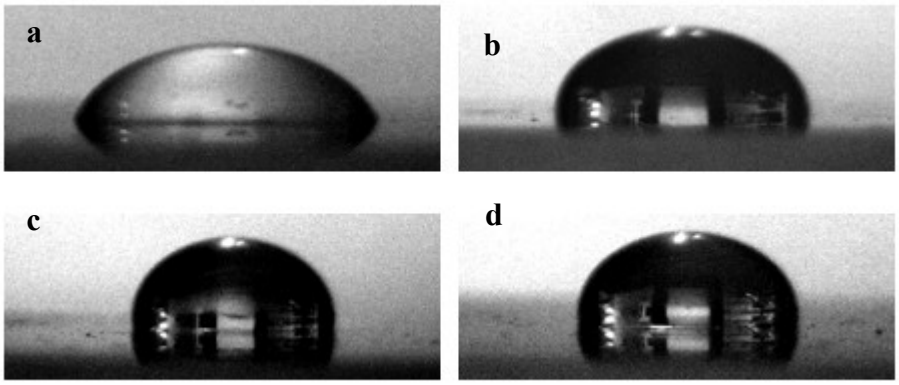

Figure 5.57. Contact angles on KPF_6 treated PPO192/Trigly PUD coatings subjected to UV exposure. DI water drops 30 seconds after contacting coatings that are treated by aqueous 0.1 *M* KPF_6 for 15 minutes: (a) without UV exposure; (b) after 1 UV pass; (c) after 2 UV passes; (d) after 3 UV passes.

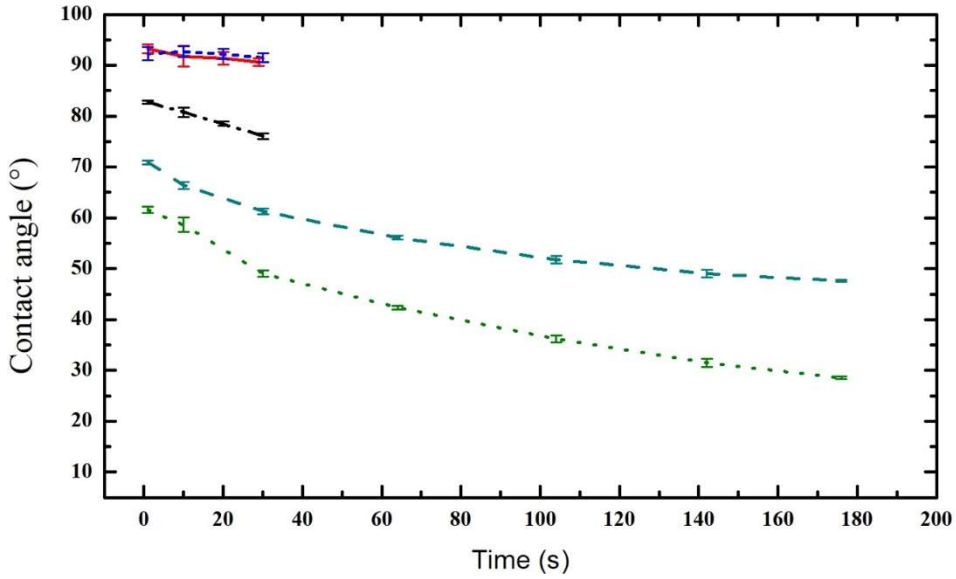

Figure 5.58. Comparison of dynamic contact angle on KPF_6 treated PPO192/Trigly PUD coatings subjected to UV exposure. DI water drops after contacting coatings that are treated by aqueous 0.1 *M* KPF_6 for 15 minutes: without UV exposure (– – –); with 1 UV pass (–·–·–); with 2 UV passes (——); with 3 UV passes (-----) and untreated coated glass slide without UV exposure (· · · ·).

5.7.2.3 Stimuli response to water

In Fig. 5.59(a), a PEO200 PUD coating treated with 0.1 *M* salt solution of KPF_6 was examined by placing a drop of DI water on it. It was observed that this coating did not re-disperse in water in that drop-coating contact area, and no visual changes in the coating's turbidity were observed. In Fig. 5.59(b), a PEO200 PUD coating that was treated with a 0.1 *M* salt solution of $NaBF_4$ was examined with a DI water drop on it. Similar behavior was observed where this coating did not re-disperse into water in that drop-coating contact area, and no visual changes were observed in the coating's turbidity. In Fig. 5.59(c), a DI water drop was placed on an untreated PEO200 PUD coating. No change in this coating's turbidity was observed. There was a higher extent of wetting compared, to Fig. 5.59(a) and Fig. 5.59(b). With time, this coating re-dispersed into the water drop.

In Fig. 5.60(a), a DI water drop was placed on a PPO192 PUD coating treated with a 0.1 *M* salt solution of KPF_6. It was observed that this coating became turbid and did not re-disperse in water in the drop-coating contact area. In Fig. 5.60(b), a DI water drop was placed on a PPO192 PUD coating treated with 0.1 *M* KI solution. Similarly, to the KPF_6-treated coating, the coating became turbid and did not re-disperse in the water droplet. In Fig. 5.60(c), a PPO192 PUD coating treated with a 0.1 M solution of $NaBF_4$ became turbid. When a DI water drop was placed on it, the coating did not disperse into the droplet. In Fig. 5.60(d), an untreated PPO192 PUD coating did not become turbid when contacted with DI water. There was a higher extent of wetting of a contacting drop of DI water compared to Fig. 5.60(a), Fig. 5.60(b), and Fig. 5.60(c), and this untreated coating re-dispersed into the droplet in the contact area.

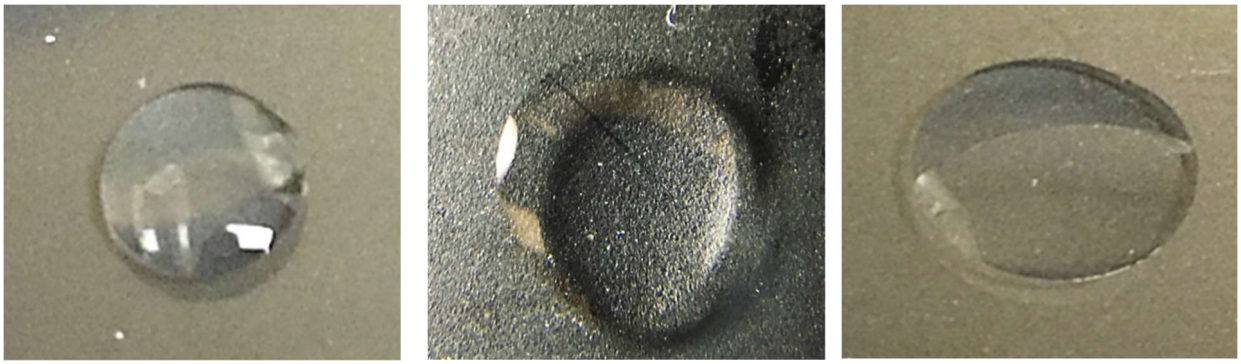

Figure 5.59. Drop of DI water placed on surface of PEO200 PUD coating that is: (a) KPF_6 treated; (b) $NaBF_4$ treated; (c) untreated.

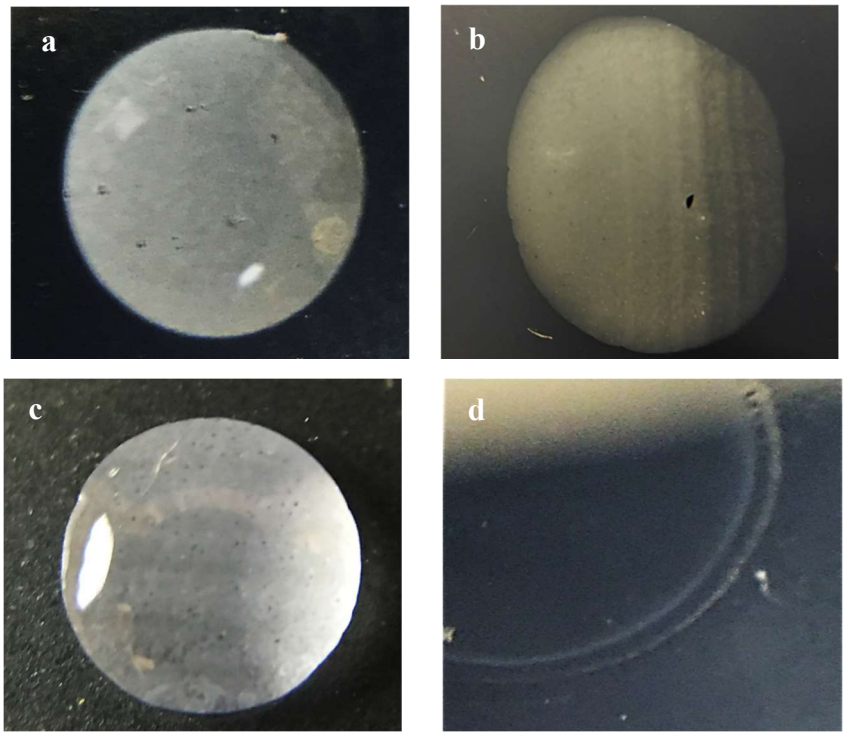

Figure 5.60. Drop of DI water placed on surface of PPO192 PUD coating that is: (a) KPF_6 treated; (b) KI treated; (c) $NaBF_4$ treated; (d) untreated.

In Fig. 5.61(a), a PPO192/Trigly PUD coating treated with 0.1 *M* KPF_6 solution was contacted with a droplet of DI water. It was observed that this coating did not re-disperse into this contacting droplet. In Fig. 5.61(b), it can be seen that turbidity forms in the contact area, but as this water evaporated from the film, it became clear again.

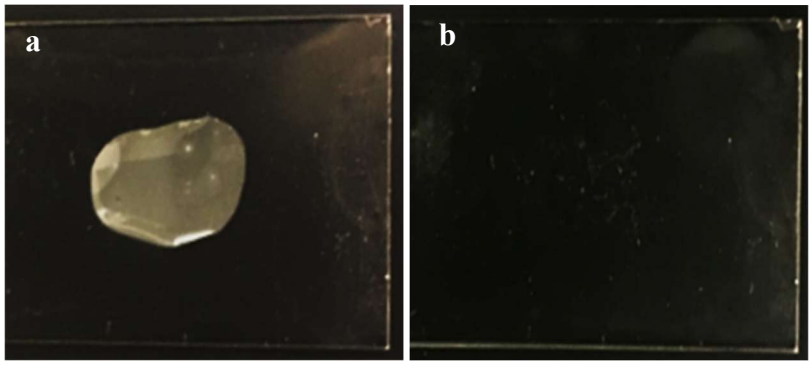

Figure 5.61. (a) Drop of DI water placed on the surface of KPF_6 treated PPO192/Trigly PUD coating. It can see that this droplet has become turbid; (b) clear film after evaporation of water droplet illustrated in frame (a).

In summary, the PPO192-based treated coatings became turbid as soon as they were contacted with water until their drop evaporated or was absorbed by the coating; see Fig. 5.60 (a, b, c). Films became clear as the evaporated as can be seen in Fig. 5.61 (b). It was also observed that untreated coatings did not turn turbid, but instead they re-dispersed into the water see Fig. 5.60(d).

PEO200-based anion treated coatings did not become turbid and did not re-disperse into water; see Fig. 5.59(a, c). An untreated film re-dispersed when contacted with water; see Fig. 5.59(b), where the drop has a higher extent of wetting.

Chapter 6

Self-dispersing Hydroxyundecyltriethyl Ammonium Bromide (HUTEAB) PUDs

6.1 Overview

HUTEAB was examined as a control monofunctional monomer material in PUD synthesis, and it was not anticipated that it would exhibit features demonstrated earlier in this work by $HOC_{11}C_1ImBr$. However, its physical and chemical behavior make it of interest in its own right with respect to PUD formulation and development. Its thermal behavior and performance in formulating self-dispersing PUDs are compared with $HOC_{11}C_1ImBr$ in a context of a PPO-based formulation described earlier (PPO192 PUDs) in this work. Particle size, rheological properties, and film properties of a resin synthesized by this monomer are studied and compared with those from PPO192 PUD results of Chapter 5.

6.2 Synthesis of Hydroxyundecyltriethyl Ammonium Bromide (HUTEAB)

HUTEAB was synthesized according to Fig. 6.1 by using bromoundecanol (solid at room temperature) and triethylamine (liquid at room temperature). Reagent components are given in Table 6.1. A reactor was put in an oil bath and sparged with nitrogen gas. An excess amount of triethylamine was refluxed with bromoundecanol at 60 °C for 24 hours under continuous stirring using a magnetic stirrer (Fig. 2.1). Bromoundecanol melted at 60 °C, making the reaction a clear liquid solution. After 24 hours, the main reaction product, HUTEAB, was observed as a white powder precipitate in the reactor.

The reaction mechanism is explained through Menshutkin reactions using SN1 and SN2 mechanisms where two neutral reactants react to produce two charged species[54] (Fig. 6.1), which

is also an explanation for the reaction mechanism during synthesis of $HOC_{11}C_1ImBr$ (section 3.1).

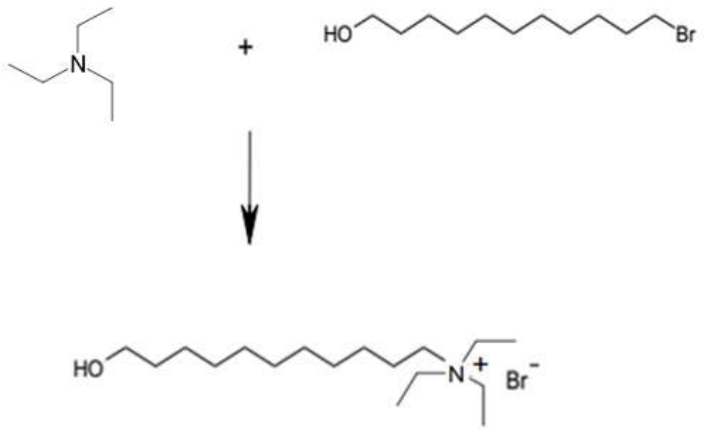

Figure 6.1. Reaction scheme to synthesize HUTEAB. It involves the coupling of neutral 11-bromoundecanol and triethylamine to yield charged HUTEAB salt.

Table 6.1. Composition of reactants used to synthesize HUTEAB

Component	Molecular Weight	Weight	Millimoles
Bromoundecanol	251.2 Da	10.31 g	41.02
Triethylamine	101.2 Da	14.14 g	139.75

The product HUTEAB was filtered using a sintered glass filter funnel and was collected in a flask. It was washed with 25 mL of THF while being stirred for 30 minutes. This product salt was insoluble in THF and was filtered. This filtered salt was washed again by using acetonitrile as solvent at room temperature, where all the salt dissolved. Salt was recovered after evaporation of acetonitrile first by evaporation in a hood and then by using a vacuum oven at

65 °C for 2 h. After this vacuum heating treatment, the product was cooled to solidify and stored in a glass vial inside a desiccator.

6.3 Thermal Characterization of HUTEAB

In Fig. 6.2, a TGA of HUTEAB after it had been recrystallized from acetonitrile, is compared with a TGA of bromoundecanol. Two derivative peaks at 250 °C and 310 °C can be seen for this HUTEAB salt. Most of bromoundecanol decomposes at around 230 °C. The boiling point of the reactant, TEA, is 89 °C. Therefore, this TGA comparison clearly shows conversion of bromoundecanol into HUTEAB.

A sample of HUTEAB washed by THF was first heated to 120 °C to remove thermal history. It then was cooled to -70 °C and then heated to 150 °C. A sample of filtrate recovered after washing of salt from THF was first heated to 110 °C to remove any thermal history, and then it was cooled to -70 °C, and then heated to 110 °C. A comparison sample of bromoundecanol was also first heated to 120 °C to get rid of thermal history, then cooled to -80 °C, and then heated to 120 °C. These data are illustrated in Fig. 6.3.

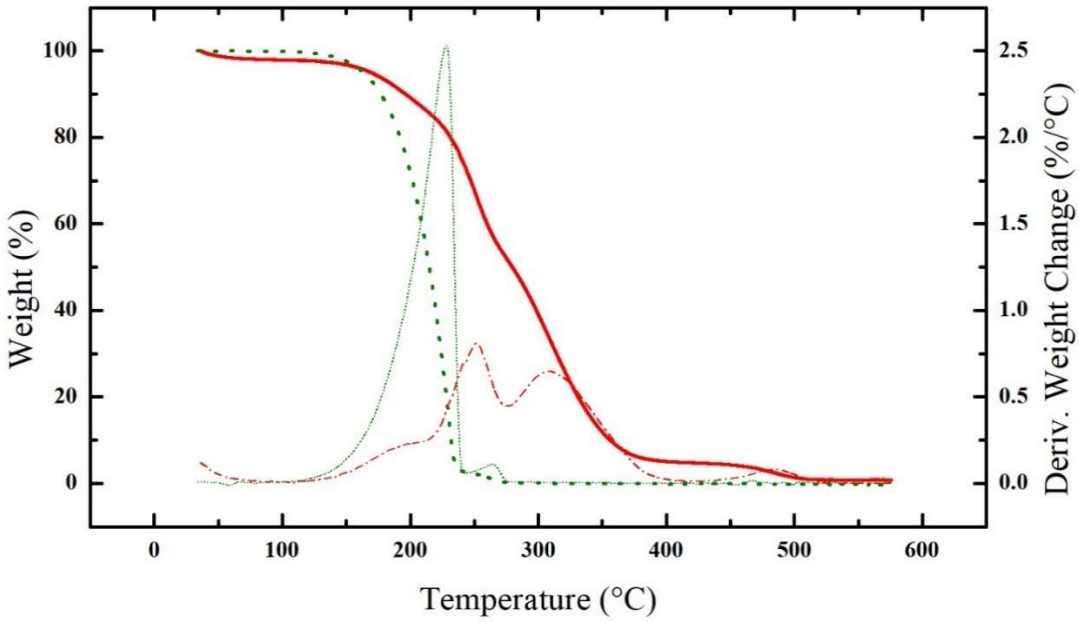

Figure 6.2. TGA of HUTEAB compared with TGA of bromoundecanol. Weight percent change of HUTEAB (——); bromoundecanol (- - - - -). Derivative weight percent change of HUTEAB (-·-·-); bromoundecanol (——).

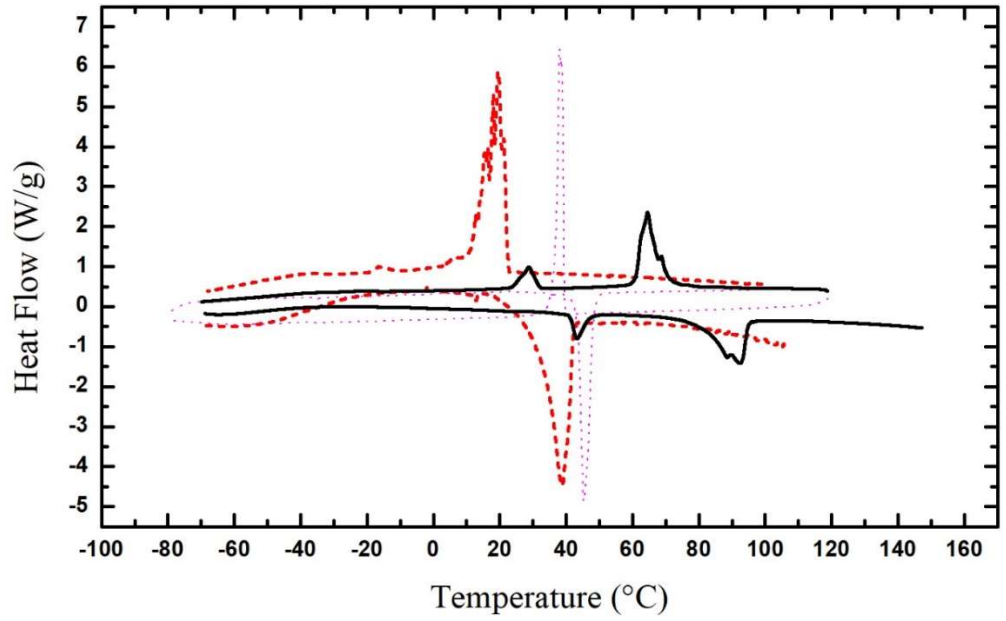

Figure 6.3. Comparison of DSCs of HUTEAB and filtrate from THF wash. DSCs using rate of 10 °C/min of: filtrate washed by THF (- - - -); HUTEAB after THF wash (——); bromoundecanol (·····) for comparison.

It was seen that filtrate had freezing and melting peaks like bromoundecanol but were at different temperatures. DSC of bromoundecanol was done using variable cycles with variable heat treatments during those runs. It was observed that freezing and melting phenomena happened at different temperatures in the cycles (Fig. 6.4). This experiment suggests that the filtrate in Fig. 6.3 may be unreacted bromoundecanol, which is also soluble in THF.

HUTEAB washed by THF showed two freezing peaks and two melting peaks during the DSC run. During cooling, a first freezing event started at 68 °C with peak freezing point of 64 °C and a freezing enthalpy of 66 J/g. During further cooling, a second freezing peak was seen starting at 32 °C with peak freezing point of 29 °C and a freezing enthalpy of 15 J/g.

During the next heating interval, a first melting was seen starting at 41 °C with peak melting temperature of 43 °C and a melting enthalpy of 15 J/g. On further heating, a second melting peak was observed starting at 65 °C with a peak melting peak of 92 °C (see Fig. A.6.1 in Appendix E). Melting of HUTEAB below 100 °C qualifies it as an ionic liquid. The peak freezing point of 29 °C and peak melting point at 43 °C are assigned to unreacted bromoundecanol, in view of the data of Fig. 6.4.

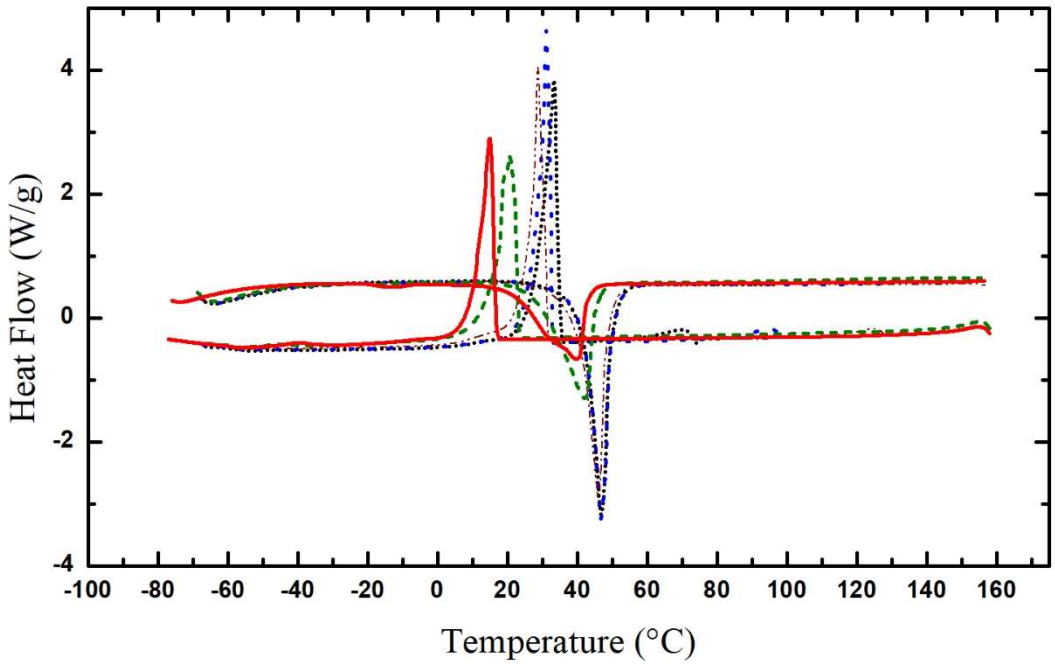

Figure 6.4. DSC of bromoundecanol with multiple cycles. DSC at heating rate of 10 °C/min, sample was first heated to 75 °C to remove thermal history then in**:** 1st cycle, where sample was cooled to -70 °C then heated to 100 °C and kept isothermal for 15 minutes (⋯⋯⋯); 2nd cycle where sample was cooled to -70 °C then heated to 130 °C and kept isothermal for 15 minutes(- - - -); 3rd cycle where sample was cooled to -70 °C then heated to 160 °C and kept isothermal for 15 minutes (-·-·-·-·-); 4th cycle, where sample was cooled to -70 °C then heated to 160 °C and kept isothermal for 30 minutes (- - - - -);5th cycle, where sample was cooled to -80 °C then heated to 160 °C (——).

After some HUTEAB was washed with THF, it was dissolved in acetonitrile and then recrystallized. It was then analyzed by TGA (Fig. 6.3) and DSC. Fig. 6.5 compares this DSC of HUTEAB after it was washed with THF and that recrystallized from acetonitrile. Samples were first heated to 120 °C to remove any thermal history. Then they were cooled to -70 °C and then heated to 150 °C.

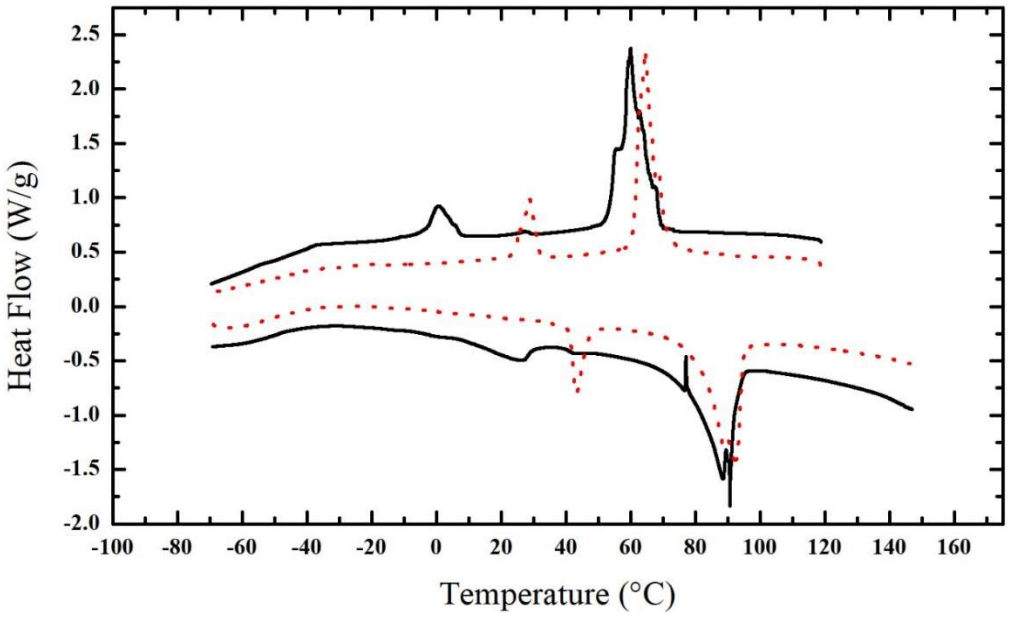

Figure 6.5. DSC of HUTEAB recovered from acetonitrile after THF wash. DSCs using rate of 10 °C/min of HUTEAB: washed by THF (· · · ·); recrystallized from acetonitrile after THF wash (——).

During cooling, it was seen that the first freezing peak started at about 70 °C with a peak freezing temperature of 60 °C; it had a freezing enthalpy of 81 J/g. A second freezing peak shifted down to start at 8 °C with a freezing peak at 1 °C and a freezing enthalpy of 12 J/g. During a heating interval, a melting peak was seen much earlier, starting at 10 °C with a peak melting temperature of 26 °C and a melting enthalpy of 12 J/g. A second melting was seen starting at about 60 °C with a peak melting temperature of 91 °C and a melting enthalpy of 71 J/g (see Fig. A.6.2 in Appendix E). These second smaller peaks could either be attributed to unreacted bromoundecanol or be characteristic of an unknow polymorph formed in HUTEAB. We believe the most likely possibility is that of a bromoundecanol impurity, and a careful silver ion potentiometric titration of the product might be definitive. A sequence of annealing treatments might also resolve whether or not the source of lower temperature melting and freezing peaks is an impurity or a polymorph.

6.4 HUTEAB/PPO192 PU

6.4.1 Synthesis

First, a pre-resin mixture comprising hydroxy functional materials was prepared by combining hydroxy reagents in a 15 mL vial prior to polymerization. Amounts of each component are specified in Table 6.2. These hydroxy-functional materials were dissolved by using methylene chloride. Then HDI was added to stoichiometrically balance the reactants (NCO/OH ratio = 0.999), and then this mixture was stirred using a vibratory stirrer. Lastly, DBTD was added as a catalyst to a transparent brownish solution of reactants. This resin solution was darker in color then other resin solutions we studied, such as illustrated in Fig. 5.3.

This reaction mixture containing vial was stirred and placed in an an oven at 80 °C for about 15 hours. After that product solution was cooled (see Fig. 6.6), it was stripped of solvent at ambient conditions by allowing the vial to vent in a hood. After this all remaining solvent was removed by heating in a vacuum oven at 100 ºC for 4.75 h.

Figure 6.6. HUTEAB/PPO192 PU in solvent, after removal from oven.

Table 6.2. Composition of HUTEAB/PPO192 PU

Ingredient	Weight (mg)	Millimoles
HUTEAB	1097.9	3.12
HDI	1050.0	6.24
PPO192	902.2	4.69
CH_2Cl_2	4560 mg	
DBTD	85.6 mg	
Solids	40.75%	
NCO/OH ratio	0.999	
Catalyst percentage based on solids	2.73 %	

The composition of HUTEAB/PPO192 PU was similar to the $HOC_{11}C_1ImBr$ containing PPO192 PU resin described in Chapter 5 (Table 5.1). Some of the hydroxy equivalents were from HUTEAB (25%) and 75% were from PPO192 in this HUTEAB/PPO192 PU. This resin served as a control resin for PPO192 PU, where differences in properties can be attributed to an interchange of $HOC_{11}C_1ImBr$ and HUTEAB. However, it was not anticipated when this "control" was suggested by committee members that HUTEAB would be an IL.

It was seen that vacuum-oven-dried 100% solid HUTEAB/PPO192 PU was solid at room temperature (Fig. 6.7(a)), but when heated to about 60-70 ºC, it softens to become a viscous liquid that could flow as seen in fig. 6.7(b) and Fig. 6.7(c). PEO200 PU, PEO200/gly PU,

PPO192 PU, PPO 192/gly PU and PPO192/Trigly PU from Chapter 5 also start flowing at about 60-70 ºC from solid material at room temperature (A.5.1 in Appendix D).

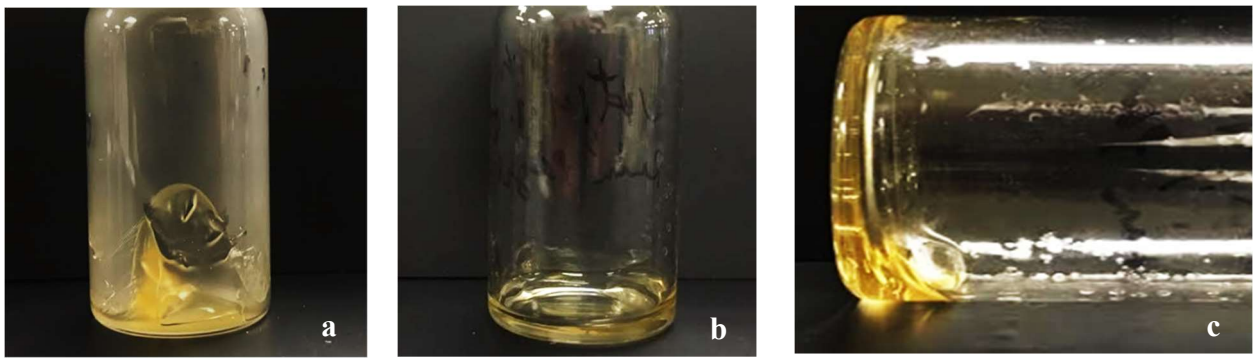

Figure 6.7. Vacuum-oven-dried 100% solid HUTEAB/PPO192 PU: (a) solid material at room temperature; (b) viscous liquid that can flow when 'a' heated to about 60-70 ºC; (c) glass vial in 'b' tilted.

6.4.2 Thermal characterization of HUTEAB/PPO192 PU

A TGA of HUTEAB/PPO192 PU was done in an inert atmosphere of nitrogen from room temperature to 580 °C at a heating rate of 10 °C/min. It can be seen in Fig. 6.8 that there was no solvent left in this 100% solid material. Four different decomposition processes can be seen with a major decomposition peak at about 350 °C.

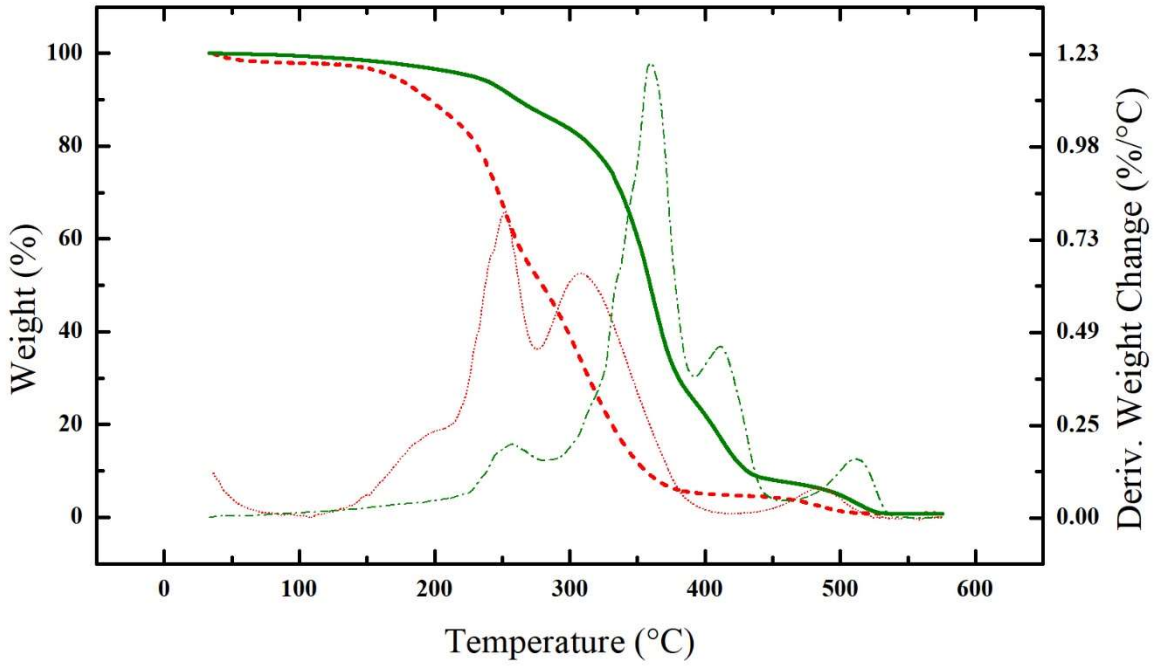

Figure 6.8. TGA of HUTEAB/PPO192 PU compared with TGA of HUTEAB monomer. Weight percent change (left axis), during TGA of HUTEAB/PPO192 PU (——); HUTEAB monomer (------). Derivative weight percent change (right axis), during TGA of HUTEAB/PPO192 PU (——); HUTEAB monomer (-·-·-·).

The TGA of HUTEAB/PPO192 PU has four different decomposition components with a major decomposition happening at 350 °C. PPO192 PU decomposition also has a major decomposition peak at 350 °C. TGAs of HUTEAB/PPO192 PU and PPO192 PU, are compared in Fig. 6.9.

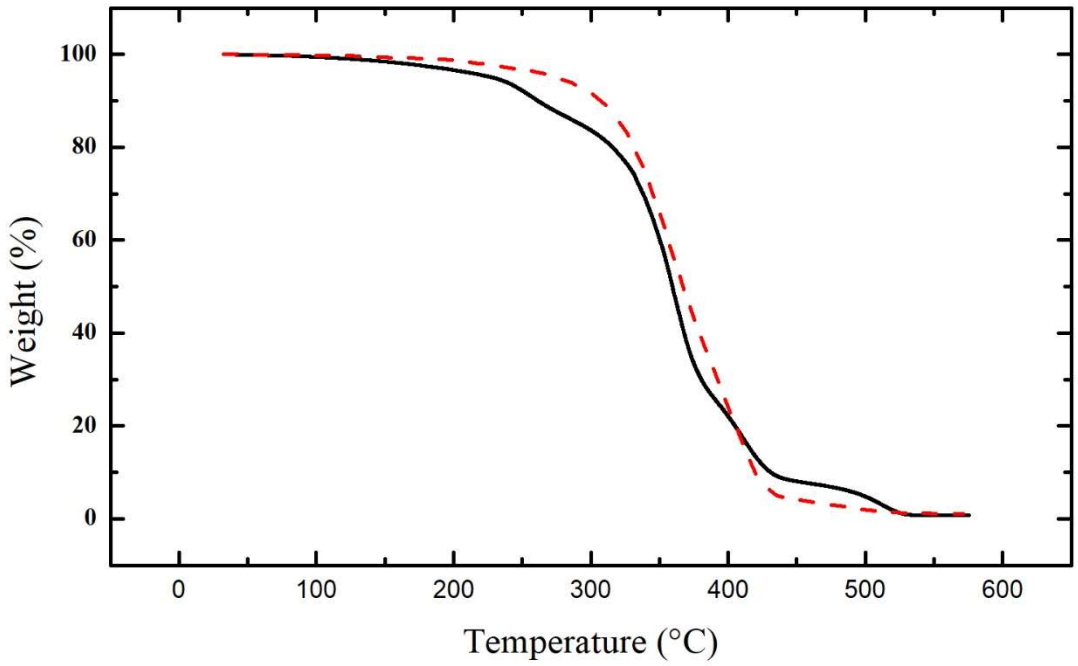

Figure 6.9. TGA of HUTEAB/PPO192 PU (——) compared with TGA of PPO192 PU (- - -).

For DSC, a sample of HUTEAB/PPO192 PU was first heated to 120 °C, and then it was cooled to -80 °C, and then heated to 150 °C (Fig. 6.10). During cooling, a glass transition was seen at -33 °C and at -28 °C during heating, which was lower than the T_g seen in PPO192 PU (-9 °C while cooling and -4 °C during heating).

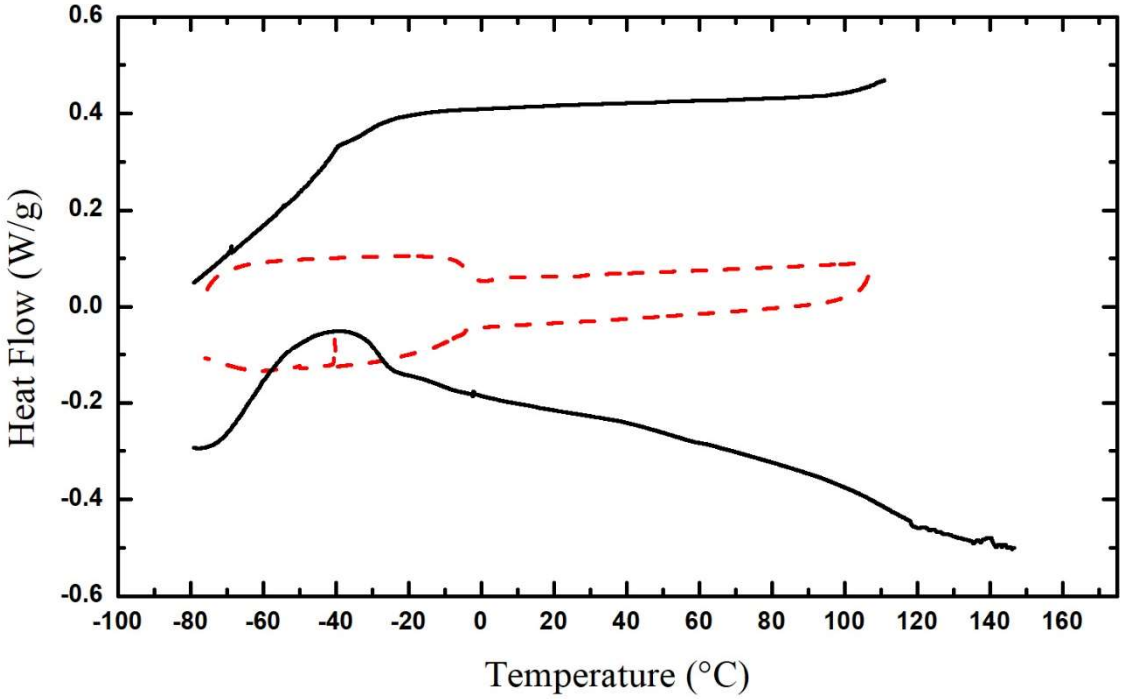

Figure 6.10. DSC of HUTEAB/PPO192 PU (——) compared to DSC of PPO192 PU (– – –) (Fig. 5.7).

6.4.3 GPC (gel permeation chromatography)

GPC of HUTEAB/PPO192 PU, PPO192 PU, and PEO200 PU was done to measure molecular weight distributions using a method described in Chapter 2. It can be seen from Table 6.3 that the average molecular weight of PPO192 PU resin was lower than that of HUTEAB/PPO192 PU samples. The molecular weight of PEO200 PU was highest and almost equal to that for this HUTEAB/PPO192 PU sample (see Fig. A.6.3 to A.6.5 in Appendix E for reference).

Table 6.3. Comparison of molecular weights among PUs

Material	M_n (Da)	M_w (Da)
HUTEAB/PPO192 PU	22,900	59,500
PPO192 PU	6,050	11,800
PEO200 PU	31,200	71,000

6.5 Self-Dispersing PUDs

A solid resin sample of HUTEAB/PPO192 PU, 94.7 mg, was put in a glass vial (Fig. 6.11(a)). To make a 0.5% dispersion by weight, 18.944 g of DI water was added, which immediately showed auto-dispersion of this sample, while particles started to form a cloudy dispersion near the solid resin chunks. After 1 h and 18 min, most of the resin was seen to have dispersed and presented as an opaque dispersion (Fig. 6.11 (c)). After 8 h and 20 min, almost all samples showed apparent auto-dispersion by forming a cloudy dispersion in the lower part of their respective vials as can be seen in Fig. 5.11(d). Vibratory stirring for 5 s produced a uniformly distributed PU dispersion illustrated in Fig. 6.11(e). PUDs 1% solids and 10% solids were made in a similar way.

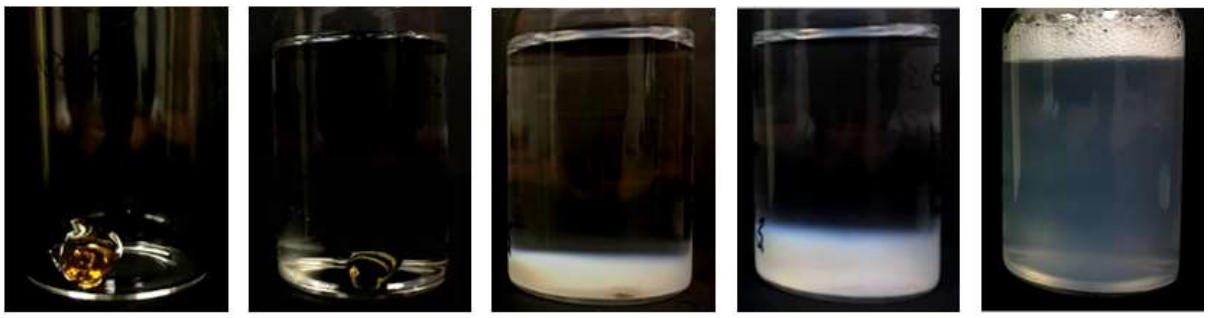

Figure 6.11. Photographic sequence illustrating self-dispersion of HUTEAB/PPO192 PU in water. (a) Added 94.7 mg of HUTEAB/PPO192 PU in a glass vial; (b) added 18.944 g DI water into (a); (c) unstirred vial after 1 h and 18 min showing cloudy formation by self-dispersion of PU particles; (d) after 8 h and 20 min showing "complete" dispersion of PU particles; (e) after 5 s of vibratory stirring showing uniform PUD.

6.6 Particle Size Characterization

To measure particle size distributions of various PUDs through dynamic light scattering, 1% by weight dispersions were made similarly as discussed in section 6.4. Self-dispersed PUD samples were put in glass cuvettes for particle size analysis. First, particle size analysis was done for PUD samples without any filtration; then samples were filtered through a 1-μm filter and were analyzed again. Lastly, 1-μm filtered samples were passed through a 0.45-μm filter and were again analyzed. Results are summarized in Table 6.4(a) and Table 6.4(b).

The "overall" particle size of 1% HUTEAB-PPO192 PUD was lower than 0.5% PPO192 PUD. There were a few bigger agglomerates in this 1% HUTEAB-PPO192 PUD, which were removed by filtration with a 1-μm filter and then by filtration with a 0.45-μm filter, and resulted in a further reduction of particle size. Without filtration, a number mean by MSD for 1%

HUTEAB-PPO192 PUD was 9 nm, whereas it was 340 nm in 0.5% PPO192 PUD. Though after consecutive filtrations from 1-μm and then 0.45-μm filters, the number mean in MSD for 0.5% PPO192 PUD became 9 nm too, which remained around 8 nm for 1% HUTEAB-

PPO192 PUD after similar filtration process. This suggests that PPO192 PUD had higher numbers of bigger agglomerates then 1% HUTEAB-PPO192, which were removed by filtration (Table 6.4(b) and Table 5.9(b)).

Table 6.4(a) Particle size parameters, solids, and turbidity for 1% (w/w) HUTEAB/PPO192 PUD subjected to filtration.

Measured Parameters	Not filtered	filtered (1 μm)	filtered (0.45 μm) (after 1 μm)
$^{LN}\langle d\rangle_l$/nm	176	149	130
$^{LN}\langle d\rangle_V$/nm	90	80	70
$^{LN}\langle d\rangle_n$/nm	40	38	34
$^{MSD}\langle d\rangle_l$/nm	244	185	160
$^{MSD}\langle d\rangle_V$/nm	17	14	11
$^{MSD}\langle d\rangle_n$/nm	9	10	8

Table 6.4(b) Multimode size distribution parameters for 1% (w/w) HUTEAB/PPO192 PUD subjected to filtration.

Measured Parameters	Not filtered	filtered (1 μm)	filtered (0.45 μm) (after 1 μm)
$^{mode1}d_I$/nm	348	250	219
% I	62	66	71
$^{mode2}d_I$/nm	81	75	50
% I	35	30	27
$^{mode3}d_I$/nm	9.8	11.5	8.6
% I	3	4	2
$^{mode1}d_V$/nm	481	250	219
% V	1	<1	<1
$^{mode2}d_V$/nm	69	65	43
% V	4	4	6
$^{mode3}d_V$/nm	8.3	8.8	7.4
% V	95	96	94
$^{mode1}d_n$/nm	481	250	219
% n	<1	<1	<1
$^{mode2}d_n$/nm	69	65	43
% n	<1	<1	<1
$^{mode3}d_n$/nm	8.3	8.8	7.4
% n	100	100	100

6.7 Rheological Observations

PPO192 PUDs at 25% (w/w) and 10% (w/w) showed an increase in viscosity at room temperature if there were no shear applied. However, the 10% HUTEAB/PPO192 PUD did not show any such effect. This difference suggests that there is less interaction between particles based on HUTEAB than those based on $HOC_{11}C_1ImBr$. The cause of this difference is hypothesized to emanate from differences in imidazolium-bromide bonding and hydroxyltriethylamonium-bromide bonding, and in short-range coulombic and dipolar interactions between such cation-anion paired ions.

Figure 6.12. HUTEAB/PPO192 PUD sample (10% w/w) at ambient temperature.

6.8. Stimuli-Responsive Films

A glass slide was coated with 10% (w/w) HUTEAB/PPO192 PUD to form a continuous film by using a small 1" x 1" square drawdown bar using a machined slot providing a wet film thickness of 75 μm. About 70% of this coated slide was dipped in 0.1 *M* KPF_6 solution for 25 min. It could be seen that after 13 min very slight turbidity was evident. Turbidity increased after 25 min in the slide area that was dipped (Fig. 6.13(b)). After 25 min of KPF_6 treatment, a wet slide was completely immersed in DI water, where an untreated portion of slide was seen to disperse and "wash away" from this slide; the treated portion did not separate from the substrate.

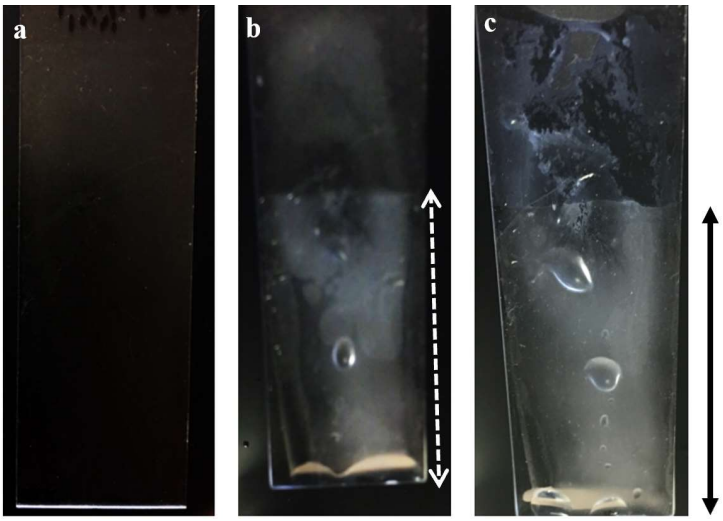

Figure 6.13. Glass slide coated by 10% (w/w) HUTEAB/PPO192 PUD: (a) untreated; (b) after lower 70% area of slide 'a' dipped in 0.1 *M* KPF_6 solution for 25 minutes. This dipped portion became turbid during the treatment; (c) after 'b' completely immersed in DI water, where top 30% area of untreated coating substantially separated from slide and re-dispersed into water; lower 70% of treated coating did not destabilize and separate from slide. Double ended arrow highlights KPF_6 treated portion.

PPO192 PUD, PPO192/Gly PUD, and PPO192/Trigly PUD coatings from Chapter 5, showed higher turbidity after 15 min of immersion in KPF_6 and in DI water after KPF_6 treatment. The mechanical properties of KPF_6 treated HUTEAB/PPO192 PUD coating were weaker than the KPF_6 treated PPO192 PUD coating because KPF_6 treated HUTEAB/PPO192 PUD washed (rubbed) off its slide substrate when rubbed with a water-soaked cheese cloth on a 500-g iron mallet in about three rubs, whereas about ten cycles of rubbing were required to remove a KPF_6 treated PPO192 PUD coating.

Chapter 7

Summary and Potential Applications

7.1 Summary

In a single pot syntheses, $HOC_{11}C_1ImBr$ ionic liquid has been incorporated into polyurethanes as chain terminating groups. This thesis work suggests that PILs made by condensation polymerization can exhibit stimuli responsive properties similar to PILs synthesized by free radical polymerization techniques. Serendipitously, using SEM techniques, it was discovered that PU gels synthesized using glycerol, hexamethylene diisocyanate, and imidazolium bromide ionic liquid chain terminator, have open-cell porous structures without having to be anion exchanged. These PU PIL gels also show stimuli responsiveness and reversible poration in water and DMSO. These gels are polymerized by condensation polymerization and offer seveal advantages over free-radical polymerized gels. Isocyanate–polyol chemistries allow these gels to form rapidly, and such chemistries can also be done on-site. Many of the raw materials used to make PU gels are cheaper then raw materials used for free radical polymerization.

When gels are dipped in 0.1 *M* KPF_6 solution, their decreased segmental solubility, due to more hydrophobic imidazolium-anion pairs involving PF_6^- after exchanging for Br^- ions, causes them to porate and become more highly light scattering and opaque (Fig. 3.11(b)). This solvation induced stimuli responsive phenomenon is analogous to what was seen in free radical polymerized poly($ILPF_6$-co-MMA) gels reported earlier.[43,52] Explanations of this phenomenon were discussed by Yan and Texter, where they stated that spinodal decomposition of hydrophobic species in 3-dimensional phase space of crosslinked polymer gel, a polymer

swelling solvent (for example, DMSO), and a nonsolvent (water), result in formation of the pores. PF_6^- ions condense onto the imidazolium rings after they are exposed to a poor solvent (water), thus causing individual and proximal copolymeric chains to condense upon themselves.[43] However, condensation polymerized systems described in this thesis work differ from those radical chain polymerized systems[43,52] in an important aspect. This condensation polymerized system, with imidazolium-Br^- ion pairs, is fundamentally more hydrophobic and can form pores on polymerization without anion exchange by PF_6^-.

DSC of the gels synthesized in this work showed melting and crystallization peaks below apparent T_gs. These peaks are assigned to separated phases of DBTD catalyst in the polymer matrix. It was found that some amount of catalyst strongly binds to the polymer matrix and dissolves in this matrix, losing its liquid phase identity. Experimentation showed that DBTL partitioning between its liquid phase and PU matrices follows a classical chemical equilibration model. Increasing amounts of DBTD drives increasing amounts of dissolved DBTL, in a ratio called swell ratio. Soxhlet extraction can remove dissolved and undissolved DBTD from these PU matrices. Effects of chemical annealing through soxhlet extraction, and effects of prolonged and high heat treatments were seen to increase the T_gs of PUs.

Incorporation of $HOC_{11}C_1ImBr$ IL into polyurethanes also provides hydrophilic sites to tune water interactions. These materials also exhibit properties of self-dispersion in water to form PUDs. These self-dispersing particles arguably form thermodynamically stable nanoparticles. Such PUDs comprise particles and aggregates of varying size, that can either be filtered or can be separated under further activation (sonication) to form sub-micron to sub-100-nm dispersions that are stable. Several stimuli-responsive characteristics of these dispersions and coatings appear similar to those reported for nanolatexes,[47] coatings of nanolatexes,[47] and of dispersions of

various materials stabilized by ionic liquid-based nanolatexes and triblock copolymers.[56,57] PEO-based dispersions produce water loving coatings and may offer new opportunities for hydrogel chemical delivery in medical applications. PO-based ($HO(PO)_3H$) coatings exhibit greater intrinsic water resistance. Both types of coatings (PEO- and PPO-based) exhibit stimuli responsiveness, where wetting and contact angles can be tuned by anion exchange. These coatings can be made resistant to redispersing in water after anion exchange by various anions like PF_6^-, $CF_3SO_3^-$, $N(CN)_2^-$, BF_4^-, and I^-. These PUDs also show gellation at room temperature without any shear and can flow after shear thinning or at elevated temperatures after melting. PPO-based coatings treated by anions also show stimuli responses to water with reversible porosity, where they become turbid when in contact with water and become clear after water is removed.

Another quaternary salt, HUTEAB, was examined as a control monofunctional monomer material in PUD synthesis, and it was not anticipated that it would exhibit features demonstrated earlier in this work by $HOC_{11}C_1ImBr$. This monomer also has a melting point below 100 °C, which defines it as an ionic liquid. A PIL resin made with HUTEAB, also showed self dispersion of particles in water to form a thermodynamically stable sub-micron to sub-100-nm dispersion. Coating made with this PUD also became resistant to re-dispersion in water after a treatment by 0.1 *M* KPF_6 solution. However, anion binding with hydroxyundecyltriethylammonium is fundamentaly different than with imidazolium groups because the former lacks any kind of π bonding.

These two-step processes of single pot synthesis followed by desolvation to make 100% resin materials reduce the number of processes involved in making PUDs. These materials can

be transported as 100% solid resin materials, and then PUDs can be formed onsite by addition of water. This reduces the transportation costs and makes handling of these materials safer.

7.2 Potential Applications

New class of stimuli-resonsive reversible porating microporous gels can have many diverse applications in various industries, including filtration, tissue scaffolding, bicontinuous materials templating, antimicrobial filtration, and fire-resistant foams. Solvent induced reversible swelling and shrinking properties of these gels can be used to make chemical detectors. Rapid crosslinking chemistry of PU using isocynates allow these gels to be made on-site cheaply.

PUDs made in this thesis could find applications in multiple industrial sectors. The stimuli responsive character of the PUDs can be harnessed in many existing products, such as in nanocarbon dispersions of MWCNTs and graphene. Nanolatexes prepared from microemulsion polymerization have excellent properties to produce concentrated nanocarbon dispersions of MWCNTs. Moreover, new types of nanocomposites can be prepared by controlling the level of stimuli responsive dispersion in it. The PUDs synthesized in this research are expected to show similar results and preliminary results have also shown facilitated formation of graphene in water dispersions at 1% (w/w) graphene in water. Similarly, an important application is to use this stimuli responsive anion destabilization of aqueous dispersions that can be restabilized in nonaqueous suspensions, such as n reactive monomers for formulating nanocomposites. By imbibing actives for local delivery, these PUDs could also be used to develop coatings for drug delivery systems.[58] These PUDs can also be used to disperse pigments which can be used in waterborne coatings including electrodeposition coatings.[38]

Another application where stimuli responsive properties of PUDs can be harnessed is in tuning hydrophobicity and surface energy of coatings by selective anion exchange. These

hydrophobic coatings can be used for masking applications where they can control relief imaging and be resistant to flowing water streams. Adhesion to anionic substrates is increased with the help of cations present in the coating and can be improved by having small particle sizes to facilitate penetration into substrates.

Such coatings can also behave as antistatic materials when ionic pairs in the resin are used to provide ionic conductivity. Anticorrosion coatings for steel and electrically conducting composites can be prepared by blending cationic PUDs with polyaniline.[59] The anion exchange property of these PUDs can be a promising approach for making new developments in phosphate pretreatments for steel in combatting corrosion.

Cationic PUDs can behave as new catalytic systems. Cationic PUDs stabilized by alkylammonium acetate groups can be used as catalysts for synthesizing 3-imidazo[1,2-*a*]pyridines. A condensation reaction is carried out between 2-amino-pyridines, benzaldehydes, and isocyanides in water to yield the mentioned pyridine product.[60] Since imidazolium has diverse catalytic activities, such PUDs can be expected to be stable and tunable in both aqueous and non-aqueous solvents.

Many research groups have shown that cationic polyurethanes can possess antibacterial properties by disrupting bacterial membranes as a result of electrostatic interaction between positively charged PUDs and negatively charged bacteria.[61,62,63] Similar behavior can be expected for resins conatining ionic liquids with ion pairs. Since cationic polymers are known to be used as nonviral carriers that carry a gene into cell nuclei forming complexes with DNA for gene transfection (gene therapy),[61] ionic liquids containing cationic PUDs are also likely to function as gene delivery carriers.

The measured destabilization seen in section 5.7.1 can prove to be a potential application of this stimuli responsive property of these PUDs. The state of anion exchange in PUDs can be modified to control the shift in distribution of attractive and repulsive interparticle potential interactions. This anion exchange is finally related to the aggregate size and composition of a PUD. Such interactions help in developing new models of steric and charge stabilization in different solvents, as they increase the number of variable degrees of freedom. Intrinsic charges can now be varied using imidazolium-anion pairs and its stimuli responsive property, which was earlier possible only using the pH effects and ion exchange of "hard" ions such as halide and alkali ions. These materials can also be used in water treatment plants where they can interact with various particles and can be destablized by addition of salt that causes agglomeration and settlement of impurities along with the polymer particles.

UV curable PUDs can be made using these IL containing resins if acrylic groups are incorporated in the polyols during PUD formulation. Du et al. have reported preparing UV curable films by modifying PUD chains with methacrylate functionality.[64] New functional coatings and monolithic solids can be explored by incorporating appropriate acrylate functionality in PUDs. One such application that can be investigated is fabrication of stimli-responsive photonic crystals, where sacrificial templates of monodisperse beads form an inverse opal structure and cross-linked PUDs form the continuous phase.[65]

We have been able to obtain solids contents in a range of 25%-30% (w/w) for these self dispersing PUDs which are comparable to the solids content of commercially available PUDs.[66] These PUDs have shown formation of gels that have reversible thinning and thickening mechanisms based on shear stress and temperature. Gel formation is due to strong interparticle interactions as a result of short interparticle distances. This property can be used to make

rheology modifiers in waterborne coatings. Self-dispersion of these 100% resin materials in water allows them to be transported as 100% solid resin materials, and up to 25% w/w PUDs can be formed onsite by addition of water under slight mechanical conditions.

References

1. Engels, H.W.; Pirkl, H.G.; Albers, R.; Albach, R.W.; Krause, J.; Hoffmann, A.; Casselmann, H.; Dormish, J. Polyurethanes: Versatile Materials and Sustainable Problem Solvers for Today's Challenges. *Agew. Chem. Int. Ed.* **2013**, 52, 9422–9441.
2. Jelle, B.P. Traditional, state-of-the-art and future thermal building insulation materials and solutions–Properties, requirements and possibilities. *Energy Buildings* **2011**, *43*, 2549-2563.
3. Chatzistergos, P.E.; Naemi, R.; Healy, A.; Gerth, P.; Chockalingam, N. Subject Specific Optimisation of the Stiffness of Footwear Material for Maximum Plantar Pressure Reduction. *Ann. Biomed. Eng*. **2017**, *45*, 1929-1940.
4. Tang, X.N.; Yan, X. Acoustic energy absorption properties of fibrous materials: A review. *Compos Part A Appl Sci Man*u. **2017**, *101*, 360-380.
5. Gonzalez, M.N.G.; Levi, M.; Turri, S. Development of polyester binders for the production of sustainable polyurethane coatings: Technological characterization and life cycle assessment. *J. Cleaner Production* **2017**, *164*, 171-178.
6. Sbegue, L.F.C.; Villar, L.D. *J.* Comparative Assessment of Stabilised Polybutadiene Binder under Accelerated Ageing. *Aerosp. Technol. Manag.* **2016**, *8*, 122-129.
7. Vallat, M.F.; Bessaha, N.; Schultz, J.; Maucourt, J.; Combette, C. Adhesive behavior of polyurethane-based materials. *J. Appl. Polym. Sci*. **2000**, *76*, 665-671.
8. Meng, H.; Li, G.Q. A review of stimuli-responsive shape memory polymer composites. *Polymer* **2013**, *54*, 2199-2221.

9. Scrinzi, E.; Rossi, S.; Deflorian, F.; Zanella, C. Evaluation of Aesthetic Durability of Waterborne Polyurethane Coatings Applied on Wood for Interior Applications. *Prog. Org. Coating* **2011**, *72*, 81-87.

10. Kauser, A. Polyurethane Composite Foams in High-Performance Applications: A Review. *Polym. Plastics Tech. Eng*. **2018**, *57*, 346-369.

11. Hill, L.W.; Prince, D.E. Waterborne Polymers for Aircraft Coatings. *ACS Symp. Ser.*: Washington, DC, **1980**, 83-104.

12. Ekin, A., Webster, D.C., Daniels, J.W. Synthesis, formulation, and characterization of siloxane–polyurethane coatings for underwater marine applications using combinatorial high-throughput experimentation. *J. Coat. Technol. Res.* **2007**, *4* (4), 435-451.

13. Akindoyo, J.C.; Beg, D.H.; Ghazali, S.; Islam, M.R.; Jeyaratnam, N.; Ar, Y. Polyurethane types, synthesis and applications - A review. *RSC Adv.*, **2016**, *6*, 114453–114482.

14. Volkova, E.R.; Tereshatov, V.V.; Karmanov, V.I. Kinetics of reactions occurring during polyurethane synthesis. *J. Appl. Spectrosc.* **2010**, 77, 5, 737-740.

15. Wicks, Z.W.; Jones, F.N.; Pappas, S.P.; Wicks, D.A. *Organic Coatings Science and Technology*, third edition; John Wiley & Sons, Inc., Hoboken, New Jersey, **2007**.

16. Kinetics of polyurethane formation. http://shodhganga.inflibnet.ac.in/bitstream/10603/58661/9/09_chapter%203.pdf (accessed 2 November, 2018).

17. Rajput, S.D.; Mahulikar, P.P.; Gite, V.V. Biobased dimer fatty acid containing two pack polyurethane for wood finished coatings. *Prog. Org. Coating* **2014**, *77*, 38-46.

18. Carlson, G. M.; et al. FT-IR and thermal-mechanical cure characterization of blocked isocyanate containing coatings. *Polym. Sci. Technol.* **1987**, *36*, 197.

19. Blank, W. J.; et al. Catalysis of blocked isocyanates with non-tin catalysts. *Polym. Mater. Sci. Eng.* **1998**, *79*, 399-400.

20. Zhiqiang, H.; Blank, W.J.; Picci, M.E. Catalyzing cationic resin and blocked polyisocyanate with bismuth carboxylate. US. Patent 6,353,057 B1, March 5, 2002.

21. Rath, S.K.; Patri, M.; Khakhar, D.V. Structure–thermomechanical property correlation of moisture cured poly(urethane-urea)/clay nanocomposite coatings. *Prog. Org. Coating* **2012**, *75*, 264-273.

22. Athawale, V.D.; Kulkarni, M.A. Polyester polyols for waterborne polyurethanes and hybrid dispersions. *Prog. Org. Coating* **2010**, *67*, 44-54.

23. Leitsch, E.K.; Beniah, G.; Liu, K.; Lan, T.; Heath, W.H.; Scheidt, K.A.; Torkelson, J.M. Nonisocyanate Thermoplastic Polyhydroxyurethane Elastomers via Cyclic Carbonate Aminolysis: Critical Role of Hydroxyl Groups in Controlling Nanophase Separation. *ACS Macro Letters* **2016,** *5*, 4, 424-429.

24. Krol, P. Synthesis methods, chemical structures and phase structures of linear polyurethanes. Properties and applications of linear polyurethanes in polyurethane elastomers, copolymers and ionomers. *Prog Mater Sci.* **2007**; *52* (6), 915-1015.

25. Klinedinst, D.B.; Yilgör, I.; Yilgör, E.; Zhang,M.; Wilkes,G.L. The effect of varying soft and hard segment length on the structure–property relationships of segmented polyurethanes based on a linear symmetric diisocyanate, 1,4-butanediol and PTMO soft segments. *Polymer* **2012**, *53*, 5358-5366.

26. Salanti, A.; Zoia, L.; Mauri, M.; Orlandi, M. Utilization of cyclocarbonated lignin as a bio-based cross-linker for the preparation of poly(hydroxy urethane)s. *RSC Adv.* **2017**, *7* (40), 25054-25065.

27. Beniah, G.; Uno, B.E.; Lan, T.; Jeon, J.H.; Heath, W.H.; Scheidt, K.A.; Torkelson, J.M. Tuning nanophase separation behavior in segmented polyhydroxyurethane via judicious choice of soft segment. *Polymer* **2017**, *110*, 218-227.

28. Mishra, A.; Aswal, V.K.; Maiti, P. *J.* Nanostructure to Microstructure Self-Assembly of Aliphatic Polyurethanes: The Effect on Mechanical Properties. *Phys. Chem.* **2010**, *114*, 5292-5300.

29. Aerospace and Aircraft Coatings. https://www.astm.org/DIGITAL_LIBRARY/MNL/PAGES/MNL12239M.htm (accessed 5 January 2019).

30. DSM Coating Resins, 2011, Carbon footprint study for industrial coatings applied on a metal substrate focus on powder coatings. https://www.dsm.com/content/dam/dsm/furniture/en_US/documents/20.-dsm-carbon-footprint-%20-disclaimer.pdf (accessed 28 January 2018).

31. Nelson, A. M.; Synthesis, Properties, and Applications of Ion-Containing Polyurethane Segmented Copolymers. Long, T. E. *Macromol. Chem. Phys*. **2014**, *215*, 2161−2174.

32. Howarth, G.A. Polyurethanes, polyurethane dispersions and polyureas: Past, present and future. *Surf. Coatings Int. B Coatings Trans*. **2003**, *86*, 111-118.

33. Duan, Y.; Sonja Stammler, S. Reduced solvent process for preparation of aqueous polyurethane dispersions with improved heat-and water resistance. U.S. Patent 5,637,639, June 10, 1997.

34. Fernandes, I.P.; Costa, M.R.P.F.N.; Ferreira, M.J.; Barreiro, M.F. Water-based poly(urethane-urea) dispersions — meeting the European Union legislation. *Polymery* **2015,** *60*, 536-540.

35. Najafi, F.; Manouchehri, F.; Shaabanzadeh, M. Synthesis and Characterization of Anionic Polyester-Polyurethane Dispersion as Environmentally-Friendly Water Based Resins. *J. Chem. Health Saf.* **2011**, 23–26.

36. Howarth, G. A.; Manock, H. L. Water-borne polyurethane dispersions and their use in functional coatings. *Surface Coatings International* **1997**, *80,*7, 324–328.

37. Lubnin, A.V.; Malaba, D.N. Aqueous cationic polyurethane dispersions. U.S. Patent 0072728 A1, 2017.

38. Nakajima, Y.; Yukawa, Y.; Kamimori, I.; Yamanouchi, A.; Hoshida,Y. Resin for pigment dispersion. U.S. Patent 7,026,392, 2006.

39. Schimmel, K.F.; Pierce, P.E.; Jones, J.E. Novel pigment paste for cationic electrodeposition. U.S. Patent 4,007,154, 1997.

40. Welton, T. Room-temperature ionic liquids. Solvents for synthesis and catalysis. *Chem. Rev.* **1999**, *99*, 2071–2084.

41. Anderson, J.; Armatrong, D.; Wei, G. Ionic Liquids in Analytical Chemistry. *Anal. Chemistry* **2006**, 2893-2902.

42. Lu, J.; Yan, F.; Texter, J. Advanced applications of ionic liquids in polymer science. *Prog. Polym. Sci*. **2009**, *34*, 431–448.

43. Gu, H. Materials and Coatings Derived from the Polymerizable Ionic Liquid Surfactants 1-(2-Acryloyloxyundecyl)-3-methylimidazolium Tetrafluoroborate and 1-(2-Acryloyloxyundecyl)-3-methylimidazolium 2-acrylamido-2-methyl-propylsulfonate. Master's Thesis, Eastern Michigan University, Ypsilati,MI (USA), August 2009. http://commons.emich.edu/theses/239 (accessed 28 January 2018).

44. Gu, H.; Yan, F.; Texter, J. Polymerized Paired Ions as Polymeric Ionic Liquid–Proton Conductivity. *Macromol. Rap. Commun.* **2016**, *37*, 1218-1225.

45. Zhou, Y.; Qiu, L.; Deng, Z.; Texter, J.; Yan, F. Low-temperature AGET ATRP of methyl methacrylate in ionic liquid-based microemulsions. *Macromolecules* **2011**, *44,* 7948–7955.

46. Qian, W.J.; Yan, F.; Texter, J. Frontiers in poly(ionic liquid)s: Syntheses and applications. *Chem. Soc. Rev.* **2017**, *46*, 1124–1159.

47. England, D.; Tambe, N.; Texter, J. Stimuli-responsive nanolatexes - Porating films. *ACS Macro Lett.* **2012**, *1*, 310–314.

48. Texter, J. Anion responsive imidazolium-based polymers. *Macromol. Rap. Commun.* **2012**, *33***,** 1996-–2014.

49. Yan, F.; Texter, J. Surfactant ionic liquid-based microemulsions for polymerization. *Chem. Commun.* **2006**, 2696-2698.

50. England, D. Materials and Coatings Derived from the Polymerizable Ionic Liquid Surfactant 1-(2-Acryloyloxyundecyl)-3-methylimidazolium Bromide. Master's Thesis, Eastern Michigan University, Ypsilanti, MI, Aug 2008. https://commons.emich.edu/theses/159 (accessed 28 January 2018).

51. England, D; Yan, F; Texter, J. Porating Anion-Responsive Copolymeric Gels. *Langmuir* **2013**, *29*, 12013-12024.

52. Yan, F.; Texter, J. Solvent-reversible poration in ionic liquid copolymers. *Angew. Chem. Int. Ed.* **2007**, *46*, 2440–2443.

53. DropSnake 2.1, contact angle measurement. https://vimeo.com/12449610 (accessed 15 April 2018).

54. Wang, Y.; Li, H.; Wu,T.; Wang,C.; Han,S. Reaction mechanism study for the synthesis of alkylimidazolium-based halide ionic liquids. *Acta Phys. Chim. Sin.* **2005**, *21* (5), 517-522.

55. Dibutyltin dilaurate. https://www.americanelements.com/dibutyltin-dilaurate-77-58-7 (accessed February 28, 2019).

56. Texter, J.; Ager, D.; Vasantha, V.A.; Crombez, R.; England, D.; Ma, X.; Maniglia, R.; Tambe, N. Advanced Nanocarbon Materials Facilitated by Novel Stimuli-responsive Stabilizers. *Chem. Lett.* **2012**, *41*, 1377-1379.

57. Ager, D.; Vasantha, V.A.; Crombez, R.; Texter, J. Aqueous Graphene Dispersions–Optical Properties and Stimuli-Responsive Phase Transfer. *ACS Nano* **2014**, *8*, 11191-11205.

58. Texter, J.; Qiu, Z.M.; Crombez, R.; Shen, W. Nanofluid Polyurethane/Polyurea Resins–Thin Films and Clearcoats. *J. Poly. Sci. A. Poly. Sci.* **2013,** *51*, 3439-3448.

59. Gurunathan, T.; Rao, C.R.K.; Narayan, R.; Raju, K.V.S.N. Synthesis, characterization and corrosion evaluation on new cationomeric polyurethane water dispersions and their polyaniline composites. *Prog. Org. Coat.* **2013**, *76*, 639–647.

60. Daemi, H.; Rad, R.R.; Barikani, M.; Adib, M. Catalytic activity of aqueous cationic polyurethane dispersions: A novel feature of polyurethanes. *Appl. Catal. A Gen*., **2013**, *468*, 10-17.

61. Wu, G.H.; Hsu S.H. Synthesis of water-based cationic polyurethane for antibacterial and gene delivery applications. *Colloids Surf.,B.* **2016**, *146*, 825–832.

62. Chen, F.; Hehl, J.; Su, Y.; Mattheis, C.; Greinerb, A.; Agarwal. Smart secondary polyurethane dispersions. *Polym Int.* **2013**, *62*, 1750–1757.

63. Garrison,T.F.; Zhang, Z.; Kim, H.J.; Mitra, D.; Xia, Y.; Pfister, D.P.; Brehm-Stecher, B.F.; Larock, R.C.; Kessler, M.R. Thermo-mechanical and antibacterial properties of soybean oil-based cationic polyurethane coatings: Effects of amine ratio and degree of crosslinking. *Macromol. Mater. Eng*. **2014**, *299*, 1042-1051.

64. Du, S.; Wang, Y.Y.; Zhang, C.X.; Deng, X.L.; Luo, X.H.; Fu, Y.X.; Liu, Y.L. Self-antibacterial UV-curable waterborne polyurethane with pendant amine and modified by guanidinoacetic acid. *J. Mater. Sci*. **2018**, *53*, 215-229.

65. Texter, J. Polymer colloids in photonic materials. *Comptes Rend. Chimie* **2003**, *6*, 1425-1433.

66. Dimmers, M. **2016**, Alberdingk Boley, New acrylics and polyurethanes for industrial wood finishing. https://www.ramspec.eu/wp-content/uploads/2016/10/5_Alberdingk.pdf (accessed 8 September 2018).

Appendix A: Supplementary Information for Chapter 2

Figure A.2.1 Fisher Scientific vibratory Stirrer used to stir samples in this thesis work.

Figure A.2.2. Setup while sonicating samples used in this thesis work.

Appendix B: Supplementary Information for Chapter 3

Fig. A.3.1 to Fig. A.3.4 are the analyses of DSC curves used in Chapter 3. These analyses were done by using TA Instrument's Universal Analysis software.

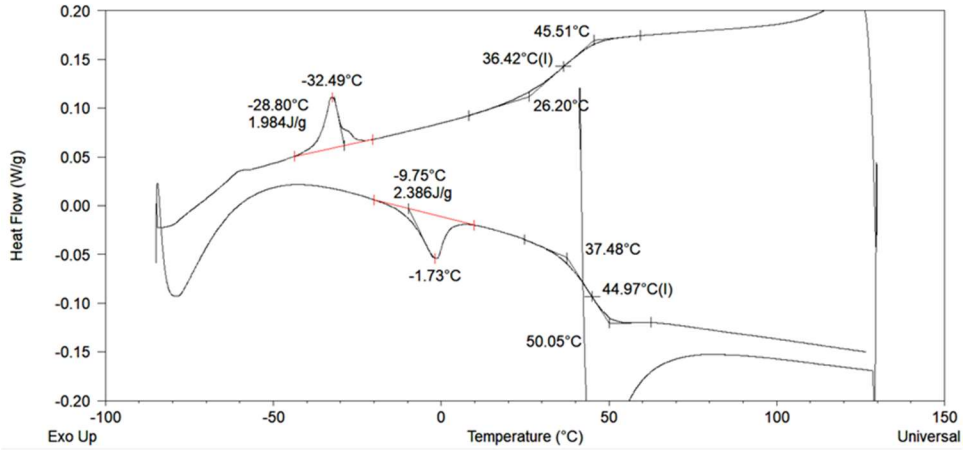

Figure. A.3.1. Analysis of DSC rate of 10 °C/min of $HOC_{11}C_1ImBr$ PU1.

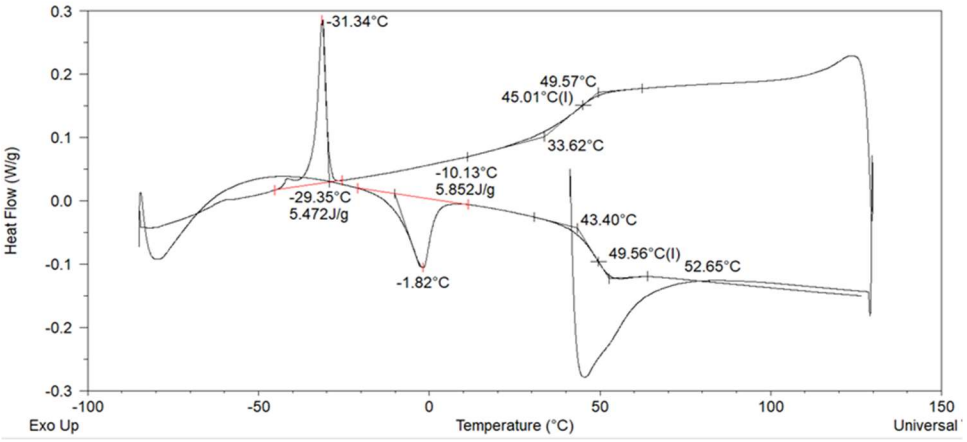

Figure. A.3.2. Analysis of DSC at rate of 10 °C/min of control PU1.

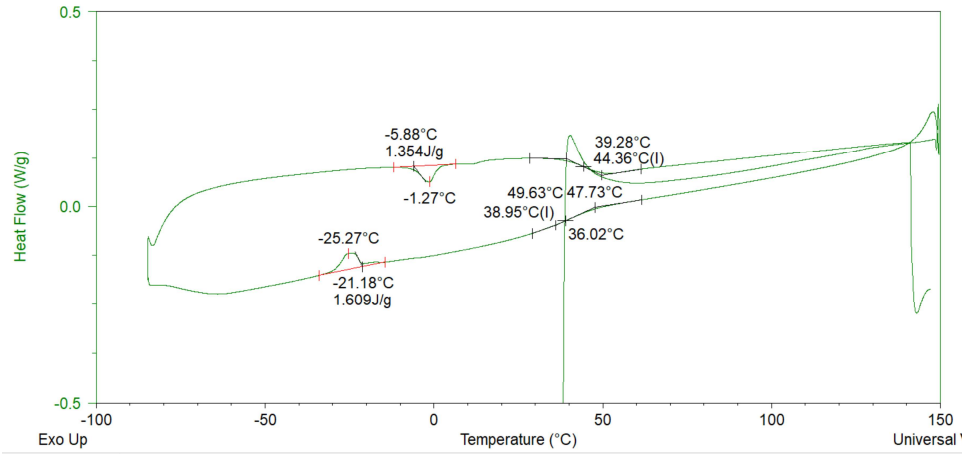

Figure. A.3.3. Analysis of DSC rate of 10 °C/min of $HOC_{11}C_1ImBr$ PU2.

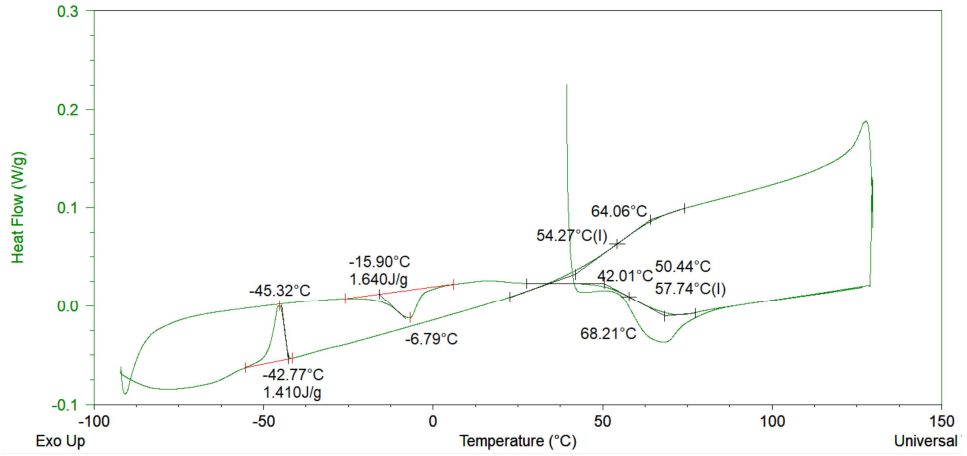

Figure. A.3.4. Analysis of DSC at rate of 10 °C/min of control PU2.

Appendix C: Supplementary Information for Chapter 4

All figures in this appendix are analyses of DSC curves by using TA Instrument's "Universal Analysis" software.

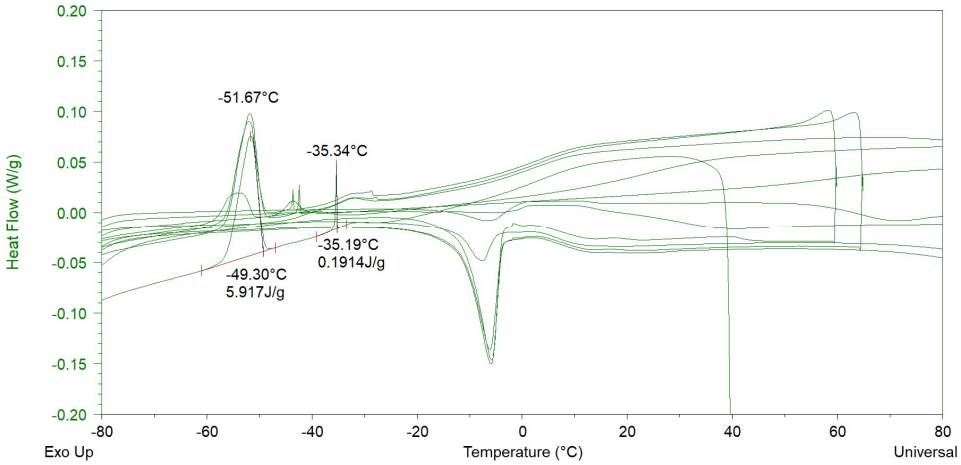

Figure A.4.1. Analysis of freezing events during cooling in 1st cycle of DSC of control PU2.

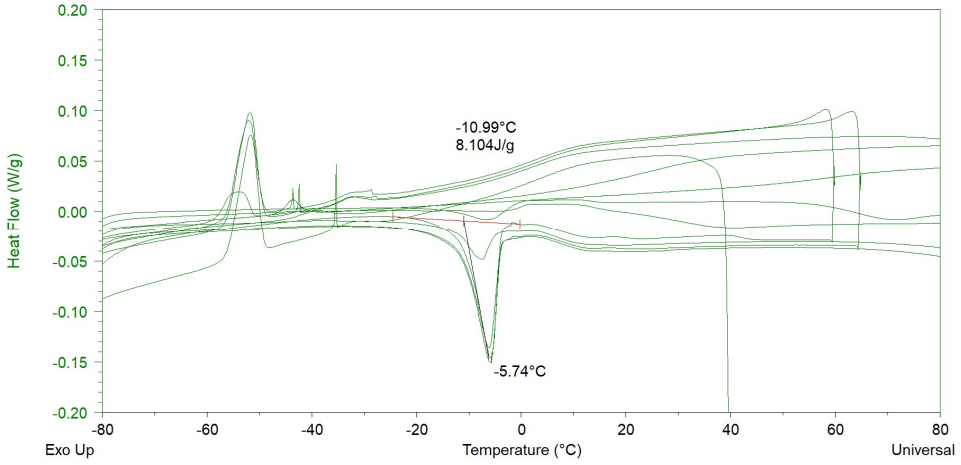

Figure A.4.2. Analysis of melting event during heating in 1st cycle of DSC of control PU2.

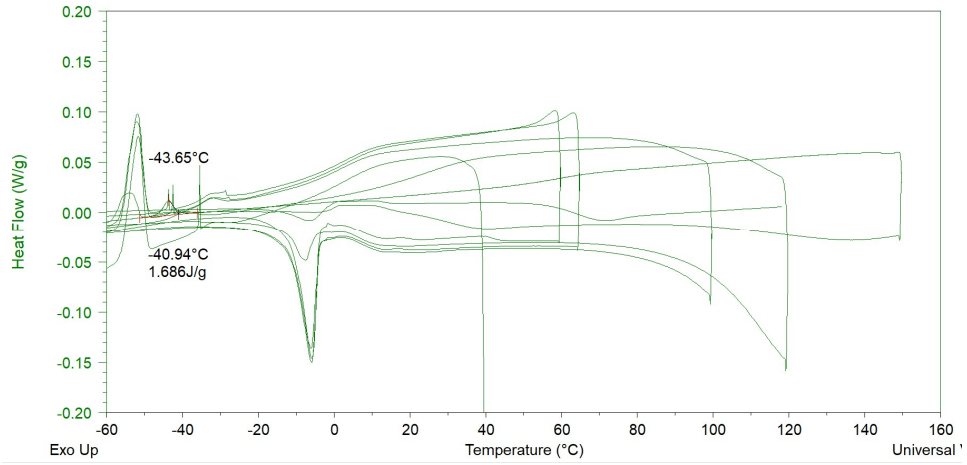

Figure A.4.3. Analysis of freezing event during cooling in 6th cycle of DSC of control PU2.

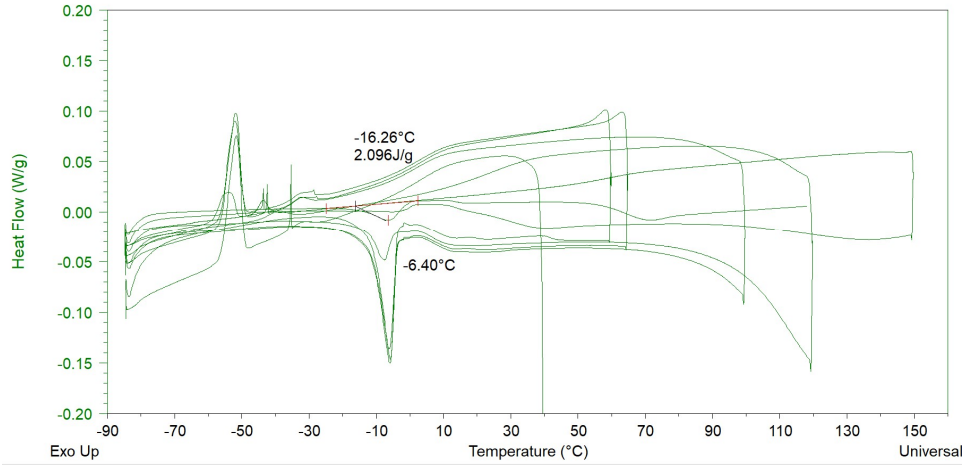

Figure A.4.4. Analysis of melting event during heating in 6th cycle of DSC of control PU2.

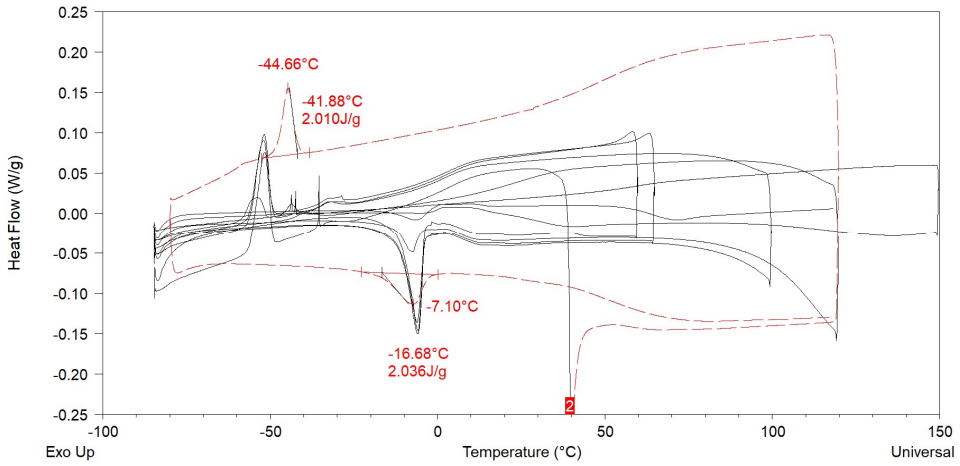

Figure A.4.5. Overlay comparison of DSC of water saturated control PU2 (scan rate 5 °C/min) (———) and vacuum dried control PU2 (10 °C/min) (– – – –).

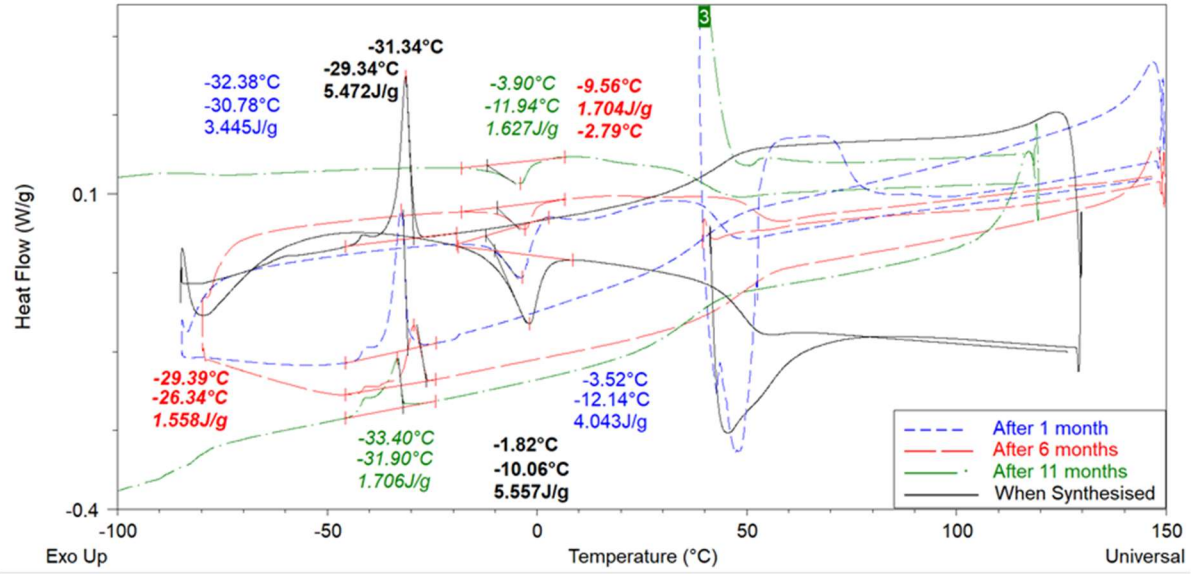

Figure A.4.6. DSC comparison of control PU1 at different periods of aging time.

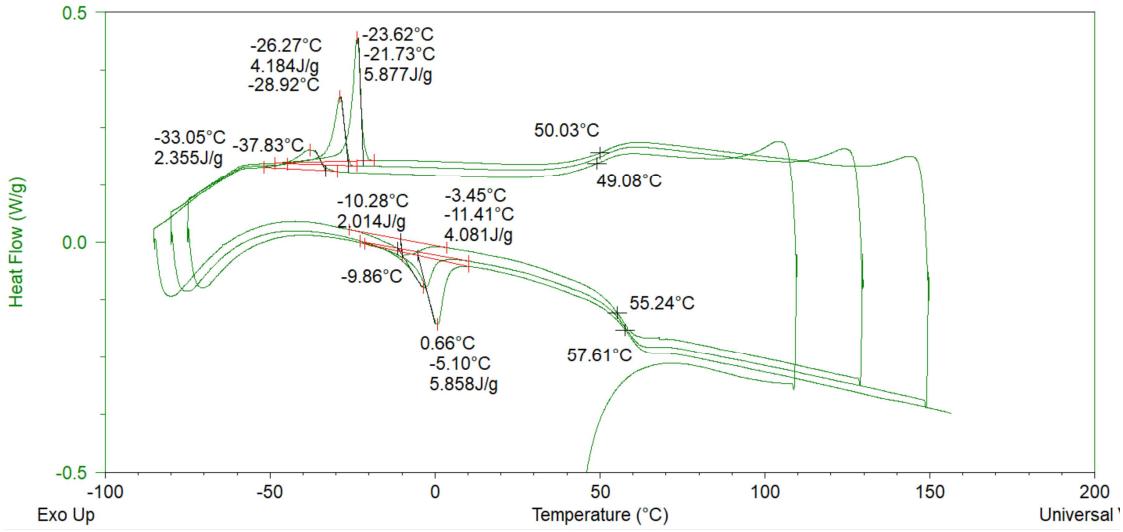

Figure A.4.7. DSC comparison of 16-month-aged control PU1. Sample was heated in vacuum oven at 130 °C for 2 hours before doing DSC at rate of 10 °C/min.

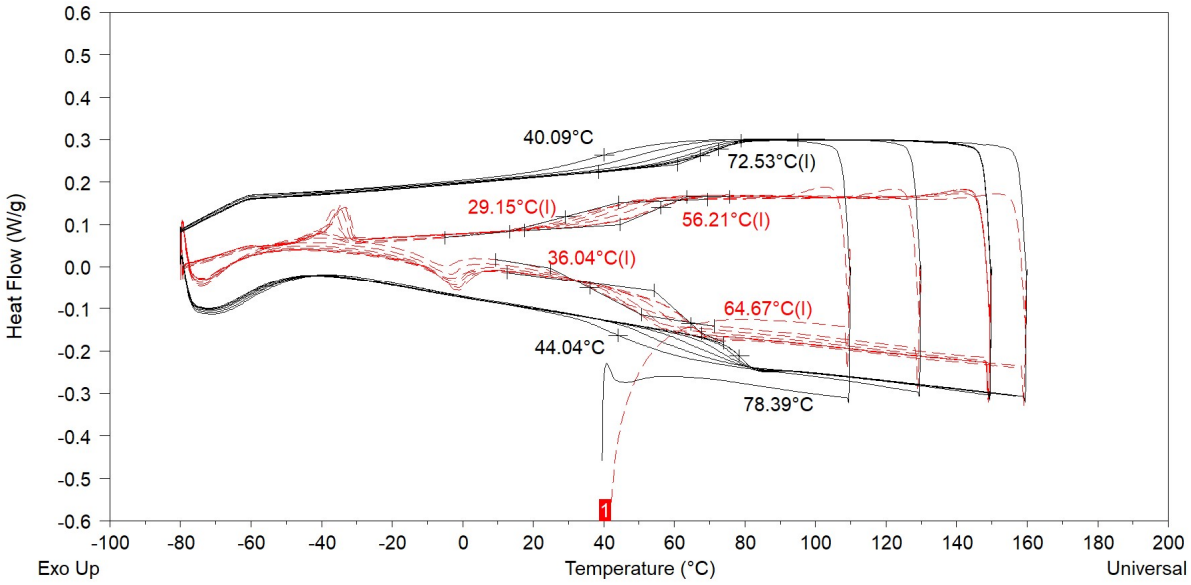

Figure A.4.8. DSC of PU3 having 10% catalyst: before soxhlet extraction (– – –); after soxhlet extraction (——).

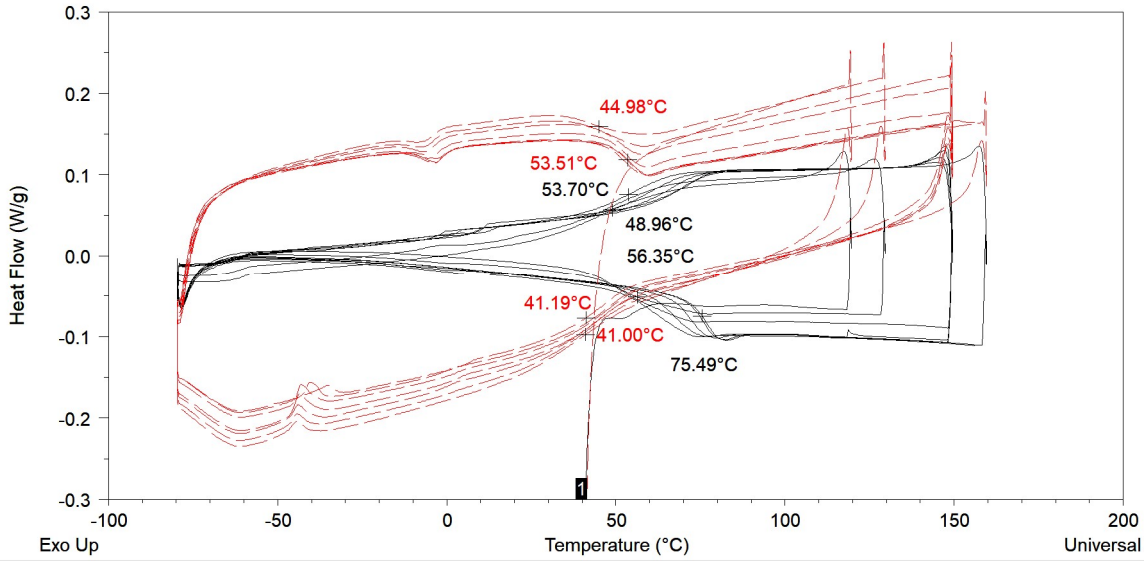

Figure A.4.9. DSC of 7 months aged PU4 having 5.6% catalyst: before soxhlet extraction (– – –); after soxhlet extraction (——).

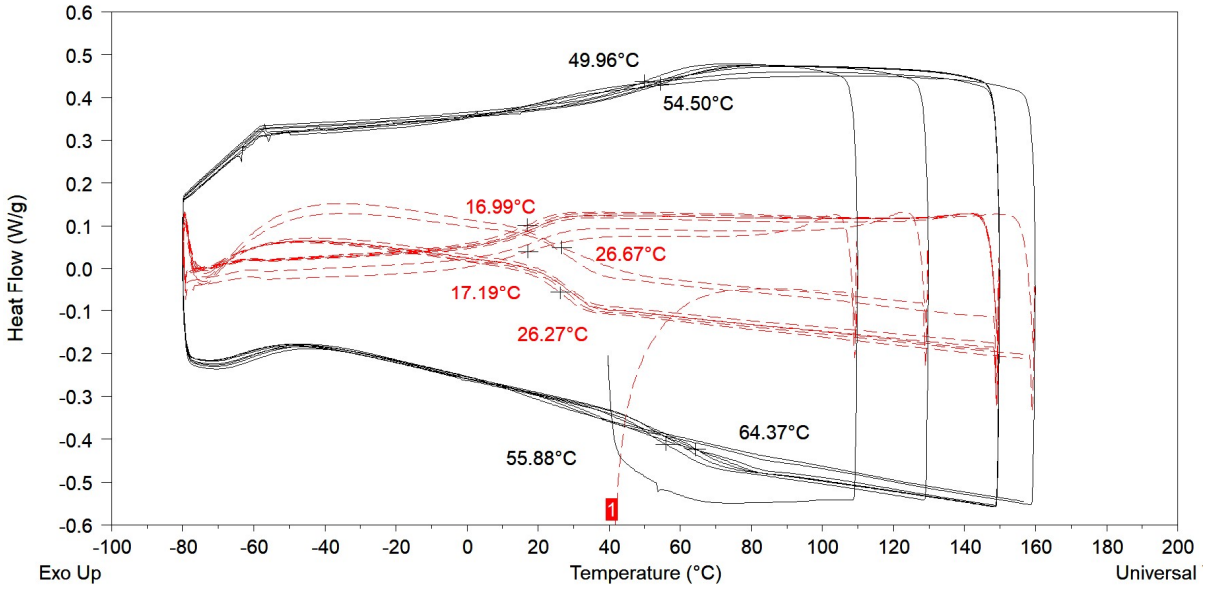

Figure A.4.10. DSC of PU5 having 3% catalyst: before soxhlet extraction (– – –); after soxhlet extraction (——).

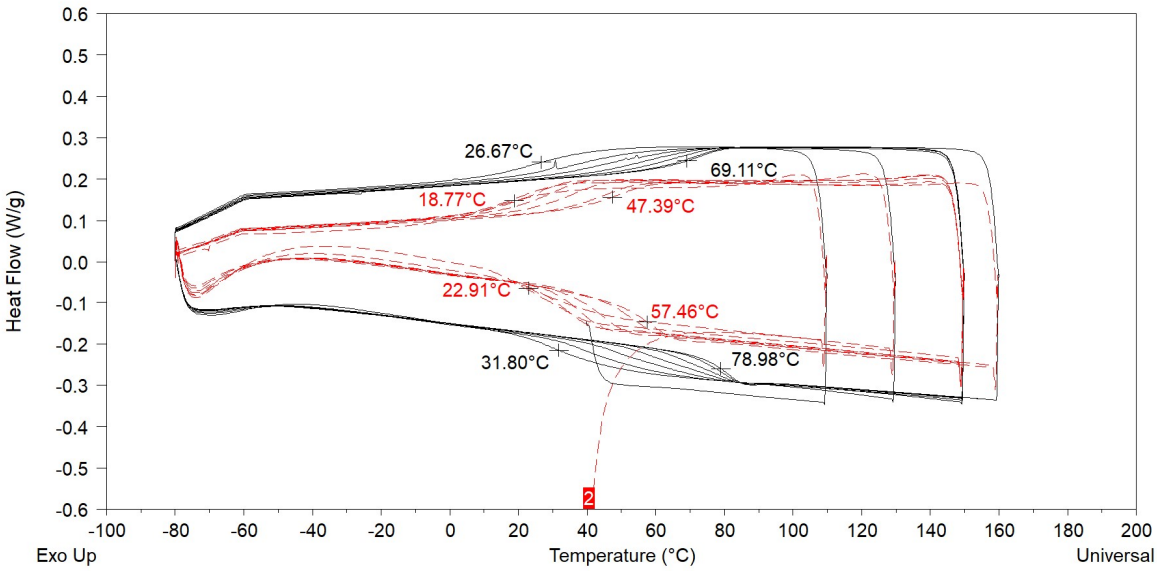

Figure A.4.11. DSC of PU6 having 1% catalyst: before soxhlet extraction (– – –); after soxhlet extraction (——).

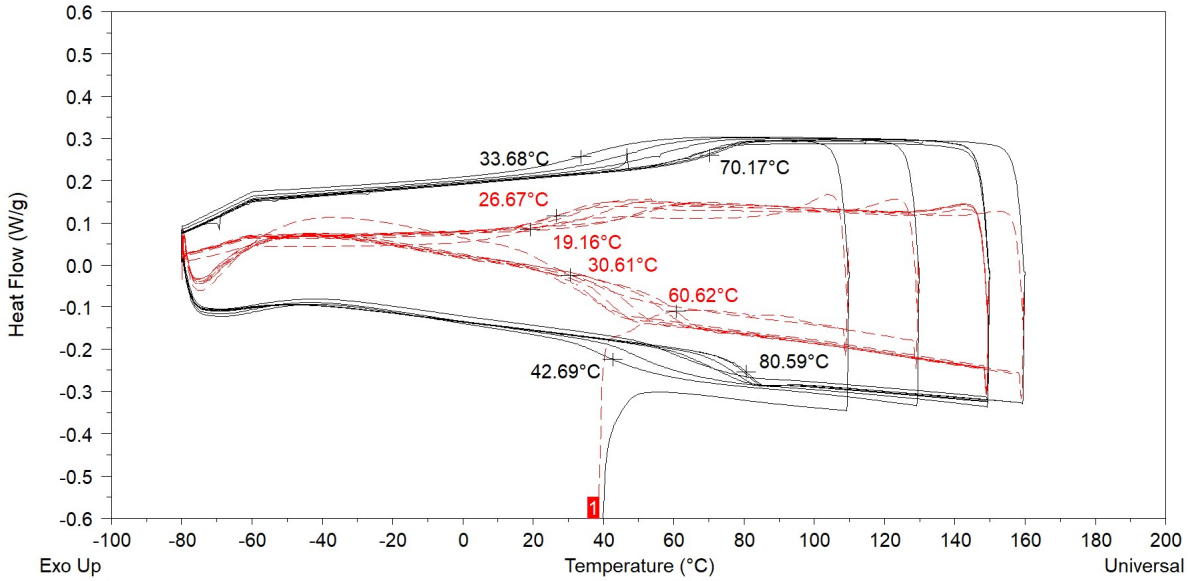

Figure A.4.12. DSC of PU7 having 0.3% catalyst: before soxhlet extraction (– – –); after soxhlet extraction (——).

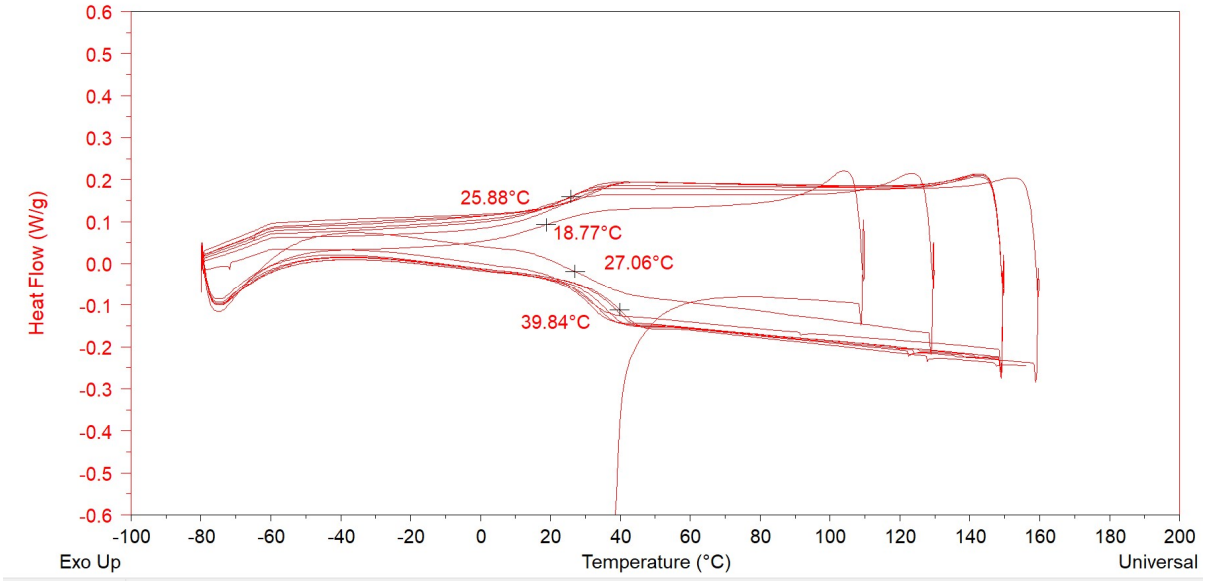

Figure A.4.13. DSC of PU8 having 0.1% catalyst without soxhlet extraction.

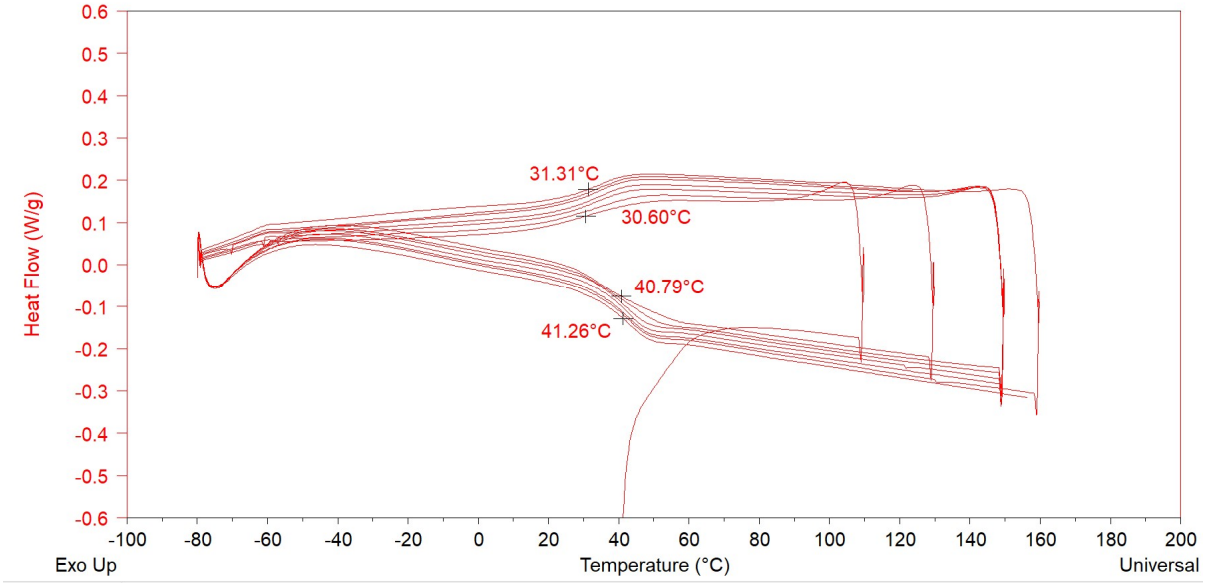

Figure A.4.14. DSC of PU9 having no catalyst without soxhlet extraction.

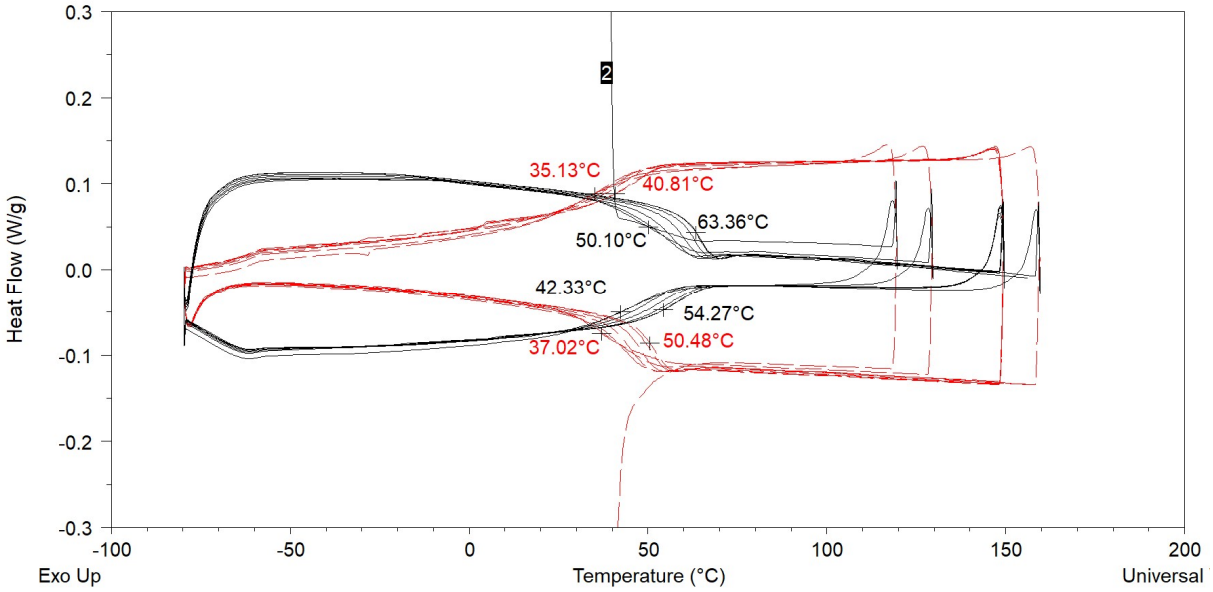

Figure A.4.15. DSC of 7 months aged PU9 having no catalyst: before soxhlet extraction (– – –); after soxhlet extraction (——).

Appendix D: Supplementary Information for Chapter 5

Figure A.5.1 shows flowing of heated 100% solid resin samples after they were removed from vacuum oven. Figure A.5.2 to Fig. A.5.6 are analyses of DSC curves by using TA Instrument's "Universal Analysis" software.

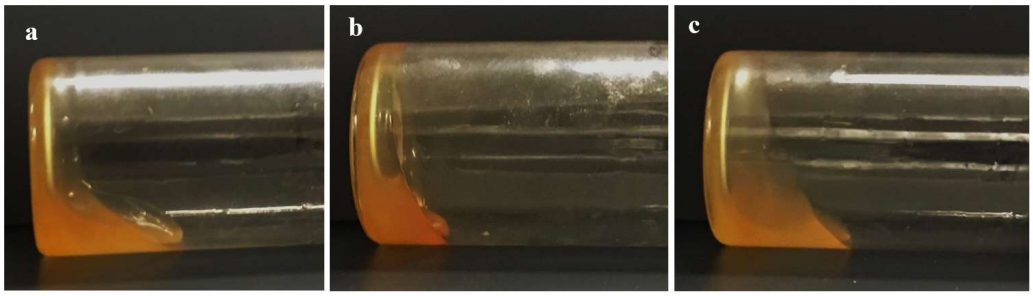

Figure A.5.1. Resins flowing as viscous liquids when heated to 60 ºC: (a) PEO200/Gly PU; (b) PPO192/Gly PU (c) PEO200 PU

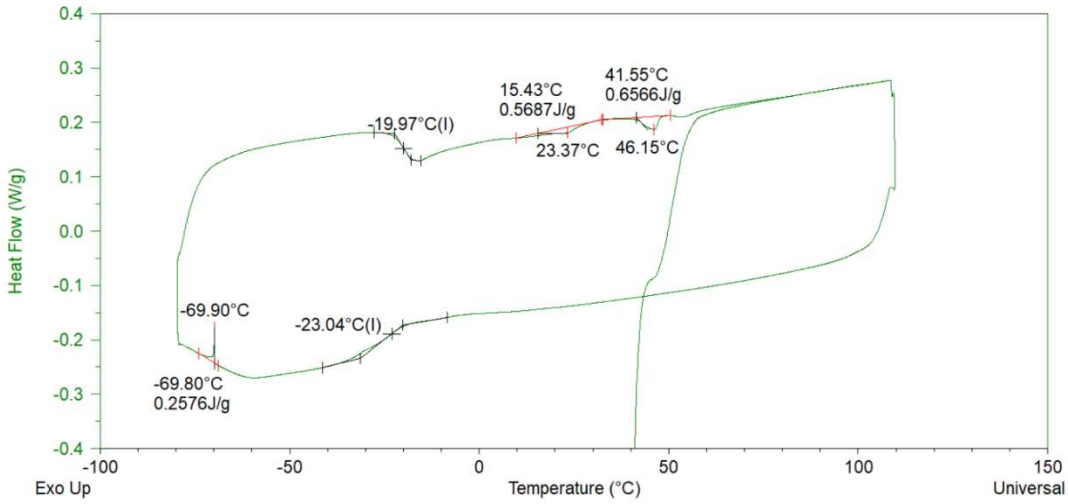

Figure A.5.2. Analysis of DSC curve of PEO200 PU at a rate of 10 °C/min. Sample was degassed in vacuum oven for two hours at 100 °C prior to DSC.

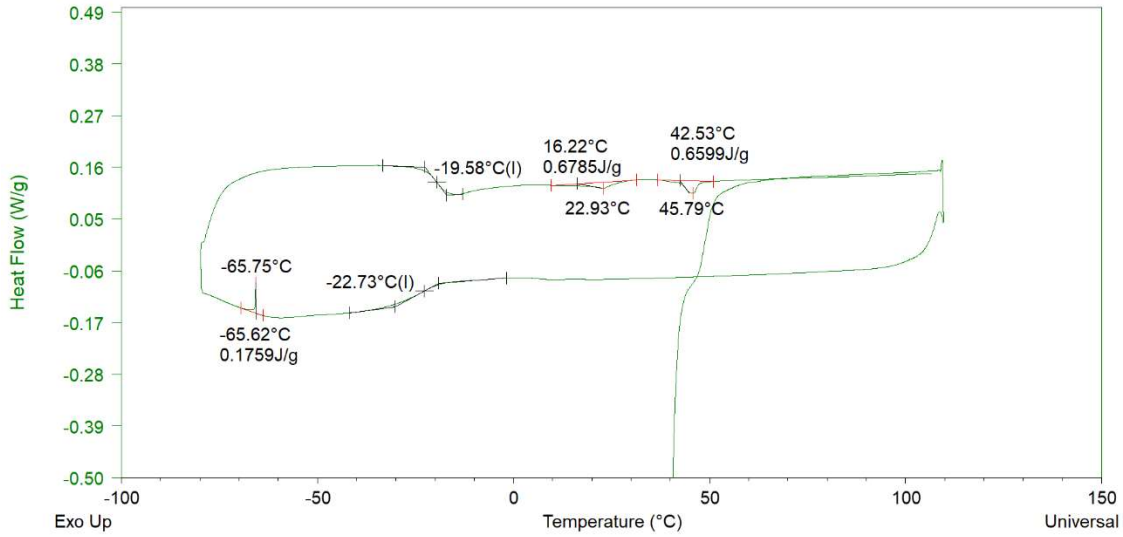

Figure A.5.3. Analysis of DSC curve of PEO200/Gly PU at a rate of 10 °C/min. Sample was degassed in vacuum oven for two hours at 100 °C prior to DSC.

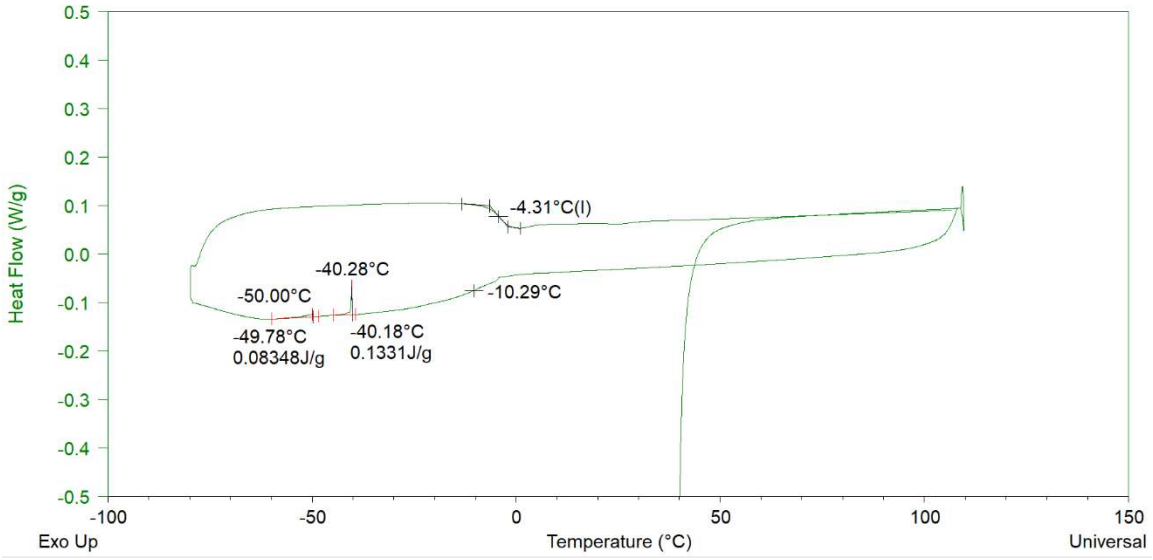

Figure A.5.4. Analysis of DSC curve of PPO192 PU at a rate of 10 °C/min. Sample was degassed in vacuum oven for two hours at 100 °C prior to DSC.

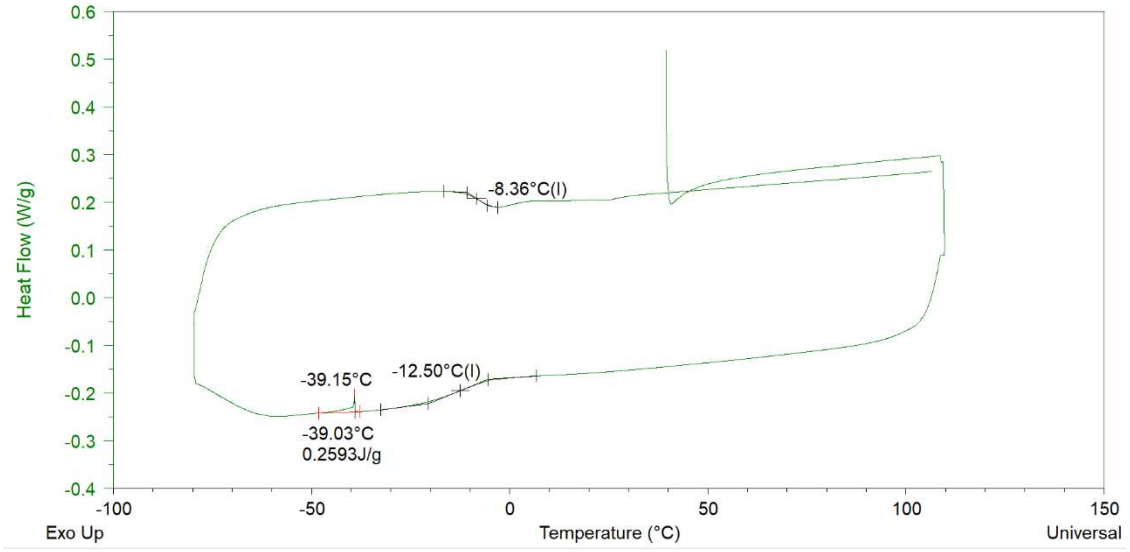

Figure A.5.5. Analysis of DSC curve of PPO192/Gly PU at a rate of 10 °C/min. Sample was degassed in vacuum oven for two hours at 100 °C prior to DSC.

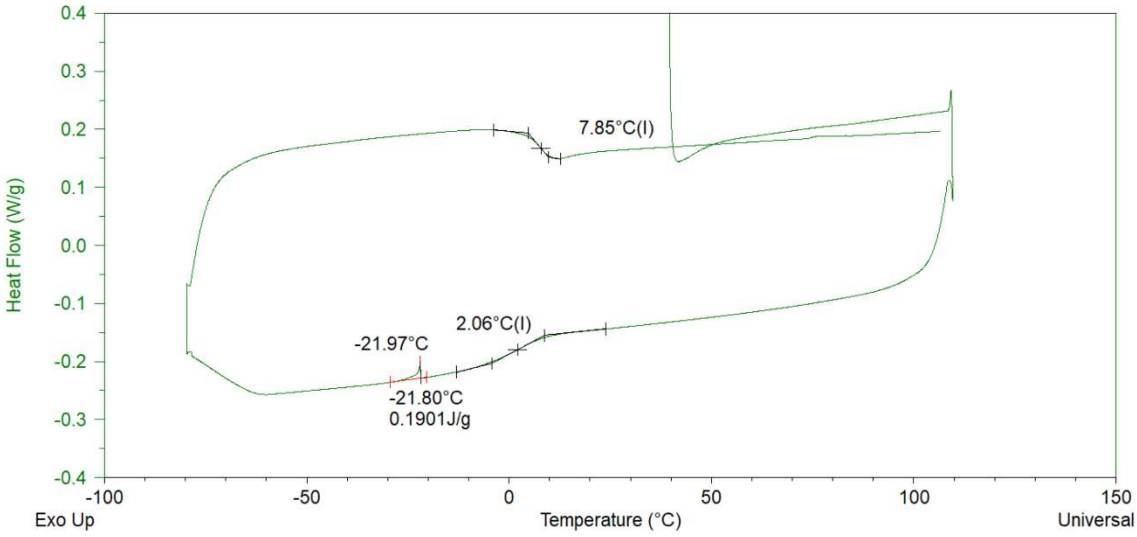

Figure A.5.6. Analysis of DSC curve of PPO192/Trigly PU at a rate of 10 °C/min. Sample was degassed in vacuum oven for two hours at 85 °C prior to DSC.

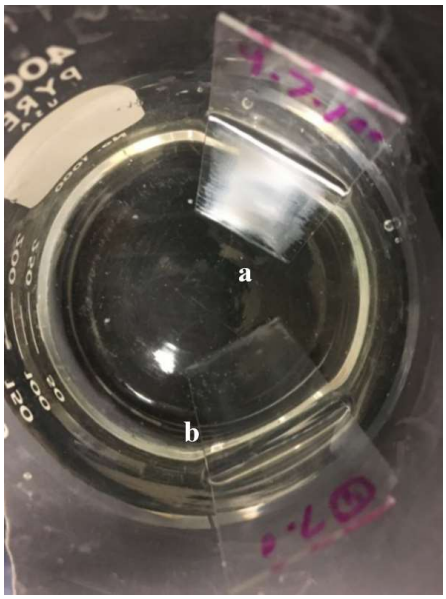

Figure A.5.7. Top view where glass slides have been dipped in a beaker containing 0.1 molar KI salt solution. (a) PPO192 PUD coated glass slide turned turbid; (b) PEO200 coated glass slide did not turn turbid.

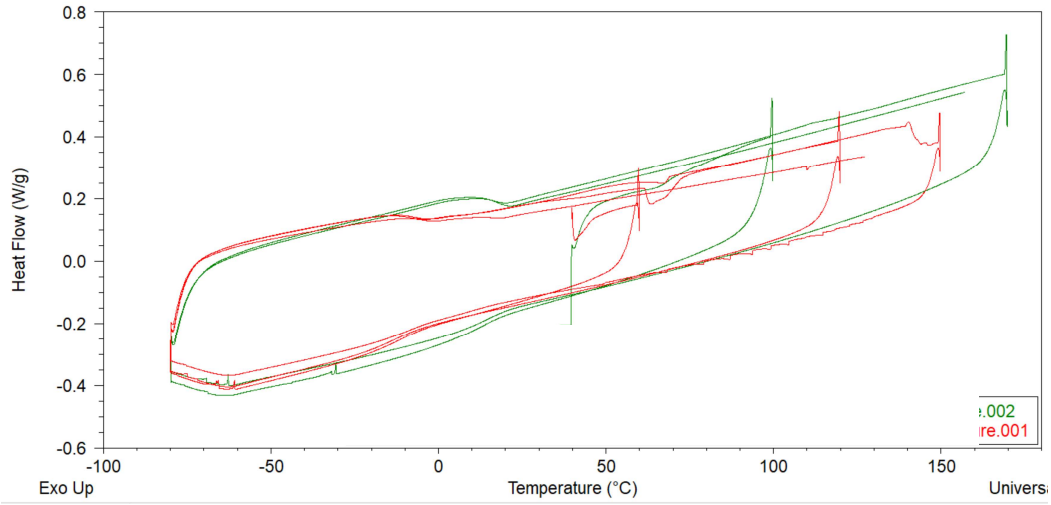

Figure A.5.8. Comparison of dried PPO192/Trigly PUD having photoinitiator before (———) and after UV exposure (———).

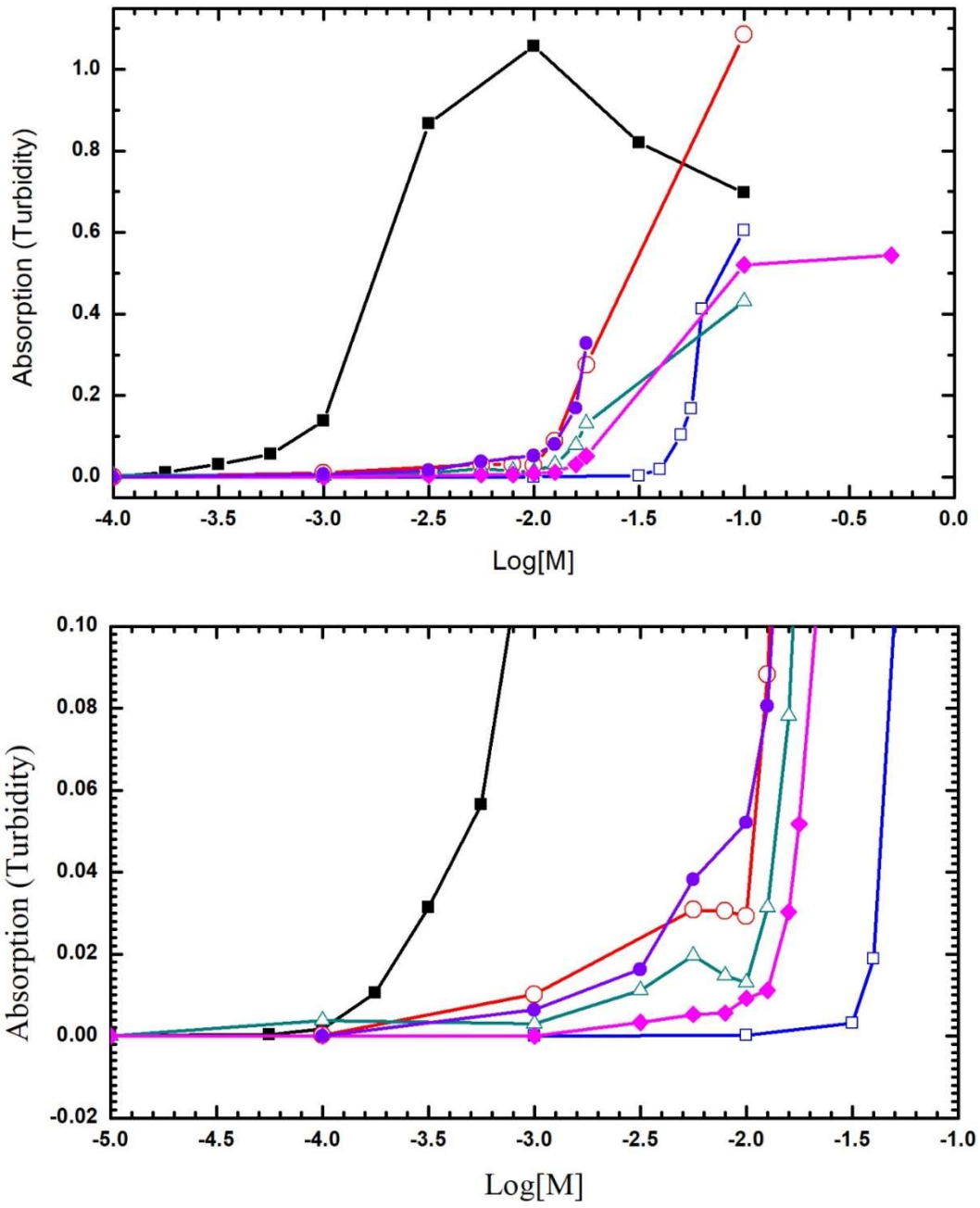

Figure A.5.9. (a) Turbidity (absorption values at 500 nm wavelength of light) of 0.5% sonicated and 1-micron and then 0.45-micron filtered PPO192/Trigly PUD sample after one hour of addition of salt solutions at different concentrations: KPF_6 (—■—); $NaN(CN)_2$ (—○—); NaBr (—□—); $NaBF_4$ (—△—); KI (—◆—); CF_3SO_3Na (—●—); (b) Zoomed-in 'a'.

Appendix E: Supplementary Information for Chapter 6

Figure A.6.1 and Fig. A.6.2 are analyses of DSC curves by using TA Instrument's "Universal Analysis" software.

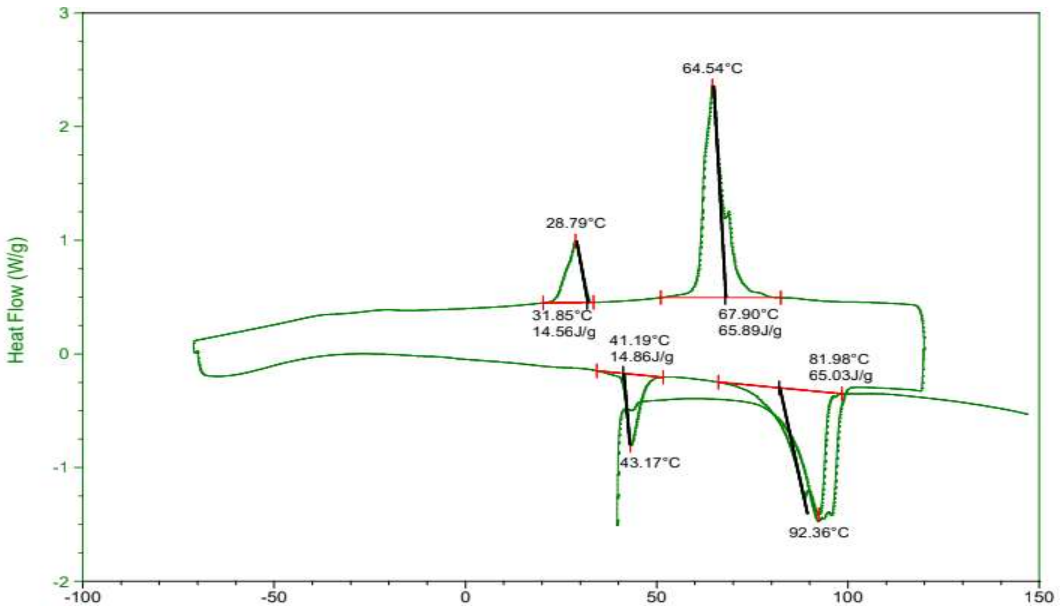

Figure A.6.1. DSCs using rate of 10C/min of HUTEAB washed by THF.

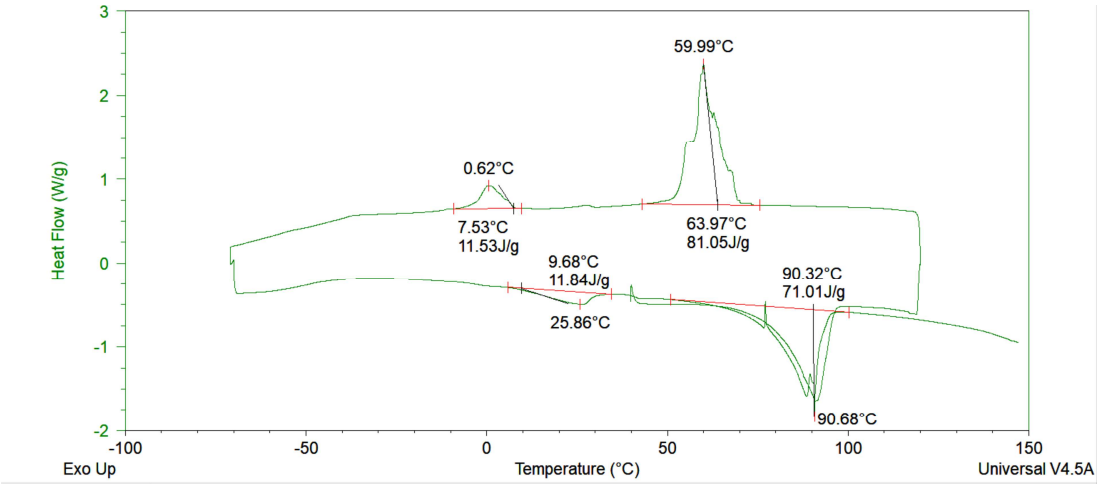

Figure A.6.2. DSCs using rate of 10C/min of HUTEAB recovered from acetonitrile after washing by THF.

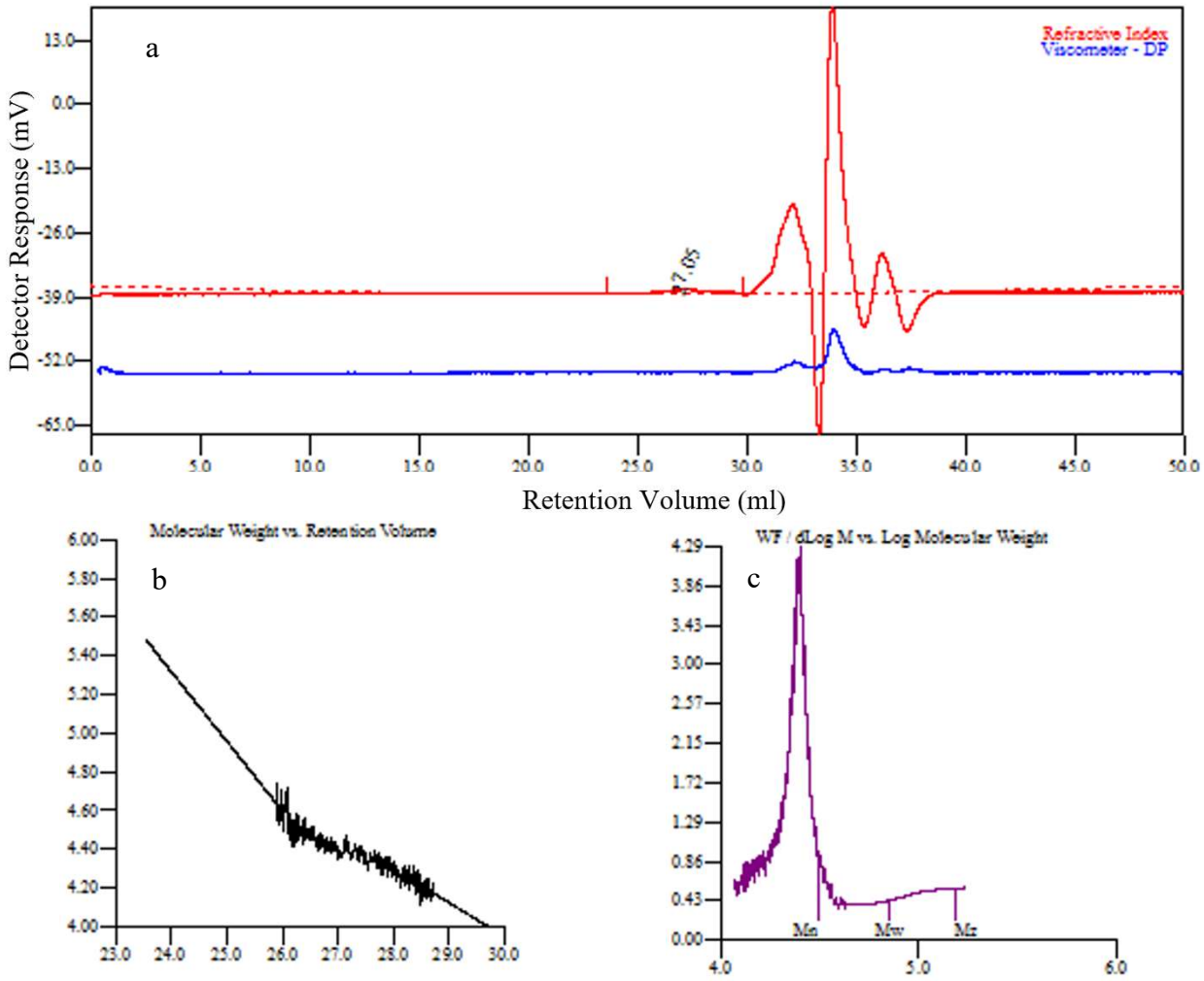

Figure A.6.3. GPC graphs for PEO200 PU resin: (a) detector response (mV) vs retention volume (ml); (b) molecular weight vs retention volume; (c) WF/dLog(M) vs Log (molecular weight).

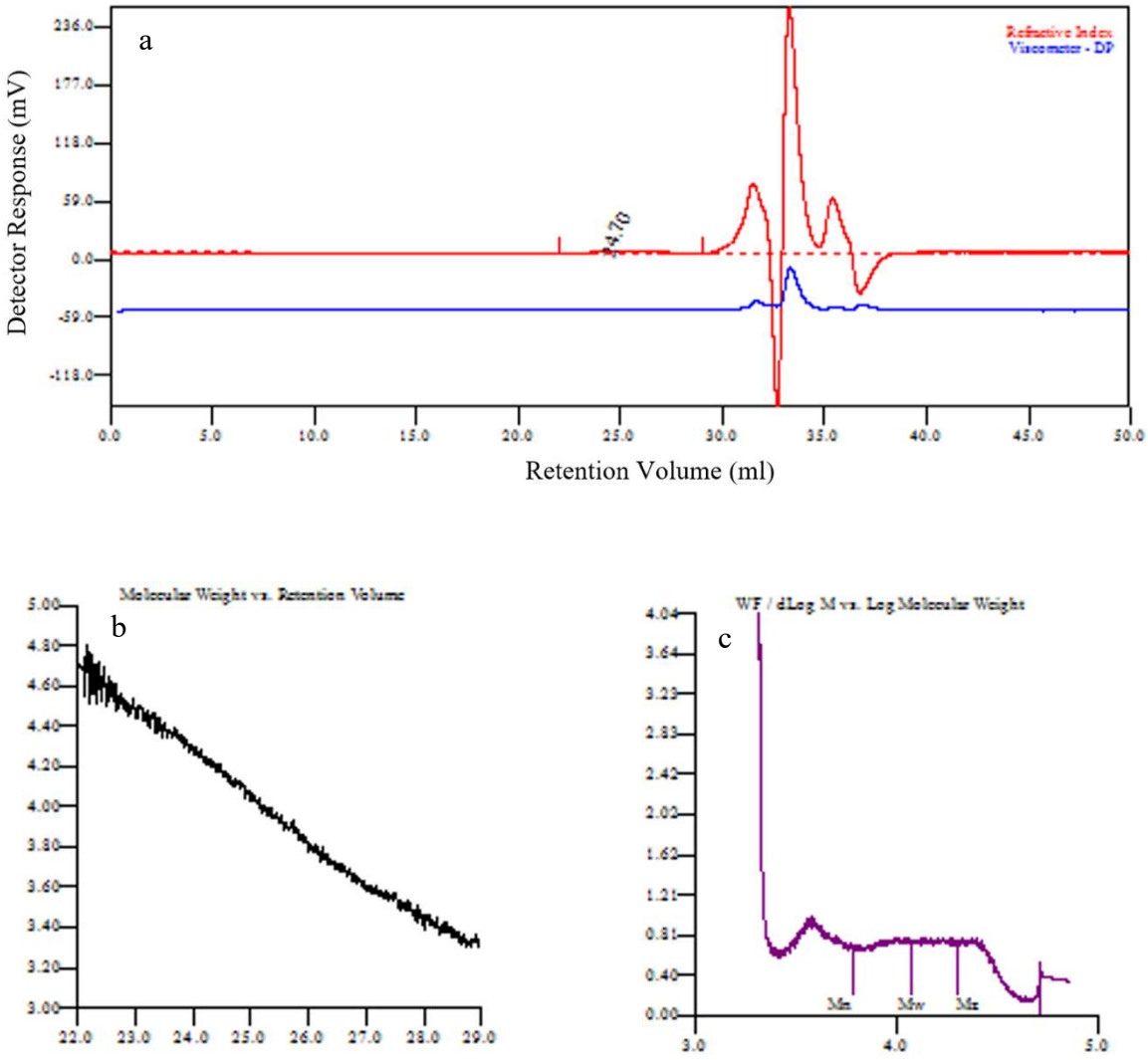

Figure A.6.4. GPC graphs for PPO192 PU resin: (a) detector response (mV) vs retention volume (ml); (b) molecular weight vs retention volume; (c) WF/dLog(M) vs Log (molecular weight).

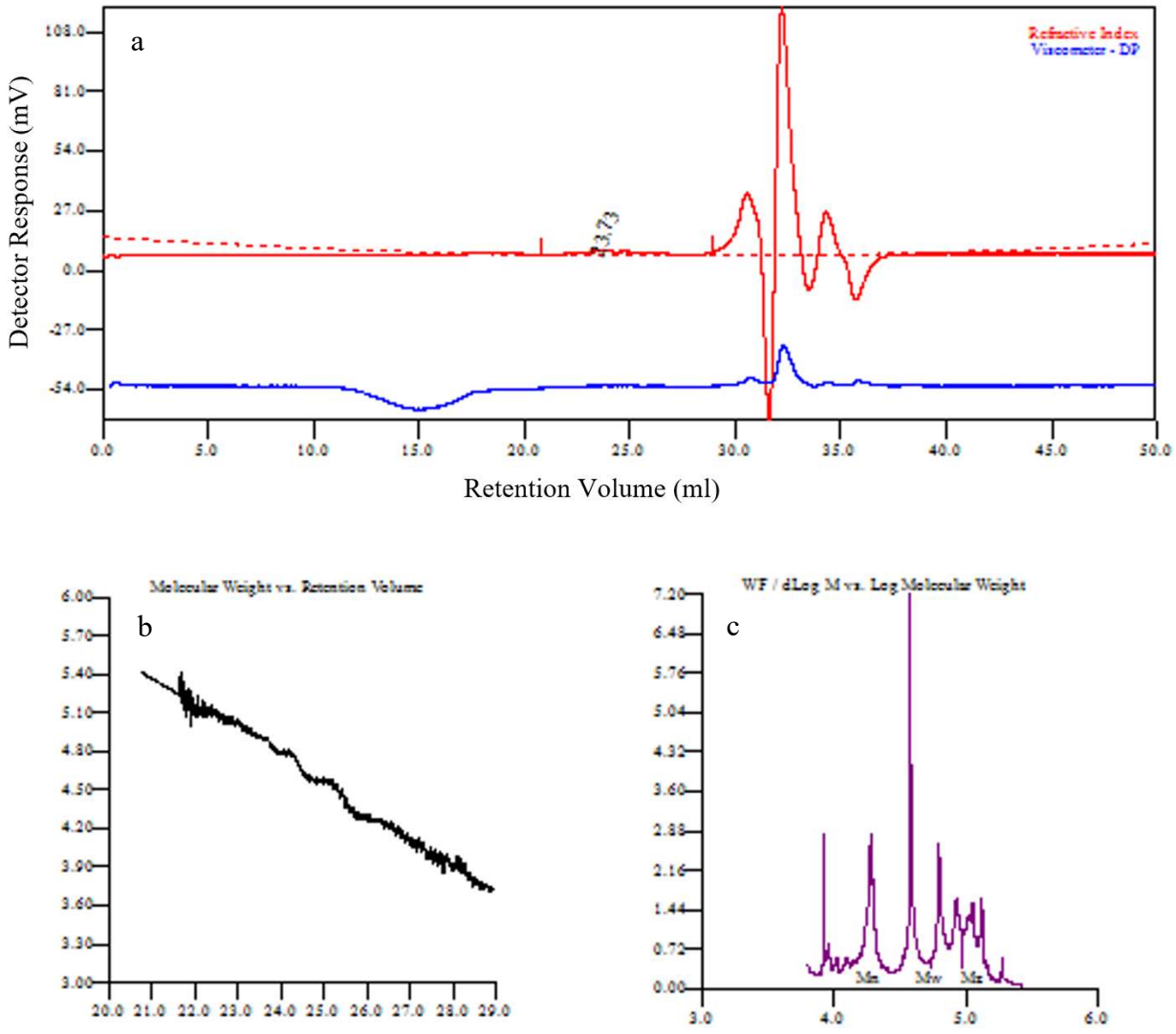

Figure A.6.5. GPC graphs for HUTEAB/PPO192 PU resin: (a) detector response (mV) vs retention volume (ml); (b) molecular weight vs retention volume; (c) WF/dLog(M) vs Log (molecular weight).